

The challenge of design

**EVALUATION OF AND IMPROVEMENTS TO  
BONDED REPAIR SOFTWARE: AOARD-98-4010,  
OCTOBER 2000**

Rhys Jones, B. Whittingham, T. Ting and David Erjavec,  
Department of Mechanical Engineering,  
DSTO Centre of Expertise in Structural Mechanics,  
PO Box 31  
Monash University,  
Monash  
Victoria, Australia. 3800

Phone: 61-3-9905-3809/3572

Fax: 61-3-9905-1825

Email: rhys.jones@eng.monash.edu.au

**DISTRIBUTION STATEMENT A**  
Approved for Public Release  
Distribution Unlimited

Research in *Engineering* at Monash University

<b>REPORT DOCUMENTATION PAGE</b>					<i>Form Approved</i> <b>OMB No. 0704-0188</b>	
<p>The public reporting burden for this collection of information is estimated to average 1 hour per response, including the time for reviewing instructions, searching existing data sources, gathering and maintaining the data needed, and completing and reviewing the collection of information. Send comments regarding this burden estimate or any other aspect of this collection of information, including suggestions for reducing the burden, to Department of Defense, Washington Headquarters Services, Directorate for Information Operations and Reports (0704-0188), 1215 Jefferson Davis Highway, Suite 1204, Arlington, VA 22202-4302. Respondents should be aware that notwithstanding any other provision of law, no person shall be subject to any penalty for failing to comply with a collection of information if it does not display a currently valid OMB control number.</p> <p><b>PLEASE DO NOT RETURN YOUR FORM TO THE ABOVE ADDRESS.</b></p>						
<b>1. REPORT DATE (DD-MM-YYYY)</b> 30-10-2000		<b>2. REPORT TYPE</b> Final			<b>3. DATES COVERED (From - To)</b> 29 Jan 99 – 30 Oct 00	
<b>4. TITLE AND SUBTITLE</b>  Evaluation of and Improvements to Bonded Repair Software					<b>5a. CONTRACT NUMBER</b> F6256299M9056	
					<b>5b. GRANT NUMBER</b>	
					<b>5c. PROGRAM ELEMENT NUMBER</b>	
					<b>5d. PROJECT NUMBER</b>	
<b>6. AUTHOR(S)</b>  Prof. Rhys Jones					<b>5e. TASK NUMBER</b>	
					<b>5f. WORK UNIT NUMBER</b>	
<b>7. PERFORMING ORGANIZATION NAME(S) AND ADDRESS(ES)</b> Monash University Dept of Mechanical Engineering Clayton Victoria 3168 Australia					<b>8. PERFORMING ORGANIZATION REPORT NUMBER</b>  N/A	
<b>9. SPONSORING/MONITORING AGENCY NAME(S) AND ADDRESS(ES)</b>  AOARD UNIT 45002 APO AP 96337-5002					<b>10. SPONSOR/MONITOR'S ACRONYM(S)</b>  AOARD	
					<b>11. SPONSOR/MONITOR'S REPORT NUMBER(S)</b> AOARD-98-10	
<b>12. DISTRIBUTION/AVAILABILITY STATEMENT</b>  Approved for public release; distribution is unlimited.						
<b>13. SUPPLEMENTARY NOTES</b>						
<p><b>14. ABSTRACT</b> Verification of procedures and mathematical tools used for bonded repair design is essential in providing an efficient and feasible repair. The RAAF Engineering standard C5033 uses such tools and was introduced to provide a conservative design approach to bonded repairs. Using this standard in conjunction with a valid design case provides for a baseline repair design that can be used to validate the CalcuRep software package. The particular cost study used for this purpose is the 1994 F-111C Lower Wing Skin Boron Repair.</p> <p>Chapter 1: Evaluation of the USAF CalcuRep Software for the Design of Bonded Repairs to Metallic Aircraft Structure  Appendix A: Corrections to Equation Discrepancies  Chapter 2: Enhancements to the Design Procedures for Bonded Repairs to Metallic Aircraft Structures Including Single Sided Unsupported Repairs  Appendix A: MathCad Modules  Chapter 3: Numerical Analysis and Testing</p>						
<b>15. SUBJECT TERMS</b>  Aging Aircraft						
<b>16. SECURITY CLASSIFICATION OF:</b>			<b>17. LIMITATION OF ABSTRACT</b>  UU	<b>NUMBER OF PAGES</b>  175	<b>19a. NAME OF RESPONSIBLE PERSON</b> Michele Gaudreault, Maj, USAF	
<b>a. REPORT</b>  U	<b>b. ABSTRACT</b>  U	<b>c. THIS PAGE</b>  U			<b>19b. TELEPHONE NUMBER (Include area code)</b> +81-3-5410-4409	

# CHAPTER 1: EVALUATION OF THE USAF CALCUREP SOFTWARE FOR THE DESIGN OF BONDED REPAIRS TO METALLIC AIRCRAFT STRUCTURE

David Erjavec<sup>1</sup> and Kevin Walker<sup>2</sup>

<sup>1</sup> Department of Mechanical Engineering, Monash University, Clayton, Vic 3168, Australia

<sup>2</sup> Airframes and Engines Division, Aeronautical Research Laboratory, Defence Science and  
Technology Organisation, 506 Lorimer St, Pt Melbourne, Victoria, 3207, Australia.

## CONTENTS

1. BACKGROUND.....	2
2. INTRODUCTION.....	3
3. EXISTING TOOLS AND TECHNIQUES .....	3
3.1 RAAF Engineering Standard C5033 .....	3
3.1.1 Overview of the C5033 Approach .....	3
3.1.1.1 Determination of Patch Thickness .....	4
3.1.1.2 Evaluate Rapid Repairability Criterion (RRC).....	5
3.1.1.3 Assess Structural Integrity of the Repaired Structure .....	6
3.1.2 Evaluate Repair and Structure for Fatigue Susceptibility.....	12
3.1.1.4 Establish Patch Dimensions.....	13
3.1.1.5 Determine Inspection requirements .....	15
3.1.2 Limitations of C5033.....	15
3.1.2.1 Strong Biaxial Loading Applications .....	15
3.1.2.2 Unsupported Single-Sided Repairs.....	16
3.1.3 Improvements made Since Release of the Original Document .....	16
3.2 CalcuRep.....	17
3.2.1 Overview of the CalcuRep Approach .....	17
3.2.2 Limitations of CalcuRep .....	28
3.2.3 Errors Identified .....	30
4 CASE STUDY OF THE F-111C LOWER WING SKIN REPAIR.....	34
4.1 Material Input Data .....	35
4.2 Analytical Comparison .....	38
4.2.1 Case1: -40 F .....	38
4.2.2 Case1: -25 F .....	38
4.2.3 Case3: 75 F.....	39
4.2.4 Case1: 167 F.....	39
5 DISCUSSION.....	39
6 CONCLUSIONS AND RECOMMENDATIONS .....	44
7 REFERENCES.....	45

## 1. BACKGROUND

Bonded repair technology provides enhanced structural efficiency to extend the fatigue life of aircraft structures. It provides industry with an efficient and cost effective solution to aircraft structural defects. This has prompted many organisations to use bonded repair technology as a preferred repair method over mechanically fastened repairs.

The USAF has utilised bonded repair technology to prolong the structural lives of aircraft such as the F-16 and the C130. But the verification process of such repairs can be expensive and time consuming, since detailed Finite Element Analysis and testing may be required to ensure an efficient repair. The use of validated analytical procedures for deriving repairs is therefore desirable to reduce verification and testing time. The US Airforce academy has developed a software package called "CalcuRep" for this purpose.

Robert Fredell and Walter VanBarneveld first developed CalcuRep at Delft University in the early 1990's. Based on work done by Robert Fredell [1] at the Delft University of Technology, CalcuRep was designed to repair cracks specifically on an Aluminium aircraft fuselage. This initial version of the software was developed in DOS and provided the user with repair design tools with a basic user interface. This prompted the development of CalcuRep for Windows (Beta) at the US Air Force Academy in 1994, which consisted of a user-friendly menu system and a graphical interface. CalcuRep for Windows Version 1.0 [2], released in 1997, incorporated user requirements and suggestions.

The RAAF Engineering Standard C5033 [3, 4, 5] was released in 1994 to provide bonded repair design tools to assist in the repair of structural defects in aircraft used by the RAAF. Aimed more towards providing engineers with a set of design standards rather than a software package, C5033 provides a set of constraints to ensure quality of repair design, specifications and application processes.

In early 1999, the US Air Force Academy awarded a contract through the DSTO Centre of Expertise at Monash University to verify and extend the capability of CalcuRep version 1.0 for Windows. The work is noted as the CalcuRep review task. The verification aspect of the task (known as part 1 of the work) was performed by comparing the CalcuRep approach with the RAAF Engineering Standard C5033 procedures. A significant example case of a RAAF F-111C wing repair was used to compare the CalcuRep and C5033 repair design techniques. The results are detailed in this report.

Part 2 of the task was to extend the capability of CalcuRep to include unsupported single-sided repairs and repairs to stiffened panels. The results for part 2 are detailed in Chapter 2.

The work compiled in reference [8] establishes a new design approach from the most recent works developed at the DSTO in the field of bonded repair design. Applying these recent findings in such a manner to design repairs will prove to benefit both the DSTO and the USAF. The content of reference [8] may also be considered by the RAAF in expanding the current RAAF Engineering Standard C5033 to deal with single-sided repairs to unsupported structure. But overall, this task proves to be beneficial to both the USAF and the DSTO by attempting to reduce any differences between the US and Australian repair design methodologies.

## 2. INTRODUCTION

Verification of procedures and mathematical tools used for bonded repair design is essential in providing an efficient and feasible repair. The RAAF Engineering standard C5033 uses such tools and was introduced to provide a conservative design approach to bonded repairs. Using this standard in conjunction with a valid design case provides for a baseline repair design that can be used to validate the CalcuRep software package. The particular case study used for this purpose is the 1994 F-111C Lower Wing Skin Boron Repair.

Part 1 of the CalcuRep review consists of two steps as follows:

- a A detailed review of the CalcuRep approach to repair design and analysis, and
- b A case study comparison using CalcuRep to analyse a bonded composite repair to the lower wing skin of a RAAF F-111C aircraft, originally designed according to the RAAF Engineering Standard C5033 [3].

Several errors and limitations were identified and corrected. A revised version of the CalcuRep code was then implemented in a Mathcad module [9] and used to analyse the F-111 repair case. The results are detailed in this report.

## 3. EXISTING TOOLS AND TECHNIQUES

### 3.1 RAAF Engineering Standard C5033

#### 3.1.1 Overview of the C5033 Approach

Designing an effective repair is essential in extending aircraft structural life. Assuring the quality of repair design, specifications and processes is fundamental in achieving this goal. The RAAF engineering standard C5033 [3] in conjunction with the following two documents, AAP 7021.016-1 [4] and AAP 7021.016-2 [5] has been developed to manage these issues. Mr Max Davis, a Senior Research Scientist for the RAAF, conducts two tuition courses on the Standard. The first is a familiarisation course centred towards providing the basic concepts behind repairs and processes,

while the second details repair design, specification and process techniques. The courses are held twice annually at the RAAF Base Amberley, Queensland. C5033 provides design methods for the following repair cases, assuming the patch and parent structure to be both isotropic:

- Double Sided Bonded Repairs
- Single Sided Supported Bonded Repairs
- Single Sided Supported Bonded Repairs to a Part Through Thickness Defect
- Single Sided Supported Bonded Doubler
- Double Sided Bonded Doubler
- Single Sided Supported Bonded Repairs for Stress Corrosion Cracking
- Double Sided Bonded Repairs for Stress Corrosion Cracking
- Scarf Repairs to Composite Structures

C5033 does not equip the user with a software package. Instead it provides strict guidelines on repair design, specification and processes. Therefore the user must perform repair design calculations either manually, or by programming them into an appropriate software package. MathCad version 8.0 [9] was used in this report for this purpose, since it provides visual inspection of the equations used and quick accessibility of user input data.

An overview of C5033's design methodology for single-sided supported repairs to a cracked structure is presented below:

### 3.1.1.1 Determination of Patch Thickness

Restoration of stability and compatibility characteristics of a cracked or cut-out structure is a result of restoring the original stiffness of the structure. C5033 restores the original stiffness of the structure by providing the following limitation on patch design thickness.

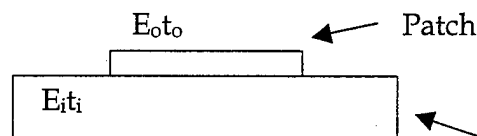


Figure 1 Parent Material or Structure

$$\frac{E_i t_i}{E_o} \leq t_o \leq \frac{1.2 E_i t_i}{E_o} \quad (1)$$

Here	$E_i$	Elastic Modulus of the Parent Material
	$E_o$	Elastic Modulus of the Patch
	$t_i$	Thickness of the Parent Material

$t_o$  Thickness of the Patch

### 3.1.1.2 Evaluate Rapid Repairability Criterion (RRC)

The rapid repairability criterion is a management tool to ensure the adhesive is never the critical element in a repaired joint.

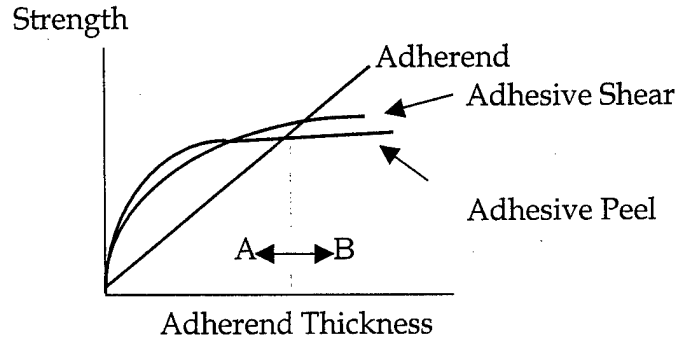


Figure 2

Provided the adhesive operates within region 'A' shown above, the parent material will fail before the adhesive does. On the other hand, adhesives operating in section B above will fail before the parent material does. An adhesive will never be the critical element (therefore operates within region A above) in a repaired joint provided its load capacity can meet the following criteria.

$$P \geq 1.2 \times \sigma_{ULT} \times t_i \quad (2)$$

where 'P' is the lesser of

$$P = 2E_i t_i \left[ (\alpha_o - \alpha_{ieff}) (RT - T_{cure}) + (\alpha_o - \alpha_i) (T_{oper} - RT) \right] + \sqrt{2\eta\tau_p \left( \frac{1}{2}\gamma_e + \gamma_p \right) E_i t_i \left( 1 + \frac{E_i t_i}{E_o t_o} \right)} \quad (3)$$

or

$$P = 2E_o t_o \left[ (\alpha_{ieff} - \alpha_o) (RT - T_{cure}) + (\alpha_i - \alpha_o) (T_{oper} - RT) \right] + \sqrt{2\eta\tau_p \left( \frac{1}{2}\gamma_e + \gamma_p \right) E_o t_o \left( 1 + \frac{E_o t_o}{E_i t_i} \right)} \quad (4)$$

$$\alpha_{ieff} = \frac{\alpha_i (1 + \nu_i)}{2} \quad (5)$$

Here P Load capacity of the adhesive  
 $\alpha_o$  Coefficient of Thermal Expansion of the Patch  
 $\alpha_i$  Coefficient of Thermal Expansion of the Parent material  
 $\alpha_{ieff}$  Effective Coefficient of Thermal Expansion of the Parent material  
RT Room Temperature  
 $T_{cure}$  Cure Temperature

$T_{oper}$	Operating Temperature
$\eta$	Adhesive Thickness
$\tau_p$	Adhesive Plastic Shear Stress Limit
$\gamma_E$	Adhesive Elastic Shear Strain Limit
$\gamma_P$	Adhesive Plastic Shear Strain Limit
$\sigma_{ULTi}$	Ultimate Strength of the Parent Material

Equations (3) and (4) were developed by Hart-Smith [10] and include a bi-linear thermal residual stress modification developed by Mr Max Davis to allow for both the cure and aircraft operating cycles, and will be discussed in more detail in Section 3.1.3.

### 3.1.1.3 Assess Structural Integrity of the Repaired Structure

#### Step 1 Calculate the Applied Stress ( $\sigma^*$ )

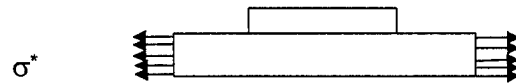


Figure 3

The applied stress is determined as follows:

- Where the design ultimate load is known, it must be used.
- Where the design limit load is known, the applied stress will be 1.5 times the design limit load.
- Where the design ultimate and/or the design limit load are not known, the applied stress is taken as the lower value of material ultimate strength or 1.5 times the yield strength. Load path, stress concentrations, net section stresses and buckling limitations must be taken into account.

#### Step 2 Assess Structural Integrity at the end of the Patch

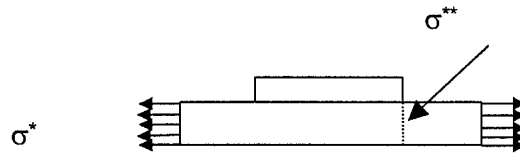


Figure 4

The stress in the structure at the end of the patch can be expressed by the following:

$$\sigma^{**} = \Omega_L \sigma^* + E_i \left( (\alpha_o - \alpha_{ieff}) (RT - T_{cure}) + (\alpha_o - \alpha_i) (T_{oper} - RT) \right) \quad (6)$$

where,  $\Omega_L$  is the load attraction factor

Equation 6 consists of two components, an applied stress component as per [11], and a thermal residual stress component as per [12].



- The Load Attraction Factor

Load is attracted into the repaired region due to the inclusion of extra stiffness provided by the patch as shown below:

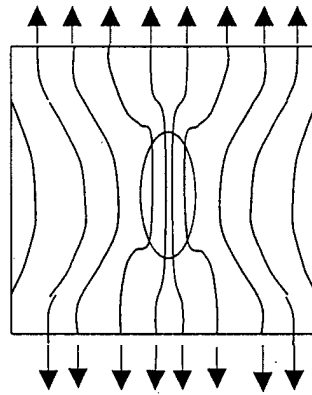


Figure 5

In a uniaxial load case, the following stresses are attracted into the repaired region, which is denoted as section A-A.

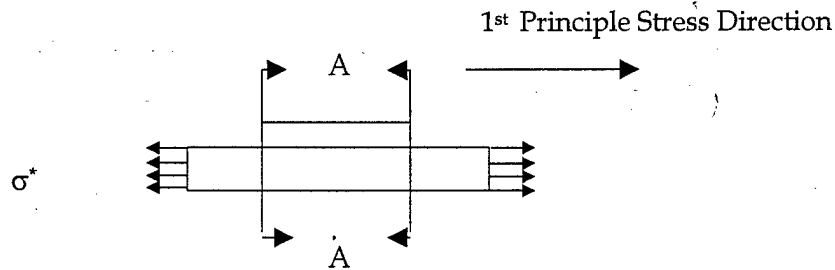


Figure 6

Section A-A is shown below

1st Principal Stress Direction



Figure 7

2nd Principal Stress Direction

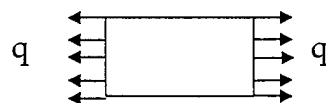


Figure 8

Here 'p' and 'q' are the resultant stress components attracted into the repaired region. Therefore the load attraction factor becomes [11]:

$$\Omega_L = \frac{\sigma^* + p}{\sigma^*} \quad (7)$$

C5033 does not calculate this value, but instead uses a typically conservative value for the load attraction as follows:

$$\Omega_L = 1.2$$

The required margin of safety for  $\sigma^{**}$  is as follows:

$$\sigma_{ULTI} / \sigma^{**} - 1 > 0.2$$

### Step 3 Determine the Stress Under the Repair

The stress in the structure at the edge of the patch is distributed between the parent material and the patch inside the repaired region. The corresponding stress distributed into the parent structure [11] is as follows:

$$\sigma_o = \frac{E_i t_i}{E_o t_o + E_i t_i} \sigma^{**} \quad (8)$$

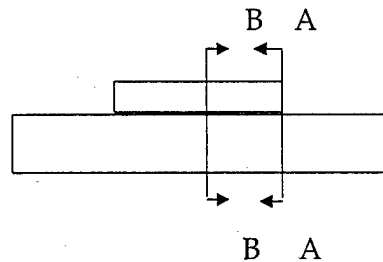


Figure 9

Here section A-B is as shown below

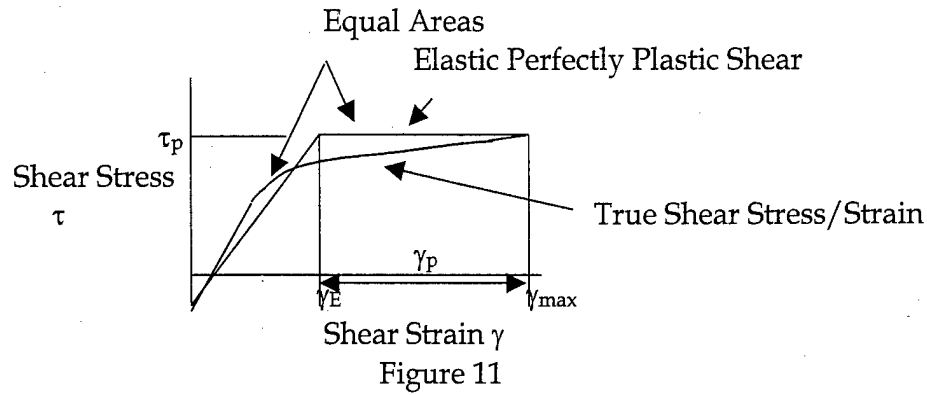


Figure 10

where  $\sigma_o$  is the stress under the repair in the absence of a flaw  
 $\sigma_R$  is the stress in the repair in the absence of a flaw

### Step 4 Evaluate the Adhesive Shear Strain

The adhesive shear strain calculation relies on an elastic perfectly plastic shear stress/strain curve assumption. This assumption is reasonable provided conservation of strain energy is achieved between the true shear stress/strain curve and the equivalent elastic perfectly plastic shear stress/strain curve, see Figure 11.



where

$$\gamma_{\max} = \gamma_E + \gamma_P \quad (9)$$

The maximum elastic shear strain [13] is given as follows:

$$\gamma_o = \frac{\sigma_o t_i \lambda}{G} \quad (10)$$

where,  $\lambda$  Elastic Exponent  
 $G$  Adhesive Shear Modulus

The elastic Exponent is given by [13]:

$$\lambda = \sqrt{\frac{G}{\eta} \left( \frac{1}{E_i t_i} + \frac{1}{E_o t_o} \right)} \quad (11)$$

If  $\gamma_o \geq \gamma_E$ , the adhesive is plastic and equation 10 is replaced by the following:

$$\gamma_o = \frac{\tau_p}{2G} \left( 1 + \left( \frac{\sigma_o t_i \lambda}{\tau_p} \right)^2 \right) \quad (12)$$

It is required that  $\frac{\gamma_E + \gamma_P}{\gamma_o} - 1 > 0.2$

**Step 5 Determine the Reduced Stress Intensity Factor in the Structure Post Repair.**

Reference [11] demonstrates that the stress intensity factor for an adhesive bonded repair never exceeds a limiting value.

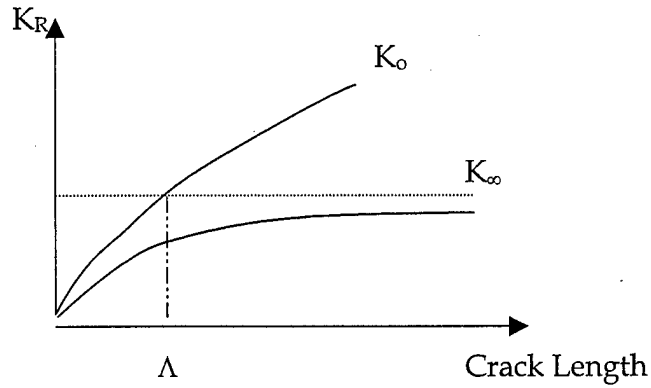


Figure 12

where  $K_R$  Stress Intensity Factor (SIF) after repair  
 $K_o$  Stress Intensity Factor before repair  
 $K_\infty$  Upper Bound or Limiting Stress Intensity Factor

#### • Characteristic Crack Length

The characteristic crack length is a physical parameter independent of actual crack length and applied stress and provides the upper bound stress intensity factor through the following relationship.

$$K_\infty = \sigma_o (\pi \Lambda)^{1/2} \quad (13)$$

Depending on whether the adhesive is elastic or plastic, the following two equations are commonly used to predict this upper bound stress intensity factor.

Elastic Behaviour in the adhesive [11]

$$K_\infty = \sigma_o \sqrt{\frac{E_i t_i \lambda \eta}{G}} \quad (14)$$

Plastic Behaviour in the adhesive [13] & [14]

$$K_\infty = \sqrt{\frac{E_i \eta}{G} \left[ \sigma_o \tau_p \left( 1 + \left( \frac{\sigma_o \lambda t_i}{\tau_p} \right)^2 \right) - \frac{\tau_p^2}{3 \lambda t_i} \left( 1 + 2 \left( \frac{\sigma_o \lambda t_i}{\tau_p} \right)^3 \right) \right]} \quad (15)$$

It is required that  $\frac{K_C}{K_\infty} - 1 > 0.2$ .

Where  $K_C$  Parent Material Fracture Toughness.

### Step 6 Calculate Peel Stress

Peel stresses occur due to load path eccentricity inherent in single-sided repairs. The maximum peel stress likely to occur in a single-sided repair is [10]:

$$\sigma_{C \max} = \tau_p \left( \frac{3E'_C t_o (1 - \nu_i^2)}{E_o \eta} \right)^{\frac{1}{4}} \quad (16)$$

where  $\sigma_{C \max}$  Maximum Peel Stress  
 $E'_C$  Effective Transverse Tensile Modulus for the Adhesive

The effective transverse tensile modulus of an adhesive for a joint comprising of dissimilar materials can be approximated by

$$\frac{1}{E'_C} = \frac{1}{E_C} + \frac{2}{E_i} + \frac{4}{E_o} \quad (17)$$

where  $E_C$  Elastic Modulus of the Adhesive System.

Reliable peel stress data is not readily available. There is also no current test procedure to determine a valid peel stress allowable, therefore Hart-Smith [15] devised the following general guide-line values:

$$\begin{aligned} \sigma_{C \max} &\leq 6000 \text{ psi (Brittle Adhesive Systems)} \\ \sigma_{C \max} &\leq 10000 \text{ psi (Ductile Adhesive Systems)} \end{aligned}$$

### Step 7 Assess the Structural Integrity of the Patch

The structural integrity of a patch is found assuming the entire load is transferred into the patch. This assumption is valid provided the actual crack length is sufficiently larger than the characteristic crack length [11]:

$$\sigma_p = \frac{t_i}{t_o} \sigma^{**} \quad (18)$$

It is required that  $\frac{\sigma_{ULTo}}{\sigma_p} > 1.2$ , where,  $\sigma_{ULTo}$  is the ultimate strength of the patch.

### 3.1.2 Evaluate Repair and Structure for Fatigue Susceptibility

This section is used to eliminate fatigue critical repairs. Note, it does not provide a crack growth calculation. To deem a repair fatigue uncritical, the repair must demonstrated fatigue resistance when subject to a constant amplitude fatigue loading with a maximum cyclic load ( $\sigma_f$ ) equal to the lower of:

- 60% of DLL (where known) or
- 40% of  $\sigma^*$

at a stress ratio of  $R=0$ .

Fatigue susceptibility is determined as follows.

- **Step 1 Evaluate the Fatigue Susceptibility of the Structure at the end of the Patch.**

$$\sigma^{##} = \Omega_L \sigma_f + E_i \left( (\alpha_o - \alpha_{ieff}) (RT - T_{cure}) + (\alpha_o - \alpha_i) (T_{oper} - RT) \right) \quad (19)$$

where  $\sigma^{##}$  is the stress at the edge of the repair due to the fatigue loading.

Check if reference data contains anticipated damage at a stress level of  $\sigma^{##}$ . If so, check whether this level of damage is acceptable for the corresponding repair case.

- **Step 2 Stress Under the Patch**

$$\sigma^{\#} = \frac{E_i t_i}{E_o t_o + E_i t_i} \sigma^{##} \quad (20)$$

Where,  $\sigma^{\#}$  Stress under the repair due to the fatigue loading.

- **Step 3 Calculating the Adhesive Shear Strain at the Defect**

$$\gamma_f = \frac{\sigma^{\#} t_i \lambda}{G} \quad (21)$$

If  $\gamma_o \geq \gamma_E$ , the adhesive has become plastic and the adhesive shear strain is given by:

$$\gamma_f = \frac{\tau_p}{2G} \left( 1 + \left( \frac{\sigma^{\#} t_i \lambda}{\tau_p} \right)^2 \right) \quad (22)$$

Where,  $\gamma_f$  Maximum Shear Strain in the adhesive due to the fatigue loading.

The adhesive is said to be fatigue resistant if the following condition is met.

$$\gamma_f < 2\gamma_E$$

- **Step 4 Calculate the Stress Intensity Factor in the Repair Parent Material**

Elastic Behaviour in the adhesive

$$K_{\infty f} = \sigma^{\#} \sqrt{\frac{E_i t_i \lambda \eta}{G}} \quad (23)$$

Plastic Behaviour in the adhesive

$$K_{\infty f} = \sqrt{\frac{E_i \eta}{G} \left[ \sigma^{\#} \tau_p \left( 1 + \left( \frac{\sigma^{\#} \lambda t_i}{\tau_p} \right)^2 \right) - \frac{\tau_p^2}{3 \lambda t_i} \left( 1 + 2 \left( \frac{\sigma^{\#} \lambda t_i}{\tau_p} \right)^3 \right) \right]} \quad (24)$$

where  $K_{\infty f}$  is the upper bound SIF due to the fatigue loading

Using crack growth data for the parent structure, compare the reduction in the crack growth rates between the SIF produced above and the unrepaired SIF. An extension to allow for visplastic adhesive behaviour is given in Chapter 3.

- **Step 5 Check the Fatigue Resistance of the Patch**

$$\sigma_{pf} = \frac{t_i}{t_o} \sigma^{\#\#} \quad (25)$$

where  $\sigma_{pf}$  Maximum stress in the patch due to the fatigue loading.

Check if reference data contains anticipated damage at a stress level of  $\sigma_{pf}$ . Determine whether this level of damage is acceptable for the repair case.

### 3.1.1.4 Establish Patch Dimensions

#### Patch Length

The elastic load transfer length is the inverse of the elastic exponent (Equation 11). To provide creep resistance, a factor of 3 has been introduced as shown in equation 27. The plastic load transfer length [18] has been derived to be sufficiently large enough to carry all of the unnotched parent material ultimate stress. The total length of the patch must include any pre-existing bond-line defects such as fastener heads.

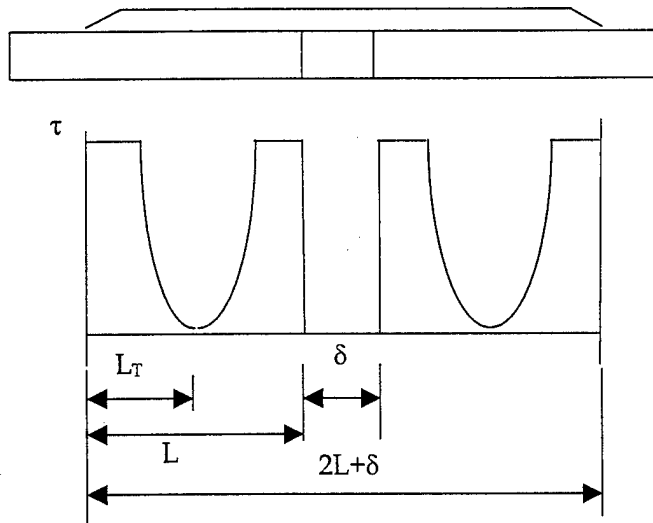


Figure 13

$$L_T = l_e + l_p \quad (26)$$

$$l_e = \frac{3}{\lambda} \quad (27)$$

$$l_p = \frac{\sigma_{ULTi} t_i}{2 \tau_p} \quad (28)$$

where  $L_T$  Total transfer length  
 $L$  Overlap Length  
 $l_e$  Elastic Load Transfer Length  
 $l_p$  Plastic Load Transfer Length  
 $\delta$  Defect Size

#### • Patch Width

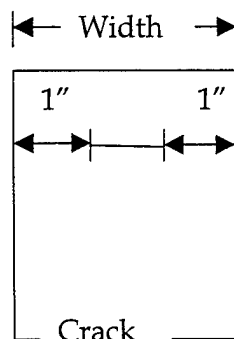


Figure 14



### 3.1.1.5 Determine Inspection requirements

In order to ensure the adhesive is never the critical element, the total length of defects in a given line must be less than or equal to  $\phi_{\max}$ :

$$\phi_{\max} = 2(l_p + l_e) - l_{\min} \quad (29)$$

where 
$$l_{\min} = 1.5 \times 2l_p \quad (30)$$

If the defect size is greater than this value, the joint will not be able to transfer material ultimate stress through the plastic zone at all times. A margin of safety of 50% is recommended.

### 3.1.2 Limitations of C5033

Two major limitations of the RAAF Engineering Standard C5033 are the inability to deal with the following scenarios:

- Strong Biaxial Loading Applications
- Unsupported single sided repairs
- Limited treatment of interlaminar failure mechanisms in the patch
- Limited treatment of visco-plastic behaviour in the adhesive.

#### 3.1.2.1 Strong Biaxial Loading Applications

If the parent structure and repair material have identical Poisson's ratios and are assumed to be isotropic, 2<sup>nd</sup> direction principal stresses, i.e.  $\sigma_y + q$  (see Figure 15), do not influence the stress in the major direction under the patch. However, if the Poisson's ratios differ in a significant biaxial stress field, the stress under the repair will be effected significantly by both principal stresses.

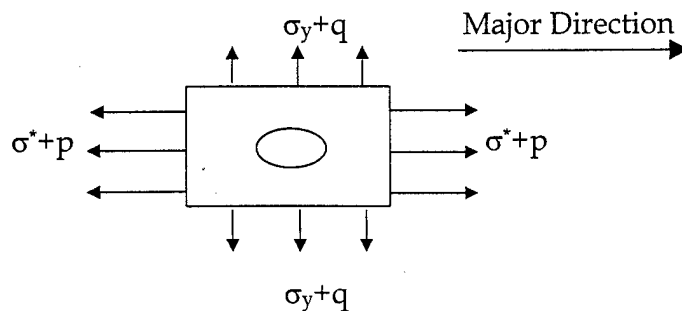


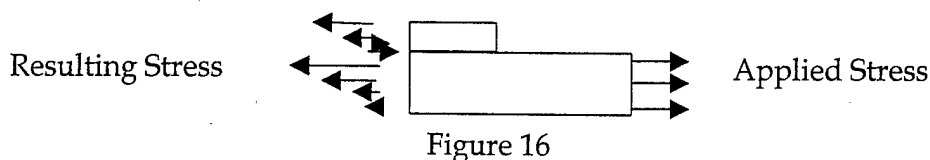
Figure 15

where,  $\sigma_y$  is the applied stress in the 2<sup>nd</sup> principal stress direction

Equation (8) produces a good approximate solution for uniaxial load cases when the parent structure and repair consist of different Poisson's ratios. For similar Poisson's ratios, equation 8 produces the exact solution.

### 3.1.2.2 Unsupported Single-Sided Repairs

When a single sided repaired structure is unsupported, out of plane bending effects are present. These effects cause the stress inside the repaired region to become non-uniform, see Figure 16.



The C5033 approach does not take these effects into account therefore is limited to only supported repair cases.

### 3.1.3 Improvements made Since Release of the Original Document

The RAAF standard C5033 is a living document and changes when new developments are made which can benefit the repair process. Improvements made to previous editions of C5033 are as follows:

- **Load Capacity of the Adhesive**

1994 Draft C5033 Document

$$P = 2(\alpha_o - \alpha_i)\Delta TE_i t_i + \sqrt{2\eta\tau_p \left( \frac{1}{2}\gamma_E + \gamma_P \right) E_i t_i \left( 1 + \frac{E_i t_i}{E_o t_o} \right)} \quad (31)$$

and

$$P = 2(\alpha_i - \alpha_o)\Delta TE_o t_o + \sqrt{2\eta\tau_p \left( \frac{1}{2}\gamma_E + \gamma_P \right) E_o t_o \left( 1 + \frac{E_o t_o}{E_i t_i} \right)} \quad (32)$$

Differences between equations 3, 4, 31 and 32 occur in the thermal residual stress component. Equations 31 and 32 contain a thermal residual stress for the cure and operational cycles as one cycle, i.e.  $2(\alpha_o - \alpha_i)\Delta TE_i t_i$  from (31), where  $\Delta T = T_{\text{cure}} - RT$ . While equations 3 and 4 deal with both the cure and operational thermal cycles independently, i.e.  $2E_i t_i ((\alpha_o - \alpha_{\text{ieff}})(RT - T_{\text{cure}}) + (\alpha_o - \alpha_i)(T_{\text{oper}} - RT))$ , developed by Mr Max Davis [3].

Cure Cycle

Operational Cycle

During the cure cycle, the repaired region is heated. Constraint is provided from cooler material surrounding the heated region, which effectively reduces the coefficient of thermal expansion of the parent material. Therefore the  $\alpha_{ieff}$  term is included in the cure cycle term above. On the other hand, when the aircraft is in operation, the repaired structure is cooled uniformly at altitude, therefore no constraint against expansion is provided. Therefore an effective coefficient of thermal expansion for the parent structure is not necessary as depicted in the operational component of equations 3 and 4.

- **Stress at the Edge of the Patch**

1994 Draft C5033 Document

$$\sigma^{**} = \Omega_L \sigma^* + \Omega_T s E_i (\alpha_i - \alpha_o) \Delta T \quad (33)$$

where  $\Omega_T$  is the thermal inclusion factor

Similarly, differences occur between equation 6 and 33 due to the inclusion of an independent operational thermal stress cycle. Including this cycle eliminates the need for the thermal inclusion factor in the current equation.

## **3.2 CalcuRep**

### **3.2.1 Overview of the CalcuRep Approach**

CalcuRep was designed to provide users with analysis tools and a user-friendly graphical interface to assist in the design of adhesive bonded repairs. It has been designed specifically for single-sided supported repairs on aircraft fuselage, although it can be adapted to design repairs to most locations on aircraft. CalcuRep considers post repair stresses in a more detailed approach to that of C5033 for single-sided supported repairs. It attempts to expand the repair design methodology to biaxial loading systems to model loads present in aircraft fuselage, assuming the patch to be orthotropic and the parent structure to be isotropic.

When the software is run, the user is prompted graphically with a choice of four input buttons. The first three buttons allow the user to input skin, patch and adhesive data, manually or by the use of CalcuRep's material data library. The fourth button allows the user to input repair geometry and loading parameters. Once the data entry is complete, the user can then choose the 'Calculate' button. CalcuRep then provides a brief summary of total stresses, strains and stress intensity factors within the repaired region along with their respective margins of safety. The user also has the option of viewing a detailed four page report on the calculated applied, thermal and bending stress contributions of the parameters previously discussed and suggestions on what to change to reducing stresses after repair.

The following sections provide an overview of CalcuRep's analytical methodology.

### 3.2.1.1 Determining the Stress at the Edge and Under the Repair

CalcuRep uses results derived from [11] to determine the stress beneath and at the edge of the repair. Reference [11] considers a single-sided supported repair containing an infinitely large orthotropic plate with an attached elliptical orthotropic repair, see Figure 17.

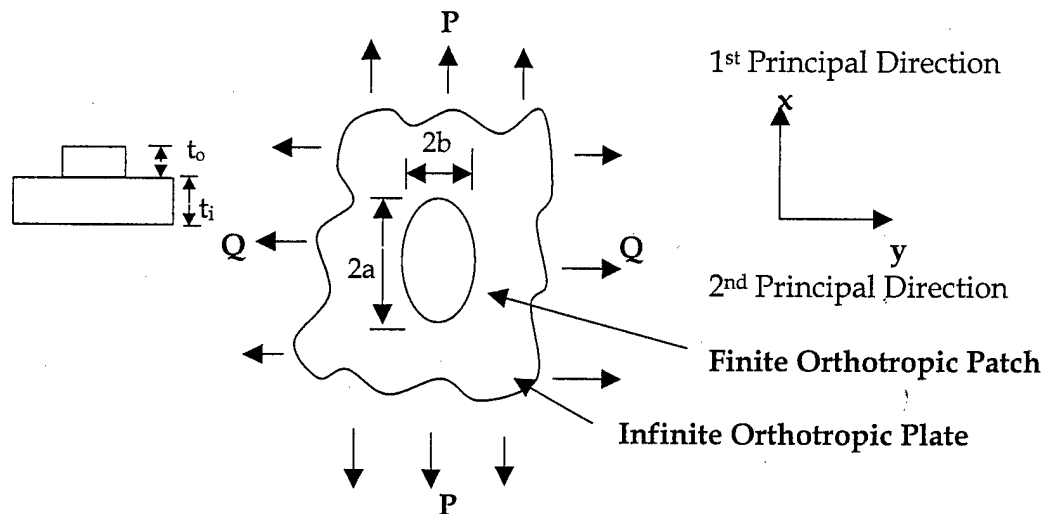


Figure 17

where,

2a	Patch length
2b	Patch width
$m = \text{patch aspect ratio} = a/b$	
P	applied stress in the 1 <sup>st</sup> principle direction
Q	applied stress in the 2 <sup>nd</sup> principal direction

The first step is to consider the repaired region as an inclusion, ie; as one separate entity with the following load applied.

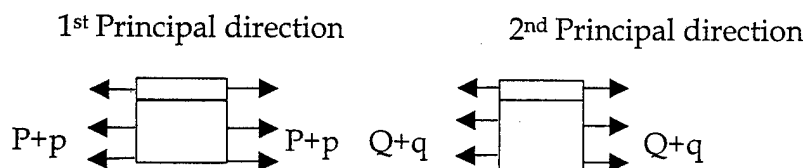


Figure 18

where 'p' and 'q' are stresses attracted into the repaired region ('x' & 'y' directions respectively).

Determining the displacement functions for an infinite plate loaded internally by tractions, tractions being functions of 'p' and 'q' [19], and the inclusion loaded as shown above, see Figure 18, matching the displacement in the 'x' and 'y' directions at the hole boundary produces the following;

(For an isotropic plate)

$$\begin{bmatrix} \frac{\alpha + \beta}{mE_x} + \frac{1}{E_{xl}} & \frac{\nu_{12} - \alpha\beta}{E_x} - \frac{\nu_{xl}}{E_{xl}} \\ \frac{\nu_{12}}{E_x} - \frac{1}{\alpha\beta E_x} - \frac{\nu_{xl}}{E_{xl}} & \frac{m(\alpha + \beta)}{\alpha\beta E_x} + \frac{1}{E_{yl}} \end{bmatrix} \begin{bmatrix} p \\ q \end{bmatrix} = \begin{bmatrix} \frac{1}{E_x} - \frac{1}{E_{xl}} & \frac{\nu_{xl}}{E_{xl}} - \frac{\nu_{12}}{E_x} \\ \frac{\nu_{xl}}{E_{xl}} - \frac{\nu_{12}}{E_x} & \frac{1}{E_x} - \frac{1}{E_{yl}} \end{bmatrix} \begin{bmatrix} P \\ Q \end{bmatrix} \quad (34)$$

where  $\alpha$  imaginary part of the first root of  $\lambda$   
 $\beta$  imaginary part of the second root of  $\lambda$

$$\lambda^4 + \left( \frac{E_x}{G} - 2\nu_{12} \right) \lambda^2 + 1 = 0 \quad (35)$$

$\lambda$  characteristic equation parameter  
 $E_x$  Plate Modulus in x-direction (isotropic plate)  
 $E_{xl}$  Inclusion Modulus in x-direction  
 $E_{yl}$  Inclusion Modulus in y-direction  
 $\nu_{xl}$  Inclusion Poisson's Ratio in xy-direction  
 $\nu_{12}$  Poisson's Ratio of the parent material

#### • Inclusion Material Constants

Using the elastic properties below (Equation 36), and the following relations within the repaired region,  $(P+p)t = \sigma_o t + \sigma_{RtR}$  and  $\epsilon_i = \epsilon_o = \epsilon_R$ , holding for arbitrary strains; the inclusion properties are derived as follows:

$$\begin{aligned} A_x &= \frac{E_x}{1 - \nu_{12}^2} \quad \& \quad A_{xR} = \frac{E_{xR}}{1 - \nu_{12R}\nu_{21R}} \\ A_y &= \frac{E_x}{1 - \nu_{12}^2} \quad \& \quad A_{yR} = \frac{E_{yR}}{1 - \nu_{12R}\nu_{21R}} \end{aligned} \quad (36)$$

where  $A_x, A_y, A_{xR}, A_{yR}$  Elastic properties for the plate and repair  
 $E_{xR}$  Elastic modulus of repair in x-direction  
 $E_{yR}$  Elastic modulus of repair in y-direction

$v_{12R}$	Repair Poisson ratios in xy-direction
$v_{21R}$	Repair Poisson ratios in yx-direction
$G \text{ \& } G_R$	Shear Modulus of plate and repair, respectively

The inclusion has the following elastic properties

$$A_{xI} = \frac{A_x t + A_{xR} t_R}{t} \text{ \& } A_{yI} = \frac{A_y t + A_{yR} t_R}{t} \quad (37)$$

$$v_{xI} = \frac{v_{12} A_y t + v_{12R} A_{yR} t_R}{A_y t + A_{yR} t_R} \quad (38)$$

$$v_{yI} = \frac{v_{12} A_x t + v_{21R} A_{xR} t_R}{A_x t + A_{xR} t_R} \quad (39)$$

$$E_{xI} = A_{xI} (1 - v_{xI} v_{yI}) \text{ \& } E_{yI} = A_{yI} (1 - v_{xI} v_{yI}) \quad (40)$$

where,  $A_{xI}$  \&  $A_{yI}$  Elastic properties of the inclusion in the 'x' \& 'y' directions  
 $v_{yI}$  inclusion Poisson's ratio in the yx-direction

Completing the analysis, see [11] for details, the stress at the edge of the repair and under the repair are as follows:

- **Stress at the Edge of the Repair**

$$\sigma_{xx}^I = P + p \quad (41)$$

$$\sigma_{yy}^I = Q + q \quad (42)$$

where  $\sigma_{xx}^I$  stress in the parent structure at the edge of the repair in the x- direction.  
 $\sigma_{yy}^I$  stress in the parent structure at the edge of the repair in the y-direction.

- **Stress Under the Repair**

$$\sigma_o = \sigma_{xx}^I \left( 1 - \frac{t_R}{t} \frac{(A_{xR} - v_{xI} v_{12R} A_{yR})}{E_{xI}} \right) + \sigma_{yy}^I \left( \frac{t_R}{t} \left( \frac{v_{xI} A_{xR}}{E_{xI}} - \frac{v_{12R} A_{yR}}{E_{yI}} \right) \right) \quad (43)$$

where  $\sigma_o$  is the stress under the repair in the x-direction

### 3.2.1.2 Thermal Residual Stresses

CalcuRep uses an approach developed by Robert S. Fredell in reference [1], which centres on satisfying various equilibrium and compatibility requirements to determine resulting stresses in the repaired and surrounding regions of the structure,

post cure. The following entails the process used by CalcuRep. (Note a separate set of notation will be used for this section to keep it consistent with the CalcuRep code and is summarised in the appendix.)

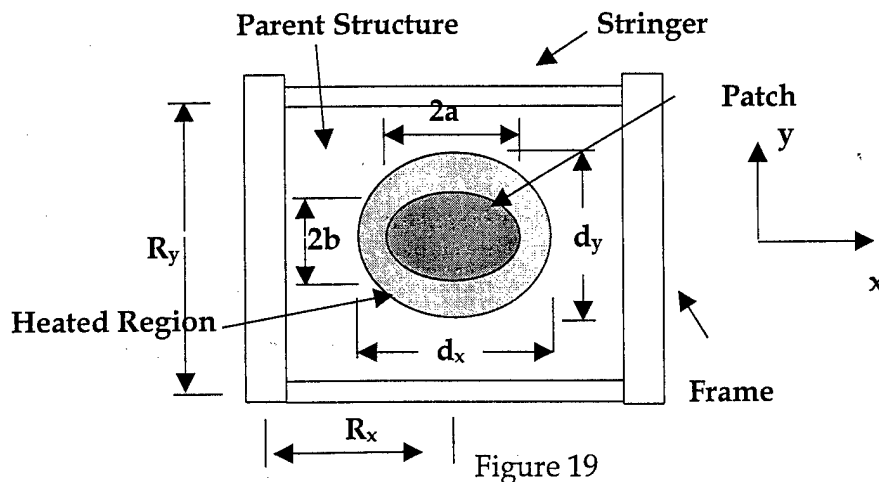
- **Geometry as Used in CalcuRep**

CalcuRep manipulates the above parameters prior to equation substitution as follows:

$$d_x = d_x/2, d_y = d_y/2, R_x = 1.2R_x \text{ and } R_y = R_y/2$$

where

$d_x$	Heated region length in the x-direction
$d_y$	Heated region length in the y-direction
$R_x$	Half frame spacing
$R_y$	Stringer spacing



- **Effective Coefficient of Thermal Expansion of the Parent Structure**

As stated previously, during the cure process, cooler material surrounding the heated area provides constraint against expansion, thus effectively reducing the coefficient of thermal expansion for the parent structure. CalcuRep uses the following equation specifically for aluminium structure as per [1].

$$\alpha_{P(eff)x} = \left( \frac{\alpha}{2} \right) \times (1 + \nu_{xy}) \left( \left( 1 - \frac{T_x}{T_c} \right) + \left( \frac{d_x}{R_x} \right)^2 \times \left( \frac{T_x}{T_c} - 1 \right) - \frac{\left( 1 - \frac{T_x}{T_c} \right)}{2 \ln \left( \frac{d_x}{R_x} \right)} \times \left( \left( \frac{d_x}{R_x} \right)^2 - 1 - 2 \left( \frac{d_x}{R_x} \right)^2 \times \ln \left( \frac{d_x}{R_x} \right) \right) \right) \quad (44)$$

$$\alpha_{P(eff)y} = \left( \frac{\alpha}{2} \right) \times (1 + \nu_{xy}) \left( \left( 1 - \frac{T_y}{T_c} \right) + \left( \frac{d_y}{R_y} \right)^2 \times \left( \frac{T_y}{T_c} - 1 \right) - \frac{\left( 1 - \frac{T_y}{T_c} \right)}{2 \ln \left( \frac{d_y}{R_y} \right)} \times \left( \left( \frac{d_y}{R_y} \right)^2 - 1 - 2 \left( \frac{d_y}{R_y} \right)^2 \times \ln \left( \frac{d_y}{R_y} \right) \right) \right) \quad (45)$$

where  $\alpha_{P(eff)x}$  &  $\alpha_{P(eff)y}$  Effective CTE of the parent structure in the 'x' and 'y' directions

$\alpha$  Parent structure coefficient of thermal expansion (CTE)

$\nu_{xy}$  Poisson's ratio of the parent structure

$$T_x = (T_c - T_{amb}) e^{-\left( \sqrt{\frac{1}{12t}} \right) (R_x - d_x)} + T_{amb} \quad (46)$$

$$T_y = (T_c - T_{amb}) e^{-\left( \sqrt{\frac{1}{12t}} \right) (R_y - d_y)} + T_{amb} \quad (47)$$

$T_x$  &  $T_y$  Temperature at the edge of the parent structure at  $R_x$  &  $R_y$   
 $T_c$  Cure temperature  
 $T_{amb}$  Ambient temperature  
 $t$  Thickness of parent structure

#### • Loads in the Repaired Structure after Cure.

As the repaired region is heated, the parent structure experiences initial thermal stresses, while the patch is free to expand. Once the adhesive is cured, a rigid bond is assumed to exist between the patch and plate. The patch and structure is then cooled to room temperature leaving thermal residual stresses in the patch and parent structure. Fredell [1] solves for unknown loads per unit width acting on the following regions within the repaired structure on cooling after cure, by considering equilibrium and compatibility conditions:

#### Enforcing the Rigid Bond Assumption Yields (noted as $P_1$ loads)

After cure, the patch is assumed to be rigidly bonded to the structure. The following loads ensure this assumption is valid.

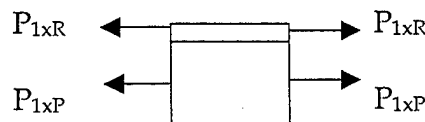


Figure 20



$$\begin{aligned} P_{1xP} &= -P_{1xR} = P_{1x} \\ P_{1yP} &= -P_{1yR} = P_{1y} \end{aligned}$$

where

$$P_{1y} = \frac{\left( B_5 + B_4 \frac{B_2}{B_1} \right)}{B_3 - \frac{B_2^2}{B_1}} \quad \text{and} \quad P_{1x} = P_{1y} \frac{B_2}{B_1} + \frac{B_4}{B_1} \quad (48)$$

- $P_{1xP}$  &  $P_{1yP}$  Load applied to plate to satisfy the rigid bond assumption in the 'x' & 'y' directions respectively
- $P_{1xR}$  &  $P_{1yR}$  Load applied to repair to satisfy the rigid bond assumption in the 'x' & 'y' directions respectively
- $P_{1x}$  &  $P_{1y}$  Load tractions equal in magnitude to the above loads ('x' & 'y' directions respectively)

The remaining constants, numbered as per [1], are:

$$\left\{ \begin{aligned} B_1 &= \frac{1}{E_x t} + \frac{1}{E_{xR} t_R} & B_2 &= \frac{\nu_{xy}}{E_x t} + \frac{\nu_{xyR}}{E_{xR} t_R} & B_3 &= \frac{1}{E_x t} + \frac{1}{E_{yR} t_R} \\ B_4 &= (\alpha_{P(eff)x} - \alpha_{xR}) \Delta T & B_5 &= (\alpha_{P(eff)y} - \alpha_{yR}) \Delta T \end{aligned} \right\} \quad (49)$$

where

- $E_x$  Elastic Modulus of plate in x-direction (same as 'y' since Isotropic)
- $E_{xR}$  Elastic Modulus of repair in the x-direction
- $E_{yR}$  Elastic Modulus of repair in the y-direction
- $\nu_{xyR}$  Poisson's ratio of repair in the xy-direction
- $\nu_{yxR}$  Poisson's ratio of repair in the yx-direction
- $\nu_{xy}$  Poisson's ratio of parent structure
- $\alpha_{xR}$  Coefficient of thermal expansion of repair in the x-direction
- $\alpha_{yR}$  Coefficient of thermal expansion of repair in the y-direction

**External Loads on the Inclusion and Surrounding Matrix (noted as  $P_2$  loads)**

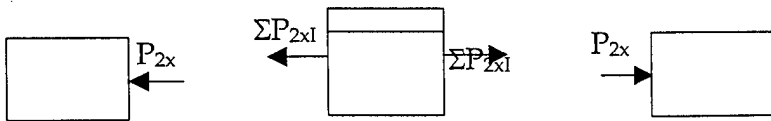


Figure 21

Similarly in the y-direction  $\Sigma P_{2xI} = -P_{2xM} = P_{2x}$   
 $\Sigma P_{2yI} = -P_{2yM} = P_{2y}$

where

$$P_{2y} = \frac{K_1}{K_o} \text{ and } P_{2x} = C_2 H_1 (P_{2y} F_1 + F_2) \quad (50)$$

$P_{2x}$  &  $P_{2y}$  Loads applied to the inclusion in the 'x' & 'y' directions  
 $\Sigma P_{2xI}$  &  $\Sigma P_{2yI}$  Sum of loads applied to the plate and repair as shown in Figure 22 below ('x' & 'y' directions)  
 $P_{2xM}$  &  $P_{2yM}$  Loads applied to the outer structural matrix

$$K_1 = D_2 \left( H_1 E_x t F_2 + H_1 F_1 F_2 C_1 \frac{C_3}{C_2} + F_3 \right) \quad (51)$$

$$K_o = 1 - D_2 H_1 E_x t F_1 + \frac{C_1}{C_2} F_1 D_2 - H_1 D_2 F_1^2 C_1 \frac{C_3}{C_2} \quad (52)$$

$$H_1 = \frac{\frac{D_1}{C_2}}{1 + D_1 F_1 \frac{C_3}{C_2}} \quad (53)$$

$$D_1 = \frac{(1 + \nu_{xy}) + (1 - \nu_{xy}) \times \left( \frac{R_x}{a} \right)^2}{(1 - \nu_{xy}^2) \left( 1 - \left( \frac{R_x}{a} \right)^2 \right)} \quad (54)$$

$$D_2 = \frac{(1 + \nu_{xy}) + (1 - \nu_{xy}) \times \left( \frac{R_y}{b} \right)^2}{(1 - \nu_{xy}^2) \left( 1 - \left( \frac{R_y}{b} \right)^2 \right)} \quad (55)$$

$$C_1 = \frac{E_x t}{1 - \nu_{xy}^2} + \frac{E_{xR} t_R}{1 - \nu_{xyR} \nu_{yxR}} \quad (56 a)$$

$$C_2 = \frac{E_x t \nu_{xy}}{1 - \nu_{xy}^2} + \frac{E_{yR} t_R \nu_{xyR}}{1 - \nu_{xyR} \nu_{yxR}} \quad (56 b)$$

$$C_3 = \frac{E_x t}{1 - \nu_{xy}^2} + \frac{E_{yR} t_R}{1 - \nu_{xyR} \nu_{yxR}} \quad (56 c)$$

$$F_1 = \frac{E_x t}{C_2 - C_1 \frac{C_3}{C_2}} \quad (57a)$$

$$F_2 = P_{1x} - v_{xy} P_{1y} \quad (57b)$$

$$F_3 = P_{1y} - v_{xy} P_{1x} \quad (57c)$$

The  $P_2$  loads are distributed between the repair and parent structure as follows:

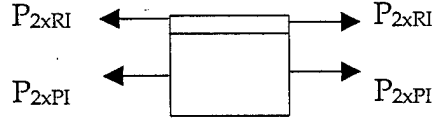


Figure 22

$$\Sigma P_{2xI} = P_{2xPI} + P_{2xRI}$$

Similarly in the y-direction

$$\Sigma P_{2yI} = P_{2yPI} + P_{2yRI}$$

where

$$P_{2xPI} = \left( \frac{\left( \frac{u_I}{a} + v_{xy} \frac{v_I}{b} \right) E_x t}{1 - v_{xy}^2} \right) \quad P_{2yPI} = \left( \frac{\left( v_{xy} \frac{u_I}{a} + \frac{v_I}{b} \right) E_x t}{1 - v_{xy}^2} \right) \quad (58)$$

$$P_{2xRI} = \left( \frac{\left( E_{xR} \frac{u_I}{a} + v_{xyR} E_{yR} \frac{v_I}{b} \right) t_R}{1 - v_{xyR} v_{yxR}} \right) \quad P_{2yRI} = \left( \frac{\left( v_{xyR} E_{yR} \frac{u_I}{a} + E_{yR} \frac{v_I}{b} \right) t_R}{1 - v_{xyR} v_{yxR}} \right) \quad (59)$$

$P_{2xPI}$  &  $P_{2yPI}$  Distributed inclusion loads in the plate ('x' & 'y' direction)

$P_{2xRI}$  &  $P_{2yRI}$  Distributed inclusion loads in the repair ('x' & 'y' direction)

where

$$\frac{u_I}{a} = \left( \frac{P_{2y} - P_{2x} \frac{C_3}{C_2}}{C_2 - C_1 \frac{C_3}{C_2}} \right), \quad \frac{v_I}{b} = \left( \frac{P_{2x}}{C_2} - \frac{u_I}{a} \times \frac{C_1}{C_2} \right) \quad (60)$$

$u^I$  Displacement of inclusion in the x-direction

$v^I$  Displacement of inclusion in the y-direction

$\Delta T$   $T_{cure} - RT$

## Loads in the Repaired Structure During Operational Altitude.

As discussed previously, at operational altitude the aircraft structure is cooled uniformly, therefore no constraint is provided against contraction of the parent structure. This results in an additional thermal cycle which effects the resulting residual stresses in the patch and the parent structure. The operational thermal stress component is found by using the same procedure listed in the previous section with the following modifications:

$$\Delta T = T_{\text{oper}} - T_{\text{amb}} \quad (61)$$

$$\alpha P_{\text{(eff)x}} = \alpha \quad (62)$$

where,  $T_{\text{amb}}$  is the temperature at sea level during operation.

The total loads due to both cure and operational thermal cycles are determined by simply adding the respective loads found for both cycles.

### Converting Loads into Stresses

Once the loads are determined within various locations of the repaired structure, see Figures 20 to 22, CalcuRep calculates the resulting stresses in the parent structure under the repair, at the edge of the plate and in the repair as follows:

$$\text{Stress under the repair in the parent structure} \quad (P_{1x} + P_{2xPI})/t \quad (63)$$

$$\text{Stress at the edge of the repair} \quad P_{2x}/t \quad (64)$$

$$\text{Stress in the repair} \quad (P_{2xRI} - P_{1x})/t_R \quad (65)$$

#### 3.2.1.3 Out of Plane Bending Stresses

Out of plane bending stresses exist due to load path eccentricity predominantly found in single sided repairs. As a result of this phenomenon, the applied load on the structure tends to shift towards the neutral axis as shown below:

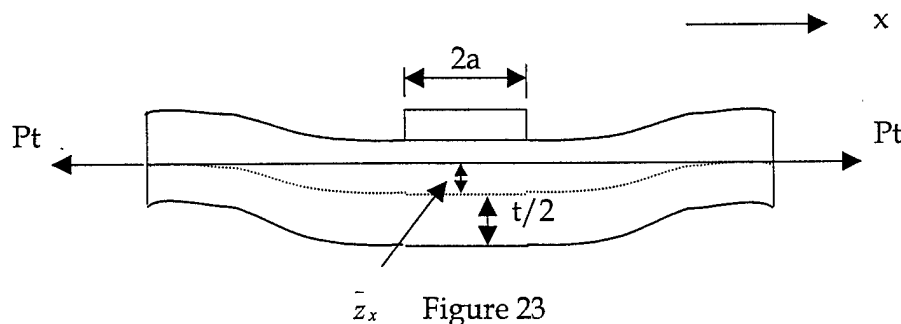


Figure 23

Here  $P$  is the applied stress and  $\bar{z}_x$  defines the location of the neutral axis.

Fredell [1] used a similar approach to L.R.F Rose [13], which considers the patch and structure as a one-dimensional infinitely wide strip with an applied load as shown above. Using a simple relationship between bending moment and deflection [1], the maximum stress at the edge of the patch is as follows:

$$\sigma_{Bend\ max} = \frac{E_x t}{2} \left( \frac{\bar{z}_x}{z_x} - \frac{t}{2} \right) \frac{\Phi_I \Phi_M^2 \tanh(\Phi_I a)}{\Phi_M + \Phi_I \tanh(\Phi_I a)} \quad (66)$$

where

$$\Phi_M = \sqrt{\frac{Pt}{EI_M}} \quad (67)$$

$$\Phi_I = \sqrt{\frac{Pt}{EI_I}} \quad (68)$$

$$EI_M = \frac{E_x t^3}{12(1 - \nu_{12}^2)} \quad (69)$$

$$EI_I = \frac{E_x \left( \left( t - \bar{z}_x \right)^3 + \bar{z}_x^3 \right)}{3(1 - \nu_{12}^2)} + \frac{E_{xR} \left( \left( t - \bar{z}_x + t_R \right)^3 - \left( t - \bar{z}_x \right)^3 \right)}{3(1 - \nu_{12R} \nu_{21R})} \quad (70)$$

$$\bar{z}_x = \frac{E_x t^2 + E_{xR} \left( (t + t_R)^2 - t^2 \right)}{2(E_x t + E_{xR} t_R)} \quad (71)$$

where

$\sigma_{Bend\ max}$	Bending stress at the edge of the repair
$EI_I$	Bending stiffness per width of the inclusion
$EI_M$	Bending stiffness per width of the plate outside the repaired region
$\Phi_M$	Root of the characteristic equation for the plate
$\Phi_I$	Root of the characteristic equation for the inclusion

CalcuRep uses the following equation to estimate the reduction in bending stress at the edge of the patch due to patch taper ratio:

$$\sigma_{Bend\ min} = \sigma_{Bend\ max} \times \left( 0.3 \times \frac{t_{R\ min}}{t_R} + 0.7 \right) \quad (72)$$

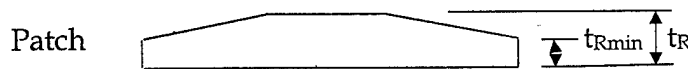


Figure 24

where  $t_{Rmin}$  Minimum patch thickness  
 $\sigma_{Bendmin}$  Reduced bending stress due to patch taper

### 3.2.1.4 Remaining Parameters

Once the stresses have been determined CalcuRep then calculates the resulting reduced stress intensity factor after repair, the maximum stress in the patch and the maximum adhesive shear strain.

- **Reduced Stress Intensity Factor after Repair**

Firstly, CalcuRep determines the total stress in the parent structure under the repair by a summation of the following;

$$\sigma_{o\ New} = (\sigma_o + (P_{1x} + P_{2xPI}) / t) \quad (73)$$

where  $\sigma_{o\ New}$  is the total Stress under the repair as used in CalcuRep. The term  $\sigma_{o\ New}$  replaces  $\sigma_o$  in either equation 14 or 15 depending on whether the adhesive is elastic or plastic, thus producing the reduced stress intensity factor.

- **Maximum Stress in the Patch**

The maximum stress in the patch is then determined as:

$$\sigma_{.p} = \sigma_{xx}^I \frac{t}{t_R} + \frac{P_{1x} + P_{2xPI}}{t} + \frac{P_{2xRI} - P_{1x}}{t_R} \quad (74)$$

- **Maximum Adhesive Strain**

CalcuRep uses either equation 10 or 12 replacing  $\sigma_o$  with  $\sigma_{o\ New}$  depending on whether the adhesive is elastic or plastic, to calculate the maximum adhesive shear strain.

### 3.2.2 Limitations of CalcuRep

CalcuRep has a number of limitations on its use, some of which are listed below:

- Input Parameters
- Material Data Library
- The Effect of Adhesive Visco-Plasticity, see Chapter 3
- Interlaminar Failure in the Patch, see Chapter 3
- Aircraft Operational Temperature
- Patch Dimension Design
- Unsupported Single-Sided Repairs

### 3.2.2.1 Input Parameters

CalcuRep enforces strict restraints on various user input data. For example, CalcuRep only accepts parent structure thickness in the following range:

$$0.02'' \leq t \leq 0.1333''$$

Most other input parameters within the software contain similar limits, which have been provided to prevent the user from placing an unrealistic parameter value into the software. This unfortunately can restrict rare, but realistic repair scenarios.

### 3.2.2.2 Material Data Library

CalcuRep's adhesive material data library contains data for FM73, FM-300-2 and AF-163-2 for one temperature case only. Since adhesive material properties are sensitive to temperature change, using the adhesive material data library can seriously limit repair design for varying temperature environments. In this case the user should manually input adhesive parameters for each temperature case into the software to determine the largest resulting stresses, strains and stress intensity factors. Then continue the design process to develop a repair, which can be adapted to all conceivable temperature environments.

### 3.2.2.3 Aircraft Operational Temperature

As shown previously, CalcuRep determines the thermal residual stresses by considering the cure and operational thermal cycles of the repaired structure. To determine the aircraft operational thermal cycle, the temperature at which the aircraft operates is necessary. CalcuRep uses atmospheric lapse rate equations to determine this temperature at a user specified altitude as follows.

$$\text{For } H_{\text{oper}} \leq 11000\text{m} \text{ then } T_{\text{oper}} = 288.15 - 0.0065H_{\text{oper}} \quad (75)$$

$$\text{For } H_{\text{oper}} > 11000\text{m} \text{ then } T_{\text{oper}} = 216.65 \text{ K}$$

where  $H_{\text{oper}}$  is the operational altitude

The above equations can be used for operating temperatures equal to or below the temperature at sea level. For aircraft that operate at higher temperatures (not necessarily related to altitude temperatures) the above equations are not valid to produce the desired operational temperature. Producing above sea level temperatures from equation 67 would require an equivalent negative height. Unfortunately CalcuRep does not allow a negative height to be used within the software therefore limiting its analysis to only a select range of aircraft.

#### **3.2.2.4 Patch Dimension Design**

CalcuRep provides no procedure to determine patch dimensions. Instead it provides the user with a set of suggestions to reduce stresses, strains and stress intensity factors by changing patch material and dimensions. This procedure is adequate if the user has a preliminary size approximation to begin design with. On the other hand, this procedure can be difficult to begin when the user has no concept of an initial patch size.

#### **3.2.2.5 Unsupported Single-Sided Repairs**

CalcuRep attempts to deal with unsupported single-sided repair effects by considering out of plane bending (section 3.2.1.3). The maximum stress contribution at the edge of the patch is determined by summing the corresponding applied, thermal and bending stress components. This calculation simply provides a maximum stress, not the actual stress variation through the thickness, and provides for a good check to see whether the material will yield.

Determining the stress under the patch, the reduced stress intensity factor and the shear strains due to out of plane bending is far more complex than the process explained above. Firstly, the stress under the repair in the structure will vary through the thickness. Secondly, the reduced stress intensity factor from equations 14 & 15 is specifically for a uniform stress variation through the thickness, therefore can't be used to predict results with a stress variation. Lastly, the maximum shear strain is not given by equations 10 & 12 since out of plane bending provides a larger contribution to the no bending solution.

CalcuRep does not deal with these issues therefore is similar in process to C5033 which limits its analysis to single-sided supported repairs.

#### **3.2.3 Errors Identified**

A number of discrepancies have been identified in CalcuRep's bonded repair analysis tools. These errors have seriously hindered reliable repair design by CalcuRep, therefore rectifying these discrepancies is fundamental in providing a software package that can be used with confidence. Errors in analysis tools used by the software have been identified in the following analysis components:

- Out of plane bending
- Thermal residual stresses post repair

Solving a non-linear differential equation derives the out of plane bending analysis tools. The moment used to form this differential equation inside the repaired region consists of a deflection contribution and a neutral axis offset contribution. The current analysis in [1] only considers the deflection contribution in setting up this



governing differential equation, thus over estimates the maximum bending stress at the edge of the patch.

Errors in the thermal residual stress analysis tools tend to produce compressive stresses at the edge of the repair in the parent structure, rather than tensile stresses for above ambient cure temperatures when the plate CTE is higher than the patch CTE. Revisiting the derivations of these formulas as listed in [1], identified where these errors occur. The following sections provide the correct derivations.

### 3.2.3.1 Out of Plane Bending Discrepancies

See Appendix A1 for the correct derivation. Equations 58 to 63 should be replaced by the following corrections. (Note: Notation as per section 3.2.1.2)

- Bending Stiffness

$$D_P = \frac{E_x t^3}{12(1 - \nu_{12}^2)}$$

$$D_I = \frac{E_x t^3}{12(1 - \nu_{12}^2)} + \frac{E_x t \bar{z}_x^2}{(1 - \nu_{12}^2)} + \frac{E_{xR} t_R^3}{12(1 - \nu_{12R} \nu_{21R})} + \frac{E_{xR} t_R \left( \frac{t}{2} + \frac{t_R}{2} - \bar{z}_x \right)^2}{(1 - \nu_{12R} \nu_{21R})} \quad (76)$$

- Neutral Axis Offset

$$\bar{z}_x = \frac{S(t + t_R)}{2(1 + S)} \quad (77)$$

where

$$S = \frac{E_{xR} t_R (1 - \nu_{12}^2)}{E_x t (1 - \nu_{12R} \nu_{21R})} \quad (78)$$

- Maximum Bending Stress at the Edge of the Patch

$$\sigma_{Bend\ max} = \frac{E_x t \bar{z}_x \Phi_M^2 \Phi_I \tanh(a\Phi_I)}{2 \Phi_M + \Phi_I \tanh(a\Phi_I)} \quad (79)$$

where

$$\Phi_M = \sqrt{\frac{Pt}{D_P}} \quad \Phi_I = \sqrt{\frac{Pt}{D_I}} \quad (80)$$

### 3.2.3.2 Thermal Residual Stress Discrepancies

In this case the corrected equations are presented in the Appendix.

- Enforcing the rigid bond assumption produces the following  $P_1$  loads:

$$P_{1yP} = \frac{B_3 B_5 - B_1 B_6}{B_2 B_3 - B_1 B_4} \quad (81)$$

$$P_{1xP} = \frac{B_6 - B_4 P_{1yP}}{B_3} \quad (82)$$

where

$$\left\{ \begin{array}{l} B_1 = \frac{1}{E_x t} + \frac{1}{E_{xR} t_R} \quad B_2 = -\left( \frac{v_{xy}}{E_x t} + \frac{v_{yxR}}{E_{yR} t_R} \right) \\ B_3 = -\left( \frac{v_{xy}}{E_x t} + \frac{v_{yxR}}{E_{xR} t_R} \right) \quad B_4 = \frac{1}{E_x t} + \frac{1}{E_{yR} t_R} \\ B_5 = (\alpha_{P(eff)x} - \alpha_{xR}) \Delta T \quad B_6 = (\alpha_{P(eff)y} - \alpha_{yR}) \Delta T \end{array} \right\} \quad (83)$$

- External Loads on the inclusion and surrounding matrix post cure produces the following  $P_2$  loads:

$$P_{2y} = \frac{A_3 A_5 - A_1 A_6}{A_2 A_3 - A_1 A_4} \quad \text{and} \quad P_{2x} = \frac{A_6 - A_4 P_{2y}}{A_3} \quad (84)$$

where

$$\left\{ \begin{array}{l} A_1 = \frac{1}{D_1} + \frac{C_3 C_4}{C_2 C_3^2 - C_1 C_3 C_4} \quad A_2 = -\frac{1}{C_3} - \frac{C_1 C_4}{C_2 C_3^2 - C_1 C_3 C_4} \\ A_3 = -\frac{C_3}{C_2 C_3 - C_1 C_4} \quad A_4 = \frac{1}{D_2} + \frac{C_1}{C_2 C_3 - C_1 C_4} \\ A_5 = \frac{P_{1x}}{E_{xl} t} - \frac{v_{yl} P_{1y}}{E_{yl} t} + (\alpha_{P(eff)x} - \alpha_{I(eff)x}) \Delta T \quad A_6 = \frac{P_{1y}}{E_{yl} t} - \frac{v_{xl} P_{1x}}{E_{xl} t} + (\alpha_{P(eff)y} - \alpha_{I(eff)y}) \Delta T \end{array} \right\} \quad (85)$$

$$\begin{aligned} C_1 &= \frac{E_x t}{1 - v_{xy}^2} + \frac{E_{xR} t_R}{1 - v_{xyR} v_{yxR}}, \quad C_2 = \frac{v_{xy} E_x t}{1 - v_{xy}^2} + \frac{v_{yxR} t_R E_{xR}}{1 - v_{xyR} v_{yxR}}, \\ C_3 &= \frac{v_{xy} E_x t}{1 - v_{xy}^2} + \frac{v_{xyR} E_{yR} t_R}{1 - v_{xyR} v_{yxR}}, \quad C_4 = \frac{E_x t}{1 - v_{xy}^2} + \frac{E_{yR} t_R}{1 - v_{xyR} v_{yxR}} \end{aligned} \quad (86)$$

and

$$\begin{aligned}
A &= \begin{bmatrix} \frac{E_x}{1-\nu_{xy}^2} & \frac{\nu_{xy}E_x}{1-\nu_{xy}^2} \\ \frac{\nu_{xy}E_x}{1-\nu_{xy}^2} & \frac{E_x}{1-\nu_{xy}^2} \end{bmatrix} \quad A_R = \begin{bmatrix} \frac{E_{xR}}{1-\nu_{xyR}\nu_{yxR}} & \frac{\nu_{xyR}E_{yR}}{1-\nu_{xyR}\nu_{yxR}} \\ \frac{\nu_{xyR}E_{yR}}{1-\nu_{xyR}\nu_{yxR}} & \frac{E_{yR}}{1-\nu_{xyR}\nu_{yxR}} \end{bmatrix} \\
A_I &= A + \frac{t_R}{t} A_R \\
C_I &= A_I^{-1} \\
C_I &= \begin{bmatrix} \frac{1}{E_{xI}} & \frac{-\nu_{xI}}{E_{xI}} \\ \frac{-\nu_{yI}}{E_{yI}} & \frac{1}{E_{yI}} \end{bmatrix} \\
\therefore \begin{bmatrix} \alpha_{I(eff)x} \\ \alpha_{I(eff)y} \end{bmatrix} &= C_I A \begin{bmatrix} \alpha_{P(eff)x} \\ \alpha_{P(eff)y} \end{bmatrix} + \frac{t_R}{t} C_I A_R \begin{bmatrix} \alpha_{xR} \\ \alpha_{yR} \end{bmatrix}
\end{aligned} \tag{87}$$

- The Inclusion Experiences Displacements due to P<sub>2</sub> Loads:

$$\frac{v'}{b} = \frac{C_3 P_{2x} - C_1 P_{2y}}{C_2 C_3 - C_1 C_4} \quad \text{and} \quad \frac{u'}{a} = \frac{P_{2y} - C_4 \frac{v'}{b}}{C_3} \tag{88}$$

- P<sub>2</sub> Loads are Distributed into the Parent Structure and Patch in the Repaired Region

$$\begin{aligned}
P_{2xPI} &= \frac{E_x t}{1-\nu_{xy}^2} \left( \frac{u'}{a} + \nu_{xy} \frac{v'}{b} \right), \quad P_{2yPI} = \frac{E_x t}{1-\nu_{xy}^2} \left( \frac{v'}{b} + \nu_{xy} \frac{u'}{a} \right), \quad P_{2xRJ} = \frac{E_{xR} t_R}{1-\nu_{xyR}\nu_{yxR}} \left( \frac{u'}{a} + \nu_{yxR} \frac{v'}{b} \right) \\
\text{and } P_{2yRJ} &= \frac{E_{yR} t_R}{1-\nu_{xyR}\nu_{yxR}} \left( \frac{v'}{b} + \nu_{xyR} \frac{u'}{a} \right) \tag{89}
\end{aligned}$$

Having the internal and external loads within the repaired structure on cooling after cure, stresses at various locations are determined as follows:

- Stress Under the Repair

$$\sigma_o = \frac{P_{1x} + P_{2xPI}}{t} \tag{90}$$

- Stress in Parent Structure at the Edge of the Patch

$$\sigma_I = \frac{P_{1x} + P_{2x}}{t} \quad (91)$$

- Maximum Stress in the Patch

$$\sigma_{R \max} = \frac{P_{1x} + P_{2x}}{t_R} \quad (92)$$

## 4 Case Study of the F-111C Lower Wing Skin Repair

In February of 1994, a fatigue crack was discovered on an Australian F-111C aircraft, tail number A8-145, located in the lower wing skin at Forward Auxiliary Spar Station 281.28. Failure to repair such a flaw on primary structure would have seen the wing discarded from service. Rather than discarding the wing, it was decided that the wing would be repaired. Two repair options were available to the RAAF, a mechanically fastened repair or an adhesively bonded repair system. Using a mechanically fastened repair would have required additional hole locations for fasteners. Additional holes induce more stress concentrations thus increase the probability of initiating fatigue problems. Also mechanically fastened repair transfer load at the fastener locations only and some fasteners take up more load than others which degrades its efficiency in load carrying capability. On the other hand, adhesive bonded repairs provide efficient load transfer since the adhesive is active throughout the repaired region. Therefore the RAAF decided to use an adhesive bonded repair.

The repair was designed using the RAAF Engineering Standard C5033 [3, 4, 5]. The repair was designed to be applicable to the following temperature cases; -40, -25 and 167 degrees Fahrenheit [16]. Repair specifications and processes were listed as per references [4, 5] to ensure the high quality of repair installation. NDI inspection found no crack growth after 850 Airframe Flight Hours prior to the wing being retired from service as a fatigue test and tear-down item.

A comprehensive repair substantiation program was conducted at the DSTO and is listed in references [6] and [7]. Repair efficiency was demonstrated by reference [6] and [7] and indicated that the C5033 repair methodology produced a good and feasible repair. The particular parameter of interest to this report from reference [6] is the reduced stress intensity factor. The Finite Element results are summarised in the 'results' section below.

Having a real-life case study from the preliminary design stage to the actual implementation of the repair is beneficial in providing a baseline standard to compare analytical results. This design case was used to compare the current RAAF engineering standard C5033 with the original CalcuRep and error free CalcuRep codes in the following sections.

Due to the limitations identified in section 3.2.2, a Mathcad module containing the exact coding of the CalcuRep software was developed. This enabled most limitations to be lifted and provided the flexibility of material data entry for the module. Likewise, the design tools used in C5033 [3] were entered into a Mathcad module. The benefit of this process allows the user to view the mathematical expressions used in each module and allows changes to be made where deemed appropriate. This also allows programmers to view the values of intermediate variables in order to verify software against the modules. Two example cases, which will be discussed later, have been provided in appendix A4 and A5, listing the current RAAF C5033 standard and the error free CalcuRep software.

#### 4.1 Material Input Data

##### Skin Data [15]

Skin Type: 2024-T851

Skin Thickness: 0.14in

Yield Strength: 59ksi

Ultimate Strength: 65ksi

Fracture Toughness: 42ksi $\sqrt{\text{in}}$

Elastic Modulus: 10.5 $\times 10^3$ ksi

Poisson's Ratio: 0.31

Coefficient of Thermal Expansion 12.6 $\times 10^{-6}$ in/in/degrees F

##### Adhesive Data [16]

Adhesive Type: FM-73 (0.06 psf)

Adhesive Thickness: 0.01 in

Cure Temperature: 180 Degrees F

Poisson's Ratio: 0.33

Material property variation per temperature environment as follows:

Parameter	-40F	-25F	75F	167F
G (ksi)	75	76	75.645	27.6
$\tau_p$ (ksi)	6.8	6.5	4.69	1.9
$\gamma_E$	0.0904	0.086	0.062	0.068
$\gamma_P$	0.428	0.476	0.811	1.5

Table 1

### Patch Material

Material Type: Boron/Epoxy 5521/4

Ultimate Longitudinal Strain: 0.00655 in/in

*Following properties per ply [3]*

Elastic Modulus Longitudinal:  $30 \times 10^3$  ksi

Elastic Modulus Transverse:  $2.7 \times 10^3$  ksi

Coefficient of Thermal Expansion (Longitudinal Direction):  $2.3 \times 10^{-6}$  /F

Coefficient of Thermal Expansion (Transverse Direction):  $10.6 \times 10^{-6}$  /F

Major Poisson's Ratio: 0.21

*Following properties [6] per the following ply lay-up [0,0,45,-45,0,0]s*

Elastic Modulus Longitudinal:  $22.6 \times 10^3$  ksi

Elastic Modulus Transverse:  $4.319 \times 10^3$  ksi

Coefficient of Thermal Expansion (Longitudinal Direction)[20]:  $3.486 \times 10^{-6}$  /F

Coefficient of Thermal Expansion (Transverse Direction)[20]:  $9.41 \times 10^{-6}$  /F

Major Poisson's ratio: 0.575

Patch Thickness: 0.0728 in

### Loading

Applied axial stress: 37.1 ksi

### Patch Dimensions

C5033 provides a method for determining the patch dimensions as discussed previously. Therefore determining the required patch dimensions in C5033 and placing them into CalcuRep will allow a feasible comparison to be made. The dimensions calculated by C5033 are summarised below.

Temperature(F)	-40	-25	75	167
Patch Length(in)	11.34	11.44	12.53	20.74
Patch Width(in)	12.7	12.7	12.7	12.7

Table 2

### Establishing a CalcuRep's Repair Geometry Similar to C5033

CalcuRep and C5033 do not run with the same assumptions. CalcuRep's repair geometry consists of a finite plate with a finite patch; the plate being fully restrained at its boundary. C5033 uses an infinite plate and a finite patch with the plate being unrestrained at its boundary. C3055 attempts to restraint the parent structure boundary by using an effective coefficient of thermal expansion, equation (5), which is derived assuming a fixed edge condition, see [20] for details. To set CalcuRep to run similarly to C5033, its plate dimension must be increased to infinity. Therefore  $R_x$  and  $R_y$ , being the outer plate radius in the 'x' and 'y' directions respectively, must be set to infinity.

### Case Study Run for C5033 and CalcuRep

Having the appropriate material data, the next step is to decide what parameters to compare. Common parameters computed by C5033 and CalcuRep are (the following notation will be used in Tables 3-6 in the results section):

- $\sigma_A$  Stress under the repair in the parent structure due to the applied stress
- $\sigma_T$  Stress under the repair in the parent structure due to thermal residual stresses
- $\sigma_o$  Total stress under the repair in the parent structure (applied+thermal)
- $\sigma_{IA}$  Stress in the parent structure at the edge of the patch due to applied stresses
- $\sigma_{IT}$  Stress in the parent structure at the edge of the patch due to thermal residual stresses
- $\sigma_I$  Total stress in the parent structure at the edge of the repair
- $\gamma_{Max}$  Maximum shear strain in the adhesive
- $K_\infty$  Upper bound or limiting stress intensity factor post repair
- $\sigma_{P Max}$  Maximum patch stress assuming the presence of a crack

## Running the F-111C Boron/Epoxy Repair Case

Using the material data listed previously, the parameters above, as calculated by C5033, the original CalcuRep and the error free CalcuRep, can be determined at each operating temperature environment, ie -40F, -25F, 75F and 167F. The parameters can then be compared for each case to determine whether the CalcuRep approach is valid against the already verified C5033 [6, 7] approach. An example of each code in MathCad form has been provided in as part of this report and consists of the -25F case for C5033 and the error free CalcuRep code. The remaining runs are summarised in the following section.

### 4.2 Analytical Comparison

#### 4.2.1 Case1: -40 F

Parameter	C5033	CalcuRep (Original)	CalcuRep (Corrected)
$\sigma_A$ (ksi)	21.01	20.58	20.58
$\sigma_T$ (ksi)	7.67	5.80	13.56
$\sigma_o$ (ksi)	28.68	26.38	34.14
$\sigma_{IA}$ (ksi)	44.52	44.50	44.50
$\sigma_{IT}$ (ksi)	16.26	-4.09	22.07
$\sigma_I$ (ksi)	60.78	40.41	66.57
$\gamma_{Max}$	0.198	0.174	0.262
$K_{\infty}$ (ksi/in)	23.02	20.97	28.15
$\sigma_{p\ Max}$ (ksi)	116.90	72.36	128.02

Table 3

#### 4.2.2 Case1: -25 F

Parameter	C5033	CalcuRep (Original)	CalcuRep (Corrected)
$\sigma_A$ (ksi)	21.01	20.61	20.61
$\sigma_T$ (ksi)	7.00	5.15	12.08
$\sigma_o$ (ksi)	28.01	25.76	32.69
$\sigma_{IA}$ (ksi)	44.52	44.56	44.56
$\sigma_{IT}$ (ksi)	14.83	-3.65	19.75
$\sigma_I$ (ksi)	59.35	40.91	64.31
$\gamma_{Max}$	0.195	0.172	0.25
$K_{\infty}$ (ksi/in)	22.48	20.48	26.91
$\sigma_{p\ Max}$ (ksi)	114.10	73.92	123.67

Table 4



#### 4.2.3 Case3: 75 F

Parameter	C5033	CalcuRep (Original)	CalcuRep (Corrected)
$\sigma_A$ (ksi)	21.01	20.92	20.92
$\sigma_T$ (ksi)	2.48	2.23	2.22
$\sigma_o$ (ksi)	23.49	23.15	23.14
$\sigma_{IA}$ (ksi)	44.52	45.19	45.19
$\sigma_{IT}$ (ksi)	5.26	-1.64	4.29
$\sigma_I$ (ksi)	49.78	43.55	49.48
$\gamma_{Max}$	0.179	0.175	0.175
$K_\infty$ (ksi $\sqrt{in}$ )	19.33	19.00	18.99
$\sigma_{p\ Max}$ (ksi)	95.72	81.70	95.16

Table 5

#### 4.2.4 Case1: 167 F

Parameter	C5033	CalcuRep (Original)	CalcuRep (Corrected)
$\sigma_A$ (ksi)	21.01	22.91	22.91
$\sigma_T$ (ksi)	-1.67	6.18	-6.85
$\sigma_o$ (ksi)	19.33	29.10	16.06
$\sigma_{IA}$ (ksi)	44.52	49.38	49.38
$\sigma_{IT}$ (ksi)	-3.55	-4.35	-9.94
$\sigma_I$ (ksi)	40.97	45.03	39.44
$\gamma_{Max}$	0.283	0.597	0.206
$K_\infty$ (ksi $\sqrt{in}$ )	21.41	36.59	17.08
$\sigma_{p\ Max}$ (ksi)	78.79	80.88	75.85

Table 6

#### 4.2.5 FE results from reference [6]

Temperature	-40F	-25F	167F
$K_\infty$ (ksi $\sqrt{in}$ )	24.25	24.25	22.82

Table 7

## 5 DISCUSSION

The RAAF Engineering Standard C5033 and CalcuRep version 1.0 are founded on almost identical mathematical analysis tools, with exception to their methods used to calculate thermal residual stresses. Other differences between the two approaches have been discussed in detail in Sections 3.1 and 3.2 and mainly consist of assumption differences. Regardless of these differences, the results produced by the two approaches are expected to correlate well.

Finite Element Analysis and testing have demonstrated validation of the RAAF standard C5033 via reference [6] and [7]. Therefore the C5033 approach has been used to provide the baseline comparison data listed in tables 3 to 6. A good correlation between C5033 and CalcuRep will directly indicate the validity and accuracy of the CalcuRep approach.

To isolate specifically where and why discrepancies occur between the three Mathcad codes, i.e C5033, CalcuRep (original) and CalcuRep (corrected), a discussion of each variable listed in Tables 3 to 6 will be provided as follows;

- **Stress Under the Repair in the Parent Structure due to Applied Stresses ( $\sigma_A$ )**

Reference [11] derives the expression, as used by CalcuRep, for the stress in the parent structure under the repair in a generic form. The formulation is given by equation 43 and assumes the parent structure to be isotropic and the patch to be orthotropic, both materials having different Poisson's ratios. Using equation 43, C5033 assumes that both the parent structure and the patch are isotropic and consist of the same Poisson's ratio, simplifying the generic form of equation 43 down to equation 8. Therefore C5033 uses a simplified form of the expression used by CalcuRep (Equation 43), and explains the good correlation of results between the two approaches as shown in Tables 3 to 6.

- **Stress Under the Repair in the Parent Structure due to Thermal Residual Stresses ( $\sigma_T$ )**

C5033 and CalcuRep (corrected) followed the expected trends for all temperature cases as shown in tables 3 to 6 above. (Note: negative residual stresses in the parent structure under the repair indicate compressive stresses. Compressive stresses result in the 167F (Table 6) temperature case since the operational thermal cycle is more dominant in compression than the cure cycle is in tensile.) The most startling result (Table 6) is produced by the CalcuRep (original) code, which indicates a tensile residual stress for the 167 degree Fahrenheit case. This problem is predominantly due to the errors identified and rectified (CalcuRep corrected) in sections 3.2.3.2.

Although C5033 and CalcuRep (corrected) correlated well in trend, any discrepancies between them can be explained by the assumptions used in their respective thermal residual stress models. Consider the following assumptions:

- **C5033 Thermal Residual Stress Model**

One-dimensional thermal residual stress model

Infinitely large structure

Unrestrained at the structures boundary

Uses an effective coefficient of thermal expansion which reduces the actual thermal expansion coefficient of the parent structure, due to cooler surrounding material resisting the expansion of the hotter material near the heated region. Equation 5 is

used to calculate the effective coefficient of thermal expansion and is based on a fixed edge infinite circular plate [20].

- **CalcuRep (corrected)**

Two-dimensional thermal residual stress model

Finite patch and finite parent structure

Fully restrained at the parent structure's boundary

Uses a more complex expression for the effective coefficient of thermal expansion of the parent structure accounting for a finite width and the effects of heat transfer from the warmer material to the cooler material.

Assumes the parent structure to be isotropic and the patch to be orthotropic.

Obviously these assumptions can explain any discrepancies, but regardless of the differences, the results correlated well in trend.

Consider the new approach developed in reference [8] for single-sided supported repairs, see Appendix. The thermal residual stress model used in the Appendix was validated by a fully three-dimensional finite element analysis [22]. Running the -25 degree Fahrenheit case for the F-111C Case Study has produced a good agreement with CalcuRep for thermal residual stress under the repair. When the edge of the structure is fully restrained at the boundary, the MathCad module [8] can produce results which can differ by a factor of two (higher) than C5033 for this stress component. This suggests that the thermal residual stress calculated by the C5033 approach may not be conservative.

- **$\sigma_o$  Total Stress Under the Repair in the Parent Structure (applied+thermal)**

The total stress under the repair in the parent structure is a summation of the applied and thermal residual stress components. Therefore errors due to these two components will be accumulated at this point. As expected, Tables 3 to 6 show that C5033 and CalcuRep (corrected) follow the expected trends for all temperature cases. CalcuRep (original) produced an odd result for the 167 Fahrenheit case, indicating errors in analysis tools as previously discussed.

- **$\sigma_{IA}$  Stress in the Parent Structure at the Edge of the Patch due to Applied Stresses**

Reference [11] derives expressions, as used by CalcuRep, to calculate the stress attracted into the repaired region, equation (34), in a generic form. The formulation assumes the parent structure to be isotropic and the patch to be orthotropic, both having different Poisson's ratios. The stress attracted into the repaired region is then related to the stress in the parent structure at the edge of the patch via equations 41 and 42. C5033 does not calculate the stress attraction factor but rather uses a constant value of 1.2.

All three Mathcad runs produced consistent results for the stress in the parent structure at the edge of the patch, demonstrating that C5033's stress attraction factor of 1.2 is a valid approximation.

- **$\sigma_{IT}$  Stress in the Parent Structure at the Edge of the Patch due to Thermal Residual Stresses**

Consistent results were produced between C5033 and CalcuRep (corrected) for all temperature cases. On the other hand, CalcuRep (Original) calculated compressive thermal residual stresses instead of tensile for the -40F, -25F and 75F temperature cases.

Errors of this nature are mostly due to incorrect algebraic manipulations (Shown in section 3.2.3.2) in the analysis tools and one major programming error. The programming error occurs in the operational thermal cycle procedure. The temperature change used in the original software is as follows:  $\Delta T = T_{op} - T_{amb}$ , where  $T_{op}$  and  $T_{amb}$  are the operational and ambient temperature, respectively. The aircraft is travelling from ambient temperature to its operational temperature, therefore the change in temperature should be given as:  $\Delta T = T_{amb} - T_{op}$  using CalcuRep's sign convention.

- **$\sigma_I$  Total Stress in the Parent Structure at the Edge of the Repair**

The total stress in the parent structure at the edge of the patch is a summation of applied and thermal residual stresses at this location. As a result of previous calculations, C5033 and CalcuRep (corrected) correlate reasonably and CalcuRep (Original) correlated inconsistently with the trends shown in tables 3 to 6.

- **$\gamma_{Max}$  Maximum Shear Strain in the Adhesive**

C5033, CalcuRep (Original) and CalcuRep (corrected) use identical expressions for the maximum shear strain in the adhesive, equations (10) and (12). Equations (10) and (12) are a function of the stress in the parent structure under the repair, therefore discrepancies in the maximum shear strain between the codes can be explained by the discrepancies between the stress under the patch. As a result, C5033 and CalcuRep (corrected) have produced consistent results while CalcuRep (original) has produced inconsistent results.

- **$K_{\infty}$  Upper Bound or Limiting Stress Intensity Factor Post Repair**

C5033, CalcuRep (Original) and CalcuRep (Corrected) use identical expressions for the upper bound stress intensity factor post repair (equations 14 and 15). Equations 14 and 15 are again a function of the stress in the parent structure under the repair, therefore discrepancies in the upper bound stress intensity factor between the codes can be explained by discrepancies in the stress under the repair. As a result, C5033

and CalcuRep (corrected) have produced consistent results and CalcuRep (original) has produced inconsistent results.

Comparing the results with the Finite Element Analysis in Table 7 shows good agreement between C5033 and CalcuRep (corrected). CalcuRep (original) has produced an odd result for the 167F temperature case, which is due to the over estimate of the stress under the patch in the parent structure.

Although comparable, some differences have occurred between the FE, C5033 and CalcuRep (corrected). Firstly, when the Finite Element Analysis was performed, it was done considering the cure and operation cycle as one cycle, (ie  $\Delta T = T_c - T_{op}$ ). The current C5033 standard now includes two independent thermal cycles, a cure and an operational cycle, see section 3.1.3. Secondly, the Finite Element Analysis did not assume the adhesive to be elastic/perfectly plastic. In stead it treated the adhesive as follows:

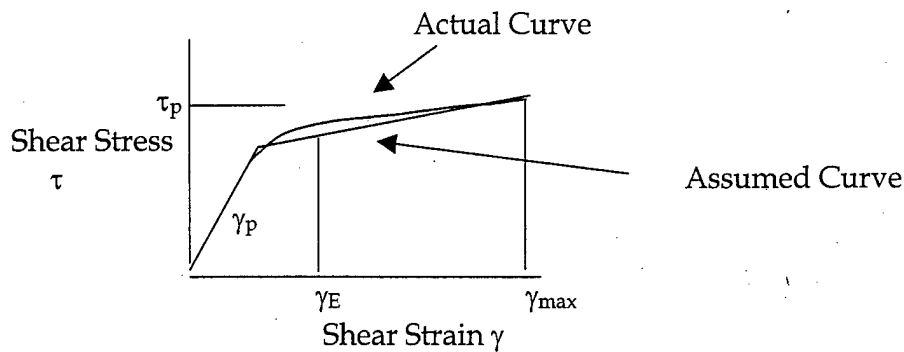


Figure 25

C5033 and CalcuRep have treated the adhesive as elastic/perfectly plastic as per the C5033 standard, see Figure 11. Lastly, the stress attraction factor used in reference [6] for the applied stress component was 1.44, which was derived from considerations out of reference [14]. This value could not be used in the above analysis since it would have required modifying the CalcuRep code. As a result, CalcuRep was allowed to calculate the stress attraction factor, which resulted in a value approximately equal to 1.2, similar to that used by C5033. Regardless of these issues, the results are consistent.

- **$\sigma_{p \text{ Max}}$  Maximum Patch Stress Assuming the Presence of a Crack**

C5033 and CalcuRep (corrected) have produced consistent results for the maximum patch stress for all temperature cases. CalcuRep (original), on the other hand has correlated poorly with the other two codes. This is directly due to the incorrect direction calculation of the stress in the parent structure at the edge of the patch for the thermal stress component, and the errors listed in section 3.2.1.2.

## 6 CONCLUSIONS AND RECOMMENDATIONS

The verification of mathematical analysis tools used in bonded repair technology is essential in providing the means for good repair design. Designing a repair with unverified design tools or software can lead to an unreliable repair. This report has provided a means of verification for the USAF bonded repair design software package called "CalcuRep Version 1.0".

During initial runs with the CalcuRep software, a number of limitations were identified as shown in section 3.2.2. These limitations led to the development of a Mathcad module containing the exact coding used in the original software. This enabled most limitations to be lifted and provided the flexibility of material data entry for the module.

A Boron/Epoxy composite repair, which was implemented on a RAAF F-111C aircraft [16] in 1994, provided the means for a verified case study to compare analytical results. This repair was designed and specified using the RAAF Engineering Standard C5033, which was verified by Finite Element Analysis and testing [6 & 7]. Repair efficiency was demonstrated at three temperature conditions (-40F, -25F and 167F). An additional temperature condition is provided in this report at 75 Fahrenheit to view post repair stresses at ambient temperature. The C5033 approach was also entered into a Mathcad module, see Appendix. The RAAF Engineering Standard C5033 in conjunction with the F-111C Boron/Epoxy Composite repair case study was used to produce baseline results for stresses, stress intensity factors and shear strain post repair.

Running the F-111C Boron/Epoxy composite case study through the Mathcad modules for CalcuRep and C5033 produced some strange findings. Inconsistent results were produced by CalcuRep, especially pertaining to the stress in the parent structure at the edge of the patch. The stresses produced for this case were in the wrong directions. This led to a further examination of the original CalcuRep code and the analytical theory it is based on.

On further investigation of CalcuRep's analysis tools and programming structure, many errors were identified. Discrepancies were found in reference [1] in the out of plane bending stress and thermal residual stress formulations. Revisiting the analysis demonstrated where and why errors occurred and rectified solutions to the problems were offered in sections 3.2.3. The software was also found to use the incorrect temperature change for an aircraft operation thermal cycle. This problem was identified as a major programming error, which led to an incorrect sign usage by CalcuRep. As a result, another Mathcad module was developed containing corrections to the original CalcuRep module: noted as CalcuRep (corrected), see Appendix.

Re-running the corrected CalcuRep version produce good results against C5033. These results were consistent in trend and good in magnitude and showed that by fixing the errors in CalcuRep, the software became consistent with C5033.

A number of recommendations for CalcuRep were established throughout this report and are summarised as follows:

- Make corrections to the original CalcuRep code as shown in sections 3.2.3
- Make a correction to the programming error shown in section 5.
- Remove the restraints on user material input and replace it with a warning flag in the software. An example is a small flashing window which warns the user that the value they have entered may not be applicable to the software.
- Allow CalcuRep to change the adhesive properties with temperature.
- Allow the user to input the aircraft operational temperature directly instead of using the aircraft operational altitude.
- Provide CalcuRep with a method to produce preliminary patch dimensions.
- Expand CalcuRep to deal with unsupported single-sided repairs and a range of other repair geometry through the use of more advanced bonded repair design tools.
- Compare the thermal residual stress formulation derived in reference [22] with the revised CalcuRep analysis from section 3.2.3.2. Reference [22] correlated excellently with Finite Element Analysis methods, therefore a good correlation between section 3.2.3.2 and reference [22] will indicate the validity of CalcuRep's revised thermal residual stress equations.
- Check if equations 44 and 45 have been derived correctly (Note: These equations are directly from [1]). Time constraints did not allow these equations to be re-derived and checked, therefore they may not be consistent with the corresponding effective coefficient of thermal expansion equations from [22].

## 7 REFERENCES

1. Fredell, R. S., Damage Tolerant Repair Techniques for Pressurised Aircraft Fuselages, Delft University of Technology, Netherlands, 1994.
2. Fredell, R. S., CalcuRep Version 1.0 for Windows, United States Air Force Academy, 1997
3. RAAF Standard C5033, Composite Materials and Adhesive Bonded Repairs, 4<sup>th</sup> September 1995.
4. AAP 7021.016-1, Composite Materials and Adhesive Bonded Repairs, Engineering and Design Procedures, Draft.

5. AAP 7021.016-2, Composite Materials and Adhesive Bonded Repairs, Repair Fabrication and Application Procedures.
6. Callinan, R. J., Sanderson, S., Keeley, D., Finite Element Analysis of an F-111 Lower Wing Skin Fatigue Crack Repair, DSTO, Australia, 1997. DSTO-TR-0067
7. Boykett, R., Walker, K., F-111C Lower Wing Skin Bonded Composite Repair Substantiation Testing, DSTO, Australia, 1996. DSTO-TR-0480
8. Erjavec, D., Walker, K., Enhancements to the Design Procedures for Bonded Repairs to Metallic Aircraft Structures including Single Sided Unsupported Repairs, DSTO Melbourne, 1999, DSTO-TR-xxxx.
9. Mathcad Version 8, 1984-1998 MathSoft.
10. Hart-Smith, J. L., Adhesive-Bonded Double-Lap Joints, NASA-CR-012235, California, 1973.
11. Rose, L. R. F., An Application of the Inclusion Analogy for Bonded Reinforcements, Int. J. Solids & Structures, Vol 17, pp 827-838, Great Britain, 1981.
12. Baker, A. A., Davis, M. J., Hawkes, G. A., Proceedings on the 10<sup>th</sup> International Committee on Aeronautical Fatigue (ICAF) Symposium, Paper 4.3, 1979.
13. Baker, A. A., Jones, R., Bonded Repair of Aircraft Structures, Martinus Nijhoff, Dordrecht, 1988.
14. Rose, L. R. F. 1994, Minute to WGCDR Eric Wilson regarding corrections to ref [13] and suggestion for the F-111 Boron repair case.
15. Hart-Smith, L. J., Design and Analysis of Adhesive Bonded Joints, Douglas Paper 6059A, 1972.
16. Design Approval Package for the Interim Repair of F-111C wing S/N A15-5, 1994.
17. Cytecfiberite Incorporated.
18. Hart-Smith, J. L., The Design of Repairable Advanced Composite Structure, Douglas Paper 7550, presented to the SAE Aerospace Conference, Long Beach, 1985.
19. Lekhnitskii, S. G., Theory of Elasticity of an Anisotropic Elastic Body, Holden-Day, San Francisco, 1963.
20. Callinan, R. J., Sanderson, Tran-Cong, T., Walker, K., Development and Validation of a Finite Element Based Method to Determine Thermally Induced Stresses in



Bonded Joints of Dissimilar Materials, DSTO, Australia, 1997. DSTO-RR-0109.  
Table 9 pg 20.

21. Wang, C. H., Rose, L. R. F., Bonded Repair of Cracks under Mixed Mode Loading, Pergamon, Great Britain, 1998. Int. J. Solids Structures, Vol 35, No 21, pp, 2749-2773.
22. Wang, C.H., Rose, L. R. F., Callinan, R., Baker, A. A., Thermal Stresses in a Plate with a Circular Reinforcement, Pergamon, Great Britain, Int. J. Solids Structures. (Submitted for printing but not currently released)

## Appendix A: Corrections to Equation Discrepancies

### Corrections to Out of Plane Bending Equations

The following derivation outlines the problems that exist in reference [1] for the out of plane bending analysis. These problems cause excessively high bending stresses at the edge of the patch. The following derivation provides the corrections to the analysis (pp D1-D7 of [1]) and indicates where these discrepancies occur.

(Note: All constants and notation listed in the following are as per section 3.2.1.3 unless otherwise stated)

### Derivation:

The geometry of the repaired structure is shown in Figure 26 below. The 'x' axis is placed about the plate centroid for convenience.

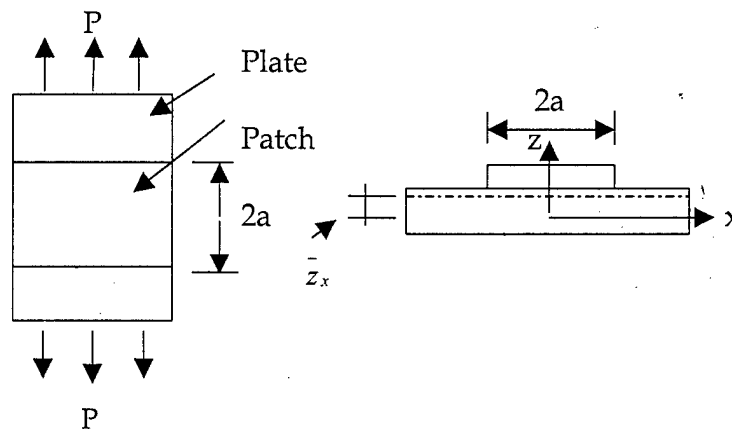


Figure 26

It is assumed that the patch covers the entire width of the parent structure.

### Bending Stiffness inside and outside the inclusion

(Note: The inclusion section refers to the repair and plate inside the repaired region as one entity.)

### Inside The Inclusion

The second moment of area of the plate and repair about the neutral axis of the inclusion is as follows:

$$I = \bar{I} + Ad^2 \quad (A1-1)$$

$$I_{Plate} = \frac{t^3}{12} + t \bar{z}_x^2 \quad (A1-2)$$

$$I_{Re\ pair} = \frac{t_R^3}{12} + t_R \left( \frac{t}{2} + \frac{t_R}{2} - \bar{z}_x \right)^2 \quad (A1-3)$$

The bending stiffness is then determined as follows:

$$\begin{aligned} D_I &= \frac{E_x I_{Plate}}{(1-\nu_{12}^2)} + \frac{E_{xR} I_{Re\ pair}}{(1-\nu_{12R}\nu_{21R})} \\ &= \frac{E_x t^3}{12(1-\nu_{12}^2)} + \frac{E_x t \bar{z}_x^2}{(1-\nu_{12}^2)} + \frac{E_{xR} t_R^3}{12(1-\nu_{12R}\nu_{21R})} + \frac{E_{xR} t_R \left( \frac{t}{2} + \frac{t_R}{2} - \bar{z}_x \right)^2}{(1-\nu_{12R}\nu_{21R})} \quad (A1-4) \end{aligned}$$

### Outside the inclusion

The second moment of area of the plate about its neutral axis is as follows:

$$I_{Plate} = \frac{t^3}{12} \quad (A1-5)$$

Therefore the bending stiffness outside the inclusion is determined as follows:

$$D_P = \frac{E_x I_{Plate}}{(1-\nu_{12}^2)} \quad (A1-6)$$

$$D_P = \frac{E_x t^3}{12(1-\nu_{12}^2)} \quad (A1-7)$$

### Neutral axis offset

Single sided repairs cause a neutral axis offset, introducing out of plane bending stresses. This offset is determined as follows:

$$\frac{E_x}{(1-\nu_{12}^2)} \int_{Plate} x dA + \frac{E_{xR}}{(1-\nu_{12R}\nu_{21R})} \int_{Re\ pair} x dA = 0 \quad (A1-8)$$

$$\bar{z}_x = \frac{S(t+t_R)}{2(1+S)} \quad (D-4) \quad (A1-9)$$

where

$$S = \frac{E_{xR} t_R (1 - \nu_{12}^2)}{E_x t (1 - \nu_{12R} \nu_{21R})} \quad (A1-10)$$

Discrepancies also exist between A1-10 above and the equivalent equation presented in reference [1]. Differences occur since plane-strain elastic moduli are used above while plane-stress elastic moduli are used in reference [1]. As shown in reference [21] page 2764, plane-strain conditions prevail rather than plane-stress conditions.

This completes the analysis of all the required material parameters.

### Secondary Bending Formulation

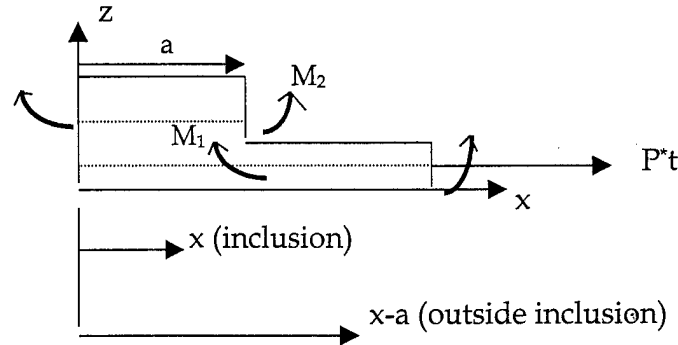


Figure 27

### Consider the region outside the inclusion

Outside the inclusion the following bending moment exists:

$$M_P = Ptw(x) \quad (A1-11)$$

Where,  $M_P$  moment outside the inclusion as a function of 'x'  
 $P$  Applied stress  
 $w(x)$  Deflection outside the inclusion

For a one-dimensional system, the deflection is given as follows:

$$\frac{d^2 w}{dx^2} = \frac{M_P}{D_P} \quad (A1-12)$$

Solving for  $w(x)$  gives the following:

$$w(x) = Ae^{x\Phi_M} + Be^{-x\Phi_M} \quad (A1-13)$$

$$\Phi_M = \sqrt{\frac{Pt}{D_P}}$$

where A, B are unknown constants. The boundary conditions outside the inclusion are as follows:

$$w(\infty)=0 \quad (A1-14)$$

$$w(a)=M_1/(Pt) \quad (A1-15)$$

Replacing 'x' in equation A1-12 with 'x-a' , see Figure 27, and solving for the boundary conditions we find that

$$W= M_1/Pt \ e^{(a-x)\Phi M} \quad (A1-16)$$

This furnishes the solution of the deflection outside the inclusion.

### Consider inside the inclusion

Inside the inclusion the following bending moment exists:

$$M_I = Pt w'(x) + Pt \bar{z}_x \quad (A1-17)$$

Equation A1-16 above considers the bending moment due to deflection and the neutral axis offset. The bending moment due to the neutral axis offset is not considered in the moment relation used in reference [1].

For a one-dimensional system, the deflection is given as follows:

$$\frac{d^2 w_I}{dx^2} = \frac{M_I}{D_I} \quad (A1-18)$$

Substituting equation A1-17 into A1-18 above and solving for  $w_I(x)$  gives the following:

$$w_I(x) = A_2 e^{x\Phi_I} + B_2 e^{-x\Phi_I} - \bar{z}_x \quad (A1-19)$$

where

$$\Phi_I = \sqrt{\frac{Pt}{D_I}}$$

where are  $A_2$ ,  $B_2$  constants to be determined

The boundary conditions inside the inclusion are as follows:

$$\frac{dw_I}{dx}(x=0) = 0, \ w_I(a)=M_2/(Pt) \quad (A1-20)$$

Note: Reference [1] has an error in the stated boundary conditions, but has used the correct boundary condition in the analysis.

Using the boundary conditions gives  $A_2 = B_2$  and

$$A_2 = \frac{1}{2} \left( \frac{M_2}{Pt} + \bar{z}_x \right) \left( \frac{1}{\cosh(a\Phi_I)} \right) \quad (A1-21)$$

$$w_I(x) = \left( \frac{M_2}{Pt} + \bar{z}_x \right) \left( \frac{\cosh(x\Phi_I)}{\cosh(a\Phi_I)} \right) - \bar{z}_x \quad (A1-22)$$

This furnishes the solution of the deflection inside the inclusion.

The bending moments  $M_1$  and  $M_2$  can be determined from considering the following compatibility requirements.

$$\begin{aligned} w_I(a) - w(a) &= 0 \\ \frac{dw_I}{dx}(x=a) &= \frac{dw}{dx}(x=a) \end{aligned} \quad (A1-23)$$

From these equations we find that  $M_1 = M_2$ , and

$$\begin{aligned} M_1 &= M_2 \\ \frac{M_2}{Pt} &= \frac{-\bar{z}_x \Phi_I \tanh(a\Phi_I)}{\Phi_M + \Phi_I \tanh(a\Phi_I)} \end{aligned} \quad (A1-24)$$

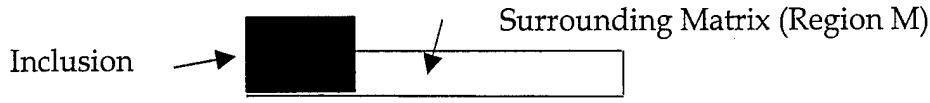
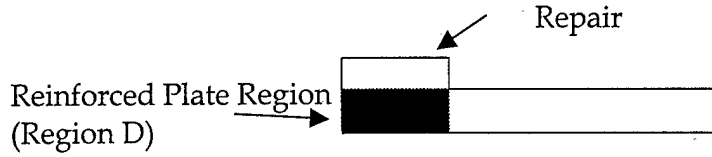
The maximum bending stress in the parent structure at the edge of the repair is given by the following:

$$\sigma_{Bend\ max} = \frac{E_x t \bar{z}_x \Phi_I \Phi_M^2 \tanh(a\Phi_I)}{2 \Phi_M + \Phi_I \tanh(a\Phi_I)} \quad (A1-25)$$

### A.1. Corrections to Thermal Residual Stress Equations

Errors in the thermal residual stress derivation in reference [1] are mostly due to incorrect algebraic manipulation throughout the entire analysis. The following provides the corrections to the analysis (pp C12-C20 of [1]) and indicates where discrepancies occur in the original analysis.

The geometry of the repaired structure is as shown in Figure 19. The repaired structure is divided into the following elements:



The patch is assumed to be rigidly bonded to the parent structure after adhesive cure has occurred. The structure is then cooled down to ambient temperature resulting in compressive and tensile residual stresses in the patch and under the patch respectively. In order to ensure the rigid bond assumption complies, internal loads are applied to the patch and region D, noted as  $P_1$  loads, as shown in Figure 20. On cooling, region D and the patch want to experience the following displacements.

$$\begin{aligned} \text{Region D} \quad x\text{-}y \text{ direction} \quad \delta &= -\alpha_{P(eff)x} \Delta T a \\ \delta &= -\alpha_{P(eff)y} \Delta T b \end{aligned} \quad (A1-26)$$

$$\begin{aligned} \text{Patch} \quad x\text{-}y \text{ direction} \quad \delta &= -\alpha_{xR} \Delta T a \\ \delta &= -\alpha_{yR} \Delta T b \end{aligned} \quad (A1-27)$$

The corresponding strains produced by the  $P_1$  loads (Figure 20) are as follows:

Region D

$$\begin{aligned} \epsilon_{xP} &= \frac{1}{E_x t} (P_{1xP} - \nu_{xy} P_{1yP}) \\ \epsilon_{yP} &= \frac{1}{E_y t} (P_{1yP} - \nu_{xy} P_{1xP}) \end{aligned} \quad (A1-28)$$

Repair

$$\begin{aligned} \epsilon_{xR} &= \frac{P_{1xR}}{E_{xR} t_R} - \frac{\nu_{yxR} P_{1yR}}{E_{yR} t_R} \\ \epsilon_{yR} &= \frac{P_{1yR}}{E_{yR} t_R} - \frac{\nu_{xyR} P_{1xR}}{E_{xR} t_R} \end{aligned} \quad (A1-29)$$

The rigid bond assumption is enforced by the following compatibility requirement inside the patched region:

$$\epsilon_{xP} = \epsilon_{xR} \text{ and } \epsilon_{yP} = \epsilon_{yR} \quad (A1-30)$$

From these equations we obtain:

$$\frac{1}{E_x t} (P_{1xP} - \nu_{xy} P_{1yP}) - \alpha_{P(eff)x} \Delta T = \frac{P_{1xR}}{E_{xR} t_R} - \frac{\nu_{yxR} P_{1yR}}{E_{yR} t_R} - \alpha_{xR} \Delta T \quad (A1-31)$$

$$\frac{1}{E_x t} (P_{1yP} - \nu_{xy} P_{1xP}) - \alpha_{P(eff)y} \Delta T = \frac{P_{1yR}}{E_{yR} t_R} - \frac{\nu_{xyR} P_{1xR}}{E_{xR} t_R} - \alpha_{yR} \Delta T \quad (A1-32)$$

It can be seen from Figure 20, that equilibrium requires the following:

$$P_{1xP} = -P_{1xR} = P_{1x} \quad (A1-33)$$

$$P_{1yP} = -P_{1yR} = P_{1y} \quad (A1-34)$$

This set of equations produces the following two simultaneous equations:

$$P_{1xP} \left( \frac{1}{E_x t} + \frac{1}{E_{xR} t_R} \right) - P_{1yP} \left( \frac{\nu_{xy}}{E_x t} + \frac{\nu_{yxR}}{E_{yR} t_R} \right) = (\alpha_{P(eff)x} - \alpha_{xR}) \Delta T \quad (A1-35a)$$

$$-P_{1xP} \left( \frac{\nu_{xy}}{E_x t} + \frac{\nu_{xyR}}{E_{xR} t_R} \right) + P_{1yP} \left( \frac{1}{E_x t} + \frac{1}{E_{yR} t_R} \right) = (\alpha_{P(eff)y} - \alpha_{yR}) \Delta T \quad (A1-35b)$$

which can be solved to give

$$P_{1yP} = \frac{B_3 B_5 - B_1 B_6}{B_2 B_3 - B_1 B_4} \quad (A1-36)$$

$$P_{1xP} = \frac{B_6 - B_4 P_{1yP}}{B_3} \quad (A1-37)$$

where

$$\left\{ \begin{array}{l} B_1 = \frac{1}{E_x t} + \frac{1}{E_{xR} t_R} \quad B_2 = -\left( \frac{\nu_{xy}}{E_x t} + \frac{\nu_{yxR}}{E_{yR} t_R} \right) \\ B_3 = -\left( \frac{\nu_{xy}}{E_x t} + \frac{\nu_{xyR}}{E_{xR} t_R} \right) \quad B_4 = \frac{1}{E_x t} + \frac{1}{E_{yR} t_R} \\ B_5 = (\alpha_{P(eff)x} - \alpha_{xR}) \Delta T \quad B_6 = (\alpha_{P(eff)y} - \alpha_{yR}) \Delta T \end{array} \right\} \quad (A1-38)$$



### Consider the Inclusion and Surrounding Matrix (M)

The internal  $P_1$  loads in region D and the patch are now applied to the inclusion. This leads to the following two expressions for the displacement the inclusion experiences due to enforcing the rigid bond assumption on cooling post cure.

$$\delta = -\alpha_{I(eff)x} \Delta T a + a \left( \frac{P_{1x}}{E_{xI} t} - \frac{\nu_{yI} P_{1y}}{E_{yI} t} \right) \quad (A1-39a)$$

Inclusion x-y directions

$$\delta = -\alpha_{I(eff)y} \Delta T b + b \left( \frac{P_{1y}}{E_{yI} t} - \frac{\nu_{xI} P_{1x}}{E_{xI} t} \right) \quad (A1-39b)$$

where  $\alpha_{I(eff)x}$  &  $\alpha_{I(eff)y}$  are the CTE of the inclusion in the 'x' and 'y' directions respectively

The derivation listed in [1] is the similar to except that it does not consider the effect the inclusion as one entity has on the coefficient of thermal expansion. The inclusion CTE is taken from [22] and is as follows:

$$A = \begin{bmatrix} \frac{E_x}{1-\nu_{xy}^2} & \frac{\nu_{xy} E_x}{1-\nu_{xy}^2} \\ \frac{\nu_{xy} E_x}{1-\nu_{xy}^2} & \frac{E_x}{1-\nu_{xy}^2} \end{bmatrix} \quad (A1-40) \quad A_R = \begin{bmatrix} \frac{E_{xR}}{1-\nu_{xyR}\nu_{yxR}} & \frac{\nu_{xyR} E_{yR}}{1-\nu_{xyR}\nu_{yxR}} \\ \frac{\nu_{xyR} E_{yR}}{1-\nu_{xyR}\nu_{yxR}} & \frac{E_{yR}}{1-\nu_{xyR}\nu_{yxR}} \end{bmatrix} \quad (A1-41)$$

$$A_I = A + \frac{t_R}{t} A_R \quad (A1-42)$$

$$C_I = A_I^{-1} \quad (A1-43)$$

where

$$C_I = \begin{bmatrix} \frac{1}{E_{xI}} & \frac{-\nu_{xI}}{E_{xI}} \\ \frac{-\nu_{yI}}{E_{yI}} & \frac{1}{E_{yI}} \end{bmatrix} \quad (A1-44)$$

$$\therefore \begin{bmatrix} \alpha_{I(eff)x} \\ \alpha_{I(eff)y} \end{bmatrix} = C_I A \begin{bmatrix} \alpha_{P(eff)x} \\ \alpha_{P(eff)y} \end{bmatrix} + \frac{t_R}{t} C_I A_R \begin{bmatrix} \alpha_{xR} \\ \alpha_{yR} \end{bmatrix} \quad (A1-45)$$

Here,  $A$ ,  $A_R$ ,  $A_I$  Plane stress Elastic Properties of the plate, repair and inclusion respectively

$E_{xI}$  Elastic Modulus of inclusion (x-direction)

$E_{yI}$  Elastic Modulus of inclusion (y-direction)

$\nu_{xI}$  Inclusion Poisson's ratio (xy-direction)

$\nu_{yI}$  Inclusion Poisson's ratio (yx-direction)

### • Surrounding Matrix (M)

As the inclusion experiences a displacement due to internal loads, the surrounding matrix experiences a displacement due to thermal stress as follows:

$$\begin{aligned} \delta &= -\alpha_{p(eff)x} \Delta T a \\ \delta &= -\alpha_{p(eff)y} \Delta T b \end{aligned} \quad (A1-46)$$

x-y directions

The second step is to consider external loads applied to the edges of the inclusion and matrix due to cooling post cure, see Figure 21. The following sections detail the inclusion and matrix reactions to these loads.

### • Inclusion Reaction to P<sub>2</sub> Loads

P<sub>2</sub> loads are applied to the inclusion, which are produced by cooling the structure after adhesive cure is complete. These loads produce corresponding displacements within the inclusion, which can be used to determine how the P<sub>2</sub> loads are distributed between region D and the patch. This procedure is as follows:

$$\begin{aligned} P_{2xPI} &= \frac{E_x t}{1 - \nu_{xy}^2} \left( \frac{u^I}{a} + \nu_{xy} \frac{v^I}{b} \right) \\ P_{2yPI} &= \frac{E_x t}{1 - \nu_{xy}^2} \left( \frac{v^I}{b} + \nu_{xy} \frac{u^I}{a} \right) \\ P_{2xRI} &= \frac{E_{xR} t_R}{1 - \nu_{xyR} \nu_{yxR}} \left( \frac{u^I}{a} + \nu_{yxR} \frac{v^I}{b} \right) \\ P_{2yRI} &= \frac{E_{yR} t_R}{1 - \nu_{xyR} \nu_{yxR}} \left( \frac{v^I}{b} + \nu_{xyR} \frac{u^I}{a} \right) \end{aligned} \quad (A1-47)$$

Where,  $u^I$  and  $v^I$  Displacements of the inclusion due to P<sub>2</sub> loads in the 'x' and 'y' directions respectively

Reference [1] used the following stress-strain relations for equations

$$\begin{aligned} P_{2xRI} &= \frac{t_R}{1 - \nu_{xyR} \nu_{yxR}} \left( E_{xR} \frac{u^I}{a} + \nu_{yxR} E_{yR} \frac{v^I}{b} \right) \\ P_{2yRI} &= \frac{t_R}{1 - \nu_{xyR} \nu_{yxR}} \left( \nu_{xyR} E_{yR} \frac{u^I}{a} + E_{yR} \frac{v^I}{b} \right) \end{aligned}$$

As can be seen, the stress-strain relations above are not correct.

Therefore the total loads applied to the inclusion are as follows, see Figure 22:

$$\Sigma P_{2xI} = P_{2xPI} + P_{2xRI}$$

$$\Sigma P_{2yI} = P_{2yPI} + P_{2yRI}$$

Therefore:

$$\Sigma P_{2xI} = \frac{u^I}{a} \left( \frac{E_x t}{1 - \nu_{xy}^2} + \frac{E_{xR} t_R}{1 - \nu_{xyR} \nu_{yxR}} \right) + \frac{v^I}{b} \left( \frac{\nu_{xy} E_x t}{1 - \nu_{xy}^2} + \frac{\nu_{yxR} E_{xR} t_R}{1 - \nu_{xyR} \nu_{yxR}} \right) \quad (A1-48a)$$

$$\Sigma P_{2yI} = \frac{u^I}{a} \left( \frac{\nu_{xy} E_x t}{1 - \nu_{xy}^2} + \frac{\nu_{xyR} E_{yR} t_R}{1 - \nu_{xyR} \nu_{yxR}} \right) + \frac{v^I}{b} \left( \frac{E_x t}{1 - \nu_{xy}^2} + \frac{E_{yR} t_R}{1 - \nu_{xyR} \nu_{yxR}} \right) \quad (A1-48b)$$

Although the stress-strain relationship used in [1] is incorrect, it still produced the same two expressions above. Therefore errors listed in [1] for the above section may only be due to typo errors.

Solving for displacements yields:

$$\frac{v^I}{b} = \frac{C_3 \Sigma P_{2xI} - C_1 \Sigma P_{2yI}}{C_2 C_3 - C_1 C_4} \quad (A1-49)$$

$$\frac{u^I}{a} = \frac{\Sigma P_{2yI} - C_4 \frac{v^I}{b}}{C_3} \quad (A1-50)$$

$$\text{where } C_1 = \frac{E_x t}{1 - \nu_{xy}^2} + \frac{E_{xR} t_R}{1 - \nu_{xyR} \nu_{yxR}} \quad C_2 = \frac{\nu_{xy} E_x t}{1 - \nu_{xy}^2} + \frac{\nu_{yxR} E_{xR} t_R}{1 - \nu_{xyR} \nu_{yxR}} \quad (A1-51)$$

$$C_3 = \frac{\nu_{xy} E_x t}{1 - \nu_{xy}^2} + \frac{\nu_{xyR} E_{yR} t_R}{1 - \nu_{xyR} \nu_{yxR}} \quad C_4 = \frac{E_x t}{1 - \nu_{xy}^2} + \frac{E_{yR} t_R}{1 - \nu_{xyR} \nu_{yxR}}$$

#### • Matrix Reaction to P<sub>2</sub> Loads

The matrix is taken as a circular plate with a hole in the centre loaded by P<sub>2</sub> loads as shown in Figure 21. The equilibrium equation for a plate with a loaded circular hole is as follows:

$$\frac{d\sigma_r}{dr} + \frac{\sigma_r - \sigma_\theta}{r} = 0 \quad (A1-52)$$

which has the following solution for the displacement

$$u = C_1 r \left( 1 - \frac{a^2}{r^2} \right) + \frac{C_2}{r} \quad (r \geq a) \quad (\text{A1-53})$$

where,  $C_1$  and  $C_2$  which are determined by the boundary conditions. For the case:

$$u=0 \text{ and } \sigma_r=P/t \text{ at } r=a \quad (\text{A1-54})$$

Where,  $P$  Resultant loading around the hole  
 $R$  Outer edge radius of plate

we obtain

$$C_1 = \frac{P(1-\nu_{xy}^2)}{E_x t} \times \frac{1}{2 + (1-\nu_{xy}) \left( \frac{R^2}{a^2} - 1 \right)}$$

$$C_2 = \frac{-P(1-\nu_{xy}^2)}{E_x t} \times \frac{R^2 - a^2}{2 + (1-\nu_{xy}) \left( \frac{R^2}{a^2} - 1 \right)} \quad (\text{A1-54})$$

Adopting the following definitions:

x-direction	$P=P_{2xM}$
y-direction	$P=P_{2yM}$
x-direction	$R=R_x$
y-direction	$R=R_y$

we obtain the following expressions:

$$u_x = \frac{-P_{2xM} a (1-\nu_{xy}^2)}{E_x t} \times \frac{\left( \frac{R_x^2}{a^2} - 1 \right)}{2 + (1-\nu_{xy}) \left( \frac{R_x^2}{a^2} - 1 \right)} \quad (\text{A1-55})$$

$$u_y = \frac{-P_{2yM} b (1-\nu_{xy}^2)}{E_x t} \times \frac{\left( \frac{R_y^2}{b^2} - 1 \right)}{2 + (1-\nu_{xy}) \left( \frac{R_y^2}{b^2} - 1 \right)} \quad (\text{A1-56})$$

This furnishes the solution for a plate with a hole loaded by  $P_2$  loads.

## • Compatibility

Compatibility requires that at the hole boundary, equal displacements in the x and y directions must exist between the inclusion and surrounding matrix. This leads to the following equation for the x-direction:

$$\delta_{P_1}^I + \delta_{P_2}^I = \delta_{P_1}^M + \delta_{P_2}^M \quad (A1-57)$$

Here,  $\delta_{P_1}^I$  Displacement of inclusion due to  $P_1$  loads  
 $\delta_{P_2}^I$  Displacement of inclusion due to  $P_2$  load  
 $\delta_{P_1}^M$  Displacement of Matrix due to  $P_1$  loads  
 $\delta_{P_2}^M$  Displacement of Matrix due to  $P_2$  loads

Equation A1-57 yields the following:

$$-\alpha_{I(eff)x} \Delta T a + a \left( \frac{P_{1x}}{E_{xt}} - \frac{\nu_{yl} P_{1y}}{E_{yl} t} \right) + a \left( \frac{\sum P_{2yl} - C_4 \frac{\nu^I}{b}}{C_3} \right) = -\alpha_{P(eff)x} \Delta T a$$

$$-\frac{P_{2xM} a (1 - \nu_{xy}^2)}{E_{xt}} \times \frac{\left( \frac{R_x^2}{a^2} - 1 \right)}{2 + (1 - \nu_{xy}) \left( \frac{R_x^2}{a^2} - 1 \right)} \quad (A1-58)$$

Reference [1] contains an error in the equivalent equation. From Figure 21 equilibrium requires;

$$\sum P_{2xl} = -P_{2xM} = P_{2x}$$

as a result we obtain:

$$P_{2x} = D_1 \left( \frac{P_{1x}}{E_{xt}} - \frac{\nu_{yl} P_{1y}}{E_{yl} t} + \frac{P_{2y}}{C_3} - \frac{C_4 \nu^I}{C_3 b} + (\alpha_{P(eff)x} - \alpha_{I(eff)x}) \Delta T \right) \quad (A1-59)$$

$$\text{where } D_1 = \frac{E_{xt} \left( 2 + (1 - \nu_{xy}) \left( \frac{R_x^2}{a^2} - 1 \right) \right)}{(1 - \nu_{xy}^2) \left( \frac{R_x^2}{a^2} - 1 \right)} \quad (A1-60)$$

Similarly, matching compatibility in the y-direction yields:

$$\delta_{P_1}^I + \delta_{P_2}^I = \delta_{P_1}^M + \delta_{P_2}^M \quad (A1-61)$$

from which we obtain:

$$-\alpha_{I(eff)y}\Delta Tb + b\left(\frac{P_{1y}}{E_{yt}} - \frac{P_{1x}v_{xl}}{E_{xt}}\right) + \frac{b(C_3\sum P_{2xl} - C_1\sum P_{2yl})}{C_2C_3 - C_1C_4} = -\alpha_{P(eff)y}\Delta Tb$$

$$-\frac{P_{2yM}b(1-v_{xy}^2)}{E_{xt}} \times \frac{\left(\frac{R_y^2}{b^2} - 1\right)}{2 + (1-v_{xy})\left(\frac{R_y^2}{b^2} - 1\right)} \quad (A1-62)$$

Reference [1] contains an error in the equivalent equation,

From Figure 21 equilibrium requires

$$\sum P_{2yl} = -P_{2yM} = P_{2y} \quad (A1-63)$$

from which we obtain:

$$P_{2y} = D_2 \left( \frac{P_{1y}}{E_{yt}} - \frac{P_{1x}v_{xl}}{E_{xt}} + \frac{C_3P_{2x} - C_1P_{2y}}{C_2C_3 - C_1C_4} + (\alpha_{P(eff)y} - \alpha_{I(eff)y})\Delta T \right) \quad (A1-64)$$

$$\text{where } D_2 = \frac{E_{xt} \left( 2 + (1-v_{xy}) \left( \frac{R_y^2}{b^2} - 1 \right) \right)}{(1-v_{xy}^2) \left( \frac{R_y^2}{b^2} - 1 \right)} \quad (A1-65)$$

from which we obtain

$$P_{2x} = D_1 \left( \frac{P_{1x}}{E_{xt}} - \frac{v_{yl}P_{1y}}{E_{yt}} + \frac{P_{2y}}{C_3} + \frac{C_1C_4P_{2y}}{C_2C_3^2 - C_1C_3C_4} - \frac{C_3C_4P_{2x}}{C_2C_3^2 - C_1C_3C_4} + (\alpha_{P(eff)x} - \alpha_{I(eff)x})\Delta T \right) \quad (A1-66)$$

This set of equations can be solved to give:

$$P_{2y} = \frac{A_3A_5 - A_1A_6}{A_2A_3 - A_1A_4} \text{ and } P_{2x} = \frac{A_6 - A_4P_{2y}}{A_3} \quad (A1-67)$$

where

$$\left\{ \begin{array}{l} A_1 = \frac{1}{D_1} + \frac{C_3 C_4}{C_2 C_3^2 - C_1 C_3 C_4} \quad A_2 = -\frac{1}{C_3} - \frac{C_1 C_4}{C_2 C_3^2 - C_1 C_3 C_4} \\ A_3 = -\frac{C_3}{C_2 C_3 - C_1 C_4} \quad A_4 = \frac{1}{D_2} + \frac{C_1}{C_2 C_3 - C_1 C_4} \\ A_5 = \frac{P_{1x}}{E_{xl}t} - \frac{\nu_{yl} P_{1y}}{E_{yl}t} + (\alpha_{P(eff)x} - \alpha_{I(eff)x}) \Delta T \quad A_6 = \frac{P_{1y}}{E_{yl}t} - \frac{\nu_{xl} P_{1x}}{E_{xl}t} + (\alpha_{P(eff)y} - \alpha_{I(eff)y}) \Delta T \end{array} \right\} \quad (A1-68)$$

This furnishes the solution to the loads applied to the edges of the inclusion and the plate hole. Having the internal and external loads, the stresses within the structure are determined as follows:

- **Stress under the repair**

$$\sigma_o = \frac{P_{1x} + P_{2xPl}}{t} \quad (A1-69a)$$

- **Stress in parent structure at the edge of the patch**

$$\sigma_I = \frac{P_{1x} + P_{2x}}{t} \quad (A1-69b)$$

- **Maximum stress in the patch**

$$\sigma_{R \max} = \frac{P_{1x} + P_{2x}}{t_R} \quad (A1-70a)$$

Reference [1] does not derive the stresses produced by equations A1-69 and A1-70. It only considers the stress at the edge of the repair and the actual stresses in the patch, i.e. not the maximum possible stress in the repair due to the presence of a crack.

CalcuRep uses equation (A1-69a) to compute the stress under the repair, but does not use equations (A1-69b) and (A1-70a) to calculate the stress at the edge of the patch and the maximum stress in the repair, respectively. (See equations 55 to 57). Instead it calculates the stress at the edge of the patch, not allowing for the extra stress (ie  $P_{1x}$ ) due to enforcing the rigid bond assumption.

#### Notation for section 3.2.1.2

$\alpha_{P(eff)x}$ & $\alpha_{P(eff)y}$	CTE of the parent structure in the 'x' and 'y' directions
$\alpha$	Parent structure CTE
$d_x$	Heated region length in the x-direction
$d_y$	Heated region length in the y-direction
$E_{xR}$	Elastic Modulus of repair in the x-direction

$E_x$	Elastic Modulus of plate in x-direction (same as 'y' since Isotropic)
$E_{yR}$	Elastic Modulus of repair in the y-direction
$P_{1xP}$ & $P_{1yP}$	Load applied to plate to satisfy the rigid bond Assumption in the 'x' & 'y' directions respectively
$P_{1xR}$ & $P_{1yR}$	Load applied to repair to satisfy the rigid bond Assumption in the 'x' & 'y' directions respectively
$P_{1x}$ & $P_{1y}$	Load tractions equal in magnitude to the above loads ('x' & 'y' directions respectively)
$P_{2x}$ & $P_{2y}$	Loads applied to the inclusion in the 'x' & 'y' directions
$\Sigma P_{2xI}$ & $\Sigma P_{2yI}$	Sum of loads applied to the plate and repair ('x' & 'y' directions)
$P_{2xM}$ & $P_{2yM}$	Loads applied to the outer structural matrix
$P_{2xPI}$ & $P_{2yPI}$	Distributed inclusion loads in the plate ('x' & 'y' direction)
$P_{2xRI}$ & $P_{2yRI}$	Distributed inclusion loads in the repair ('x' & 'y' direction)
$R_x$	Half frame spacing
$R_y$	Stringer spacing
$T_x$ & $T_y$	Temperature at the edge of the parent structure at $R_x$ & $R_y$
$T_c$	Cure temperature
$T_{amb}$	Ambient temperature
$T$	Thickness of parent structure
$\Delta T$	$T_{cure} - RT$
$T_{amb}$	Temperature at sea level during operation
$\nu_{xy}$	Parent structure Poisson's ratio
$\nu_{xyR}$	Poisson's ratio of repair in the xy-direction
$\nu_{yxR}$	Poisson's ratio of repair in the yx-direction
$\nu_p$	Poisson's ratio of parent structure
$u^I$	Displacement of inclusion in the x-direction
$v^I$	Displacement of inclusion in the y-direction



# CHAPTER 2: ENHANCEMENTS TO THE DESIGN PROCEDURES FOR BONDED REPAIRS TO METALLIC AIRCRAFT STRUCTURES INCLUDING SINGLE SIDED UNSUPPORTED REPAIRS

David Erjavec<sup>1</sup> and Kevin Walker<sup>2</sup>

<sup>1</sup> Department of Mechanical Engineering, Monash University, Clayton, Vic 3800,  
Australia

<sup>2</sup> Airframes and Engines Division, Aeronautical Research Laboratory, Defence Science  
and Technology Organisation, 506 Lorimer St, Pt Melbourne, Victoria, 3207, Australia.

## CONTENT

1. BACKGROUND.....	3
2. INTRODUCTION.....	4
3. APPROPRIATE TOOLS FROM THE CALCUREP AND C5033 APPROACHES .	5
3.1 New Approach.....	5
3.2 Overview of Appropriate C5033 and CalcuRep tools for the New Approach .....	6
3.2.1 Patch Dimensions .....	6
3.2.2 Evaluate the Rapid Repairability Criterion (RRC) C5033 .....	8
3.2.3 Check the Adhesive Shear Strain .....	9
3.2.5 The Upper Bound Stress Intensity Factor .....	10
4. NEW TECHNIQUES .....	10
4.1 Single Sided Repair Methods.....	10
4.2 In plane and Out of plane loading due to Thermal stresses.....	11
4.3 In Plane and Out of Plane Loading due to Applied Stresses .....	17
4.4 Stress intensity .....	20
4.5 Maximum Adhesive Shear Strain Under the repair.....	23
4.6 Peel Stresses .....	23
5. RECOMMENDED APPROACH FOR AN IMPROVED DESIGN.....	24
5.1 Repair Methodology for Single Sided Unsupported Repairs.....	25
5.1.1 Patch Dimensions (Single Sided Unsupported Repairs) .....	25
5.1.2 Determining the Stress Under and at the edge of the Repair (Single Sided Unsupported Repairs) .....	25
Where, $\Delta T$ Temperature Change .....	26
5.1.3 Finding the Total Stress (Single Sided Unsupported Repairs) .....	26
5.1.4 Determining the Maximum Adhesive Shear Strain (Single Sided Unsupported Repairs) .....	27
5.1.5 Determining the upper bound stress intensity factor (Single Sided Unsupported Repairs) .....	27
5.1.6 Determining the Maximum Peel Stress at the Crack and at the Edge of the Patch (Single Sided Unsupported Repairs) .....	27
5.1.7 Calculating the Maximum Stress in the Patch (Single Sided Unsupported Repairs).....	27
5.2 Repair Methodology for Single Sided Fully Supported Repairs .....	28

5.2.1 Patch Dimensions (Single Sided Fully Supported Repairs).....	28
5.2.4 Finding the Total Stress (Single Sided Fully Supported Repairs) .....	29
5.2.5 Determining the Maximum Adhesive Shear Strain (Single Sided Fully Supported Repairs) .....	29
5.2.6 Determining the upper bound stress intensity factor (Single Sided Fully Supported Repairs) .....	29
5.2.7 Determining the Maximum Peel Stress at the Edge of the Patch (Single Sided Fully Supported Repairs) .....	29
5.2.8 Calculating the Maximum Stress in the Patch (Single Sided Fully Supported Repairs) .....	30
5.3.1 Patch Dimensions (Double Sided Repairs) .....	30
5.3.4 Finding the Total Stress (Double Sided Repairs) .....	31
5.3.5 Determining the Maximum Adhesive Shear Strain (Double Sided Repairs).....	31
5.2.6 Determining the upper bound stress intensity factor (Double Sided Repairs).....	31
5.3.7 Determining the Maximum Peel Stress at the Edge of the Patch (Double Sided Repairs) .....	31
5.3.8 Calculating the Maximum Stress in the Patch (Double Sided Repairs)....	31
 6. CASE STUDY COMPARISON .....	 33
6.1 Single Sided Unsupported Repair Configuration.....	34
6.2 Results .....	35
 7. MAIN DISCUSSION .....	 36
 8. CONCLUSION AND RECOMMENDATIONS .....	 39
 9. ACKNOWLEDGMENTS.....	 40
 10. REFERENCES .....	 40
 APPENDIX A: MATHCAD MODULES.....	 43
A.1. Unsupported Single Sided Repairs (Case Study from [8]) .....	43
A.2. Fully Supported Single Sided Repairs (F-111 Boron Repair Case) .....	43
A.3. Double Sided Repairs (F-111 Boron Repair Case) .....	43
A.4. Unsupported Single Sided Repairs (F-111 Boron Repair Case) .....	43
A.5. Repairs to Stiffened Panels (F-111 Boron Repair Case).....	43

## 1. BACKGROUND

Bonded repair technology provides enhanced structural efficiency to extend the fatigue life of aircraft structures. It provides industry with an efficient and cost effective solution to aircraft structural defects. This has prompted many organisations to use bonded repair technology as a preferred repair method over mechanically fastened repairs.

The USAF has utilised bonded repair technology to prolong the structural lives of aircraft such as the F-16 and the C130. But the verification process of such repairs can be expensive and time consuming, since detailed Finite Element Analysis and testing may be required to ensure an efficient repair. The use of validated analytical procedures for deriving repairs is therefore desirable to reduce verification and testing time. The US Airforce academy has developed a software package called "CalcuRep" for this purpose.

Robert Fredell and Walter VanBarneveld first developed CalcuRep at Delft University in the early 1990's. Based on work done by Robert Fredell [1] at the Delft University of Technology, CalcuRep was designed to repair cracks specifically on an Aluminium aircraft fuselage. This initial version of the software was developed in DOS and provided the user with repair design tools with a basic user interface. This prompted the development of CalcuRep for Windows (Beta) at the US Air Force Academy in 1994, which consisted of a user-friendly menu system and a graphical interface. CalcuRep for Windows Version 1.0 [2], released in 1997, incorporated user requirements and suggestions.

The RAAF Engineering Standard C5033 [3, 4, 5] was released in 1994 to provide bonded repair design tools to assist in the repair of structural defects in aircraft used by the RAAF. Aimed more towards providing engineers with a set of design standards rather than a software package, C5033 provides a set of constraints to ensure quality of repair design, specifications and application processes.

In early 1999, the US Air Force Academy awarded a contract through the DSTO Centre of Expertise at Monash University to verify and extend the capability of CalcuRep version 1.0 for Windows. The work is noted as the CalcuRep review task. The verification aspect of the task (known as part 1 of the work) was performed by comparing the CalcuRep approach with the RAAF Engineering Standard C5033 procedures. A significant example case of a RAAF F-111C wing repair was used to compare the CalcuRep and C5033 repair design techniques. The results are detailed in reference [8].

Part 2 of the task was to extend the capability of CalcuRep to include unsupported single-sided repairs and repairs to stiffened panels. The results for part 2 are detailed in this report.

The work compiled in this report establishes a new design approach from the most recent works developed at the DSTO in the field of bonded repair design. Applying these recent findings in such a manner to design repairs will prove to benefit both the DSTO and the USAF. The content of this report may also be considered by the RAAF in expanding the current RAAF Engineering Standard C5033 to deal with single-sided repairs to unsupported structure. But overall, this task proves to be beneficial to both the USAF and the DSTO by attempting to reduce any differences between the US and Australian repair design methodologies.

## 2. INTRODUCTION

An evaluation and comparison between the bonded repair design software package CalcuRep version 1.0 and the RAAF Engineering Standard C5033 for single sided fully supported repairs confirmed a good correlation of results. The focus of this report is to expand and develop CalcuRep to deal with a wider range of repair cases. As a result, this has led to a revised package, which considers the best aspects of CalcuRep and C5033 and extends its capability. This package has been designated as the "USA/ Australia Bonded Repair Design Module". For convenience, this module has been developed in a software package called Mathcad [9] to provide users with visual inspection of equations and quick accessibility of user input. Although the package is in Mathcad form, it can be programmed by any software package the user desires, while the Mathcad sheet provided in this report can provide the means to verify the package.

The package allows the user to design bonded repairs to metallic aircraft structure under the following circumstances:

- Double sided repairs and/or single sided fully supported repairs to centre cracked biaxially loaded metallic structure. Thermal and applied in-plane loading effects are included. The scope of this work allows for plastic behaviour in the adhesive should the adhesive become plastic.
- Single sided repairs to unsupported centre cracked biaxially loaded metallic structure. Thermal and applied in plane and out of plane loading effects are included. The scope of this work is limited to a geometric linear analysis and elastic behaviour in the adhesive. Justification of these points will be described in this report.
- Repair to structures with riveted stringers. The scope of this work can be applied to two scenarios, a stiffened panel with a crack in the stiffener and a stiffened panel with a centre crack in the skin beneath the centre stringer.

### **3. APPROPRIATE TOOLS FROM THE CALCUREP AND C5033 APPROACHES**

#### **3.1 New Approach**

Part 1 of the CalcuRep task [8] outlined the approach adopted by the RAAF Engineering standard C5033 and CalcuRep Version 1.0 for adhesive bonded repair design. Many limitations were identified in the single sided repair methodologies used by the two approaches [8] and are summarised below:

##### **C5033**

- Unable to deal with biaxial loading systems
- Limited to single sided repairs to fully supported structure

##### **CalcuRep**

- Restraint against user input
- Does not allow the user to change the adhesive properties with temperature via the adhesive data library
- Does not allow operational temperatures above see level to be used.
- Does not provide a method to estimate preliminary patch dimensions
- Limited to single sided repairs to fully supported structure
- Contains errors in the out of plane bending and thermal residual stress analysis tools.

Many repair cases consist of cracks in unsupported structure accessible from only one side of a panel. In such cases, out of plane bending effects become significant and cannot be ignored. Feasible preliminary design is therefore difficult using packages such as C5033 and CalcuRep due to the limitations listed above.

This type of analysis requires the use of more advanced analysis tools to account for out of plane bending effects inherent in single sided unsupported repairs. Tools that deal with these effects have been developed [10, 11, 12, 13] and will be discussed in detail latter in this report. The approach developed in this report attempts to utilise these tools to provide users with the ability to design repairs for a wider range of cases. This package has been named the "USA/Australia Bonded Repair Design Module". It can deal with the following repair scenarios:

- Single Sided Fully supported repairs
- Double Sided repairs
- Single Sided Unsupported repairs
- Stiffened Panels with a crack in either the stiffener or the skin beneath the stiffener

CalcuRep and C5033 contain good design tools for single sided supported repairs and double sided repair. Since the new design module will account for such repair cases, it is beneficial to use some of these existing tools. The following sections will provide a brief summary of useful tools from C5033 and CalcuRep for the new approach as listed in reference [8].

### **3.2 Overview of Appropriate C5033 and CalcuRep tools for the New Approach**

Part 1 of the CalcuRep review task [8] outlined an overview of the RAAF Engineering Standard C5033 approach. To summarise C5033's capability, the standard is able to deal with the following repair cases:

- Double Sided Bonded Repairs
- Single Sided Supported Bonded Repairs
- Single Sided Supported Bonded Repairs to a Part Through Thickness Defect
- Single Sided Supported Bonded Doubler
- Double Sided Bonded Doubler
- Single Sided Supported Bonded Repairs for Stress Corrosion Cracking
- Double Sided Bonded Repairs for Stress Corrosion Cracking
- Scarf Repairs to Composite Structures

Part 1 of the CalcuRep review task [8] also outlines an overview of the CalcuRep version 1.0 approach. To summarise briefly, CalcuRep can provide users with analysis tools to deal with the following:

- Single sided fully supported repairs to aluminium structure.
- Biaxial stress fields.
- Orthotropic patch bonded to an isotropic structure.
- Provides the out of plane bending stress component at the edge of the patch in the parent structure.

CalcuRep, similarly to C5033, is limited to single sided fully supported repairs, but proves to be advantageous in dealing with orthotropic patches and biaxial stress fields.

A summary of appropriate tools from C5033 and CalcuRep is as follows:

#### **3.2.1 Patch Dimensions**

C5033 provides the means for determining preliminary patch dimensions and can be adapted to the following cases.

Single-sided fully supported repairs for uniaxial loadings (See sections 3.1.1.2 and 3.1.1.5 of [8] for details).

Double-sided repairs for uniaxial loadings.

For a two-sided repair case, the stiffness of the patch is doubled [3, 4, 5]. Therefore the required patch thickness can be determined by modifying equation 1 of reference [8] as follows:

$$\frac{E_i t_i}{2E_o} \leq t_o \leq \frac{1.2E_i t_i}{2E_o} \quad (1)$$

where,  $E_i$  Elastic Modulus of the Parent Material  
 $E_o$  Elastic Modulus of the Patch  
 $t_i$  Thickness of the Parent Material  
 $t_o$  Thickness of the Patch

The patch length for two sided repairs [3, 4, 5] can also be determined by modifying equations 11 and 25 to 27 of reference [8] as follows:

$$L_T = l_e + l_p \quad (2)$$

$$l_e = \frac{3}{\lambda} \quad (3)$$

$$l_p = \frac{\sigma_{ULT} t_i}{4\tau_p} \quad (4)$$

$$\lambda = \sqrt{\frac{G}{\eta} \left( \frac{2}{E_i t_i} + \frac{1}{E_o t_o} \right)} \quad (5)$$

where  $L_T$  Total transfer length  
 $L$  Overlap Length  
 $l_e$  Elastic Load Transfer Length  
 $l_p$  Plastic Load Transfer Length  
 $\lambda$  Elastic Exponent  
 $G$  Adhesive Shear Modulus  
 $\eta$  Adhesive thickness  
 $\sigma_{ULT}$  Ultimate Strength of the Parent Material

The patch width for a double sided repair is determined using the same method as for a single sided supported repair and can be calculated using section 3.1.1.5 of [8]. To summarise, the patch is required to extend at least 1 inch over both crack tips.

For a biaxial load case, load transfer is assumed in both directions. The patch length calculation remains unchanged and can still be found as shown

previously. But in such a case, the patch width is no longer determined from section 3.1.1.5 of [8], but is calculated as follows:

Patch width for single sided supported repair (Biaxial Loading)

$$L_T = l_e + l_p \quad (6)$$

$$l_e = \frac{3}{\lambda} \quad (7)$$

$$l_p = \frac{\sigma_{ULTI} t_i}{2\tau_p} \quad (8)$$

$$\lambda = \sqrt{\frac{G}{\eta} \left( \frac{1}{E_i t_i} + \frac{1}{E_{yR} t_o} \right)} \quad (9)$$

Patch width for double sided repair (Biaxial Loading)

$$L_T = l_e + l_p \quad (10)$$

$$l_e = \frac{3}{\lambda} \quad (11)$$

$$l_p = \frac{\sigma_{ULTI} t_i}{4\tau_p} \quad (12)$$

$$\lambda = \sqrt{\frac{G}{\eta} \left( \frac{2}{E_i t_i} + \frac{1}{E_{yR} t_o} \right)} \quad (13)$$

where,  $E_{yR}$  is the elastic modulus of the patch in the y-direction

Note: The total length of pre-existing bond-line defects must be taken into account in determining patch dimensions [3,8].

### 3.2.2 Evaluate the Rapid Repairability Criterion (RRC) C5033

The rapid repairability criterion is a management tool to ensure the adhesive is never the critical element in a repaired joint, see section 3.1.1.2 of reference [8] for details. Section 3.1.1.2 [8] outlines the rapid repairability criterion for fully supported single sided repairs and can be expanded to double-sided repairs by replacing equations 3 and 4 in [8] by the following:

$$P = E_i t_i \left[ (\alpha_o - \alpha_{ieff}) (RT - T_{Cure}) + (\alpha_o - \alpha_i) (T_{oper} - RT) \right] + \sqrt{2\eta\tau_p \left( \frac{1}{2} \gamma_e + \gamma_p \right) 2E_i t_i \left( 1 + \frac{E_i t_i}{2E_o t_o} \right)} \quad (14)$$



$$P = 2E_o t_o \left[ (\alpha_{ieff} - \alpha_o)(RT - T_{Cure}) + (\alpha_i - \alpha_o)(T_{oper} - RT) \right] + \sqrt{2\eta\tau_p \left( \frac{1}{2}\gamma_e + \gamma_p \right) 4E_o t_o \left( 1 + \frac{2E_o t_o}{E_i t_i} \right)} \quad (15)$$

where,

P	Load capacity of the adhesive
$\alpha_o$	Coefficient of Thermal Expansion of the Patch
$\alpha_i$	Coefficient of Thermal Expansion of the Parent material
$\alpha_{ieff}$	Effective Coefficient of Thermal Expansion of the Parent material
RT	Room Temperature
$T_{cure}$	Cure Temperature
$T_{oper}$	Operating Temperature
$\tau_p$	Adhesive Plastic Shear Stress Limit
$\gamma_e$	Adhesive Elastic Shear Strain Limit
$\gamma_p$	Adhesive Plastic Shear Strain Limit

### 3.2.3 Check the Adhesive Shear Strain

The adhesive shear strain is calculated using equations 10 to 12 from section 3.1.1.3 in [8] for single sided fully supported repairs. Both C5033 and CalcuRep use these equations. To expand these equations to deal with two sided repairs, equations 10 to 12 in [8] can be changed as follows:

- Elastic behaviour in the adhesive

$$\gamma_o = \frac{\sigma_o t_i \lambda}{2G} \quad (16)$$

- Plastic behaviour in the adhesive

$$\gamma_o = \frac{\tau_p}{2G} \left( 1 + \left( \frac{\sigma_o t_i \lambda}{2\tau_p} \right)^2 \right) \quad (17)$$

where,  $\sigma_o$  is the stress in the parent structure under the repair and where  $\lambda$  is given by equation 5.

### 3.2.4 Peel Stress

Peel stress is predominantly due to load path eccentricity inherent in single sided repairs. Although load path eccentricity effects are eliminated when a double-sided repair or a fully supported single sided repair is used, a localised peel stress is still evident when each bond-line is considered in isolation. Section 3.1.1.3 of [8] outlines the equation used to calculate the peel stress for both fully supported single-sided and double-sided repairs. The equation is as follows:

$$\sigma_{C \max} = \tau_p \left( \frac{3E_c' t_o (1 - \nu_i^2)}{E_o \eta} \right)^{\frac{1}{4}} \quad (18)$$

where  $\sigma_{C \max}$  Maximum Peel Stress  
 $E_c'$  Effective Transverse Tensile Modulus for the Adhesive

### 3.2.5 The Upper Bound Stress Intensity Factor

The upper bound stress intensity factor for single sided supported repairs is detailed in section 3.1.1.3 step 5 of reference [8]. Both C5033 and CalcuRep use this analysis tool. Equation 13 and 14 of [8] can be changed to deal with double-sided repairs as follows:

- Elastic Behaviour in the adhesive

$$K_{\infty} = \sigma_o \sqrt{\frac{E_i t_i \lambda \eta}{2G}} \quad (19)$$

- Plastic behaviour in the adhesive

$$K_{\infty} = \sqrt{\frac{E_i \eta}{G} \left[ \sigma_o \tau_p \left( 1 + \left( \frac{\sigma_o \lambda t_i}{2\tau_p} \right)^2 \right) - \frac{2\tau_p^2}{3\lambda t_i} \left( 1 + 2 \left( \frac{\sigma_o \lambda t_i}{2\tau_p} \right)^3 \right) \right]} \quad (20)$$

## 4. NEW TECHNIQUES

### 4.1 Single Sided Repair Methods

Double-sided repair methodology was initially idealised by a double-lap joint system. This system was found to be ideal since no load path eccentricity exists. Shortly following, it was found that most repair cases required patch application to one surface rather than two, due to a lack of accessibility of both surfaces of many aircraft structure, ie cracks in wings. This prompted the development of single-sided repair analysis tools. Previous analytical theory for two-sided repairs were then manipulated by cutting the repair geometry in half. This effectively produced the analysis tools for fully supported single-sided repairs. It was then found that these tools were not sufficient to design for single-sided repair cases where insufficient localised structural support was provided and load path eccentricity effects became apparent. As a result, repairs were found to exhibit the out of plane bending phenomena. Works from references [10, 11, 14, 15] have developed analytical tools to deal with load path eccentricity effects.

Existing tools to date can deal with the following cases:

- Fully supported single sided repairs with applied stresses [16]
- Out of Plane Bending in unsupported single sided repairs due to applied stresses [10, 11]
- Fully supported single sided repairs with thermal residual stresses [17]

Recent works at the DSTO by C.H. Wang and D. Erjavec, have developed tools that consider the following systems:

- In plane and out of plane stresses in unsupported single sided repairs due to applied stresses [13]
- In plane and out of plane stresses in unsupported single sided repairs due to thermal residual stresses [12]

The following sections will outline some of these most recent analytical contributions to bonded repair analysis methodology.

#### **4.2 In plane and Out of plane loading due to Thermal stresses**

A commonly used thermal residual stress model (equation 6 [8]) developed in reference [18], assumes a one-dimensional fully supported repair system consisting of an isotropic patch and plate. Such an approach is very simplistic and does not consider the effects of an orthotropic patch in a two-dimensional stress field, or the load attracted into the repair region due to the extra stiffness provided by the patch. A fully supported single sided repair model developed by Wang, C. H., Rose, L. R. F., Callinan, R. and Baker, A. A [17] deals with these issues by the use of Eshelby's inclusion analogy [20]. The report derives equations for thermal residual stresses post cure considering the following two cases; 1) an orthotropic patch bonded on to an infinite isotropic plate; 2) an orthotropic patch bonded on to a finite isotropic plate.

Since reference [17] is limited to fully supported single-sided repairs, expanding the analysis to unsupported single sided repairs would enhance the models capability. This has lead to the development of design tools for thermal residual stresses post repair for unsupported single sided repairs by C. H. Wang and D. Erjavec [12]. The following provides the results of the formulation as shown in [12]:

##### **Repaired Structure Geometry**

The curvature and mean strains are postulated to be uniform throughout the inclusion [12]. The inclusion region refers to the repair and the plate under the repaired region as one entity. A free body diagram of the system is as follows:

## Repair Geometry

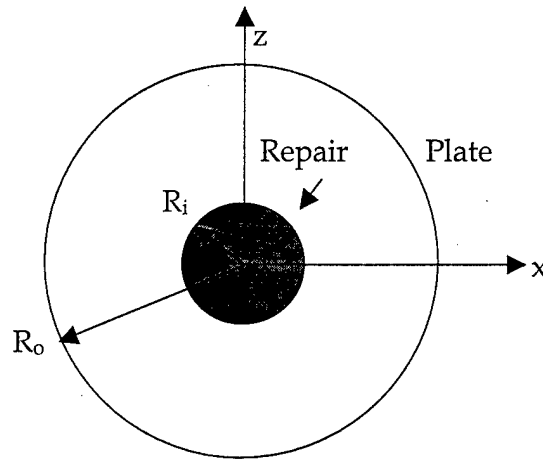


Figure 1

Where,  $R_i$  Radius of patch  
 $R_o$  Radius of plate

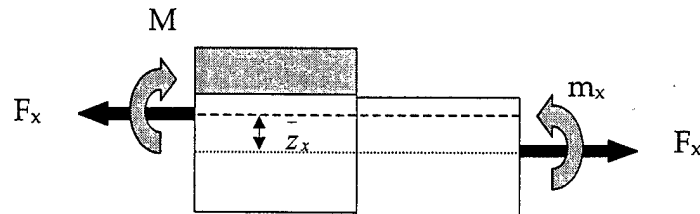


Figure 2

Equilibrium requires the following:

$$M_x = m_x + F_x \bar{z}_x \quad (21)$$

$$M_y = m_y + F_y \bar{z}_y \quad (22)$$

where,

$M_x$	$M_y$	are the total Moments in the 'x' and 'y' directions respectively
$m_x$	$m_y$	Moment in the plate region in the 'x' and 'y' directions respectively
$F_x$	$F_y$	Total Force in the 'x' & 'y' directions respectively
$\bar{z}_x$	$\bar{z}_y$	Neutral axis offset in the 'x' & 'y' directions respectively

The stresses in the plate and reinforcement inside the repaired region are related through Hooke's law as follows:

$$\begin{Bmatrix} \sigma_{xx}(z) \\ \sigma_{yy}(z) \end{Bmatrix} = A \begin{Bmatrix} \bar{\varepsilon}_x - \kappa_x(z - \bar{z}_x) - \alpha \Delta T \\ \bar{\varepsilon}_y - \kappa_y(z - \bar{z}_y) - \alpha \Delta T \end{Bmatrix} \quad (23)$$

$$\begin{Bmatrix} \sigma_{xx}^R(z) \\ \sigma_{yy}^R(z) \end{Bmatrix} = A_R \begin{Bmatrix} \bar{\varepsilon}_x - \kappa_x(z - \bar{z}_x) - \alpha_{1R} \Delta T \\ \bar{\varepsilon}_y - \kappa_y(z - \bar{z}_y) - \alpha_{2R} \Delta T \end{Bmatrix} \quad (24)$$

Where,	$\sigma_{xx}(z) \text{ \& } \sigma_{yy}(z)$	Stress variation through the plate ('x' & 'y' directions respectively)
	$\sigma_{xx}^R(z) \text{ \& } \sigma_{yy}^R(z)$	Stress variation through the repair ('x' & 'y' directions respectively)
	$\bar{\varepsilon}_x \text{ \& } \bar{\varepsilon}_y$	Mean strains inside the inclusion ('x' & 'y' directions respectively)
	$\kappa_x \text{ \& } \kappa_y$	Curvatures inside the inclusion ('x' & 'y' directions respectively)
	$\alpha$	Coefficient of thermal expansion of the plate
	$\alpha_{1R}$	Coefficient of thermal expansion of the repair in the x-direction
	$\alpha_{2R}$	Coefficient of thermal expansion of the repair in the y-direction
	$\Delta T$	Temperature change
	$A$	In-plane Plate Properties
	$A_R$	In-plane Repair Properties

The total forces and moments can be determined as follows:

$$\begin{Bmatrix} F_x \\ F_y \end{Bmatrix} = (t + t_R) A_I \begin{Bmatrix} \bar{\varepsilon}_x - \alpha_{1I} \Delta T \\ \bar{\varepsilon}_y - \alpha_{2I} \Delta T \end{Bmatrix} + [\delta] \begin{Bmatrix} \kappa_x \\ \kappa_y \end{Bmatrix} \quad (25)$$

$$\begin{Bmatrix} M_x \\ M_y \end{Bmatrix} = [D_I] \begin{Bmatrix} \kappa_x \\ \kappa_y \end{Bmatrix} + (t + t_R) [A_I] \begin{Bmatrix} \bar{\varepsilon}_x - \alpha_{1I} \Delta T \\ \bar{\varepsilon}_y - \alpha_{2I} \Delta T \end{Bmatrix} - \frac{1}{2} t_R (t + t_R) [A_R] \begin{Bmatrix} \bar{\varepsilon}_x - \alpha_{1R} \Delta T \\ \bar{\varepsilon}_y - \alpha_{2R} \Delta T \end{Bmatrix} \quad (26)$$

where,

In-plane Inclusion Properties

$$A_I = \frac{t}{t + t_R} A + \frac{t_R}{t + t_R} A_R \quad (27)$$

$$A = \begin{bmatrix} \frac{E_x}{1-\nu_{12}^2} & \frac{\nu_{12}E_x}{1-\nu_{12}^2} \\ \frac{\nu_{21}E_x}{1-\nu_{12}^2} & \frac{E_x}{1-\nu_{12}^2} \end{bmatrix} \quad (28) \quad A_R = \begin{bmatrix} \frac{E_{xR}}{1-\nu_{12R}\nu_{21R}} & \frac{\nu_{12R}E_{yR}}{1-\nu_{12R}\nu_{21R}} \\ \frac{\nu_{21R}E_{xR}}{1-\nu_{12R}\nu_{21R}} & \frac{E_{yR}}{1-\nu_{12R}\nu_{21R}} \end{bmatrix} \quad (29)$$

$$\begin{Bmatrix} \alpha_{1I} \\ \alpha_{2I} \end{Bmatrix} = \frac{t}{t+t_R} [A_I]^{-1} [A] \begin{Bmatrix} \alpha_x \\ \alpha_y \end{Bmatrix} + \frac{t_R}{t+t_R} [A_I]^{-1} [A_R] \begin{Bmatrix} \alpha_{xR} \\ \alpha_{yR} \end{Bmatrix} \quad (30)$$

Neutral Axis Offset

$$\bar{z} = \begin{bmatrix} \bar{z}_x & 0 \\ 0 & \bar{z}_y \end{bmatrix} \quad (31)$$

$$\begin{aligned} \bar{z}_x &= \frac{S_x(t+t_R)}{2(1+S_x)} \\ \bar{z}_y &= \frac{S_y(t+t_R)}{2(1+S_y)} \end{aligned} \quad (32)$$

Stiffness Ratios

$$\begin{aligned} S_x &= \frac{E_{xR}t_R(1-\nu_{12}^2)}{E_x t(1-\nu_{12R}\nu_{21R})} \\ S_y &= \frac{E_{yR}t_R(1-\nu_{12}^2)}{E_x t(1-\nu_{12R}\nu_{21R})} \end{aligned} \quad (33)$$

Bending Force Coefficient

$$\delta = \frac{E_x t}{1-\nu_{12}^2} \begin{bmatrix} 0 & (\nu_{12} - \nu_{12R})\bar{z}_y \\ (\nu_{12} - \nu_{21R})\bar{z}_x & 0 \end{bmatrix} \quad (34)$$

Rigidity of Inclusion

$$D_I = \frac{t^3}{12} [A] + \frac{t_R^3}{12} [A_R] + t [A] \begin{bmatrix} \bar{z} \\ \bar{z} \end{bmatrix}^2 + \frac{t_R}{4} [A_R] \begin{bmatrix} (t+t_R-2\bar{z}_x)^2 & 0 \\ 0 & (t+t_R-2\bar{z}_y)^2 \end{bmatrix} \quad (35)$$

Where,

- $E_x$  Parent structure Elastic Modulus
- $E_{xR}$  Repair Elastic Modulus in the x-direction
- $E_{yR}$  Repair Elastic Modulus in the y-direction
- $t$  Parent structure thickness
- $t_R$  Repair thickness
- $\nu_{12}$  Poisson's ratio of Parent structure
- $\nu_{12R}$  Poisson's ratio of repair in the xy-direction

By determining the displacement and deflection functions for the inclusion and outer structure, the mean strains and curvatures inside the inclusion can be determined by matching compatibility conditions at the inclusion boundary. Enforcing these compatibility conditions results in the following formulation.

$$\begin{bmatrix} L_1 & L_2 \\ L_3 & L_4 \end{bmatrix} \begin{bmatrix} \bar{\varepsilon}_x \\ \bar{\varepsilon}_y \\ \kappa_x \\ \kappa_y \end{bmatrix} = \begin{bmatrix} R_1 \\ R_2 \end{bmatrix} \Delta T \quad (36)$$

Where,

$$L_1 = -\frac{t+t_R}{6D(1-\nu_{12})} \left[ G \left( 2 \begin{bmatrix} \bar{z} \\ \bar{z} \end{bmatrix} [A_I] - 2[A_I] \begin{bmatrix} \bar{z} \\ \bar{z} \end{bmatrix} + t_R [A_R] \right) \right] \quad (37)$$

$$L_2 = \begin{bmatrix} 1 & 1 \\ 1 & -1 \end{bmatrix} + \frac{1}{3D(1-\nu_{12})} \left[ G \left( [D_I] - \begin{bmatrix} \bar{z} \\ \bar{z} \end{bmatrix} [\delta] \right) \right] \quad (38)$$

$$L_3 = \frac{t+t_R}{E_x t} [H] [A_I] + \begin{bmatrix} 1 & 0 \\ 0 & 1 \end{bmatrix} \quad (39)$$

$$L_4 = \begin{bmatrix} \bar{z} \\ \bar{z} \end{bmatrix} + \frac{[H] [\delta]}{E_x t} \quad (40)$$

$$R_1 = -\frac{t+t_R}{6D(1-\nu_{12})} \left[ G \left( \left( 2 \begin{bmatrix} \bar{z} \\ \bar{z} \end{bmatrix} [A_I] - 2[A_I] \begin{bmatrix} \bar{z} \\ \bar{z} \end{bmatrix} \right) \begin{bmatrix} \alpha_{1I} \\ \alpha_{2I} \end{bmatrix} + t_R [A_R] \begin{bmatrix} \alpha_{xR} \\ \alpha_{yR} \end{bmatrix} \right) \right] \quad (41)$$

$$R_2 = (t+t_R) \frac{[H] [A_I]}{E_x t} \begin{bmatrix} \alpha_{1I} \\ \alpha_{2I} \end{bmatrix} + \begin{bmatrix} \omega \\ \omega \end{bmatrix} \quad (42)$$

The remaining constants are as follows:

$$G = \begin{bmatrix} 3 & 3 \\ 1 & -1 \end{bmatrix} \quad (43)$$

Matrix 'H' is given from [17] for a finite structure as:

$$H = \begin{bmatrix} \gamma_1 & -\gamma_2 \\ -\gamma_2 & \gamma_1 \end{bmatrix} \quad (44)$$

Where,

$$\gamma_1 = \frac{(3 - \nu_{12})\eta + (1 + \nu_{12})\lambda}{2} \quad (45)$$

$$\gamma_2 = \frac{(3 - \nu_{12})\eta - (1 + \nu_{12})\lambda}{2} \quad (46)$$

$$\lambda = \frac{1 + \beta \left( \frac{1 - \nu_{12}}{1 + \nu_{12}} \right) \frac{R_i^2}{R_o^2}}{1 - \beta \left( \frac{R_i^2}{R_o^2} \right)} \quad (47)$$

$$\eta = \frac{3 - \nu_{12} + (7 + 3\nu_{12}) \left( \frac{R_i^2}{R_o^2} \right) + (1 - 3\nu_{12}) \left( \frac{R_i^4}{R_o^4} \right) + (1 + \nu_{12}) \left( \frac{R_i^6}{R_o^6} \right)}{(3 - \nu_{12}) \left( 1 - \frac{R_i^2}{R_o^2} \right)^3} \quad (48)$$

$$\beta = \frac{1 - (1 + \nu_{12})kR_o}{1 + (1 - \nu_{12})kR_o} \quad (49)$$

Where,  $k$  Spring Stiffness at the edge of the parent structure.  $k$  can be set to 0 or  $\infty$  for a free edge and clamped edge condition, respectively.

Effective coefficient of thermal expansion of the parent structure

$$\omega = \frac{-\alpha_x \beta \left\{ \frac{T_o}{T_i} - \frac{R_i^2}{R_o^2} - \frac{\left( 1 - \frac{R_i^2}{R_o^2} \right) \left( 1 - \frac{T_o}{T_i} \right)}{2 \ln \left( \frac{R_i}{R_o} \right)} \right\}}{1 - \beta \frac{R_i^2}{R_o^2}} \quad (50)$$

Where,  $T_i$  Cure temperature  
 $T_o$  Temperature in parent structure at a distance  $R_o$

Having determined the mean strains and curvatures of the inclusion, the corresponding stress in the plate and repair is given by equations 23 and 24. The results above reduce to the results presented in reference [17] by setting the curvatures in equation 36 to zero, which yields the following:

$$\begin{Bmatrix} \bar{\epsilon}_x \\ \bar{\epsilon}_y \end{Bmatrix} = [L_3]^{-1} [R_2] \Delta T \quad (51)$$



The above analysis was compared to a fully 3-D finite element repair case using Abaqus 6.8 for a number of repair material variations. The results correlated well against the FE results.

### 4.3 In Plane and Out of Plane Loading due to Applied Stresses

As discussed previously, out of plane bending is due to load path eccentricity inherent in single sided repairs. Its effects cannot be neglected when a single-sided repaired structure is unsupported. Previous works conducted on this subject can be found in references [14, 15]. One of the most commonly used out of plane bending formulations was derived by L.R.F Rose [14] which considers a one-dimensional strip model of a repaired structure under an uniaxial applied stress and is summarised in section 3.2.1.3 of reference [8]. It derives the stress variation through the thickness of the parent structure and repair due to a neutral axis offset using a non-linear analytical formulation.

The most recent works conducted in this area are listed in references [10, 11] and also consider a one-dimensional model with applied stresses, but introduces additional applied bending moments to account for acoustic fatigue problems. Both reports comprise of a linear stress analysis [10], and an approximate non-linear stress analysis [11], excluding load attraction effects.

Expanding these methodologies to include biaxial loading systems and load attraction effects would be beneficial in providing a set of comprehensive analysis tools for this particular repair case. This has lead to the development of reference [13] by C. H. Wang and D. Erjavec, which deals with these effects. The following provides a brief summary of the findings:

The loading configuration in the x-direction is as follows:

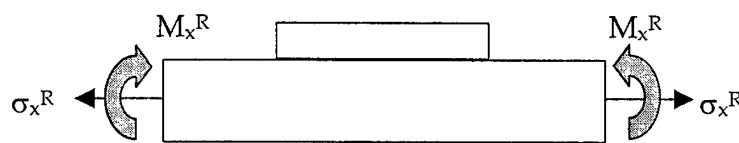


Figure 3

Similarly in the y-direction

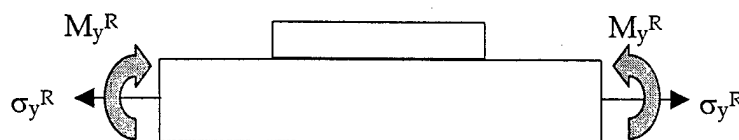


Figure 4

Where,  $\sigma_x^R$  Applied stress in the x-direction at the edge of the structure

$\sigma_y^R$  Applied stress in the y-direction at the edge of the structure

$M_x^R$  Applied moment per unit length in the x-direction at the edge of the structure

$M_y^R$  Applied moment per unit length in the y-direction at the edge of the structure

Free Body Diagram of Repaired Region

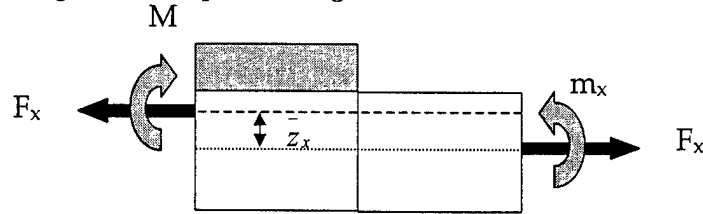


Figure 5

Equilibrium requires the following:

$$M_x = m_x + F_x \bar{z}_x \quad (52)$$

Similarly in the y-direction

$$M_y = m_y + F_y \bar{z}_y \quad (53)$$

The stresses in the plate and reinforcement inside the repaired region are related through Hooke's law as follows:

$$\begin{Bmatrix} \sigma_{xx}(z) \\ \sigma_{yy}(z) \end{Bmatrix} = A \begin{Bmatrix} \bar{\epsilon}_x - \kappa_x(z - \bar{z}_x) \\ \bar{\epsilon}_y - \kappa_y(z - \bar{z}_y) \end{Bmatrix} \quad (54)$$

$$\begin{Bmatrix} \sigma_{xx}^R(z) \\ \sigma_{yy}^R(z) \end{Bmatrix} = A_R \begin{Bmatrix} \bar{\epsilon}_x - \kappa_x(z - \bar{z}_x) \\ \bar{\epsilon}_y - \kappa_y(z - \bar{z}_y) \end{Bmatrix} \quad (55)$$

The total forces and moments can be determined as follows:

$$\begin{Bmatrix} F_x \\ F_y \end{Bmatrix} = (t + t_R) A_I \begin{Bmatrix} \bar{\epsilon}_x \\ \bar{\epsilon}_y \end{Bmatrix} + [\delta] \begin{Bmatrix} \kappa_x \\ \kappa_y \end{Bmatrix} \quad (56)$$

$$\begin{bmatrix} M_x \\ M_y \end{bmatrix} = [D_I] \begin{Bmatrix} \kappa_x \\ \kappa_y \end{Bmatrix} + (t+t_R)[A_I] \begin{bmatrix} \bar{z} \\ \bar{z} \end{bmatrix} \begin{Bmatrix} \bar{\epsilon}_x \\ \bar{\epsilon}_y \end{Bmatrix} - \frac{1}{2}t_R(t+t_R)[A_R] \begin{Bmatrix} \bar{\epsilon}_x \\ \bar{\epsilon}_y \end{Bmatrix} \quad (57)$$

By determining the displacement and deflection functions for the inclusion and outer structure, the mean strains and curvatures inside the inclusion can be determined by matching the compatibility conditions at the inclusion boundary. Enforcing these compatibility conditions results in the following formulation.

$$\begin{bmatrix} L_1 & L_2 \\ L_3 & L_4 \end{bmatrix} \begin{bmatrix} \bar{\epsilon}_x \\ \bar{\epsilon}_y \\ \kappa_x \\ \kappa_y \end{bmatrix} = \begin{bmatrix} R_1 \\ R_2 \end{bmatrix} \quad (58)$$

Where,

$$L_1 = -\frac{t+t_R}{6D(1-\nu_{12})} \left[ G \left( 2 \begin{bmatrix} \bar{z} \\ \bar{z} \end{bmatrix} [A_I] - 2[A_I] \begin{bmatrix} \bar{z} \\ \bar{z} \end{bmatrix} + t_R[A_R] \right) \right] \quad (59)$$

$$L_2 = \begin{bmatrix} 1 & 1 \\ 1 & -1 \end{bmatrix} + \frac{1}{3D(1-\nu_{12})} \left[ G \left( [D_I] - \begin{bmatrix} \bar{z} \\ \bar{z} \end{bmatrix} [\delta] \right) \right] \quad (60)$$

$$L_3 = \frac{t+t_R}{E_x t} [H][A_I] + \begin{bmatrix} 1 & 0 \\ 0 & 1 \end{bmatrix} \quad (61)$$

$$L_4 = \begin{bmatrix} \bar{z} \\ \bar{z} \end{bmatrix} + \frac{[H][\delta]}{E_x t} \quad (62)$$

$$R_1 = \frac{1}{D} \begin{bmatrix} \frac{1}{\nu_{12}+1} & \frac{1}{\nu_{12}+1} \\ \frac{1}{1-\nu_{12}} & \frac{-1}{1-\nu_{12}} \end{bmatrix} \begin{Bmatrix} M_x^R \\ M_y^R \end{Bmatrix} \quad (63)$$

$$R_2 = \left( \frac{1}{E_x} \begin{bmatrix} 1 & -\nu_{12} \\ -\nu_{12} & 1 \end{bmatrix} + \frac{[H]}{E_x} \right) \begin{Bmatrix} \sigma_x^R \\ \sigma_y^R \end{Bmatrix} \quad (64)$$

The remaining constants are given in section 4.2 by setting the temperature terms to zero.

Verification of this formulation will be provided on release of reference [13]. In the mean time, a repair case study has been provided in section 6 of this report and provides a preliminary means of verifying section 4.3 (To be discussed later).

#### 4.4 Stress intensity

One of the most commonly used formulations of a stress intensity factor was derived by L.R.F Rose [14, 16] and is given by equations 19 and 20. These expressions can only be applied to fully supported single-sided repairs and double-sided repairs, since they do not take load path eccentricity into account. Two such reports that deal with stress intensity factors due to load patch eccentricity are references [10] and [11]. Reference [10] determines the limiting strain energy release rate for an unsupported single-sided one-dimensional repair due to applied loads. In such a case, load path eccentricity causes a non-uniform stress under the repair, thus resulting in a varying stress intensity factor through the thickness. The report found that when load path eccentricity effects were included, the stress intensity factor still exhibited asymptotic properties as crack length increased, as shown in figure 12 of reference [8]. This report provides expressions for maximum, minimum and root mean square limiting stress intensity factors in the bounds of a geometrical linear analysis.

Reference [11] provides a crack-bridging model that replaces the patch by a set of distributed springs bridging the two cracked faces. Similarly, considering a one-dimensional unsupported single-sided repair, the report considers a geometrically linear analysis and an approximate geometrical non-linear analysis. The findings produced an equivalent spring compliance matrix representing the patch and determined the corresponding variations of stress intensity factor through the thickness using Kirchhoff's Poisson plate bending theory and Reissner's shear deformation theory.

Repairs that are unsupported can yield peel delamination shortly after the adhesive become plastic (See the strap joint in the figure below). Therefore the scope of references [10] and [11] retain the adhesive in the elastic regime.

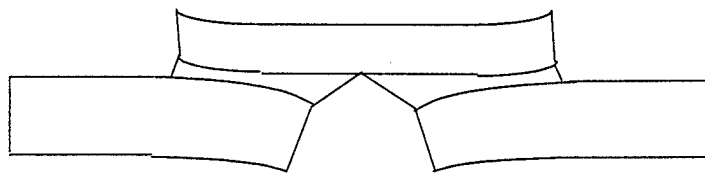


Figure 6

#### Formulation

Using reference [10] and [11], a solution can be determined for the limiting minimum, maximum and root mean squared stress intensity factors as functions of the mean and bending stresses. The following describes the analysis:

The total mean force and bending moment, assuming no crack to be present, can be given as follows [10]:

$$N = \bar{\sigma} t \quad (65)$$

$$M = \frac{\sigma_b t^2}{6} \quad (66)$$

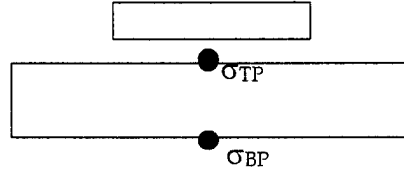


Figure 7

where,

- $\bar{\sigma}$  Mean stress component
- $\sigma_b$  Bending stress component
- $\sigma_{TP}$  Stress at the top of the plate in the major direction ('x' direction)
- $\sigma_{BP}$  Stress at the bottom of the plate in the major direction ('x' direction)

$$\bar{\sigma} = \frac{\sigma_{TP} + \sigma_{BP}}{2} \quad (67)$$

$$\sigma_b = \sigma_{BP} - \bar{\sigma} \quad (68)$$

As the crack propagates, work is extracted to relax the first stage stresses to zero. (ie, first stage stresses refer to the stress calculated in the parent structure under the repair from sections 4.2 & 4.3) The strain energy release rate can be found by the following equation [10]:

$$tG_{\infty}^* = [N \quad M] \begin{Bmatrix} u_o \\ \theta_o \end{Bmatrix} \quad (69)$$

where,

- $G_{\infty}^*$  Asymptotic strain energy release rate
- $u_o$  Crack opening displacement
- $\theta_o$  Crack face rotation

Using the results from [11], the crack opening displacement and crack face rotation can be expressed as functions of the mean force and bending moment as follows:

$$\begin{Bmatrix} u_o \\ \theta_o \end{Bmatrix} = \begin{bmatrix} c_{11} & c_{12} \\ c_{21} & c_{22} \end{bmatrix} \begin{Bmatrix} N \\ M \end{Bmatrix} \quad (70)$$

where,

$$c_{11} = \frac{t(t_R + t)}{4\kappa D_R} + \left[ \frac{(1 - \nu_{12R}\nu_{21R})}{E_{xR}t_R} + \frac{(1 - \nu_{12}^2)}{E_x t} + \frac{t_R(t + t_R)}{4D_R} \right] \left[ \frac{1}{2\beta} - \frac{\mu_A t}{16\kappa^2 \beta t_A} \left( \frac{t_R}{D_R} - \frac{t}{D_P} \right) \right] \quad (71)$$

$$c_{12} = \frac{t}{2\kappa D_R} \left( 1 + \frac{D_R}{D_P} \right) + \left( \frac{t_R}{2D_R} - \frac{t}{2D_P} \right) \left( \frac{1}{2\beta} - \frac{\mu_A t}{16\kappa^2 \beta t_A} \left( \frac{t_R}{D_R} - \frac{t}{D_P} \right) \right) \quad (72)$$

$$c_{21} = \frac{t_R + t}{2\kappa D_R} - \frac{\mu_A}{8\kappa^2 \beta t_A} \left( \frac{t_R}{D_R} - \frac{t}{D_P} \right) \left( \frac{(1 - \nu_{12R}\nu_{21R})}{E_{xR}t_R} + \frac{(1 - \nu_{12}^2)}{E_x t} + \frac{t_R(t + t_R)}{4D_R} \right) \quad (73)$$

$$c_{22} = \frac{1}{\kappa D_R} \left( 1 + \frac{D_R}{D_P} \right) - \frac{\mu_A}{16\kappa^2 \beta t_A} \left( \frac{t_R}{D_R} - \frac{t}{D_P} \right)^2 \quad (74)$$

where,

$$\kappa^4 = \frac{2\mu_A(1 + \nu_{12A})}{4t_A} \left[ \frac{1}{D_P} + \frac{1}{D_R} \right] \quad (75)$$

$$4\beta^2 = \frac{4\mu_A}{t_A} \left( \frac{(1 - \nu_{12R}\nu_{21R})}{E_{xR}t_R} + \frac{(1 - \nu_{12}^2)}{E_x t} \right) \quad (76)$$

$$D_P = \frac{E_x t^3}{12(1 - \nu_{12}^2)} \quad (77)$$

$$D_R = \frac{E_{xR} t_R^3}{12(1 - \nu_{12R}\nu_{21R})} \quad (78)$$

where,  $\mu_A$  adhesive shear modulus  
 $t_A$  adhesive thickness

Once the crack opening displacement and crack face rotation is determined, the results can be placed into equation 69 to determine the limiting strain energy release rate.

The root mean square of the upper bound stress intensity factor is determined as follows:

$$K_{\infty, RMS}^* = \sqrt{E_x G_{\infty}^*} \quad (79)$$

The ratio between the minimum and maximum stress intensity factors is as follows [10]:

$$R = \frac{K_{\min}}{K_{\max}} = \frac{\bar{\sigma} - \sigma_b}{\bar{\sigma} + \sigma_b} \quad (80)$$

The corresponding asymptotic maximum and minimum stress intensity factors (ie due to a varying stress through the thickness) can be determined as follows:

$$K_{\infty, \max}^* = \left( \frac{3}{1 + R + R^2} \right)^{1/2} K_{\infty, RMS}^* \quad (81)$$

$$K_{\infty, \min}^* = \left( \frac{3}{1 + R + R^2} \right)^{1/2} RK_{\infty, RMS}^* \quad (82)$$

#### 4.5 Maximum Adhesive Shear Strain Under the repair

Equations 10 [8], 12 [8], 16 and 17 were developed assuming a uniform-stress state through the thickness of the parent structure. They do not consider out of plane bending effects and therefore cannot be used to evaluate the maximum adhesive shear strain in unsupported single sided repairs.

Reference [11] derives the maximum adhesive shear strain likely to occur under the repair including load patch eccentricity effects. The formulation is in-terms of the mean force and bending moment (equations 65 and 66), which follows on from the results obtained from the previous section, 4.4. The maximum adhesive shear strain under the repair is given by the following [11]:

$$\gamma_{Max}^A = -\frac{1}{2\beta t_A} \left[ \frac{(1 - \nu_{12R}\nu_{21R})}{E_{xR}t_R} + \frac{(1 - \nu_{12}^2)}{E_x t} + \frac{3(t + t_R)(1 - \nu_{12R}\nu_{21R})}{E_{xR}t_R^2} \right] N + \frac{6}{2\beta t_A} \left[ \frac{(1 - \nu_{12R}\nu_{21R})}{E_{xR}t_R^2} - \frac{(1 - \nu_{12}^2)}{E_x t^2} \right] M \quad (83)$$

The shear strain occurring at the crack location is given by  $-\gamma_{Max}^A$ .

#### 4.6 Peel Stresses

Hart-Smith [21] derived the maximum peel stress at the end of the repair (Equation 18), as used by C5033 [3]. This expression is derived considering a one-dimensional lap repair joint subject to applied loads. Considering vertical equilibrium requirements allow the peel stresses to be solved as a function of position from the centre of the patch.

More recent works, reference [11], derives a more complex expression for a strap joint, which is more representative of a bonded cracked plate than a lap joint configuration (See figure 6). The patch is replaced by distributed springs, which are used to formulate the effective spring compliance matrix (Equation (70)). The peel strain expression is determined from the following [11]:

$$\varepsilon_A = (A \cos(\kappa x) + B \sin(\kappa x)) e^{-\kappa x} \quad (84)$$

where 'A' and 'B' can be determined from the following:

$$\begin{bmatrix} 0 & -2\kappa^2 \\ 2\kappa^3 & 2\kappa^3 \end{bmatrix} \begin{Bmatrix} A \\ B \end{Bmatrix} = \begin{bmatrix} \frac{t+t_R}{2D_R t_A} & \frac{1}{D_R t_A} \left(1 + \frac{D_R}{D_P}\right) \\ 0 & 0 \end{bmatrix} \begin{Bmatrix} N \\ M \end{Bmatrix} + \begin{bmatrix} 0 & 0 \\ \frac{\mu_A t_R}{2D_R t_A} & \frac{-\mu_A t}{2D_P t_A} \end{bmatrix} \begin{Bmatrix} \gamma_{Max}^A \\ \gamma_{Max}^A \end{Bmatrix} \quad (85)$$

(Note: Constants used in equations above are previously defined)

Knowing the peel strain distribution from equation 84, the peel strain near the crack and at the end of the patch can be found by substituting  $x=0$  and  $x=a$  (ie  $a$ =half patch length) respectively. The corresponding peel stress is given by the following:

$$\sigma_A = E_A \varepsilon_A \quad (86)$$

$$E_A = 2\mu_A(1 + \nu_A) \quad (87)$$

where,  $E_A$  Elastic modulus of adhesive  
 $\nu_A$  Poisson's Ratio of adhesive

## 5. Recommended Approach for an Improved Design

C5033 and CalcuRep provide designers with analysis tools to develop appropriate repair designs for a range of cases. These tools have a number of limitations as previously discussed. The development of more advanced tools, as discussed in section 4, have removed many of these limitations. Therefore it would be beneficial to apply these tools in an appropriate manner to provide the means to design a repair.

This section entails the development of a design approach using new and already established design tools to provide a more versatile package. The package deals with the following cases:

- Single Sided Fully supported repairs
- Double Sided repairs
- Single Sided Unsupported repairs
- Stiffened Panels with a crack in either the stiffener or the skin beneath the stiffener

The following will outline the steps and tools required to produce such a package.



## 5.1 Repair Methodology for Single Sided Unsupported Repairs

### 5.1.1 Patch Dimensions (Single Sided Unsupported Repairs)

Determine the patch dimensions using section 3.2.1

Note: The load transfer length used by C5033, i.e. equation (11) [8] and (5), has been derived assuming plane stress conditions. References [10] and [11] show that plane strain conditions prevail rather than plane stress conditions, see [8] for details. Therefore the load transfer length used for the following sections will be changed to equation 76.

### 5.1.2 Determining the Stress Under and at the edge of the Repair (Single Sided Unsupported Repairs)

- **Applied Stresses**

Using section 4.3, calculate the stress at the top and bottom of the parent structure under the repair in the x-direction and denote their values as  $\sigma_{TP}$  and  $\sigma_{BP}$  respectively. Calculate the total force in the parent structure at the edge of the repair in the x-direction, denoted its value as  $F_x$ .

- **Thermal Stresses**

The thermal residual stress variation through the thickness under the repair is effected by two thermal cycles. The first is the cure cycle, while the second is the operational cycle. Consider the effect these two cycles have on the structure outside the repaired region and inside the repaired region:

#### Outside the Repaired Region

##### Cure Cycle

During the cure cycle the repaired region is heated to the cure temperature ( $T_i$ ). At the edge of the structure away from the patch, the temperature is a lower temperature  $T_o$ . Due to this non-uniform temperature distribution, constraint is provided from the cooler material that effectively resists the expansion of the warmer material. This phenomenon effectively reduces the thermal expansion coefficient of the plate, given by equation 50. It can be assumed that  $T_o$  is at room temperature (RT) provided the edge of the parent structure is sufficiently remote from the heated region.

After cure, the heated region of the structure is cooled down to room temperature. Therefore a negative temperature change occurs, which is the reversal of the heating cycle. As a result,  $T_i$  and  $T_o$  become negative.

## Operational Cycle

During this cycle it can be assumed that a uniform temperature change exists throughout the repaired structure. This can occur in aircraft fuselage, as the aircraft gains altitude. Therefore  $T_o/T_i$  can be set to unity in equation 50.

## The Inclusion Region (Inside the repaired region)

### Cure Cycle

During the cure cycle, the inclusion experiences the following temperature change

$$\Delta T = RT - T_i$$

### Operational Cycle

During the operational cycle, the inclusion experiences the following temperature change.

$$\Delta T = T_i - RT$$

Where,  $\Delta T$  Temperature Change  
 $T_{oper}$  Operational Temperature  
 $RT$  Room Temperature

Using section 4.2, calculate the stress at the top and bottom of the parent structure under the repair in the x-direction and denote their values as  $\sigma_{TP}$  and  $\sigma_{BP}$  respectively. Calculate the total force in the parent structure at the edge of the repair in the x-direction, denoted its value as  $F_x$ . This procedure should be completed twice, for both the cure and operational thermal cycles. Then add the corresponding stresses from these two cycles to produce the total thermal stress components.

### 5.1.3 Finding the Total Stress (Single Sided Unsupported Repairs)

Add the following components,  $\sigma_{TP}$ ,  $\sigma_{BP}$  and  $F_x$ , calculated from the applied and thermal stress procedures. The margin of safety of safety as per [3, 4, 5] for the stress in the parent structure at the edge of the repair is as follows:

$$MOS = \frac{\sigma_{ULT}}{F_x/t} - 1$$

where

$$MOS > 0.2$$

(88)

#### 5.1.4 Determining the Maximum Adhesive Shear Strain (Single Sided Unsupported Repairs)

The maximum adhesive shear strain can be determined using section 4.5. The margin of safety as per [3, 4, 5] for the maximum adhesive shear strain retained in the elastic regime is as follows:

$$MOS = \frac{\gamma_E}{\gamma_{Max}^A} - 1$$

(89)

where

$$MOS > 0.2$$

#### 5.1.5 Determining the upper bound stress intensity factor (Single Sided Unsupported Repairs)

Using the values of  $\sigma_{TP}$ ,  $\sigma_{BP}$  and  $F_x$  calculated from section 5.1.3, determine the maximum, minimum and root mean squared upper bound stress intensity factor using section 4.4. The margin of safety as per [3, 4, 5] for the upper bound stress intensity factor is as follows:

$$MOS = \frac{K_C}{K_{\infty, max}^*} - 1$$

(90)

where

$$MOS > 0.2$$

#### 5.1.6 Determining the Maximum Peel Stress at the Crack and at the Edge of the Patch (Single Sided Unsupported Repairs)

The peel stress at the crack and at the edge of the repair can be determined using section 4.6. The margin of safety as per [3, 4, 5] for the maximum adhesive shear strain is as follows:

$$\sigma_A \leq 6000 \text{ psi (Brittle Adhesive Systems)}$$
$$\sigma_A \leq 10000 \text{ psi (Ductile Adhesive Systems)}$$

#### 5.1.7 Calculating the Maximum Stress in the Patch (Single Sided Unsupported Repairs)

It is assumed that all the stress at the edge of the repair is transferred into the patch. This is valid providing the actual crack length is greater than the characteristic crack length (See [8] for details). This results in the following equation:

$$\sigma_{Max}^P = \frac{F_x}{t_R} \quad (91)$$

The margin of safety as per [3, 4, 5] for the maximum patch stress is as follows:

$$MOS = \frac{\sigma_{ULT0}}{\sigma_{Max}^P} - 1$$

where

$$MOS > 0.2 \quad (92)$$

where,  $\sigma_{ULT0}$  Patch ultimate strength

## 5.2 Repair Methodology for Single Sided Fully Supported Repairs

### 5.2.1 Patch Dimensions (Single Sided Fully Supported Repairs)

Determine the patch dimensions using section 3.2.1.

### 5.2.2 Adhesive Management

Check the Rapid Repairability Criterion using section 3.2.2. The margin of safety as per [3, 4, 5] for the adhesive load capacity is as follows:

$$P \geq 1.2\sigma_{ULT}t_i \quad (93)$$

### 5.2.3 Stress Under and at the Edge of the Repair (Fully supported single sided repairs)

- **Applied Stress**

For a repair to fully support structure, a uniform stress will result. Therefore by setting the curvatures to zero, equation 58 in section 4.3 reduces to the following:

$$\begin{Bmatrix} \varepsilon_x \\ \varepsilon_y \end{Bmatrix} = [L_3]^{-1}[R_2] \quad (94)$$

Using section 4.3 with zero curvatures and equation 94, calculate the stress in parent structure under the repair in the x-direction and denote its value as  $\sigma_o$ . Calculate the total force in the parent structure at the edge of the repair in the x-direction using section 4.3, denoted its value as  $F_x$ .

- **Thermal Stresses**

Since restraint is provided against out of plane bending no curvatures exist. Therefore equation 36 in section 4.2 reduces to equation 51:

Using section 4.2 with zero curvatures and equation 51, calculate the stress in the parent structure under the repair in the x-direction and denote its value as  $\sigma_0$ . Calculate the total force in the parent structure at the edge of the repair in the x-direction using section 4.2, denoted its value as  $F_x$ . This procedure should be completed twice, for both the cure and operational thermal cycles. Then add the corresponding stresses from these two cycles to produce the total thermal stress components.

#### **5.2.4 Finding the Total Stress (Single Sided Fully Supported Repairs)**

Add the values of  $\sigma_0$  and  $F_x$ , determined from the applied and thermal stress procedures. The margin of safety of safety as per [3, 4, 5] for the stress in the parent structure at the edge of the repair is given by equation 88.

#### **5.2.5 Determining the Maximum Adhesive Shear Strain (Single Sided Fully Supported Repairs)**

The maximum adhesive shear strain can be determined using section 3.2.3. The margin of safety as per [3, 4, 5] for the maximum adhesive shear strain is given by the following:

$$MOS = \frac{\gamma_E + \gamma_P}{\gamma_{Max}^A} - 1$$

where (95)

$$MOS > 0.2$$

#### **5.2.6 Determining the upper bound stress intensity factor (Single Sided Fully Supported Repairs)**

Calculate the upper bound stress intensity factor using section 3.2.4. The margin of safety of safety as per [3, 4, 5] for the upper bound stress intensity factor is given by equation 90.

#### **5.2.7 Determining the Maximum Peel Stress at the Edge of the Patch (Single Sided Fully Supported Repairs)**

The peel stress at the edge of the repair can be determined using section 3.2.4. The margin of safety as per [3, 4, 5] for the maximum adhesive shear strain is as follows:

$$\sigma_A \leq 6000 \text{ psi (Brittle Adhesive Systems)}$$
$$\sigma_A \leq 10000 \text{ psi (Ductile Adhesive Systems)}$$

### 5.2.8 Calculating the Maximum Stress in the Patch (Single Sided Fully Supported Repairs)

It is assumed that all the stress at the edge of the repair is transferred into the patch. This is valid providing the actual crack length is greater than the characteristic crack length (See [8] for details). Calculate the maximum stress transferred into the patch, given by equation 91. The margin of safety as per [3, 4, 5] for the maximum patch stress is given by equation 92.

## 5.3 Repair Methodology for Double Sided Repairs

### 5.3.1 Patch Dimensions (Double Sided Repairs)

Determine the patch dimensions using section 3.2.1.

### 5.3.2 Adhesive Management

Check the Rapid Repairability Criterion using section 3.2.2. The margin of safety as per [3, 4, 5] for the adhesive load capacity is given by equation 93

### 5.3.3 Stress Under and at the Edge of the Repair (Double sided repairs)

- **Applied Stress**

Including an additional patch will correspondingly change some of the inclusion properties. In such a case, equations 27 and 30 of section 4.2 become:

$$A_I = \frac{t}{t+t_R} A + \frac{2t_R}{t+t_R} A_R \quad (96)$$

$$\begin{Bmatrix} \alpha_{1I} \\ \alpha_{2I} \end{Bmatrix} = \frac{t}{t+t_R} [A_I]^{-1} [A] \begin{Bmatrix} \alpha_x \\ \alpha_y \end{Bmatrix} + \frac{2t_R}{t+t_R} [A_I]^{-1} [A_R] \begin{Bmatrix} \alpha_{xR} \\ \alpha_{yR} \end{Bmatrix} \quad (97)$$

Using section 4.3 with zero curvatures, noting equations 94, 96 and 97, calculate the stress in parent structure under the repair in the x-direction. Denote its value as  $\sigma_o$ . Calculate the total force in the parent structure at the edge of the repair in the x-direction using section 4.3, denoting its value as  $F_x$ .

- **Thermal Stresses**

Using section 4.2 with zero curvatures, noting equations 51, 96 and 97, calculate the stress in the parent structure under the repair in the x-direction. Denote its value as  $\sigma_o$ . Calculate the total force in the parent structure at the edge of the repair in the x-direction using section 4.2, denoting its value as  $F_x$ . This procedure should be completed twice, for both the cure and operational

thermal cycles. Then add the corresponding stresses from these two cycles to produce the total thermal stress components.

#### **5.3.4 Finding the Total Stress (Double Sided Repairs)**

Add the values of  $\sigma_o$  and  $F_x$ , determined from the applied and thermal stress procedures. The margin of safety of safety as per [3, 4, 5] for the stress in the parent structure at the edge of the repair is given by equation 88.

#### **5.3.5 Determining the Maximum Adhesive Shear Strain (Double Sided Repairs)**

The maximum adhesive shear strain can be determined using section 3.2.3. The margin of safety as per [3, 4, 5] for the maximum adhesive shear strain is given by equation 95:

#### **5.2.6 Determining the upper bound stress intensity factor (Double Sided Repairs)**

Calculate the upper bound stress intensity factor using section 3.2.4. The margin of safety of safety as per [3, 4, 5] for the upper bound stress intensity factor is given by equation 90.

#### **5.3.7 Determining the Maximum Peel Stress at the Edge of the Patch (Double Sided Repairs)**

The peel stress at the edge of the repair can be determined using section 3.2.4. The margin of safety as per [3, 4, 5] for the maximum adhesive shear strain is as follows:

$$\begin{aligned}\sigma_A &\leq 6000 \text{ psi (Brittle Adhesive Systems)} \\ \sigma_A &\leq 10000 \text{ psi (Ductile Adhesive Systems)}\end{aligned}$$

#### **5.3.8 Calculating the Maximum Stress in the Patch (Double Sided Repairs)**

It is assumed that all the stress at the edge of the repair is transferred into the patch. This is valid providing the actual crack length is greater than the characteristic crack length (See [8] for details). Calculate the maximum stress transferred through the patch, given by equation 91. The margin of safety as per [3, 4, 5] for the maximum patch stress is given by equation 92.

#### **5.4 Unsatisfactory Margin of Safety**

The margin of safeties listed in the previous section are provided to ensure the proposed repair design is appropriate in repairing the cracked region efficiently. The inability to satisfy any of these criteria may lead to an ineffective repair. If one or more of the criteria cannot be met by the designer,

there are a number of options available to improve the design. C5033 and CalcuRep contain a number of options to reduce stresses and other specified variables in order to meet design criteria. The following is a list of advice given by C5033 and CalcuRep to the user.

### C5033

Insufficient overlap length

- Use a higher modulus patch material

Insufficient load capacity

- Select an adhesive with a higher plastic strain capacity
- Match repair stiffness with parent structure stiffness
- Match thermal expansion coefficients of repair and parent structure
- Increase the adhesive thickness

If the upper bound stress intensity factor is too high

- Use an adhesive with a high shear modulus
- Increase the stiffness of the patch (Note: do not exceed  $1.2 E_t t_p$ )

Peel stress too high

- Taper the ends of the repair
- Use a higher modulus patch material
- Use serrated ply ends

### CalcuRep

If the upper bound stress intensity factor is too high, try the following:

- Use a thicker or shorter patch
- Use a patch material with a higher coefficient of thermal expansion

If the patch stress is too high

- Use a thicker or wider patch
- Use a shorter overlap length
- Stronger patch material

If the stress in the parent structure at the edge of the patch is too high

- Use a thinner or wider or tapered patch
- Use a shorter overlap length



- Use a patch material with a lower coefficient of thermal expansion

If the adhesive Shear Strain is too high

- Use a thicker patch
- Use a patch material with a higher coefficient of thermal expansion

If the load transfer is too high

- Use a longer or thinner patch
- Use a less stiff patch

## 6. Case Study Comparison

A finite element model case study was developed in reference [22] and demonstrated the significance of out of plane bending effects in unsymmetric bonded repairs. The results produced from this study were alarming and suggested that the stress intensity factor for a single sided unsupported repair increased indefinitely with increasing crack length. An earlier model developed in reference [15] supported these findings. As a result, serious doubt was cast over the validity of existing bonded repair technology. Therefore an independent study was conducted in references [10] and [11] using this case study to confirm or otherwise the findings produced by references [15] and [22]. The results of the independent study showed that the stress intensity factor in single sided unsupported repairs approaches an asymptote value for increasing crack length.

The case study used above is a standard repair case consisting of a boron patch bonded to a centre cracked aluminium plate with a uniaxial stress applied. The patch covers the entire width of the plate, therefore load attraction effects are neglected. The repair case configuration and material properties are listed in section 6.1.

Verification of previous single sided supported and double-sided repair analysis tools used by C5033 and CalcuRep has been provided in reference [8]. Verification of analyse tools listed in sections 4.2 [12], 4.4 [10, 11], 4.5 [11], 4.6 [11] and 4.7 [21] have previously been confirmed by the references shown above. Complete verification of the analysis tools shown in section 4.3 have yet to be provided and will be demonstrated on release of reference [13]. In the mean time, a preliminary verification process will be provided by the use of the finite element cases study discussed previously.

The following section is denoted as a preliminary verification process for the following two reasons:

- (1) The case study used in reference [8] and [9] excludes load attraction effects. The procedure listed in section 5.1 (which includes the use of section 4.3) includes load attraction effects and cannot be modified to exclude these effects.
- (2) Comparing the results produced from section 5.1 with those obtained from reference [8] and [9] will not provide a completely fair comparison due to the point above. It will rather demonstrate whether the results approximately coincide and how the differences listed in point 1 above effect the results.

### 6.1 Single Sided Unsupported Repair Configuration

Part	Elastic Modulus (MPa)	Poisson's Ratio	Thickness (m)	Length (m)	Width (m)
Plate	71000	0.3	0.003	0.5	0.5
Repair	207000	0.3	0.00102	0.1	0.5
Adhesive	1890	0.33	0.000203	0.1	0.5

(Table 1)

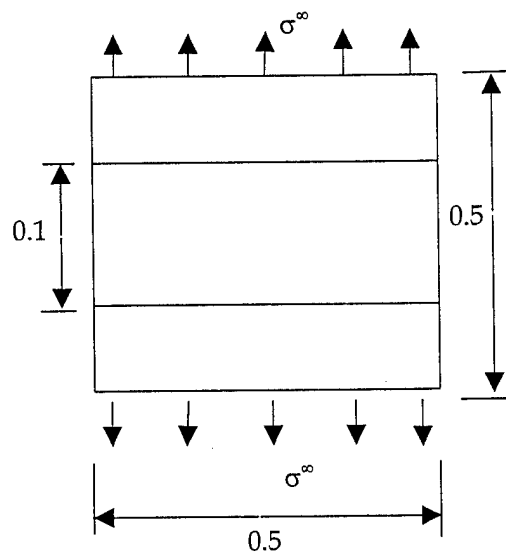


Figure 8

The above repair configuration is a single sided unsupported repair with an applied stress at the plate boundary. No thermal effects have been taken into account. The load attraction can be assumed to be zero, since the patch covers the entire width of the plate. Reference [8] and [9] provide results for the upper bound minimum, root mean squared and maximum stress intensity factors due to an applied stress.

## 6.2 Results

The methodologies discussed in section 5 of this report have been programmed into Mathcad [9]. The Mathcad output listed in the appendices are as follows: Single Sided Unsupported repairs section 5.1 (A1), Single Sided Fully supported repairs section 5.2 (A2), Double Sided repairs section 5.3 (A3), Single Sided Unsupported repairs section 5.1 (A4), Stiffened Panels with a crack in either the stiffener or the skin beneath the stiffener section 5.4 (A5).

The appendices listed above detail the following:

- A1            Section 5.1 applying the case study above.
- A2 to A5      The remaining appendices relay examples of the methods listed in sections 5.2 to 5.4 for the F-111 Boron repair discussed in reference [8]. This is provided for two reasons; 1) to allow the user to view how the mathematical expressions in section 5 are arranged, 2) to provide a means to verify any future software developments against the methods discussed in section 5.

Using the single sided unsupported repair design mathcad module (ie Section 5.1 Appendix A1) and running the case study produced the following results.

Reference	$K^*_{Min}/\sigma^\infty (\sqrt{m})$	$K^*_{RMS}/\sigma^\infty (\sqrt{m})$	$K^*_{Max}/\sigma^\infty (\sqrt{m})$
[10 & 11]	0.102	0.282	0.430
Section 5.1	0.125	0.261	0.376

Table 2

### Relative Asymptote Stress Intensity Factor Comparison Post Repair Including and Excluding Load Attraction

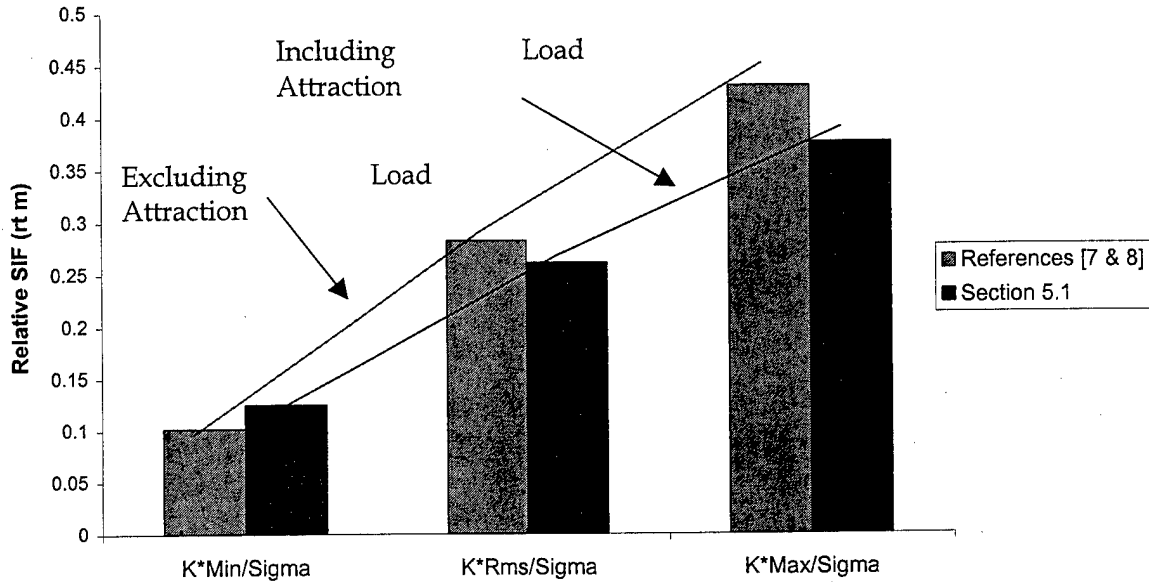


Figure 9

## 7. Main Discussion

Applying the case study using section 5.1, the minimum, root mean squared and maximum stress intensity factors were calculated. The results are shown in table 2 and figure 9 above. Figure 9 demonstrates that load attraction reduces the root mean squared and maximum stress intensity factors. This phenomenon can be explained by considering the following equation from [13]:

$$L_3 \begin{Bmatrix} - \\ \varepsilon_x \\ - \\ \varepsilon_y \end{Bmatrix} + L_4 \begin{Bmatrix} \kappa_x \\ \kappa_y \end{Bmatrix} = R_2 \quad (98)$$

Rearranging equation 98 to make the mean strains in the inclusion the subject gives the following:

$$\begin{Bmatrix} - \\ \varepsilon_x \\ - \\ \varepsilon_y \end{Bmatrix} = L_3^{-1} \left[ R_2 - L_4 \begin{Bmatrix} \kappa_x \\ \kappa_y \end{Bmatrix} \right] \quad (99)$$

Applying a stress to the boundary of an unsupported single sided repair will cause a positive curvature inside the inclusion section (See figure 6). This is predominantly due to the neutral axis of the plate shifting towards the neutral axis of the inclusion section. With this concept in mind, consider equation 99

for positive curvatures and positive  $L_4$ . A positive curvature in the inclusion section will result in a reduction of the mean strains inside the inclusion. If the curvatures are large enough, as in this case study, load is extracted from the repaired region rather than attracted into the repaired region.

In establishing the above point, now consider the strain energy release rate provided by equation 43 of reference [10], listed as follows:

$$G_{\infty}^* = \frac{(\Omega \sigma^{\infty})^2 (1 - \nu_{12}^2)}{(1 + S) S \beta E_p} \omega^2 \quad (100)$$

Where,	$G_{\infty}^*$	Upper bound strain energy release rate
	$\sigma^{\infty}$	Applied stress
	$S$	Stiffness Ratio
	$\beta$	Inverse of the load transfer length
	$E_p$	Plate Modulus
	$\omega$	Bending correction factor
	$\Omega$	Load attraction factor (Not included in reference [10])

Note: The upper bound strain energy release rate provided in section 4.4 is derived considering crack bridging by springs and compares well with equation 100. The above equation is used in this case to provide a simpler mean to justify the following argument, rather than using the more complex form of equation 68 in section 4.4.

The upper bound root mean squared stress intensity factor is therefore given by equation 79 as following:

$$K_{\infty, RMS}^* = \sqrt{E_p G_{\infty}^*}$$

or

$$\frac{K_{\infty, RMS}^*}{\sigma^{\infty}} = \Omega \omega \sqrt{\frac{(1 - \nu_{12}^2)}{(1 + S) S \beta}} \quad (101)$$

Equation 101 demonstrates that a decrease in load attraction will result in a decrease in the upper bound root mean square stress intensity factor, thus confirming the load extraction effect previously discussed and shown figure 9.

Consider the gradients of the two curves plotted in figure 9. The difference in the gradient between the two results is predominantly due to the 'R' ratio effect shown in equation 81 and 82. For larger 'R' values (See equation 80) the maximum upper bound stress intensity factor will decrease and the minimum upper bound stress intensity factor will increase. The actual 'R' value

calculated by reference [10] and section 5.1 are 0.236 and 0.333 respectively and confirms the gradient trend shown in figure 9.

Consider the dominating factors effecting the 'R' ratio, equation 80:

$$R = \frac{\frac{\bar{\sigma}}{\sigma_b} - 1}{\frac{\bar{\sigma}}{\sigma_b} + 1} \quad (102)$$

For larger mean to bending stress ratios ( $\frac{\bar{\sigma}_m}{\sigma_b}$ ), a larger 'R' value is produced.

The mean to bending stress ratios produced by reference [10] and section 5.1 are 1.62 and 2 respectively. From these two figures it can be seen that the load extraction from section 5.1 has significantly reduced maximum bending stress ( $\sigma_b$ ). This consequently results in a larger 'R' value and is the predominant factor producing the gradient differences in figure 9.

Consider the effects of thermal stresses in the analysis. Conclusions from reference [12] demonstrate the following:

- Load is attracted into the repaired region
- The stress at the top of the plate under the repair has increased from the mean value.
- The stress at the bottom of the plate under the repair has decreased from the mean value

The above results have demonstrated the following for an unsupported repair with a uniaxial load applied:

- Load is extracted from the repaired region
- The stress at the top of the plate under the repair has decreased from the mean value.
- The stress at the bottom of the plate under the repair has increased from the mean value

These points show that out of plane bending effects produced by applied stresses counteract out of plane bending effects caused by thermal residual stresses in single sided unsupported repairs. Further work would be required to establish which of these two applications may be dominant and under which conditions.

## 8. CONCLUSION AND RECOMMENDATIONS

Bonded repair technology is widely becoming the preferred method of repair over mechanically fastened repairs. An efficient and effective repair requires the use of validated analytical formulations that describe events occurring in reality. Such analytical tools exist and are becoming more developed as the technology becomes the preferred repair method. A summary of these existing tools as used by C5033 and CalcuRep has been provided in CalcuRep review task 1 [8].

CalcuRep review task 2 has been centred toward developing a new approach that includes the best tools from both CalcuRep and C5033, as well as utilising the most recent developments in this area. The key to extending CalcuRep's capability has been to logically arrange existing and new design tools to develop an appropriate repair design approach for a wider range of repair cases. The methods used for this procedure are listed in section 5 of this report. This report has been successful in providing users with a new approach that deals with the following repair scenarios:

- Single Sided Fully supported repairs
- Double Sided repairs
- Single Sided Unsupported repairs
- Stiffened Panels with a crack in either the stiffener or the skin beneath the stiffener

This report has also provided mathcad modules in appendices A1 to A5 which detail the new approach (section 5) for each case shown above. Designers using these approaches can either use the mathcad modules provided in the appendices or program a software package ensuring verification against these modules.

Section 6 of this report details a case study, which was used to provide a preliminary validation of the approach developed in section 4.3. This case study consisted of an unsupported single sided repair with a uniaxial stress applied to the plate boundary. The results of this study produced the upper bound stress intensity factor post repair excluding load attraction effects by the use of Finite Element Analysis [10, 11]. Using the new approach described in section 5.1 for this particular repair case, corresponding upper bound stress intensity factors, taking into account load attraction affects, were calculated. Discrepancies in the results were directly due to the inclusion of load attraction effects, which reduced the root mean and maximum upper bound stress intensity factors. Reductions of this nature were found to be predominantly due to load being extracted from the repaired region, rather than attracted into the repair region. The findings also demonstrated that out of plane bending stresses produced by thermal residual stresses can be beneficial in counteracting those produced by applied stress.

Further work can be developed on the following points:

- Complete verification of the approach listed in section 5.1 has yet to be performed by a finite element comparison allowing for load attraction effects. This can be done as follows: Develop a 2-stage finite element model of an unsupported finite circular plate bonded by a finite circular orthotropic patch. The first stage of the analysis is to determine the stresses in the repair region including thermal and applied stress effects (Biaxial) assuming no crack present. Compare these results against the method described in section 5.1. Introduce a centre crack in the finite element model and determine the upper bound minimum, root mean squared and maximum stress intensity factor. Compare against results from section 5.1.
- Confirm the approach listed in section 5.1 and the finite element analysis by the use of experimental test data.
- Expand the analysis to consider an elliptical patch and plate. This allows the user to adjust the patch and plate length and width rather than corresponding radii, giving the user more scope in the design method.
- Develop a software package that includes the recommended approaches listed in section 5 of this report.
- Determine whether out of plane bending effects due to applied stresses are more dominant than those produced by thermal stresses, or visa versa.

## 9. ACKNOWLEDGMENTS

The authors wish to acknowledge the following people for their advice throughout this report:

Rhys Jones, Francis Rose, Thomas Ting, Peter Chalkley, Richard Chester. A special thanks goes to Max Davis and Chun H. Wang whose advice and help have been invaluable throughout the duration of this report.

## 10. REFERENCES

1. Fredell, R. S., Damage Tolerant Repair Techniques for Pressurised Aircraft Fuselages, Delft University of Technology, Netherlands, 1994.
2. Fredell, R. S., CalcuRep Version 1.0 for Windows, United States Air Force Academy, 1997



3. RAAF Standard C5033.
4. AAP 7021.016-1
5. AAP 7021.016-2
6. Callinan, R. J., Sanderson, S., Keeley, D., Finite Element Analysis of an F-111 Lower Wing Skin Fatigue Crack Repair, DSTO, Australia, 1997. DSTO-TR-0067
7. Boykett, R., Walker, K., F-111C Lower Wing Skin Bonded Composite Repair Substantiation Testing, DSTO, Australia, 1996. DSTO-TR-0480
8. Erjavec, D., Walker, K., Evaluation of the USAF CalcuRep software for the design of Bonded Repairs to Metallic Aircraft Structure, DSTO Melbourne, 1999. DSTO-TR-xxxx.
9. Mathcad Version 8, 1984-1998 MathSoft.
10. Wang, C. H., Rose, L. R. F., Callinan, R., Analysis of Out-of-Plane Bending in One-Sided Bonded Repair, Pergamon, Great Britain, 1998. Int. J. Solids Structures, Vol 35, No 14, pp, 1653-1675.
11. Wang, C. H., Rose, L. R. F., A Crack Bridging Model for Bonded Plates Subjected to Tension and Bending, Pergamon, Great Britain, 1999. Int. J. Solids Structures, Vol 36, pp, 1985-2014.
12. Wang, C. H., Erjavec, D., Geometrically Linear Analysis of the Thermal Stresses in One-Sided Composite Repairs, J. Thermal Stresses 1999, Not currently printed.
13. Wang, C. H., Erjavec, D., Geometrically Linear Analysis of out of plane bending stresses due to applied stresses in One-Sided Composite Repairs, Int J. Solids Structures 1999, Not currently printed
14. Baker, A. A., Jones, R., Bonded Repair of Aircraft Structures, Martinus Nijhoff, Dordrecht, 1988.
15. Ratwani, M. M., Cracked, Adhesively Bonded Laminated Structures. AIAA Journal Vol 17, pp 988-994, 1979
16. Rose, L. R. F., An Application of the Inclusion Analogy for Bonded Reinforcements, Int. J. Solids & Structures, Vol 17, pp 827-838, Great Britain, 1981.

17. Wang, C.H., Rose, L. R. F., Callinan, R., Baker, A. A., Thermal Stresses in a Plate with a Circular Reinforcement, Pergamon, Great Britain, Int. J. Solids Structures. (Submitted for printing but not currently released)
18. Baker, A. A., Davis, M. J., Hawkes, G. A., Proceedings on the 10<sup>th</sup> International Committee on Aeronautical Fatigue (ICAF) Symposium, Paper 4.3, 1979.
19. Rose, L. R. F. 1994, Minute to WGCDR Eric Wilson regarding corrections to ref [14] and suggestion for the F-111 Boron repair case.
20. Eshelby, J. D., The Determination of the Elastic Field of an Ellipsoidal Inclusion and Related Problems. Proceedings of Royal Society of London, Vol A241, pp 376-396, 1957.
21. Hart-Smith, J. L., Adhesive-Bonded Double-Lap Joints, NASA-CR-012235, California, 1973.
22. Arendt, C., Sun, C. T., Bending Effects of Unsymmetric Adhesively bonded composite repairs on Cracked Aluminium Panels. Proceedings of FAA/NASA International Symposium on Advanced Structural Integrity Methods for Airframe Durability and Damage Tolerance, NASA Conference Publication 3274, Part 1 pp 33-48, 1994.

## **Appendix A: MathCad Modules**

- A.1. Unsupported Single Sided Repairs (Case Study from [8])**
- A.2. Fully Supported Single Sided Repairs (F-111 Boron Repair Case)**
- A.3. Double Sided Repairs (F-111 Boron Repair Case)**
- A.4. Unsupported Single Sided Repairs (F-111 Boron Repair Case)**
- A.5. Repairs to Stiffened Panels (F-111 Boron Repair Case)**

## CHAPTER 3: NUMERICAL ANALYSIS AND TESTING

T. Ting, B. Whittingham, R. Jones, W. K. Chiu and I. H. Marshall

Department of Mechanical Engineering, Monash University, Clayton, Vic 3168,  
Australia

### CONTENTS

<b>1. NUMERICAL ANALYSIS &amp; EXTENSION OF 2D FORMULAE TO ALLOW FOR 3D EFFECTS</b>	<b>3</b>
1.1 Repair of thin skins	4
<b>2. DEVELOPMENTS IN THE STRESS ANALYSIS OF BONDED REPAIRS</b>	<b>7</b>
2.1 Background	7
2.2 Structural Response Of Thin Film Adhesives	8
2.2.1 Specimen preparation	8
2.2.2 Experimental procedure	8
2.2.3 Experimental results	9
2.2.4 Discussion	11
2.4 Governing Differential Equations For Bonded Joints/Repairs	13
2.4.1 Glinka's Approach For Estimating The Peak Stresses and Strains	14
2.4.2 Validation	16
2.4.3 Application to the analysis of double lap joints	16
2.4.4 Remarks	18
2.5 Interlaminar failure	19
<b>3. ANALYSIS OF REPAIRS TO RIB STIFFENED PANELS</b>	<b>24</b>
3.1 Large Panel Fatigue Test Specimens	24
3.2 Finite Element Analysis	24
3.3 Results for stress-intensity calculations from the finite element analysis of a boron epoxy composite repair of a crack over a stiffening element	27
3.3.1 Comparison of results for several different stiffener spacing and two different skin thicknesses	28
3.3.2 Comparison of results for several stiffener spacings and stiffener depths and two different skin thicknesses	29
3.3.3 Comparison of results for various stiffener spacing and patch thickness for two different skin thicknesses	30
3.3.4 Comparison of results for various stiffener widths and depths for two different skin thicknesses	32
3.3.5 Relationship between the ratio of the patch thickness to skin thickness and the stress intensity factor $K_I$ for 5 different crack lengths	34
3.3.6 Effect of the interlaminar shear modulus	35
3.4 Summary of the finite element analysis	36
3.5 Load flow in a rib stiffened panel	37
3.6 Simple analytical formulae for predicting the limiting behaviour	42
3.7 Effect of riveted stiffeners	44
<b>4. THE EXPERIMENTAL TEST PROGRAM</b>	<b>47</b>
4.1 Alteration to the narrow panel specimen design	52
4.2 Summary of Test Program	52
4.3 Test results	54
4.4 Failure surface	58
4.5 Comments	59
<b>5. EFFECT OF VARIABLE ADHESIVE THICKNESS</b>	<b>59</b>
5.1 Analytical solutions for variable adhesive thickness	61
5.2 Effective mechanical properties of micro-inhomogeneous joints	65
5.3 The effect of variable adhesive thickness and material non-linearity	67
<b>6. REFERENCES</b>	<b>68</b>

## SUMMARY

There are several methods available for obtaining a first estimate for the design of composite repairs to cracks in thin metallic skins. The program Calcurep is based on one such technique, which builds on an analogy with the problem of a bonded symmetric lap joint.

The present report begins by comparing the results of a 3D finite element analysis of various composite repairs with these analytical estimates. Finite element studies of composite repairs to (cracked) rib stiffened panels are then presented. This study reveals the stress intensity factors to be a weak function of the stiffener spacing. The current analytical formulae are then extended to allow for repairs to rib stiffened panels and verified by comparison with the results of a detailed experimental test program.

To complete this section a simple test methodology, based on the ASTM thick adherend test, ASTM D-1002, for determining the true visco-plastic behaviour of structural film adhesives, is also presented. A methodology for accounting for the observed visco-plasticity is then presented.

The analytical formulae make extensive use of the analytical solution for a simple lap joint. Unfortunately, this solution is restricted to uniformly thick adhesives, monotonic loading and an idealised inelastic response. To extend the range of applicability of these formulae a range of new solutions are developed that include:

- i) variable adhesive thicknesses;
- ii) random variations in the adhesive thickness;
- iii) more representative adhesive behaviour, e.g. visco-plastic response.

As a result of this work we find that, even for extensive plasticity, even if there is variability in the thickness of the adhesive bond the energy field  $W_{\max}$  can be computed using only the elastic solution for the repair. Consequently, we show that for repairs with significant variability in the thickness of the adhesive bond the strength of the repair, provided failure is due to failure of the adhesive, can be then estimated from a purely linear elastic analysis. This will occur at the load level when  $W_{\max} = W_{\text{crit}}$ . This finding significantly simplifies the design process for repairs with a variable thickness adhesive.

It is also mentioned that the majority of commercially available finite element programs, e.g. ABAQUS, MSC-Nastran, NENastran, MARC, ANSYS etc, use isoparametric elements. When analysing three dimensional problems involving composites the use of elements with mid-side nodes is essential, i.e. 20 noded hex (brick) elements, 15 noded wedge elements, etc. Unfortunately, ABAQUS, MSC-Nastran, MARC, ANSYS use formulations based on that given in Zienkiewicz [23]. This means that for accurate results the aspect ratio's are limited to less than  $\sim 5:1$ , even if reduced integration, i.e. the use of  $2 \times 2 \times 2$  Gauss points in formulating the element stiffness matrix, is used. In contrast NENastran use an enriched 20 noded element, where the basic formulation is extended to include additional shape functions. This means that the NENastran 3D (mid-side noded) elements can be used with dramatically greater aspect ratio's and as such are better suited to the analysis of composite repairs.

# 1. NUMERICAL ANALYSIS & EXTENSION OF 2D FORMULAE TO ALLOW FOR 3D EFFECTS

Externally bonded composite patches have proved to be an effective method of repairing cracked, or damaged, structural components, [1-3, 6-12, 16, 17, 19]. A variety of approaches are now available for the design of composite repairs to cracks in thin metallic skins, i.e. typical thickness less than ~ 3 mm. One such technique is based on the fact that the stress intensity factor for a patched crack approaches a constant (limiting) value, defined as  $K_\infty$ , as the crack length increases. This approach was based on the premise that, for a sufficiently long crack in a structure, which is subjected to a remote uniform stress field, the central region of the patch, over the crack, behaves like an overlap joint [3, 2]. From this premise it follows that the stress distribution in this central region and the stress intensity factor should become independent of crack length.

As a result of this analogy it has been found that the problem of a bonded symmetric lap joint can be used in the initial design process. Indeed, the resultant analytical formulae are particularly easy to use and provide a first estimate for the patch design.

It is possible to increase the accuracy of the current approximate 2D formulae, initially developed by Rose in [2, 3], for the limiting stress intensity factor  $K_\infty$  for a crack repaired with an externally bonded composite repair, by (partially) accounting for through-the-thickness effects. To this end the value of  $K_\infty$  can be approximated by the formulae;

$$K_\infty = Y \Omega_L \sigma_0 \sqrt{\pi \lambda} \quad (1)$$

$$\text{where} \quad \sigma_0 = \sigma E_p t_p / (E_p t_p + E_r t_r) \quad (2)$$

$Y$  is a geometry factor, which accounts for repairs to centre or edge cracks;

$$\begin{aligned} Y \text{ is a geometry factor} &= 1 \quad \text{for a repair to a centre crack} \\ &= 0.9 \quad \text{for a repair to an edge crack} \end{aligned}$$

and  $\Omega_L$  is the load attraction factor. For long uni-directional fibre patches it has been found that the term  $\Omega_L$  can be approximated as follows

$$\Gamma = 3/8 \cdot 1 / (1 + X E_r t_r / (B E_p t_p)) - E_p t_p / (E_r t_r + E_p t_p) \quad (3)$$

$$\Omega_L = (E_p t_p / (E_r t_r + E_p t_p) + \Gamma) / \sigma_0 \quad (4)$$

$$\pi \lambda = \sqrt{E_p t_p / \beta (1 + t_p E_p / E_r t_r)} \quad (5)$$

and

$$\beta = (t_a / G_a + t_r / 3 G_r + t_p / 3 G_p) / (t_a / G_a + 3 t_r / 8 G_r + 3 t_p / 8 G_p)^2 \quad (6)$$

Here  $X$  is the width of the patch,  $B$  is the width of the plate/skin,  $t_a$ ,  $t_p$  and  $t_r$  are the thickness' of the adhesive, plate, and patch respectively,  $G$  and  $E$  denote the shear and

Young's modulus and the subscripts a, p and r denote their values for the adhesive, plate, and patch respectively.

This expression<sup>1</sup> has been found to produce results in good agreement with three dimensional finite element analysis, see Section 1.1. The program utilising this approximation will be termed CalcuRep\*.

Until now we have ignored bending effects. However, even if the wing skin is in a state of plane stress, the location of the neutral axis of the patch-adhesive-skin section will differ from the neutral axis of the wing skin itself. Hence, forces applied to the skin will result in an out of plane bending, which will reduce the efficiency of the repair.

There are several methods that can be used. One approach is presented in Chapter 1. The method developed at Northrop, see [14] for more details, can also be used to account for this out of plane bending. In this method, the apparent stress intensity factor  $K_p^*$  at the mid surface of the sheet is given by:

$$K_p^* = (1 + BC) K_p \quad (7)$$

where  $BC$  is a bending correction factor. Here,

$$BC = a y_{max} (1 - K_p / K_s) (t_p + t_r) / I \quad (8)$$

where  $K_s$  is the value of the stress intensity factor before patching,  $t_p$  and  $t_r$  are the thicknesses of the sheet and patch respectively,  $y_{max}$  is the distance of the lower unpatched surface of the plate from the neutral axis of the section (i.e., sheet plus patch).  $I$  is the moment of inertia of the section and  $a$  is the crack half length.

The value of  $K_p^*$  can be related to  $J$ , the energy release rate for self similar crack growth, in the usual way, viz:

$$J = K_p^{*2} / E \quad (9)$$

When growth is non self-similar with the maximum growth occurring at the lower free surface, it is best not to use  $K_p^*$  or  $J$  but to design on the basis of the maximum stress intensity factor  $K_p^{max}$  which is given by:

$$K_p^{max} = (1 + 2BC) K_p \quad (10)$$

### 1.1 Repair of thin skins

To illustrate the accuracy of these formulae let us first consider an externally bonded composite repair (patch) to a centre crack in a 3mm thick aluminium panel with  $E = 72,000$  MPa and  $\nu = 0.33$ . Two patch thicknesses were analysed viz: 1.0 and 1.85

<sup>1</sup> The derivation is both cumbersome and tedious and hence for simplicity will be omitted.

mm, and the patch was assumed have the following mechanical properties:  $E_{11} = 208,000$  MPa,  $E_{22} = 25432$  MPa,  $\nu_{12} = 0.183$ , and  $G_{12} = G_{13} = G_{23} = 7241$  MPa. The plate was assumed to have dimension of 200 (length) x 290 (width) x 3 mm and the patch was assumed to have a planform of 100 (length) mm x 82 (width) mm. The adhesive was taken to be 0.25 mm thick with a shear modulus of 375 MPa and  $\nu = 0.33$ . The analysis used 20 noded isoparametric 3D brick elements with 2 layers of elements through each of the plate, patch and adhesive. The plate was subjected to a remote uniform stress of 229.8 MPa and global bending, after patching, was prohibited.

In this analysis symmetry was used and only a quarter of the structure was modeled. The resultant mesh consisted of 4,889 nodes and 1132 elements and, to simulate the crack tip singularity, the near tip elements had the mid side nodes moved to the  $\frac{1}{4}$  points. The resultant solution was well conditioned and the accuracy of the solution was evaluated by performing two separate analyses. The first used optimum integration, i.e.  $2 \times 2 \times 2$  Gaussian quadrature points, to form the stiffness matrices of the elements whilst the second used full integration, i.e.  $3 \times 3 \times 3$  Gaussian quadrature points, to form the stiffness matrix. Both analyses gave results, which agreed to within 1%.

Following this analysis the composite repair to edge notch cracks in a 200 (length) x 145 (width) x 3 mm plate was then considered. In this study the patch was assumed to be 1.85 mm thick and have a plan form of 100 (length) mm x 41 (width) mm. The results both these repair configurations are presented in Tables 1.1-1.4.

The third study involved similar repair configurations where skin thicknesses of 2mm, 3.15 and adhesive shear moduli of 700 MPa were also considered.

For the first two repair configurations the differences between the present approximation, which we refer to as CalcuRep<sup>+</sup>, and those used in C5033 and CalcuRep are summarised in Tables 1.4. The differences for the third study are summarised in Table 1.5.

The C5033 solution assumed equal stresses in the patch and the plate. This was not the case. The (corrected) CalcuRep<sup>+</sup> solution underestimated the solution by  $\sim 18\%$ . Accounting for through-the-thickness effects CalcuRep<sup>+</sup> reduced this error to within the error bound of the finite element solution, see Table 1.4. Although the error in the C5033 solution was similar to that of CalcuRep<sup>+</sup> its other assumptions were further from the true values. For comparison the CalcuRep<sup>+</sup> results for repairs to centre notch and edge notch panels are shown in Table 1.5 along with the corresponding finite element solutions. In each case the agreement is shown to be quite good.

Table 1.1: K for a repaired edge notch panel, patch thickness 1.85mm.

Crack Length	5 mm	6 mm	7 mm	10 mm	20 mm
patched surface	10.6	10.8	10.9	10.9	10.4
middle	11.6	11.7	11.9	12.1	12.9
bottom	11.7	11.9	12.0	12.2	12.7



Table 1.2: K values for repaired centre notch panel, patch thickness 1.85mm

Crack half Length	5 mm	6 mm	7 mm	10 mm	20 mm
patched surface	11.2	11.5	11.8	12.0	11.6
middle	11.9	12.4	12.7	13.3	14.3
bottom	12.0	13.16	12.9	13.4	14.1

Table 1.3: K for a repaired centre notch panel, patch thickness 1 mm.

Crack half Length	5 mm	6 mm	7 mm	10 mm	20 mm
patched surface	14.6	15.2	15.6	16.1	15.7
middle	15.5	16.3	16.8	17.8	19.4
bottom	15.6	16.4	17.0	17.9	19.1

Table 1.4: Comparison of solutions for  $K_{\infty}$  for a patch thickness 1.85 mm

Crack Configuration	Crack length	C5033	CalcuRep <sup>†</sup>	CalcuRep <sup>*</sup>	K Finite element
Centre crack	20 mm	17.4	11.8	14.1	~14.1 to 14.3
Edge crack	20 mm	13.8	10.3	12.7	~12.7 to 12.9

<sup>†</sup> Initial corrected and modified version of CalcuRep

<sup>\*</sup> CalcuRep\* incorporates through thickness effects.

Table 1.5: Comparison of prediction for  $K_{\infty}$  for various patch configurations

Crack Configuration	Crack length	Configuration	CalcuRep	K Finite element
Edge crack $\sigma = 344.8$ MPa	20 mm	Skin <sup>A</sup> 2 mm, patch = 0.75mm $G_a = 375$ MPa $t_a = 0.25$ mm	21.6	17.8 -22.4
Centre crack $\sigma = 344.8$ MPa	20 mm	Skin <sup>A</sup> 2 mm, patch = 0.75mm $G_a = 375$ MPa $t_a = 0.25$ mm	23.6	19.8 -24.0
Centre crack $\sigma = 229.8$ MPa	20 mm	Skin <sup>A</sup> 3. mm, patch = 1.00 mm, $G_a = 375$ MPa $t_a = 0.25$ mm	19.2	15.7- 19.1
Centre crack $\sigma = 229.8$ MPa	20 mm	Skin <sup>B</sup> 3. mm, patch = 0.889mm, $G_a = 750$ MPa $t_a = 0.165$ mm	16.2	15.7-15.8

<sup>†</sup> Initial corrected and modified version of CalcuRep

<sup>\*</sup> CalcuRep\* incorporates through thickness effects.

<sup>A</sup> The planform of the skin and patch were as previously described.

<sup>B</sup> Planform of plate was 320 mm x 150 mm (wide) with a semi-circular patch, radius = 80mm

The analytical formulae are also quite accurate for the case when bending is allowed, see Tables 1.6, 1.7 and 1.8. However, in this case the accuracy of the simple analytical formulae decreases when the crack length approaches a half of the patch width (X).

Table 1.6: Comparison of prediction for bending problems, Case 1.

$K_{max}$ MPa $\sqrt{m}$	Edge Centre	a mm	$t_p$ mm	$E_p$ MPa	$t_r$ mm	$G_r$ MPa	$t_a$ mm	$G_a$ MPa	$\sigma$ MPa	X mm	B mm
	Centre	40	3.16	72000	1	208030	0.2	375	158	200	200
predictd	48.3										
f.e.	47.4										

Table 1.7: Comparison of prediction for bending problems, Case 2.

$K_{max}$ MPa $\sqrt{m}$	Edge Centre	a mm	$t_p$ mm	$E_p$ MPa	$t_r$ mm	$G_r$ MPa	$t_a$ mm	$G_a$ MPa	$\sigma$ MPa	X mm	B mm
	Edge	20	2	72000	0.75	208030	.25	375	345	200	200
predictd	85.2										
f.e.	83.4										

Table 1.8: Comparison of prediction for bending problems, Case 3.

$K_{max}$ MPa $\sqrt{m}$	Edge Centre	a mm	$t_p$ mm	$E_p$ MPa	$t_r$ mm	$G_r$ MPa	$t_a$ mm	$G_a$ MPa	$\sigma$ MPa	X mm	B mm
	Centre	20	3	71000	0.89	208000	.17	750	230	41	145
predictd	62.7										
f.e.	59.2										

## 2. DEVELOPMENTS IN THE STRESS ANALYSIS OF BONDED REPAIRS

### 2.1 Background

When designing bonded repairs, or adhesively bonded joints, the stress/strain response of the adhesive plays a central role in determining both the load carrying capacity and the fatigue performance of the repair or joint, see [4, 9]. To this end we need a test methodology capable of accurately and consistently reproducing this behaviour.

In this context Chiu et al. [13] have developed a variant of the ASTM thick-adherend short over-lap adherend test specimen for characterising the stress/shear behaviour of thin film adhesives. The results revealed that the properties of the film adhesive FM73 exhibited significant visco-plasticity, even at room temperature. Chiu et al. [13] also used a unified constitutive model to describe the visco-plastic behaviour of the adhesive.

This section also assesses the structural significance of this visco-plastic behaviour, in a realistic symmetric double lap joint, via a detailed finite element analysis. Here we show that the stress/strain behaviour of the adhesive in a bonded joint is dependent on both the loading rate and the load history. When the joint is subjected to monotonic loading with a constant loading rate the energy density, which is the primary adhesive design variable in a bonded repair, at the worst point in the joint is essentially time independent. This is very important as it allows the existing design tools to be used

even though the adhesive exhibits significant visco-plastic behaviour, and as a result is strongly rate dependent.

Unfortunately, the peak adhesive shear stresses and strains are strongly effected by the loading history. Since the shear stresses are continuous across the interface an accurate knowledge of the interlaminar stresses in the composite repair requires these visco-plastic effects to be incorporated in the analysis. To this end a simple fortran program has been developed, which uses the Glinka hypothesis [14], and negates the need for a complex non-linear finite element analysis.

## 2.2 Structural Response Of Thin Film Adhesives

As has been previously mentioned the stress/strain behaviour of the adhesive plays a central role in determining both the load carrying capacity and the fatigue performance of a bonded repair, see [4, 9, 10, 11]. This section presents a methodology for determining the stress/strain response using a thick adherend test specimen and illustrates it by considering the commonly used adhesive FM73.

### 2.2.1 Specimen preparation

The results presented in this section were obtained using the symmetric, thick adherend, short overlap, shear test specimen. The dimensions of the lap shear specimen are shown in Figure 2.2. These specimens were made from hardened tool steel.

The bond surfaces of the specimen, after being grit blasted, were immersed in a 1.0% silane solution for about 10 minutes. They were then dried in an oven at 80°C. The dried specimens were subsequently assembled with a FM73 film adhesive at room temperature. These assembled specimens were then vacuum bagged and placed in an autoclave where the adhesive was cured under a pressure of 105 kPa and at a temperature of 120°C. The bond line thickness of this joint was approximately 0.2 mm (i.e. this is a typical adhesive thickness for 2 layers of FM73).

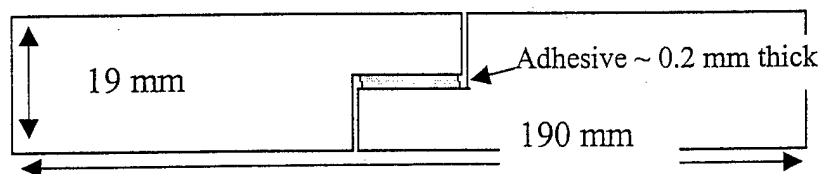


Figure 2.2 Schematic diagram of the ASTM D 1002 thick adherend test specimen.

### 2.2.2 Experimental procedure

The specimens were loaded under strain control, in a 10kN Instron test machine and the shear strain was measured using a pair of linear variable displacement transducers (LVDT). A clip gauge was attached to the LVDT to provide a feedback signal for the control unit in the Instron. This clip-gauge was necessary because the control signal from the LVDT was too noisy for the Instron control circuit.

The load cell, LVDT's and the clip gauge were calibrated prior to each experiment. Readings from the LVDT and the load cell were acquired using an IBM Personal Computer. The sampling frequency of the acquisition unit was varied according to the strain rates used in each experiment.

The results presented in this paper were obtained from a set of experiments performed at room temperature. The nominal temperature in the test laboratory was approximately 19°C.

It is known that the stress distribution in the adhesive layer of the lap shear joint is complex, especially around the corner of the joint. The material discontinuity (i.e. at the adhesive and steel adherend interface) results in a region of high peel stress. This region of high stress, although highly localised, is a potential failure location. To avoid failure, the experiments were terminated at a shear strain of  $\sim 0.4$ .

### 2.2.3 Experimental results

To determine the visco-plastic response of the adhesive the experiments were conducted at a range of strain rates,  $\sim 1.0\text{e-}2$ ,  $1.0\text{e-}3$ , and  $1.0\text{e-}4$  and temperatures, viz: 23°C (room temperature) and 60°C. A set of initial tests was also performed to test repeatability and the deviation in the results was found to be in the order of 5%, which can be attributed to various sources of experimental error.

The results of these tests, together with an analytical prediction based on the analytical formulation outlined in section 3 are presented in Figures 2.3 and 2.4. These diagrams reveal that the FM73 adhesive exhibits significant visco-plasticity, which in these tests was reflected in strain-rate dependency, even at room temperature, (i.e. well below its glass transition temperature). It should be noted that it was difficult to control the test at the slowest strain rate. This was the result of endeavouring to control the experiment at a strain rate close to the lower limit of the machine, in terms of cross-head speed. The yield stresses tabulated in Table 2.1 are calculated from the experimental data using Considere's construction. This Table also shows a consistent value of the shear modulus obtained from this set of experiments.

Since the yield stress of the adhesive is dependent on the strain rate, it follows that the adhesive properties must have a strong dependence on the loading history. One method of revealing this time dependency, is via a stress-relaxation test (i.e. strain hold test). Figure 2.5 shows the result of loading the specimen past yield at a particular strain-rate and then holding the strain at a constant value. This figure reveals a very large stress drop, to its "threshold" value, as a result of the strain hold. The level of the stress relaxation seen in these figures reveals that the "threshold" to which the stress relaxes is independent of the value of the plastic strain, see [9, 13]. The threshold value is also independent of the strain rate and determines the inelastic (irreversible), and thus the fatigue, threshold of the adhesive, i.e. the level beneath which irreversible effects do not occur.

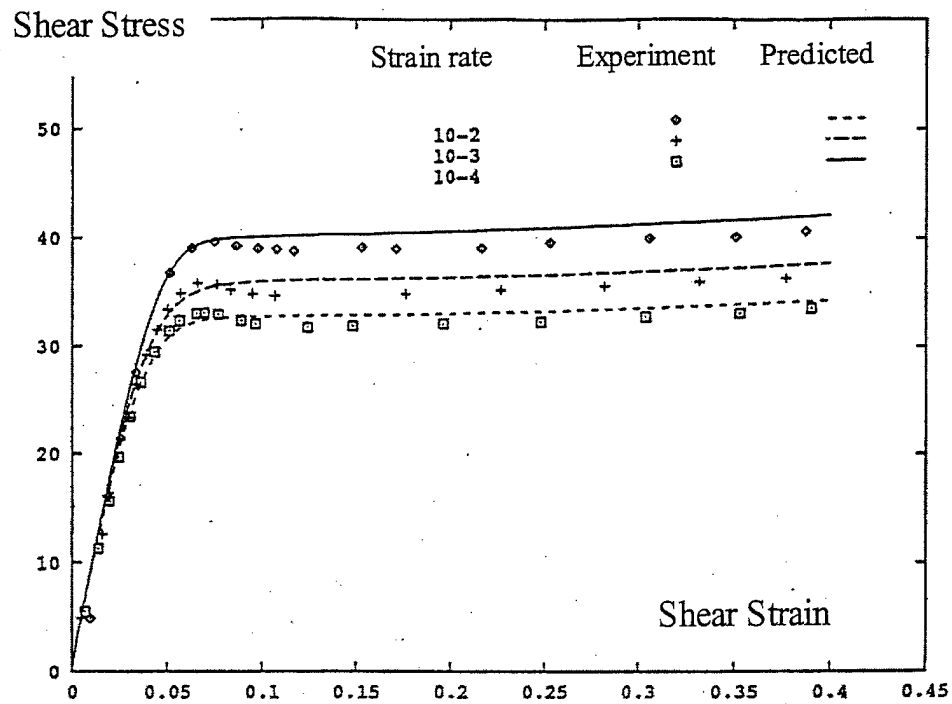


Figure 2.3 Stress strain curves for FM73 at room temperature.

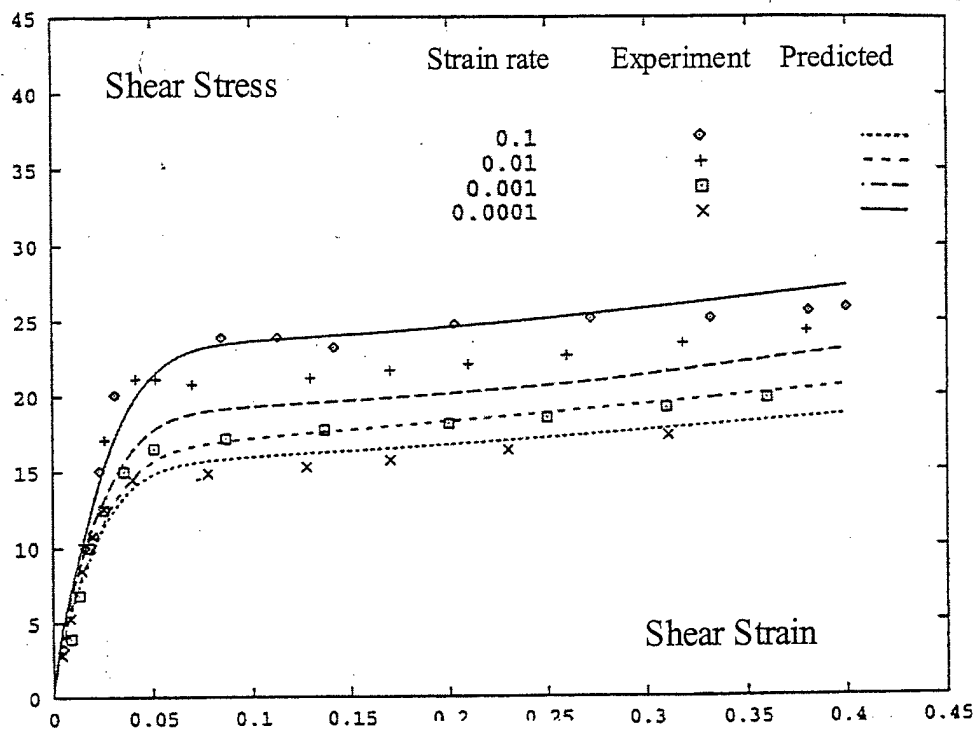


Figure 2.4 Stress strain curves for FM73 at 60C.

The stress drop during stress-relaxation to its "threshold" value results in a conversion of elastic strain into inelastic (irreversible) strain, with the total strain remaining constant. This results in recoverable (i.e. elastic) strain energy being converted into irreversible energy, and as such is a direct reflection of the degradation of the adhesive.

- This degradation can be avoided by designing such that the adhesive stresses/strains are beneath the "threshold" value. In this case inelastic (irreversible) strains, and hence damage, will not occur, see [10,11].

For the adhesive under consideration this "threshold" stress is approximately 25 MPa, which corresponds to a "threshold" energy  $W_f$  of 0.416 MPa. As can be seen from Table 2.1 the "threshold" stress corresponds to the lower limit of the yield (shear) stress, i.e. the value of the yield (shear) stress at vanishingly small strain rates. This finding is intuitively valid.

Table 2.1: Yield shear stress and shear modulus as a function of strain rate.

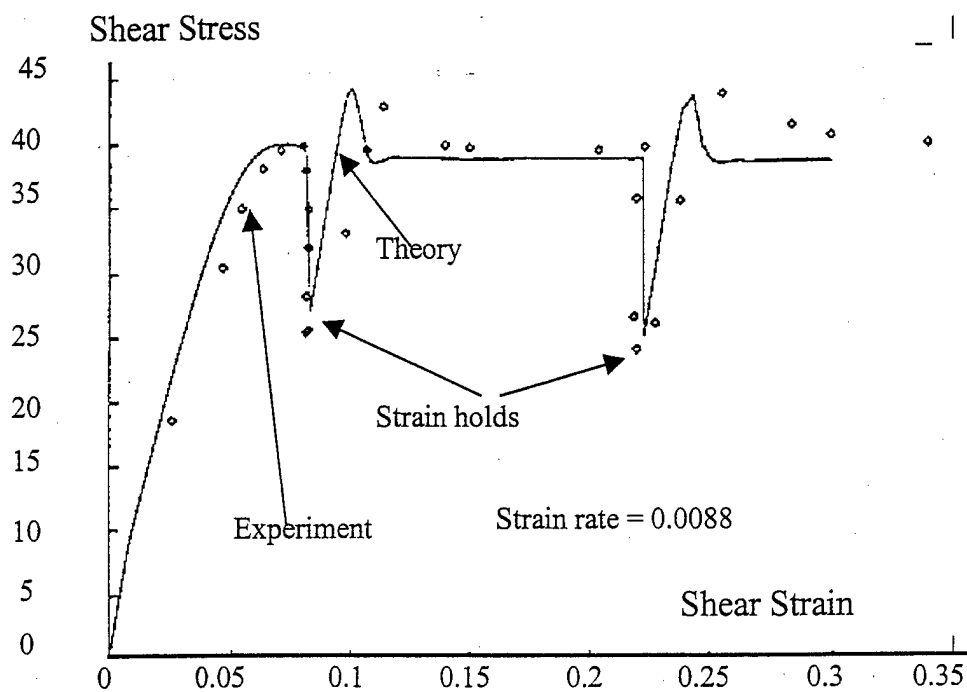
Strain Rate (/sec)	Yield Stress (MPa)	Shear Modulus (MPa)
8.68e-5	26.78	753
8.78e-4	32.81	746
8.67e-3	35.94	766
8.80e-2	39.06	758

#### 2.2.4 Discussion

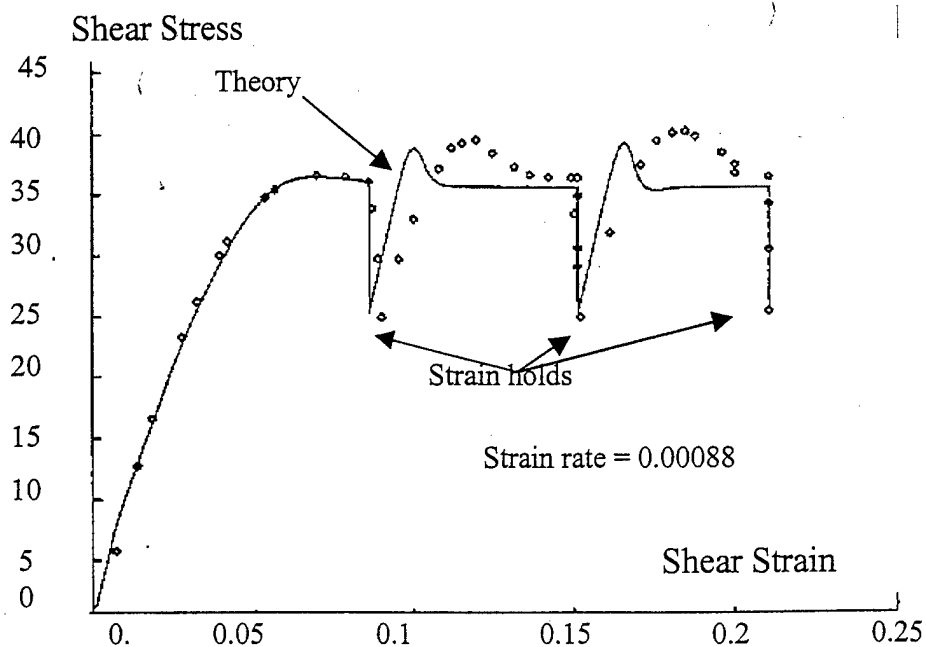
The section has shown how to use the ASTM thick adherend tests to measure the structural response of a typical thin film adhesive, viz: FM73, at both room temperature and at elevated temperature.

The stress-relaxation resulting from a strain hold was significant and reveals the "threshold" state, below which irreversible effects, and hence fatigue damage, do not occur. This "threshold" value is independent of strain rate and of the degree of prior plastic deformation. The extensive stress-relaxation, which occurs in a matter of seconds or minutes, can severely degrade the performance of the adhesive. This degradation is due to the conversion of recoverable elastic energy to irreversible inelastic energy, and can be avoided by designing such that the design state is below the "threshold" value.

An analytical methodology enabling this time-dependent inelastic deformation of the adhesive to be included in the design process is given in Section 2.4.



(a)



(b)

Figure 2.5 Experimental and predicted response of FM73 during strain holds.

## 2.4 Governing Differential Equations For Bonded Joints/Repairs

In the previous section we have outlined a simple test methodology, based on the ASTM thick adherend test specimen, for measuring the structural response of thin film adhesives. This has then been used to determine the structural response for the adhesive FM73, which is commonly used in composite repair technology. From the test results presented we have seen that this response exhibits significant visco-plastic effects. The question thus arises:

How do we account for this in both the analysis and design of a composite repair/joint?

To this end let us consider a symmetric double lap joint, see Figure 2.6, subjected to a remote load  $P$  where the lower and the upper adherend thicknesses and Moduli are  $T_1$ ,  $E_1$  and  $T_2$ ,  $E_2$  respectively and where the adhesive has a thickness  $t$  and an elastic shear modulus of  $G_a$ . The governing differential equations relating the stresses in the adherends  $\sigma_1$ ,  $\sigma_2$ , where the subscript differentiates between the lower and the upper adherend, to the adhesive shear stress  $\tau$ , in the joint are:

$$\frac{\partial \sigma_1}{\partial x} - \frac{\tau}{T_1} = 0 \quad (11)$$

$$\frac{\partial \sigma_2}{\partial x} + \frac{\tau}{T_2} = 0 \quad (12)$$

If the adherends are elastic then Hooke's law applies and the displacements in the lower and the upper adherends, defined as  $u_1$  and  $u_2$  respectively, are related to the stresses through the Young's moduli; viz:

$$E_1 \frac{\partial u_1}{\partial x} = \sigma_1 \quad (13)$$

$$E_2 \frac{\partial u_2}{\partial x} = \sigma_2 \quad (14)$$

whilst the shear strain  $\gamma$  in the adhesive is related to the relative displacements in the adherends; viz:

$$\gamma = (u_1 - u_2)/t \quad (15)$$

This system of equations results in the following relationship between the adhesive shear stresses and shear strains; viz:

$$\frac{\partial^2 \gamma}{\partial x^2} = \tau(1/t E_2 T_2 + 1/t E_1 T_1) \quad (16)$$

where from equilibrium considerations the load  $P$  applied to the upper adherend must equal the integral of the adhesive shear stresses; viz:



$$P = \int_0^l \tau \, dx \quad (17)$$

where  $l$  is the overlap length of the joint. To complete this system of equations it is necessary to prescribe the relationship between the adhesive shear strain  $\gamma$  and the adhesive shear stress  $\tau$ . Since this relationship is usually in-elastic it best to consider a general functional form; viz:

$$\dot{\gamma}^I = f(\tau, \dot{\gamma}^I) \quad (18)$$

where the inelastic shear strain rate  $\dot{\gamma}^I$  is considered to be an arbitrary function,  $f(\tau, \dot{\gamma}^I)$  of the shear stress  $\tau$  and the shear strain rate  $\dot{\gamma}^I$ .

*This formulation extends the approach, used by Hart-Smith [4], to allow for the visco-plastic response of the adhesive.*

The solution to this set of non-linear time dependent equations can be quite messy and time consuming. To overcome this we use Glinka's [14] technique for estimating the peak stresses and strains in the adhesive.

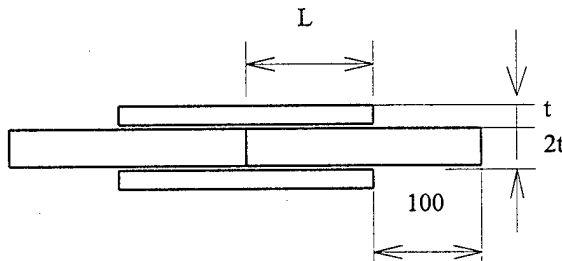


Figure 2.6: A schematic diagram of a symmetric double lap joint

#### 2.4.1 Glinka's Approach For Estimating The Peak Stresses and Strains

Structural components, albeit composite repairs, bonded joints or stiffener runnouts, are frequently subjected to complex loading spectra. These alternating loads tend to initiate fatigue cracks at notches and at other regions of high stresses. Historically the field of fatigue has been classified into a number of specific areas; viz: high-cycle and low-cycle fatigue; fatigue of notched members; the initiation and propagation of cracks and fatigue life extension techniques. Fatigue initiation and crack growth programs require an accurate knowledge of the local notch tip stresses and strains. These quantities can be determined in several ways, viz: via direct strain gauge measurements, using finite element analysis or by using approximate methods, such as the Glinka's approach [14], that relate local stresses and strains to their remote

values. To this end the present report briefly outlines the Glinka approach for calculating the peak shear stresses and shear strains. Attention is then focused on developing a simple method, which combines modern constitutive theory with the Glinka approach to calculate the peak (visco-plastic) adhesive stresses and strains.

The design of composite repairs requires a knowledge of the interlaminar shear stresses and strains. These quantities are necessary to design against interlaminar failure in the composite repair. At the moment these stresses can only be determined using finite element analysis.

Let us first define the peak adhesive shear stresses and strains obtained via an elastic solution as  $\underline{\tau}$  and  $\underline{\gamma}$  ( $=\underline{\tau}/G$ ) respectively. Let us next define the peak adhesive shear stresses and strains obtained via an in-elastic solution as  $\tau$  and  $\gamma$  respectively. In this case, Hooke's law cannot be used to relate the peak shear stress,  $\tau$ , to the peak strain,  $\gamma$ . Instead Glinka's rule [2] can be used to compute the peak stresses and strains. According to this hypothesis the peak in the strain energy density field obtained via an elastic plastic analysis is the same as the peak strain energy obtained via a purely elastic analysis; viz:

$$1/2 \underline{\tau} \underline{\gamma} = \underline{\tau}^2 / 2G = \int \sigma_{ij} d\epsilon_{ij} = \int \tau d\gamma \quad (19)$$

It should be noted that this relationship also follows from the Hart-Smith solution [4]. As such the Hart-Smith solution is contained as a special case of Glinka's hypothesis. However, in [4] visco-plastic effects were not considered.

The solution process thus involves first solving for the peak elastic stresses and strains in the repair. Once a valid stress strain relationship for the epoxy is known we then use equation (19) together with the elastic solution to determine the peak (in-elastic) adhesive stresses and strains. A simple fortran based computer code has been developed to do this. This program was given to the USAF at the June 99 meeting.

In the past few years there has been an increasing interest in the use of unified constitutive models for predicting the inelastic response of structural materials, i.e. visco-plasticity, creep, stress relaxation etc. These models overcome many of the deficiencies of the classical approaches to the inelastic behaviour of materials. The present work uses the formulation presented in [9, 13] to represent the visco-plastic response of thin film adhesives.

This formulation uses two internal state variables, back stress  $\Omega_{ij}$  (deviatoric) tensor and drag stress  $Z$  to define the state of the material. Here the inelastic deformation is driven by the over stress which is defined as  $(S_{ij} - \Omega_{ij})$ . Similar types of theories have been widely used to describe the behaviour of thermoplastics.

In this approach, the flow equation is defined as:

$$\dot{\epsilon}_{ij}^i = D \exp \left[ \frac{-A}{2} \left( \frac{Z^2}{3K_2} \right)^n \right] \frac{(S_{ij} - \Omega_{ij})}{\sqrt{K_2}} \quad (20)$$

where  $\dot{\epsilon}_{ij}^i$  is the inelastic strain rate tensor,  $S_{ij}$  is the deviatoric stress and  $K_2 = \frac{1}{2} (S_{ij} - \Omega_{ij})(S_{ij} - \Omega_{ij})$ . Here  $D$ ,  $A$  and  $n$  are material constants. The term

$(S_{ij} - \Omega_{ij}) / \sqrt{K_2}$  in equation (20) is the normalised overstress and defines the straining direction. The drag stress is history dependent and evolves with the effective inelastic strain  $\varepsilon^i$ . The initial drag stress is  $Z_0$ , final  $Z_1$ , and  $m_0$  controls the rate of evolution. The "growth" of the drag stress is defined by equation (21).

$$Z = Z_1 + (Z_0 - Z_1)e^{-m_0 \varepsilon^i} \quad (21)$$

The back stress is initially zero and its evolution is controlled by an evolution equation, viz:

$$\dot{\Omega}_{ij} = f_2 \dot{S}_{ij} + f_1 \dot{\varepsilon}_{ij}^i - \frac{3}{2} f_1 \frac{\Omega_{ij}}{\Omega_{\max}} \dot{\varepsilon}^i \quad (22)$$

where  $\dot{\varepsilon}^i = \sqrt{\frac{2}{3} \dot{\varepsilon}_{ij}^i \dot{\varepsilon}_{ij}^i}$  is the effective inelastic strain rate. Here,  $f_1$ ,  $f_2$  and  $\Omega_{\max}$  are material constants. The effective inelastic strain rate is defined in the normal fashion.

#### 2.4.2 Validation

Consider the symmetric double lap joint shown in Figure 2.6. This joint has an overlap length of 90 mm, and consists of two identical aluminium adherends with an elastic modulus  $E = 70000$  MPa, and  $t=1.5$  mm. The aluminium adherends and doublers were assumed to be bonded together using FM73. The adhesive, FM73 film, was 0.2 mm thick and had a shear modulus  $G$  of 750 MPa. Its visco-plastic behaviour is described using the state variable formulation described above. The material parameters for the constitutive law for FM73 at room temperature are given in Table 2.2.

This joint was analysed using both the Glinka approach, described above, and the ABAQUS analysis program together with the associated UMAT material subroutine. In each case a remote stress of 401 MPa was assumed to be monotonically applied to the ends of the inner adherend with the load increasing from 0 to its maximum load in either 0.1 sec, 1 sec, 10 sec or 100 sec. A comparison of the calculated peak shear strains  $\gamma$  in the joint is shown in Table 2.3.

#### 2.4.3 Application to the analysis of double lap joints

Having thus validated the Glinka approximation a further series of finite element analysis of various double lap joints (Figure 2.7) were then performed. The joints analysed in this paper had  $(L/2t)$  ratios of 7.5 and 15 and a range of load histories were evaluated, see (Figure 2.7). These joints had overlap lengths of 90 mm (for  $L/2t=15$ ), and 45 mm (for  $L/2t=7.5$ ) respectively. The elastic modulus of the adherends was  $E=70000$  MPa. The thicknesses were 3 mm (for the inner adherend) and 1.5 mm (for the doubler). The aluminium adherends and doublers were assumed to be bonded together using FM73. The FM73 adhesive was 0.2 mm thick and had a shear modulus of 750 MPa. These joints were loaded to a maximum remote stress of 401 MPa. with the load going from 0 load to its maximum value in either 0.1 sec, 1 sec, 10 sec or 100 sec. The stress/strain relationship at the worst (critical) point in the

adhesive layer during these load up sequences is shown in Figures 2.8 ( $L/2t=15$ ) and 4 ( $L/2t=7.5$ ).

Table 2.2: Typical material parameters for FM73 film at room temperature, see [3]

	A	D	$f_1$ (MPa)	$f_2$	n	$m_0$	$\Omega_{\max}$	$Z_0$ (MPa)	$Z_1$ (MPa)
Room temp.	1	10000	800	0.2	0.85	10	12.5	120	350

These figures illustrate that the stress/strain behaviour of the adhesive exhibits significant visco-plasticity and, as a results, is dependent on the loading rate (the higher the loading rate, the higher is the apparent yield stress). The maximum stress level (apparent yield stress) in the adhesive is higher when the joint is loaded more rapidly. These figures also show that the strain level in the adhesive is dependent on the loading history. Here the higher loading rate resulted in lower adhesive strain levels.

Table 2.3 Comparison of peak shear strain  $\gamma$  with 1D Glinka formulation,  $L/2t = 15$

Dimension	Loading Time (sec)			
	0.1	1	10	100
1D algorithm	0.143	0.152	0.163	0.177
Finite element 2D/3D	0.152	0.165	0.179	0.189
% Diff	5.9	7.9	8.9	6.3

In contrast to the stress or strain based approaches Hart-Smith's [4] analysis of a double lap joint revealed that the load carrying capacity of the bond can be estimated from the energy density at the worst point in the adhesive. This design methodology was based on the assumption that the adhesive behaviour can be approximated using a single bi-linear stress/strain curve. This simplification is not necessary. With the extended analysis given in this report the adhesive can be allowed to undergo both creep and visco-plastic behaviour. As shown in Figures 2.8 and 2.9 the stress/strain relationship at any location along the adhesive layer will be governed by the local adhesive strain rate (i.e. the higher the local adhesive strain rate, the larger will be the apparent yield stress of the adhesive).

To determine how the visco-plastic behaviour of the adhesive affects the load carrying capacity of the joint the energy density at the worst point in the adhesive layer was also calculated. The results are shown in Table 2.4. The first observation, apparent from this Table, is that the energy density at the worst point is slightly higher when the ( $L/2t$  ratio) is 7.5. Hence one would expect the joint with a lower ( $L/2t$ ) ratio to have a slightly lower load carrying capacity. More importantly we find that, whilst the local stress/strain behaviour of the adhesive are largely dependent on the loading rate, the energy density at the worst point in the adhesive is relatively independent of the loading rate. There is only approximately 8% variation (refer to Table 2.4) in the energy density from the slowest to the fastest loading rate.

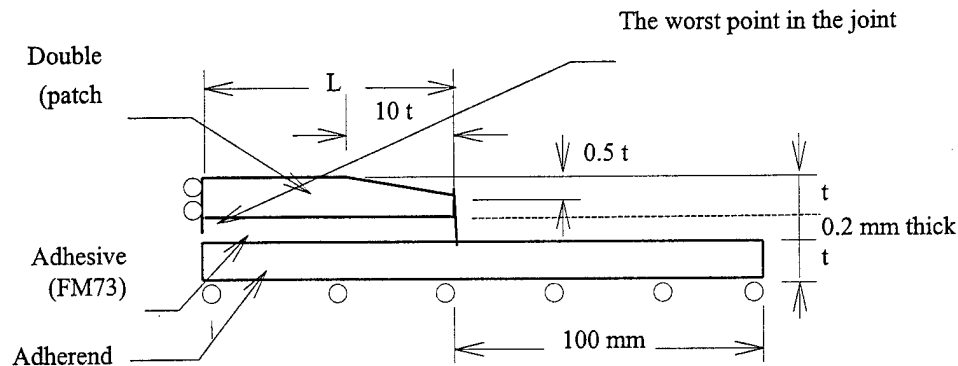


Figure 2.7: A quarter of a symmetric double lap joint

This work thus confirms that the design hypothesis first presented by the Hart-Smith [4] for estimating the load carrying capacity of a double lap joint can be used for thin film adhesives, such as FM73 and FM300, which exhibit significant visco-plastic effects provided that failure occurs in the adhesive.

*The Hart-Smith approach does not cover interlaminar failure in the composite patch, see Section 2.5.* In this case, since the shear stresses are continuous across the patch adhesive interface it is necessary to determine the stress state in the adhesive which, as we have seen, requires an allowance for the visco-plastic response of the adhesive.

Table 2.4: Effect of loading rate on energy density both  $L/2t=7.5$  and 15 at room temp

Energy Density (MPa)	$L/2t$	Loading Time (sec)	0.1	1	10	100	% Diff
	7.5	Adhesive layer	42.6	44.4	46.1	47.1	9.5
	15	Adhesive layer	41.6	43.7	44.9	45.1	7.8

#### 2.4.4. Remarks

This analysis reveals that, at room temperature, when the loading history is simply monotonic the visco-plastic nature of the adhesive in the double lap joint has limited effects on the strain energy density, and thus on the load carrying capacity of the adhesive bond (repair), see Figures 2.8 and 2.9.

In contrast the peak adhesive shear stresses and strains are strongly effected. Consequently, since the shear stresses are continuous across the composite patch-adhesive interface, for an accurate knowledge of the interlaminar stresses in the composite repair it is important that these visco-plastic effects to be incorporated in the design. This can be achieved by using Glinka's approach. To this end a simple fortran program has been developed thereby negating the need for a complex non-linear finite element analysis. This formulation has been validated and was given to the USAF at the June meeting. In this fashion we are now able to assess for failure in the adhesive, the metal skin, fibre failure, or interlaminar failure of the composite patch.

## 2.5 Interlaminar failure

In the previous sections we have concentrated on failure due to failure of the adhesive bond. However, when selecting the damage/degradation to be considered in the repair design/substantiation, the following failure modes, unique to composite materials, should also be included; viz:

- (a) Failure of doubler/repair by fibre failure,
- (b) Failure in the adhesive (cohesion failure),
- (c) Failure at the adhesive/substrate interface(s) (adhesion failure), and
- (d) Failure of the doubler/repair by interlaminar failure.

a more comprehensive review of the potential failure mechanisms is given in [15].

For repairs to primary structures interlaminar failure is particularly common as can be seen in Figure 2.10 which shows interlaminar failure of a composite doubler on an F111 aircraft, see [16] for details of this repair.

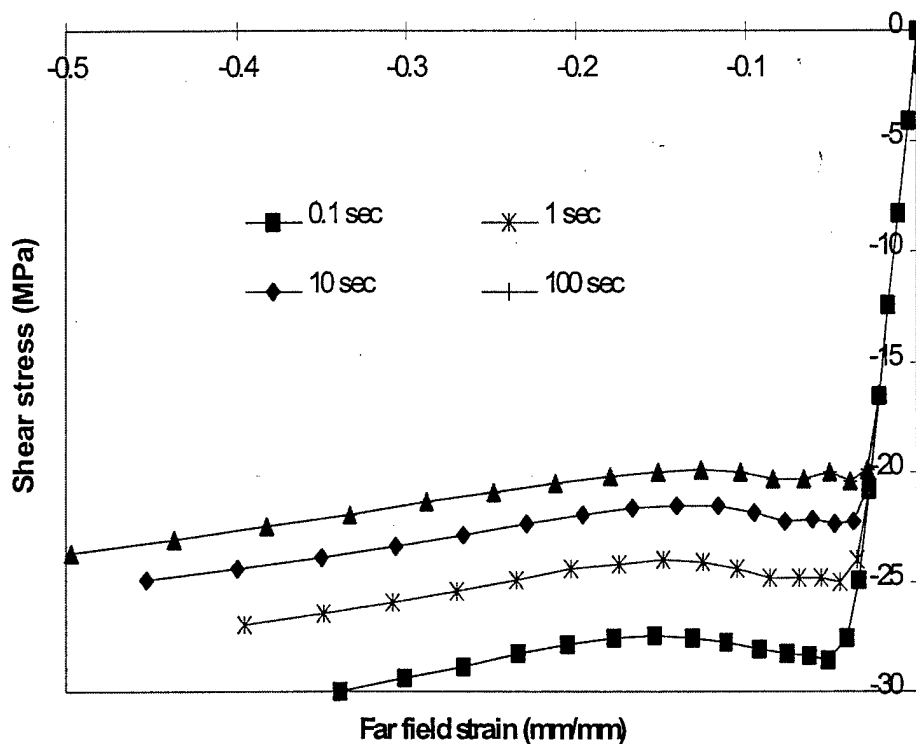


Figure 2.8: Adhesive shear stress-strain curves at a critical point in the joint,  $L/2t=15$ .

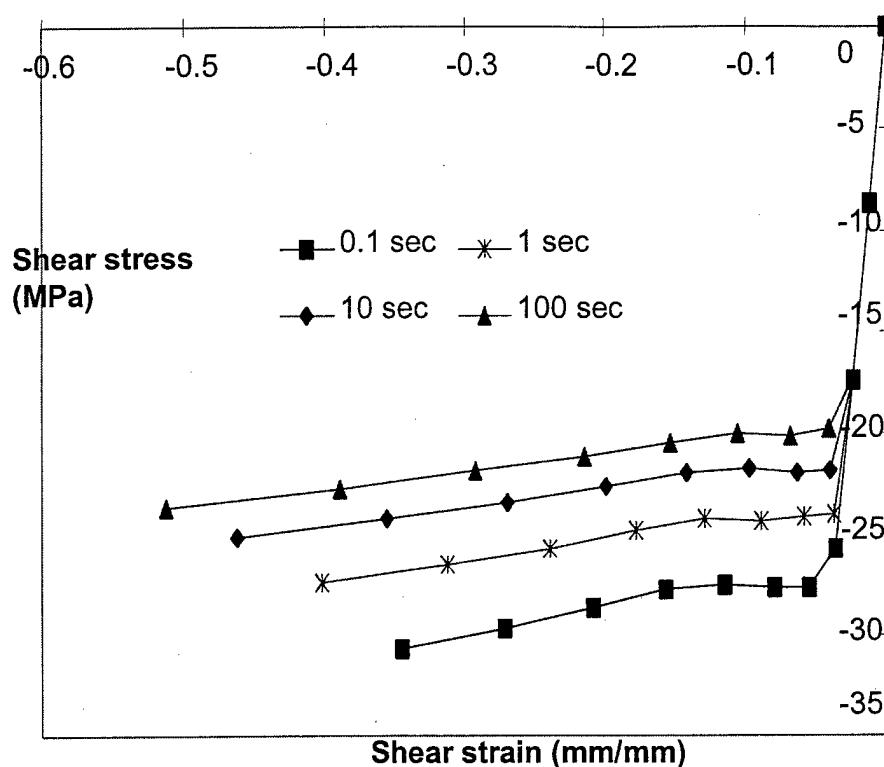


Figure 2.9: Adhesive shear stress-strain curves at a critical point in the joint,  $L/2t=7.5$ .

This interlaminar failure mechanism is also frequently seen in laboratory tests, see Figure 2.11 [15, 17, 18], on boron epoxy repairs to surface flaws. This test program, which is documented in [17], dealt with the repair of surface cracks 40 mm long and 5.7 mm deep in an 11.2 mm x 106.8 x 304.8 aluminium alloy specimen which was subjected to constant amplitude loading with a peak stress of 69.4 MPa, with a stress ratio  $R$  of 0.01. In these tests the failure mechanism was generally similar to that seen in the F-111C repair program in that failure was in the boron epoxy repair. This is clearly shown in Figure 2.10 where boron fibres can (again) be seen attached to the surface of the aluminium. This failure mechanism is also evident in the test program reported in section 4.4.

It is thus clear that the major design considerations that need to be addressed for a composite repair are, viz:

1. The maximum stress intensity factor should be as low as possible and preferably below the critical value for fatigue crack growth  $K_{th}$  in the material.
2. The maximum adhesive design state should be below the value at which fatigue damage accumulates in the adhesive. To minimise errors in measuring and computing the adhesive stresses and allowables it is best to follow the Hart-Smith methodology and use the energy in the adhesive  $W$ ,  $=1/2 \sigma_{ij} \epsilon_{ij} = \int \sigma_{ij} d\epsilon_{ij}$ , as the design variable. These critical design state measurements can be obtained using the ASTM thick adherend test, ASTM D 1002, see above. This approach, which was originally proposed in [9], has been validated in [10, 11].

3. The rate of delamination growth in the adhesive can be determined from a knowledge of the peak adhesive shear stresses and strains. For FM73 one such formulae relating the delamination length  $b$  to the number of cycles experienced  $N$  is given in [18] as

$$db/dN = 5.43 \cdot 10^5 (\Delta\gamma)^{10.96}$$

4. The composite patch must not experience failure by interply delamination. This can be checked by ensuring that the polynomial failure criteria is not greater than one. The commonly used failure criteria are: Tsai-Hill, Hoffman and Tsai-Wu. These failure criteria are generally written in the form:

Tsai-Hill criterion: In this case failure is assumed to occur when

$$\frac{\sigma_1^2}{X^2} - \frac{\sigma_1\sigma_2}{X^2} + \frac{\sigma_2^2}{Y^2} + \frac{\tau_{12}^2}{S^2} = 1 \quad (23)$$

Here the material is assumed to have equal strengths in tension and compression, i.e.  $X_t = X_c = X$  and  $Y_t = Y_c = Y$ .

Hoffman criterion: Failure is assumed to occur when

$$\left(\frac{1}{X_t} - \frac{1}{X_c}\right)\sigma_1 + \left(\frac{1}{Y_t} - \frac{1}{Y_c}\right)\sigma_2 + \frac{\sigma_1^2}{X_t X_c} + \frac{\sigma_2^2}{Y_t Y_c} + \frac{\sigma_{12}^2}{S^2} - \frac{\sigma_1\sigma_2}{X_t X_c} = 1 \quad (24)$$

Tsai-Wu criterion: Failure is assumed to occur when

$$\left(\frac{1}{X_t} - \frac{1}{X_c}\right)\sigma_1 + \left(\frac{1}{Y_t} - \frac{1}{Y_c}\right)\sigma_2 + \frac{\sigma_1^2}{X_t X_c} + \frac{\sigma_2^2}{Y_t Y_c} + \frac{\sigma_{12}^2}{S^2} + 2F_{12}\sigma_1\sigma_2 = 1 \quad (25)$$

The coefficient  $F_{12}$  is experimentally determined from test specimens under bi-axial loading and  $F_{12}$  must satisfy a stability criterion of the form

$$\left[\frac{1}{X_t X_c}\right] \left[\frac{1}{Y_t Y_c}\right] - F_{12}^2 > 0 \quad (26)$$

creates some complication in the use of this theory. It has been suggested that  $F_{12}$  be set to zero.



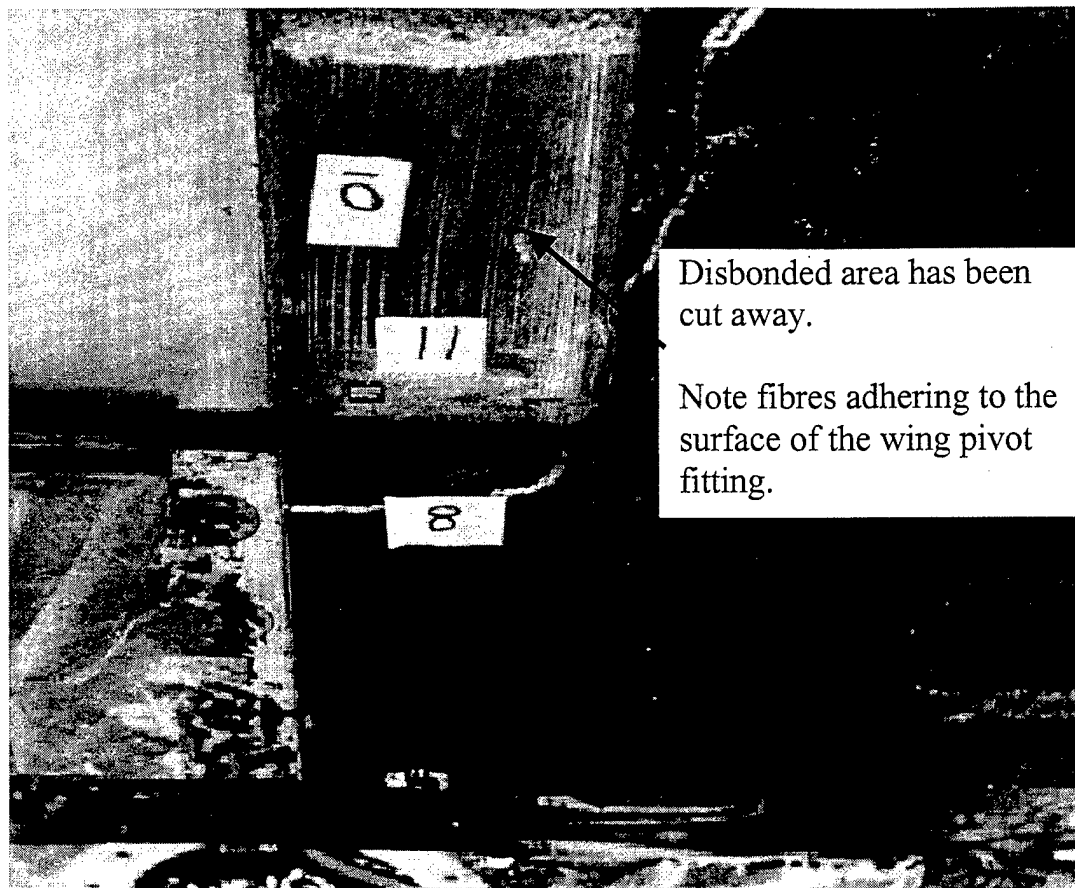


Figure 2.10. Close of delaminated doubler on F111 aircraft, looking from above the repair, showing boron fibres still attached to the wing pivot fitting.

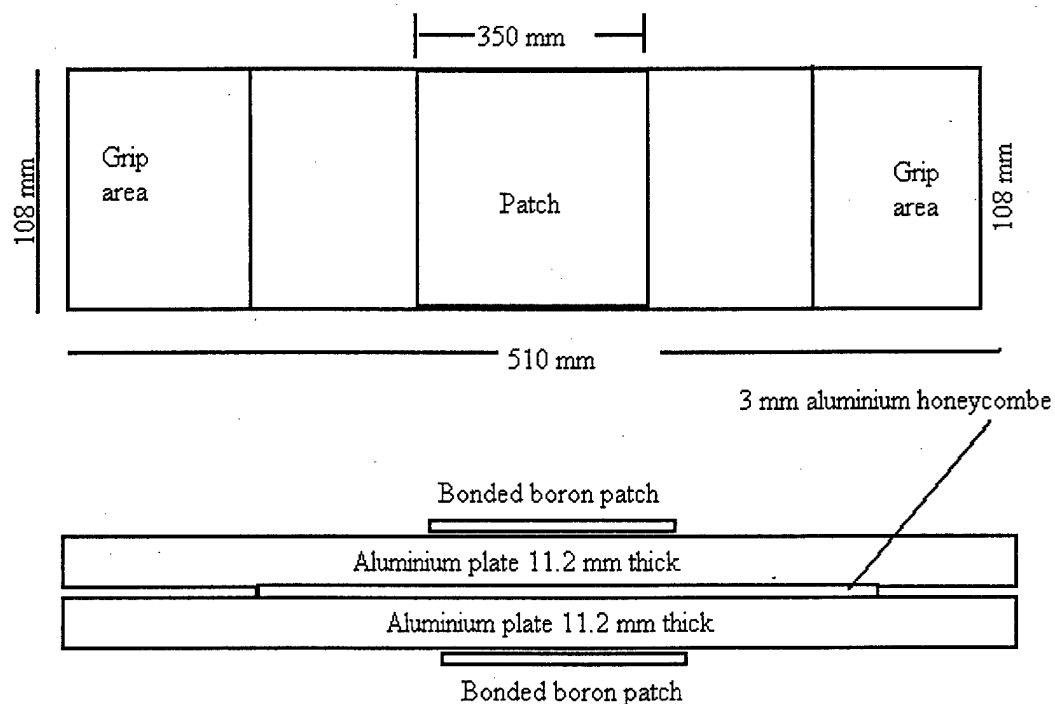


Figure 2.11 Geometry of the surface flaw specimen

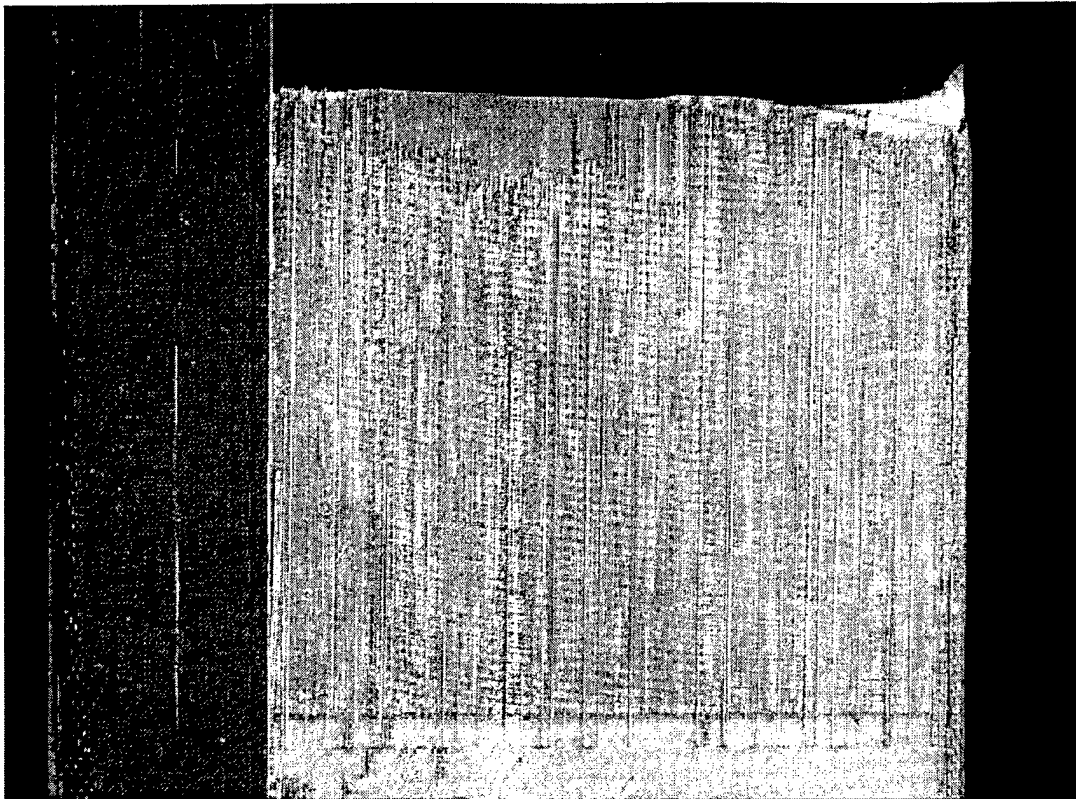


Figure 2.12 Close up of failure surface showing the 1<sup>st</sup> layer of the repair still attached to the specimen

The symbols used in Equations (23) to (26) are defined as:

$X_t$	Allowable tensile stress in the principal x (or 1)-direction of the material
$X_c$	Allowable compressive stress in the principal x (or 1)-direction of the material
$Y_t$	Allowable tensile stress in the principal y (or 2)-direction of the material
$Y_c$	Allowable compressive stress in the principal y (or 2)-direction of the material
$S$	Allowable shear stress in the principal material system

*The interlaminar stresses can be estimated using the Glinka formulation outlined earlier in this report.*

For relatively thin repairs the average stress through the thickness of the boron patch should not exceed 1000 MPa. This failure rule is a modification of the average stress failure criterion, which is commonly used for composite materials.

It must be stressed that for repairs to primary structures a 3-D finite element analysis should be performed. To ensure continued airworthiness this analysis should include a damage tolerant assessment of both the structure and the composite repair.

At this stage it should be noted that the majority of commercially available finite element programs, e.g. ABAQUS, MSC-Nastran, NENastran, MARC, ANSYS etc, use iso-parametric elements. Furthermore, when analysing three dimensional problems involving composites the use of elements with mid-side nodes is essential, i.e. 20 noded hex (brick) elements, 15 noded wedge elements, etc. Unfortunately, ABAQUS, MSC-Nastran, MARC, ANSYS still use formulations based on that given in Zienkiewicz [23], which means that for accurate results the aspect ratio's are limited to less than  $\sim 5:1$ , even if reduced integration, i.e. the use of  $2 \times 2 \times 2$  Gauss points in formulating the element stiffness matrix, is used. In contrast NENastran use an enriched 20 noded element, where the basic formulation is extended to include additional shape functions. This means that the NENastran 3D (mid-side noded) elements can have dramatically greater aspect ratio's. Consequently, when analysing composite repairs, and consequently performs better when analysing composite repairs. Equally important is the fact that, unlike MSC NASTRAN, the NENastran 20 noded bricks can be used when analysing repairs in which the adhesive is behaving plastically and when there may be non-linear geometric effects. This feature is particularly important when determining the residual strength of a repair with delamination damage in the adhesive.

### **3. ANALYSIS OF REPAIRS TO RIB STIFFENED PANELS**

#### **3.1 Large Panel Fatigue Test Specimens**

After consultation with the USAF it was decided to use narrow single stiffener panels. These panels are currently being fabricated for shipment to Australia. Testing is awaiting the fabrication and delivery of these specimens.

#### **3.2 Finite Element Analysis**

A finite element study for the composite repair of cracked rib stiffened panels has now been completed. In this study the stiffeners were assumed to be riveted to the skin. Symmetry considerations enabled only a  $\frac{1}{4}$  of the structure to be model. Several typical examples are shown in Figures 3.1-3.5. In this study the crack length, patch thickness, skin thickness, stiffener width, stiffener spacing, and stiffener depth were varied to determine their effects on the stress intensity factors.

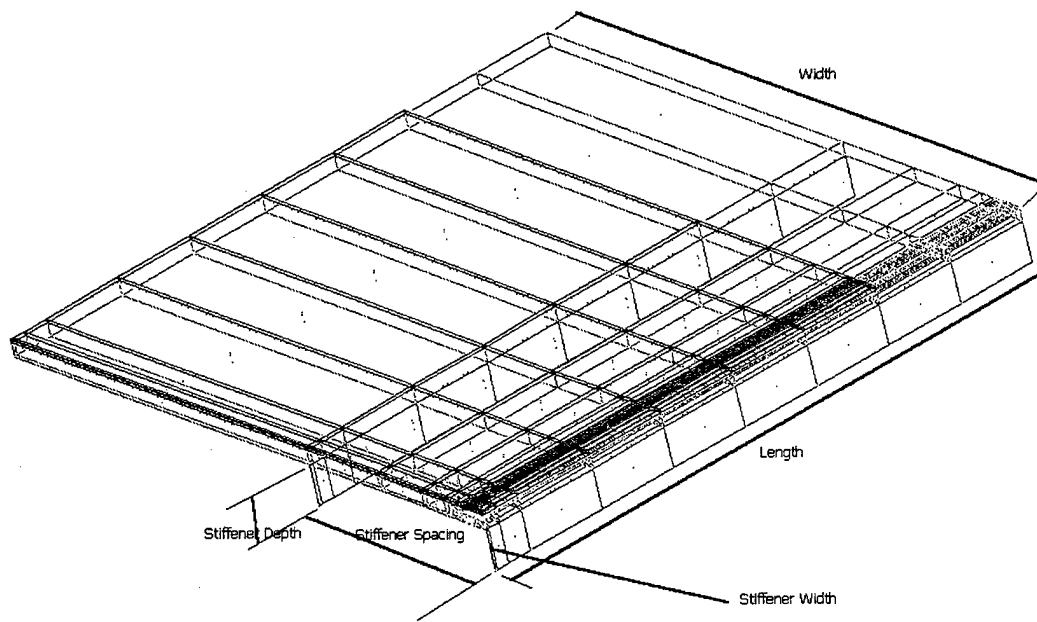


Figure 3.1 Schematic of three dimensional  $\frac{1}{4}$  finite element model of stiffened panel. Note the definitions with respect to stiffener dimensions.

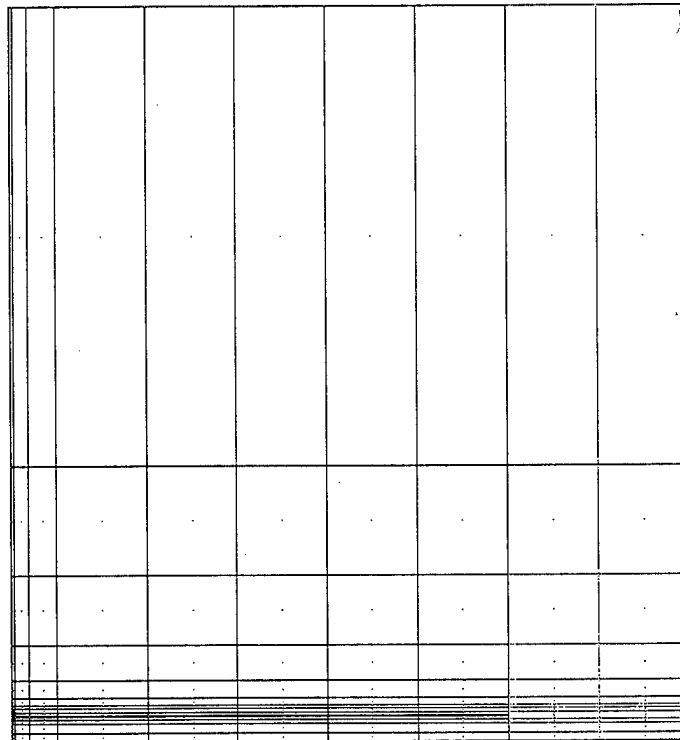


Figure 3.2. Plan view of a finite element model shown in Figure 3.1 showing mesh spacing in and around the crack tip. 8mm crack length, 4mm skin, 1mm patch thickness, 5.5mm stiffener width, 75mm stiffener spacing and 12 mm stiffener depth

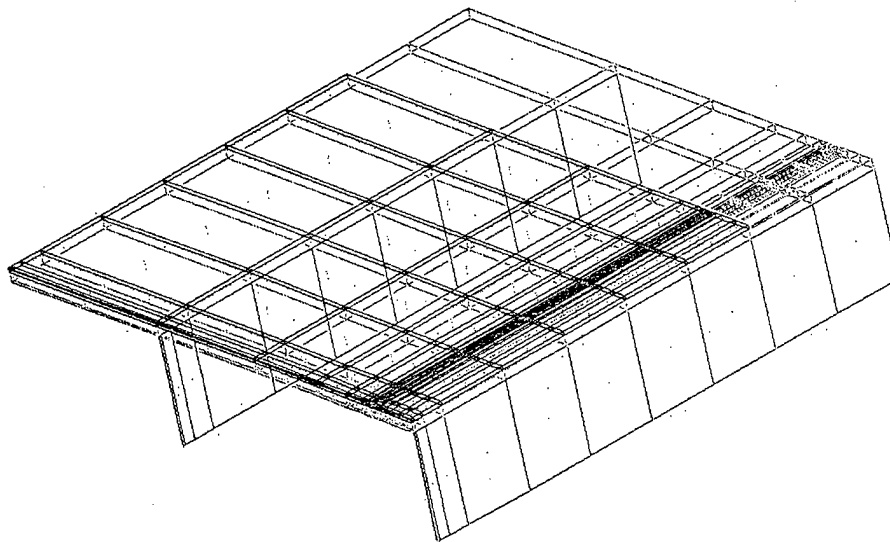


Figure 3.3 Schematic of a finite element model with 20mm crack length, 3.16mm skin, 1.4mm patch thickness, 3.5mm stiffener width, 127.5mm stiffener spacing and 37.5 mm stiffener depth

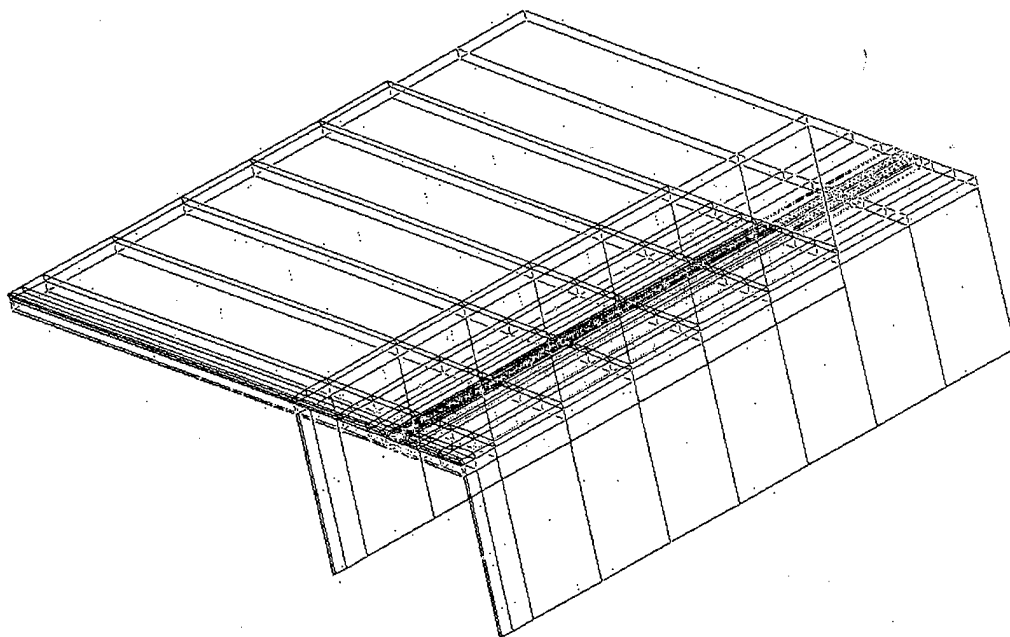


Figure 3.4 Schematic of a finite element model with 30mm crack length, 3.16mm skin, 1.8mm patch thickness, 5.5mm stiffener width, 75mm stiffener spacing and 50mm stiffener depth.

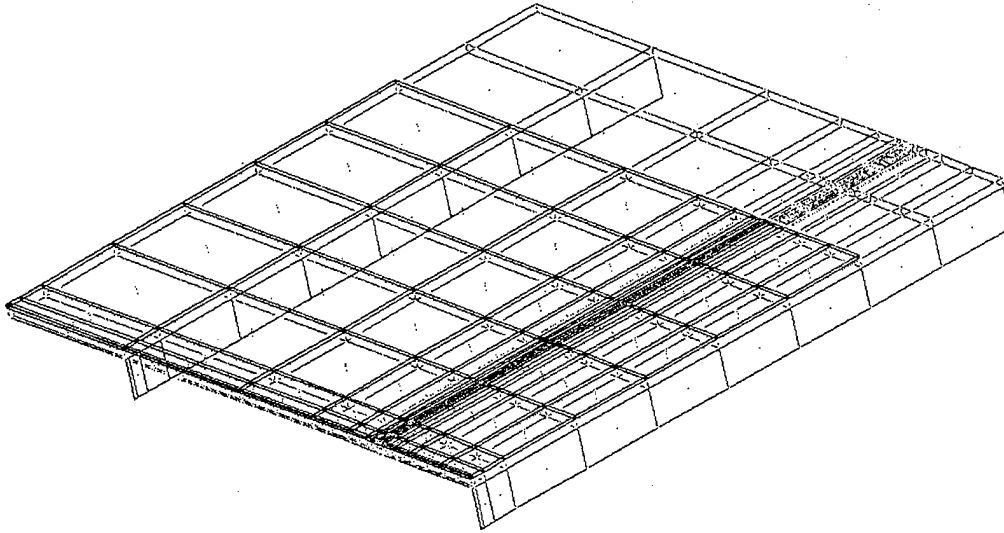


Figure 3.5 Schematic of another finite element model with 40mm crack length, 2.5mm skin, 1mm patch thickness, 3.5mm stiffener width, 150mm stiffener spacing and 12mm stiffener depth.

To create the required solution space this process was automated and a large number of geometrical configurations, ~ 1500, were evaluated. Each run took ~ 6 minutes of cpu time on an SGI R10000 workstation..

The resultant solutions are summarised below. It is hoped that the differences (if any) in the stress intensity factors caused by the change in geometry may be explained by simple analytical relationships. The results from the finite element analysis will subsequently be used to predict the behaviour of composite repairs to cracks in rib stiffened panels.

### 3.3 Results for stress-intensity calculations from the finite element analysis of a boron epoxy composite repair of a crack over a stiffening element

In this study the adhesive thickness ( $t_a$ ) was kept constant at 0.2mm and the following labelling convention was adopted :

"File name" = Skin-thickness..Stiffener-width..Patch-thickness..Stiffener-spacing..Stiffener-depth

Thus a designation with 3.16..3.5..1..127.5..12 describes a stiffened skin with :

3.16 mm skin thickness,  
3.5 mm stiffener width,  
1 mm patch thickness  
127.5 mm stiffener spacing  
12mm stiffener depth

For the analyses, the following conditions were considered :

A centre crack in a 2.5, 3.16 or 4mm thick aluminium stiffened panel with  $E = 72,000$  MPa, and  $\nu = 0.33$ . Three patch thicknesses were considered, viz: 1, 1.4 and 1.85 mm thick and the moduli of the patch were taken to be  $E_{11} = 208,000$  MPa,  $E_{22} = 25432$  MPa,  $\nu_{12} = 0.183$ ,  $G_{12} = G_{13} = G_{23} = 7241$  MPa.

The panel had dimension of 375 mm (length) x 400 mm (width) and the plan form of the composite repair was 275 mm (length) x 400 mm (width). The adhesive was taken to be 0.20 mm thick with a shear modulus of 375 MPa and  $\nu = 0.33$ . The analysis used 20 noded isoparametric 3D bricks with single layer of elements through the skin, adhesive and patch. 15 noded isoparametric 3D wedge shaped bricks were used at the crack tip location through the entire thickness of the specimen. The skin in the panel was subjected to a remote uniform stress of 229.8MPa.

The solution was well conditioned and the accuracy of the solution was evaluated by performing two separate analyses. One used optimum integration to form the stiffness matrix, i.e.  $2 \times 2 \times 3$  Gauss quadrature points, the second used full integration. Both analyses gave results within less than 1% of each other.

To illustrate the asymptotic effects of the solution the results for repairs to centre notch cracks will now be presented. To this end various plots of stress intensity factors vs. crack length are presented. They are used to illustrate the effects of varying the various individual geometrical parameters on  $K_I$ .

The values presented in these analyses are taken from the bottom surface of the skin (just above the stringer). As expected, these gave consistently higher values of  $K_I$  when compared to the stress intensity values at the skin-adhesive interface.

### 3.3.1 Comparison of results for several different stiffener spacing and two different skin thicknesses.

This study focused on determining the effect of stiffener spacing on the stress intensity factor. The geometrical parameter considered are shown in Table 3.1. The results are summarised in Figures 3.6 and 3.7 where in each case the stiffener width and depth was 3.5mm and 12mm respectively. From these figures we see that the stress intensity factor  $K_I$  is a weak function of the stiffener spacing.

Table 3.1 Geometrical parameters considered.

Skin thickness (mm)	Stiffener spacing (mm)	Patch thickness
2.5	75	1.0
3.6	127.5	1.8
	150	

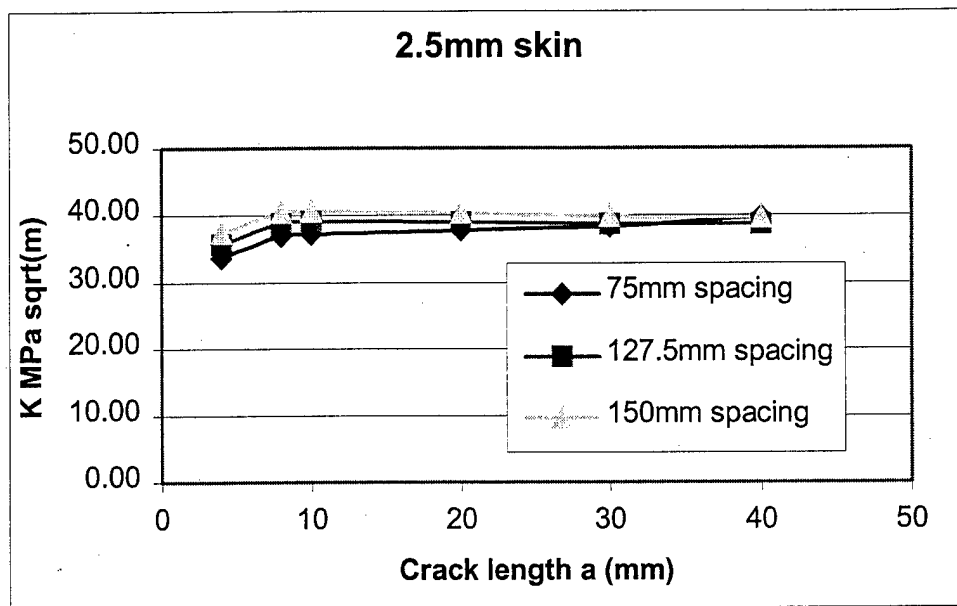


Figure 3.6 : Plot of  $K_I$  vs.  $a$  for 2.5mm stiffened skin with three different stiffener spacings. Data files analysed were : 2.5..3.5..1..75..12, 2.5..3.5..1..127.5..12, and 2.5..3.5..1..150..12.

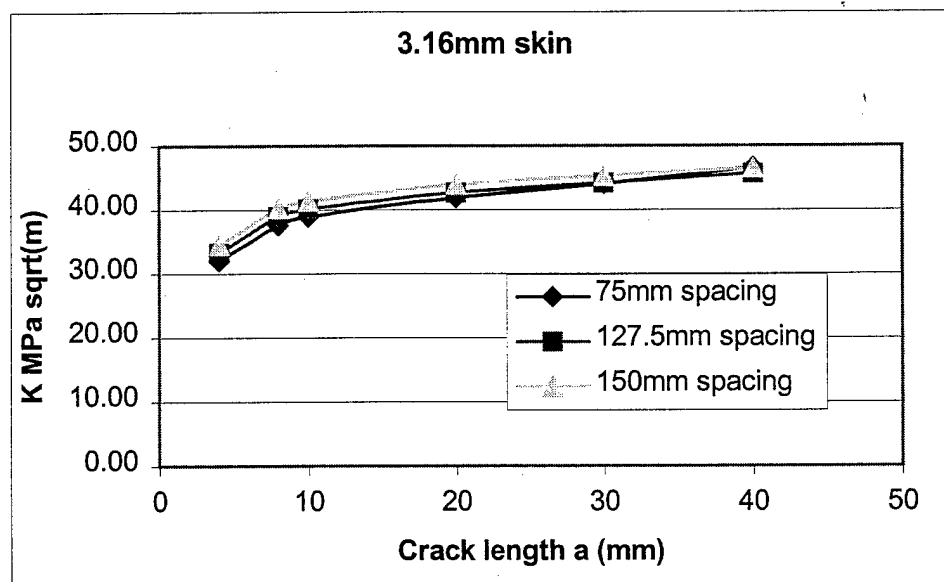


Figure 3.7 : Plot of  $K_I$  vs.  $a$  for 3.16mm stiffened skin with three different stiffener spacings. Data files analysed were: 3.16..3.5..1..75..12, 3.16..3.5..1..127.5..12, and 3.16..3.5..1..150..12

### 3.3.2 Comparison of results for several stiffener spacings and stiffener depths and two different skin thicknesses.

This study focused on confirming the effect of stiffener spacing on the stress intensity factor. In this study the stiffener depths were varied, see Table 3.2, and the results are summarised in Figures 3.8 and 3.9 and we again see that the stress intensity factor  $K_I$  is a weak function of the stiffener spacing.



Table 3.2 Geometrical parameters considered.

Skin thickness (mm)	Stiffener spacing (mm)	Patch thickness	Stiffener depth (mm)
2.5	75	1.0	12
3.16	127.5		50
	150		

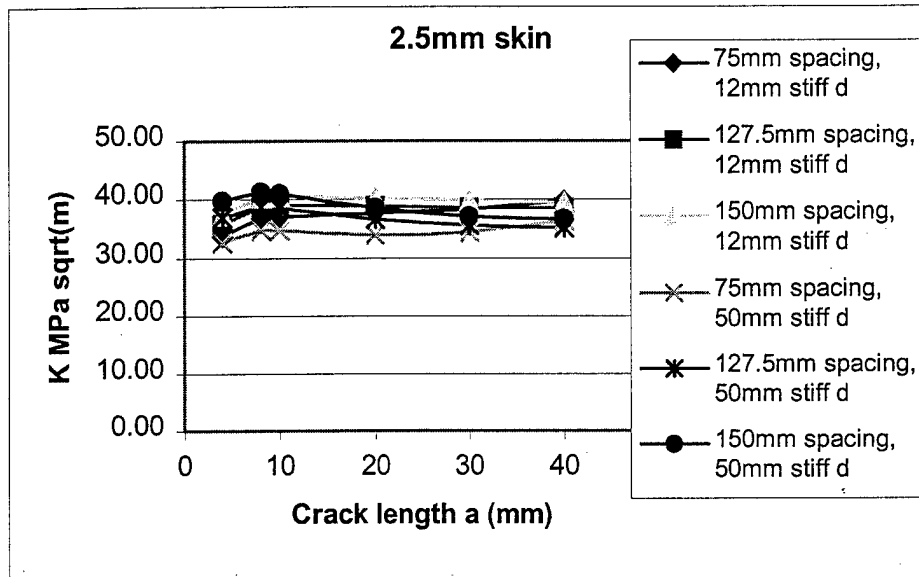


Figure 3.8 : Plot of  $K_1$  vs.  $a$  for 2.5mm stiffened skin with three different stiffener spacings and two different stiffener depths. Data files were : 2.5..3.5..1..75..12, 2.5..3.5..1..127.5..12, 2.5..3.5..1..150..12, 2.5..3.5..1..75..50, 2.5..3.5..1..127.5..50, 2.5..3.5..1..150..50.

### 3.3.3 Comparison of results for various stiffener spacing and patch thickness for two different skin thicknesses.

This study focused on confirming the effect of stiffener spacing on the stress intensity factor. In this study the patch thickness was varied, see Table 3.3, and the results are summarised in Figures 3.10 and 3.11 and we again see that the stress intensity factor  $K_1$  is a weak function of the stiffener spacing.

Figures 3.6 to 3.11 show that the stress intensity factors  $K_1$  exhibit an asymptotic behaviour as the crack length increases, see Figure 3.18, although as the skin thickness increases the crack length required to achieve this asymptote,  $K_\infty$  also increases. Indeed, for the 2.5 mm sheet thickness with a 1. mm patch the limiting value of  $K_\infty$  has essentially been reached at a crack length of between 20 - 30mm, see Figure 3.10.

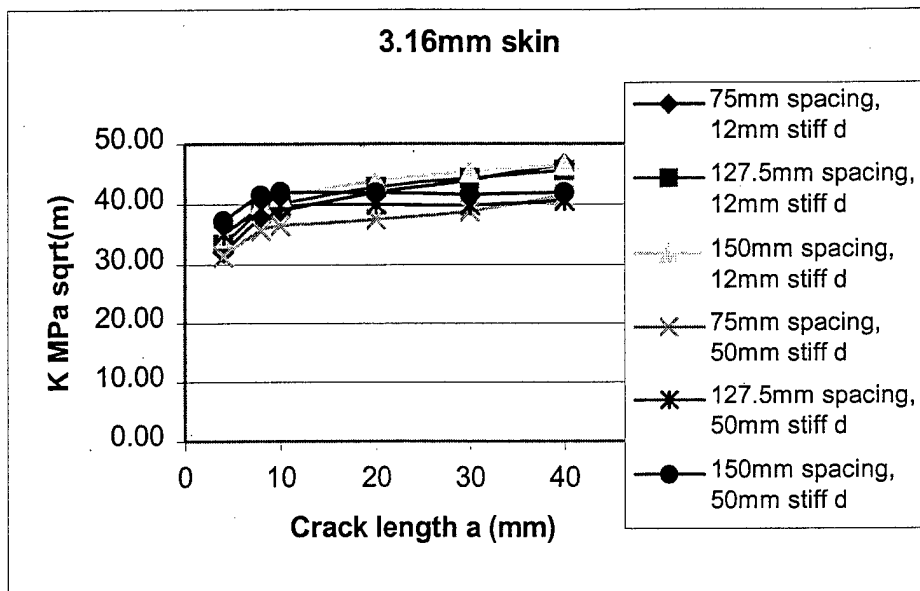


Figure 3.9: Plot of  $K_I$  vs.  $a$  for 3.16mm stiffened skin with three different stiffener spacings and two different stiffener depths. Data files were : 2.5..3.5..1..75..12, 2.5..3.5..1..127.5..12, 2.5..3.5..1..150..12, 2.5..3.5..1..75..50, 2.5..3.5..1..127.5..50, 2.5..3.5..1..150..50.

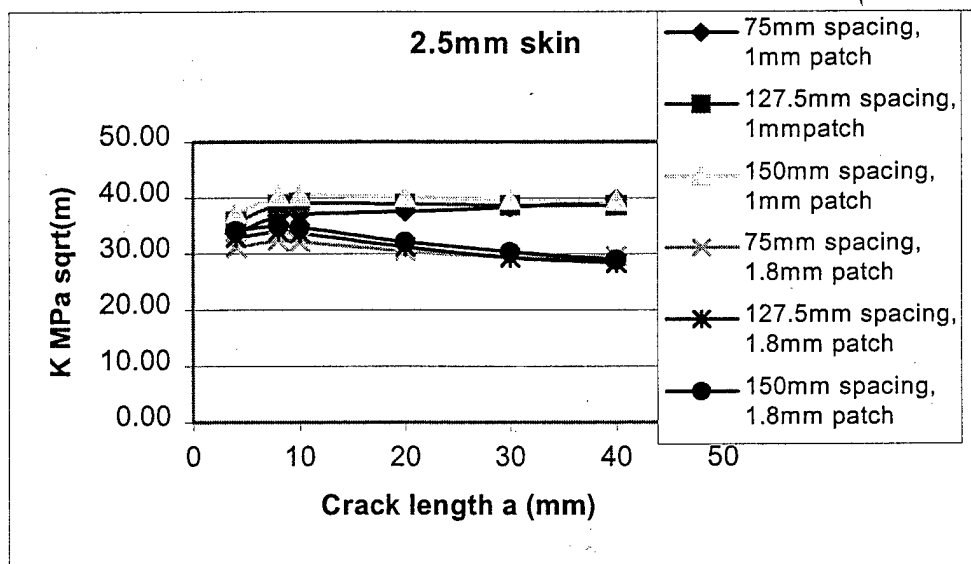


Figure 3.10: Plot of  $K_I$  vs.  $a$  for 2.5mm stiffened skin with three different stiffener spacings and two different patch thicknesses. Data files were: 2.5..3.5..1..75..12, 2.5..3.5..1..127.5..12, 2.5..3.5..1..150..12, 2.5..3.5..1.8..75..12, 2.5..3.5..1.8..127.5..12, 2.5..3.5..1.8..150..12

In contrast for the 3.16 mm sheet thickness with a 1. mm patch the limiting value has not been reached by 40 mm, see Figure 3.11. Similarly the crack length required to reach  $K_\infty$  is also a function of the patch thickness. For example in the case considered

above when the 3.16 mm sheet thickness has a 1.8 mm thick patch this limiting value is essentially achieved with a crack length of (say) 20 mm, see Figure 3.11.

This asymptotic process is also a function of the depth of the stiffener. For example for the 2.5 mm skin by the time the crack length is 40mm the limiting value of  $K_{\infty}$  has been reached for stiffener depths of both 12 and 50mm, see Figure 3.8. In contrast for the 3.16 mm thick skin with a crack length of 40 mm the solution associated with a 50 mm deep stiffener has reached its asymptote whilst that for a 12 mm deep stiffener has not, see Figure 3.9.

Table 3.3 Geometrical parameters considered.

Skin thickness (mm)	Stiffener spacing (mm)	Patch thickness	Stiffener depth (mm)
2.5	75	1.0	12
3.16	127.5	1.8	
	150		

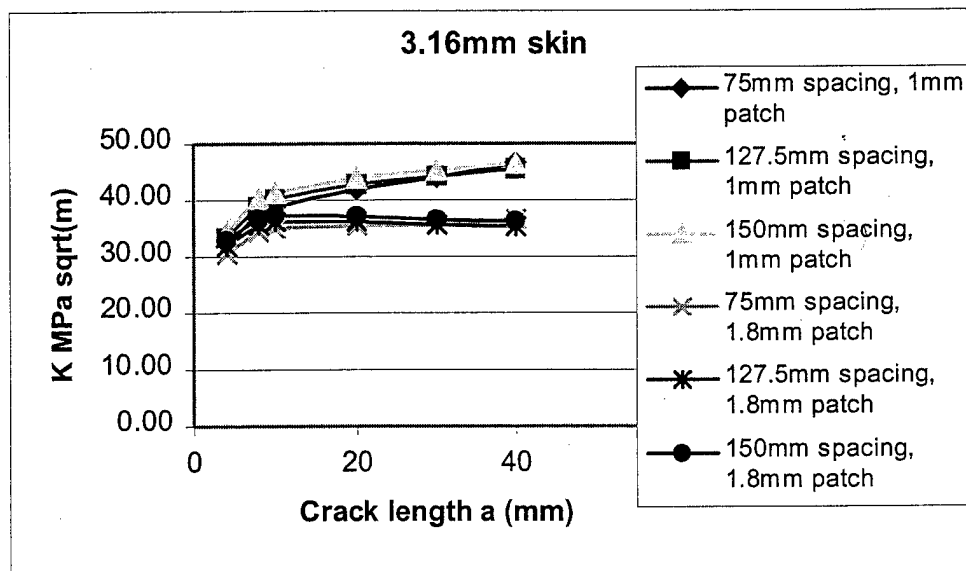


Figure 3.11: Plot of  $K_I$  vs.  $a$  for 3.16mm stiffened skin with three different stiffener spacings and two different patch thicknesses. Data files were: 3.16..3.5..1..75..12, 3.16..3.5..1..127.5..12 3.16..3.5..1..150..12, 3.16..3.5..1.8..75..12, 3.16..3.5..1.8..127.5..12, 3.16..3.5..1.8..150..12

### 3.3.4 Comparison of results for various stiffener widths and depths for two different skin thicknesses.

This study focused on determining whether the stress intensity factor  $K_I$  was more strongly effected by the stiffener depth than the stiffener width. The parameters considered are shown in Table 3.4 and the results of this study are shown in Figures 3.12 – 3.14. This study found that  $K_I$  was more strongly influenced by the depth than by the width of the stiffener. Indeed, as can be seen from Figures 3.13 and 3.14 the stiffener width had little effect on stress intensity factor(s). It thus appears that the stress intensity factor  $K_I$  is more strongly influenced by the moment of inertia  $I$  than by the cross sectional area of the stiffener.

Table 3.4 Geometrical parameters considered.

Skin thickness (mm)	Stiffener width (mm)	Stiffener depth (mm)
2.5	3.5	12
3.16	4.6	23.24
	5.5	37.5
	6	50

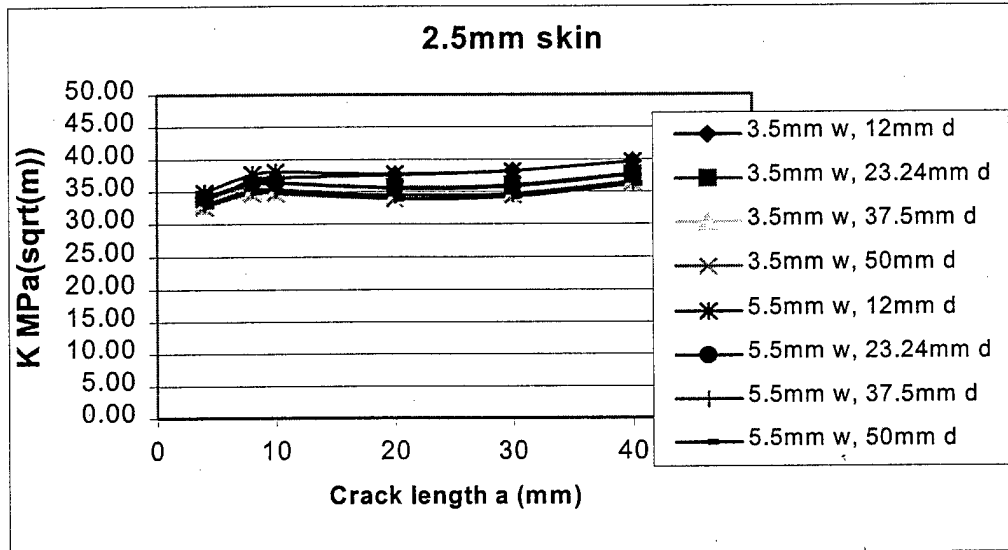


Figure 3.12: Plot of  $K$  vs.  $a$  for 2.5mm stiffened skin with two different stiffener widths ( $w$ ) and four different stiffener depths ( $d$ ). Data files were: 2.5..3.5..1..75..12, 2.5..3.5..1..75..23.24, 2.5..3.5..1..75..37.5, 2.5..3.5..1..75..50, 2.5..5.5..1..75..12, 2.5..5.5..1..75..23.24, 2.5..5.5..1..75..37.5, 2.5..5.5..1..75..50

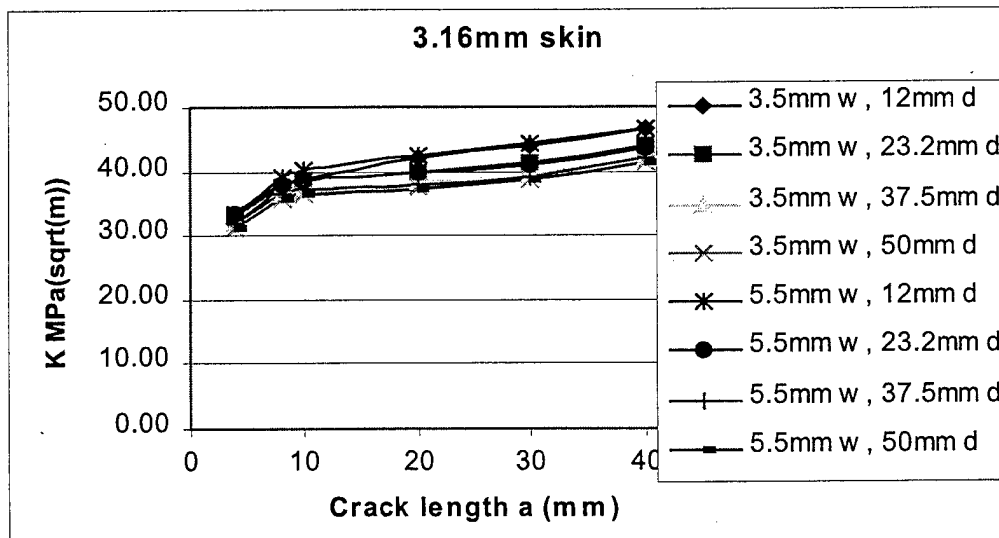


Figure 3.13: Plot of  $K$  vs.  $a$  for 3.16mm stiffened skin with two different stiffener widths ( $w$ ) and four different stiffener depths ( $d$ ). Data files were: 3.16..3.5..1..75..12, 3.16..3.5..1..75..23.24, 3.16..3.5..1..75..37.5, 3.16..3.5..1..75..50, 3.16..5.5..1..75..12, 3.16..5.5..1..75..23.24, 3.16..5.5..1..75..37.5, 3.16..5.5..1..75..50

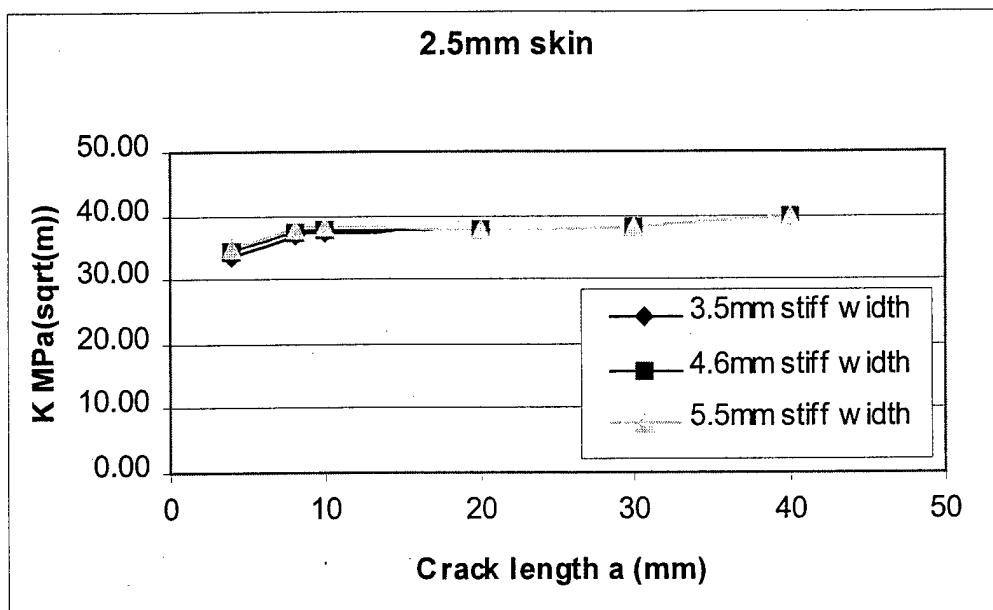


Figure 3.14: Plot of K v's. a for a 2.5mm stiffened skin with three different stiffener widths. Data files were 2.5..3.5..1..75..12, 2.5..4.6..1..75..12, 2.5..5.5..1..75..12

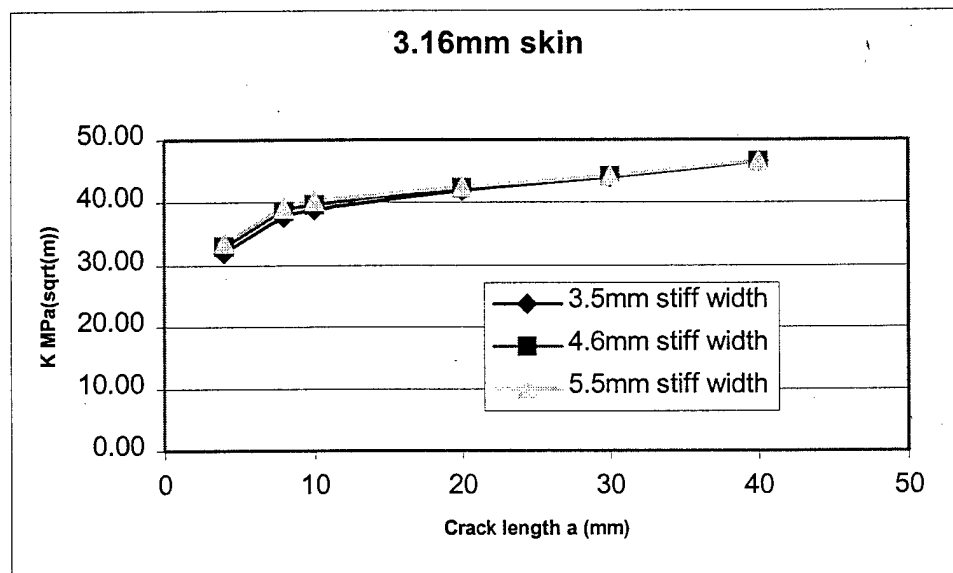


Figure 3.15: Plot of K vs. a for 3.16mm stiffened skin with three different stiffener widths Data files were 3.16..3.5..1..75..12, 3.16..4.6..1..75..12, 3.16..5.5..1..75..12

### 3.3.5 Relationship between the ratio of the patch thickness to skin thickness and the stress intensity factor $K_I$ for 5 different crack lengths.

This study has focused on determining the effect of the ratio of patch thickness to skin thickness ( $t_p/t_s$ ) on the stress intensity factor  $K_I$ . To this end nine different geometrical configurations with three different skin thicknesses were considered, see Table 3.5, and results of this study are shown in Figure 3.16.

This study found that to a first approximation  $K_1$  was a linear function of the ratio of patch thickness to skin thickness ( $t_p/t_s$ ).

Table 3.5 Geometry configurations studied

Panel/model geometry descriptors	$t_p/t_s$
2.5..3.5..1..127.5..23.24	0.40
2.5..3.5..1.4..127.5..23.24	0.56
2.5..3.5..1.8..127.5..23.24	0.72
3.16..3.5..1..127.5..23.24	0.32
3.16..3.5..1.4..127.5..23.24	0.44
3.16..3.5..1.8..127.5..23.24	0.57
4..3.5..1..127.5..23.24	0.25
4..3.5..1.4..127.5..23.24	0.35
4..3.5..1.8..127.5..23.24	0.45

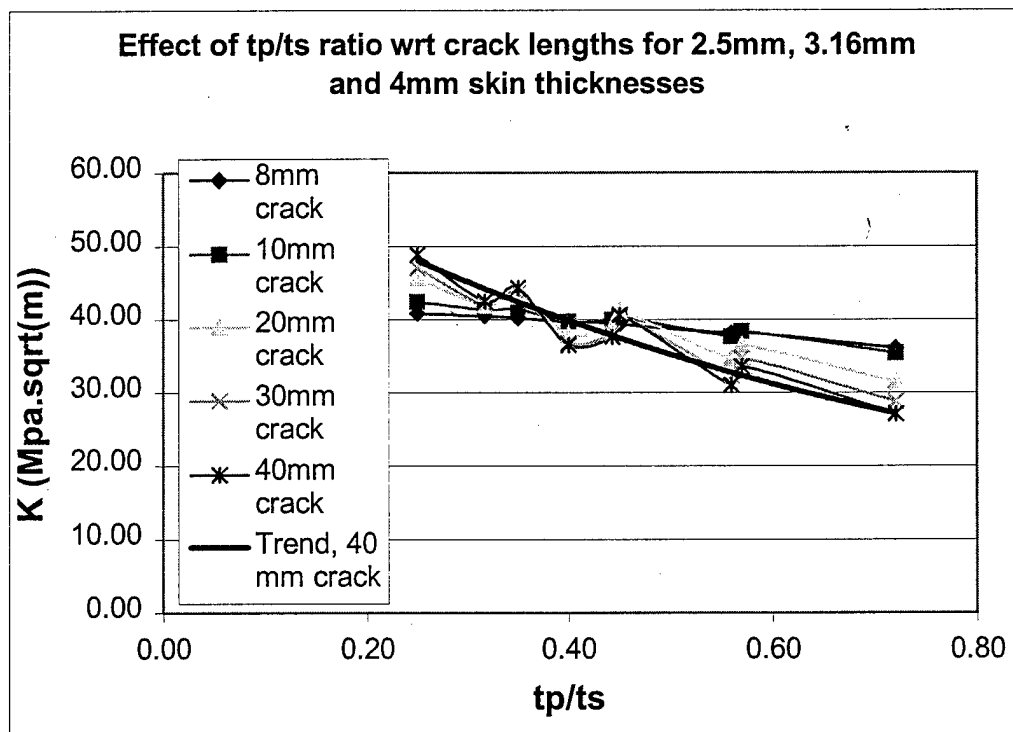


Figure 3.16: Plot of  $K_1$  vs.  $t_p/t_s$  ratio keeping stiffener width, stiffener spacing and stiffener depth the same.

### 3.3.6 Effect of the interlaminar shear modulus

The initial studies used an interlaminar shear modulus  $G_{23} = G_{13} = G_{12}$ . To investigate the effect of this assumption analyses were performed using  $G_{23} = \frac{1}{2} (G_{13} + G_{12})$ . The results of these analyses are shown in Figures 3.17 and 3.18 and reveal that the stress intensity factor is a weak function of the interlaminar shear moduli.

These Figures also highlight how the stress intensity factor asymptotes to a limiting value as the crack length increases.

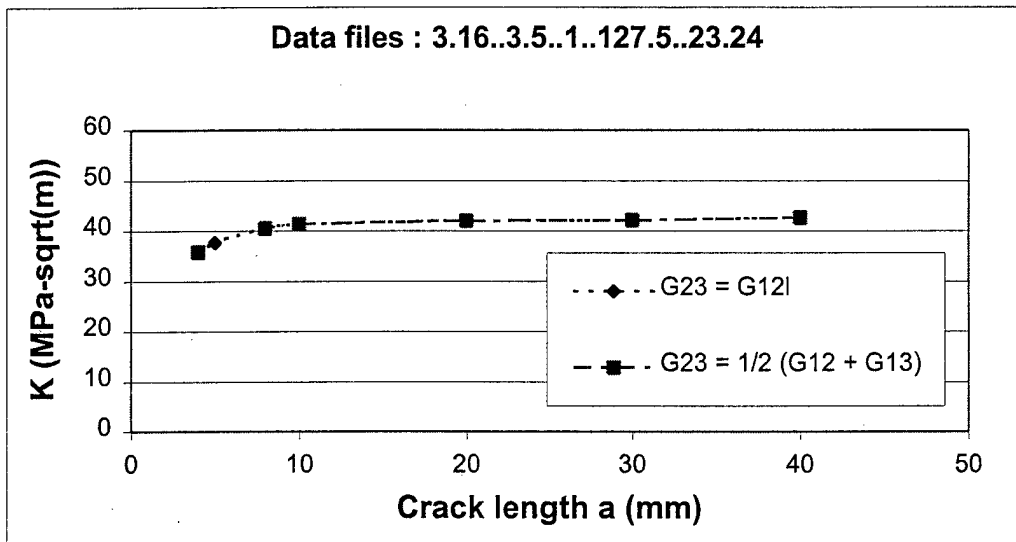


Figure 3.17: Effect of interlaminar shear modulus on  $K_1$ .

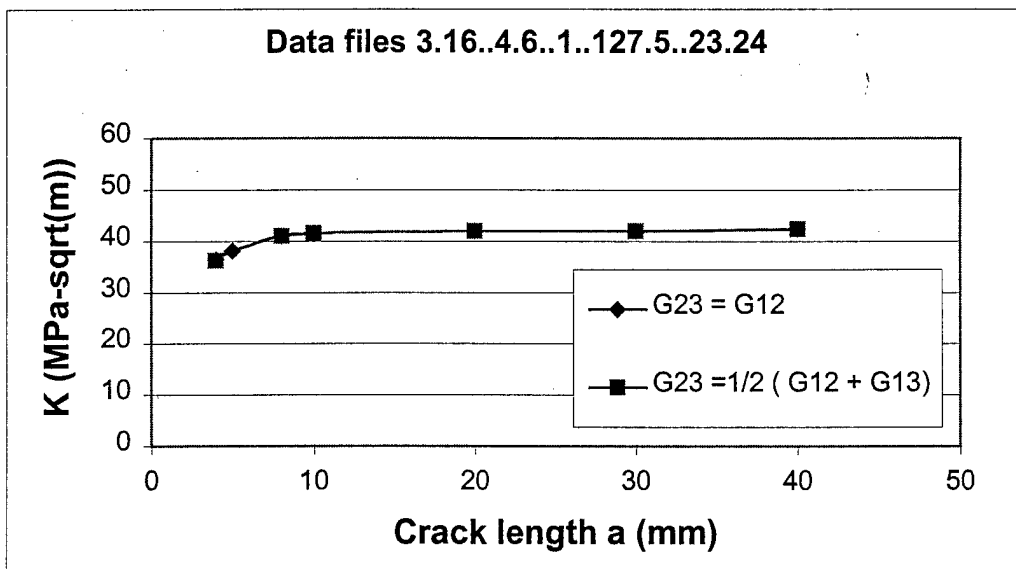


Figure 3.18: Effect of interlaminar shear modulus on  $K_1$ .

### 3.4 Summary of the finite element analysis

From these results it appears that

- i) The solution for the stress intensity factors  $K_1$  exhibit an asymptotic behaviour as the crack length increases, see Figures 3.8, 3.16 and 3.18.
- ii) The stress intensity factor  $K_1$  is a weak function of the stiffener spacing, see Figures 3.6 and 3.7.

- iii) The stress intensity factor  $K_1$  is more strongly effected by stiffener depth than stiffener width, see Figures 3.12 to 3.15. As such  $K_1$  is essentially a function of the moment of inertia  $I$  for the stiffener rather than the area of the stiffener.
- iv) As a first approximation the asymptotic value of  $K_1$  appears to decay linearly with increasing values of the ratio of the patch thickness to the skin thickness, see Figure 3.16. In comparison to the other geometrical panel cross-section parameters, the ratio of patch to skin thickness has the largest affect on the asymptotic value of the stress intensity factor.
- v) The stress intensity factor is a weak function of the interlaminar shear moduli of the Boron epoxy, see Figures 3.17 and 3.18.

### 3.5 Load flow in a rib stiffened panel

In the previous sections we have seen that the stress intensity factor  $K_1$  is a weak function of the stiffener spacing. This can be explained by understanding the load flow in a typical rib stiffened panel. To this end let us consider the case of a (rib stiffened) panel containing a centrally located 10 mm diameter hole. The skin is 1mm thick, the stiffeners are 5 mm thick and are 100mm apart. For simplicity the stiffeners are not tapered at the ends. The panel is loaded via the end stingers, at locations A and B, which are each subjected to a uniform displacement. At this location the skin is assumed to be completely cracked, i.e. the load is only being carried by the stiffeners. The stiffeners are uncracked. The stiffeners stop before the opposite end of the panel and the load is taken out of the skin at points C and D, see Figure 3.19. This represents an extreme loading case and is chosen to illustrate the load flow from the stiffeners into the skin.

To visualise the load flow from points C and D to A and B, after which the load is completely carried in the stiffeners, we plot the energy vector  $E$  where the components  $E_i$ ,  $i=1,3$ , are defined as:

$$E_1 = (\int \sigma_{1j} de_{1j}), E_2 = (\int \sigma_{2j} de_{2j}), E_3 = (\int \sigma_{3j} de_{3j}), \text{ summed over } j, \quad (27)$$

Here  $\sigma_{ij}$  and  $e_{ij}$  are the stress and (mathematical) strain tensors respectively and the summation is over  $j$ ,  $j=1,3$ . For simplicity the components of  $E$  are evaluated in principle stress space and the sign of the components is taken as that of the associated principal stresses.

Figures 3.19 and 3.20 presents a view of the flow field, the  $E$  vector, in the panel. In Figure 3.20 the view looks directly down so that the stiffeners appear as a (thick black) line. Both Figures clearly show the stress/load concentration at points A and B where the load is entering the panel and the stiffener. A more detailed view of this flow is given in Figure 3.21. Here we see how the load/energy is flowing from the stiffener to the upper skin.

At the edges of the panel, points E, F, G and H in Figure 3.20, we see well defined recirculation zones, which indicate that the material there is redundant. The disturbance of the flow field caused by the central hole is also very clear, see Figures



3.19-3.20. Indeed, the prime purpose for putting a hole in the skin was to enable us to contrast the effect that the hole has on the flow with that resulting from the stiffeners.

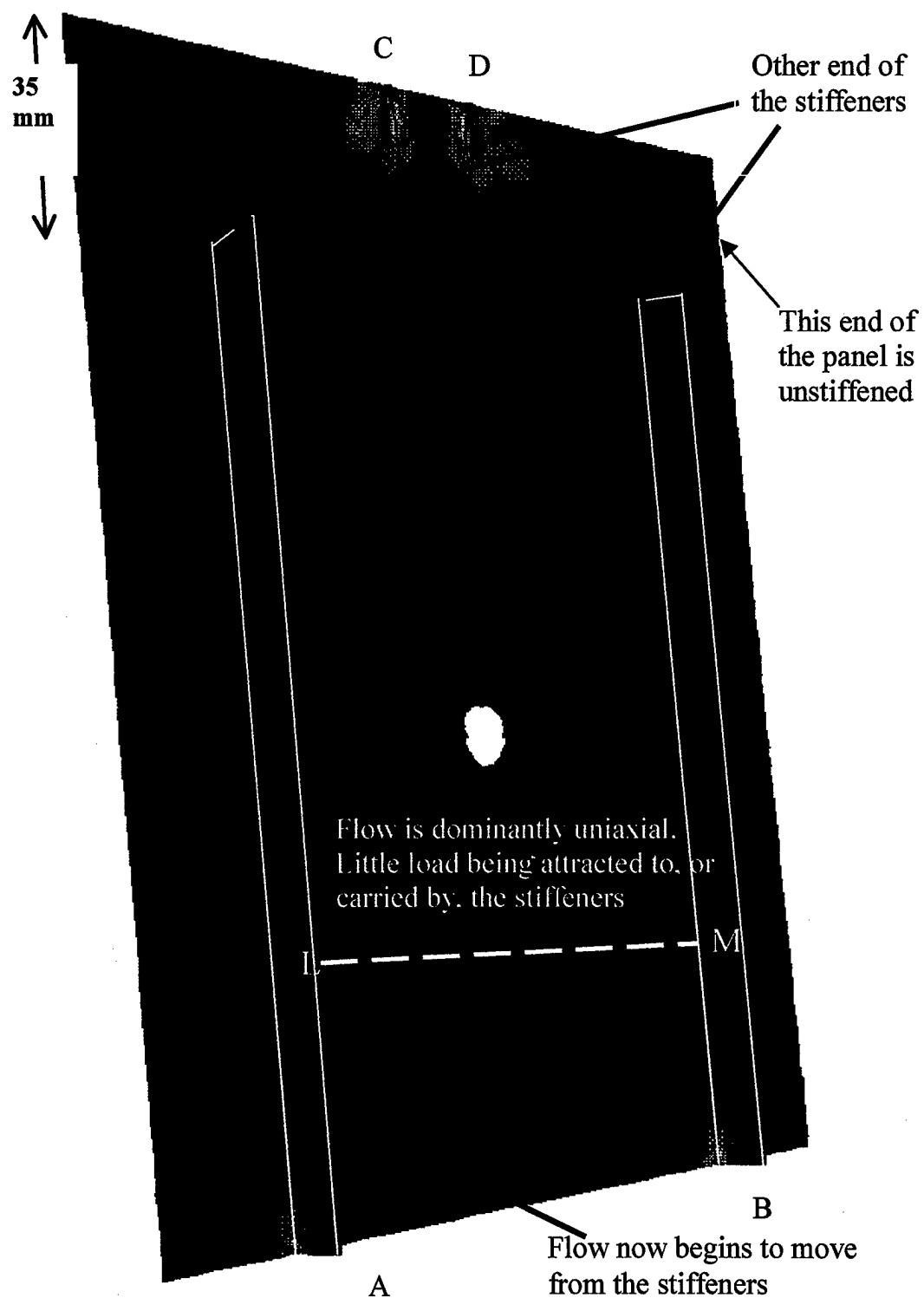


Figure 3.19. The normalised flow field in a rib stiffened panel.

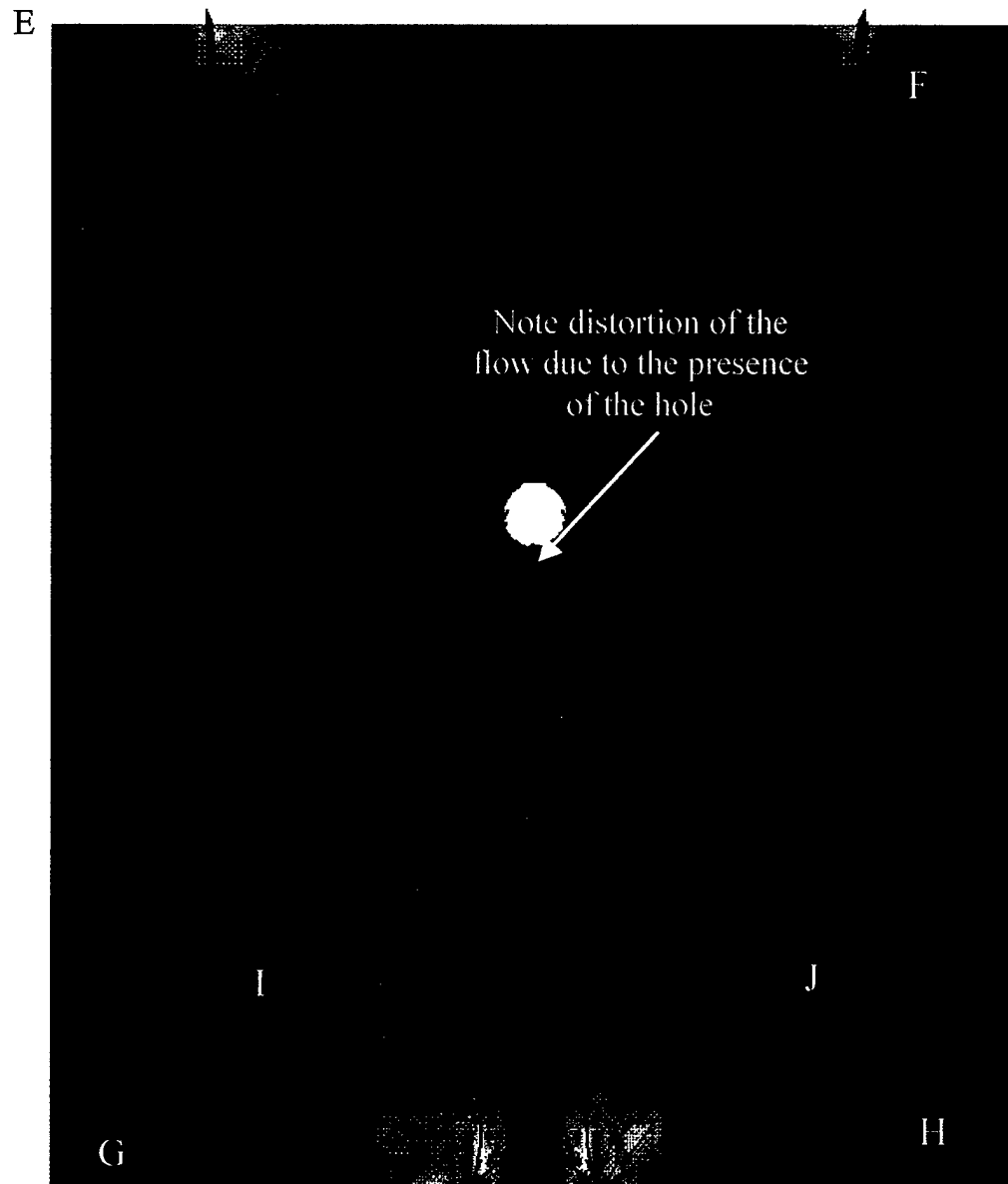


Figure 3.20. Plan view of the rib stiffened panel.

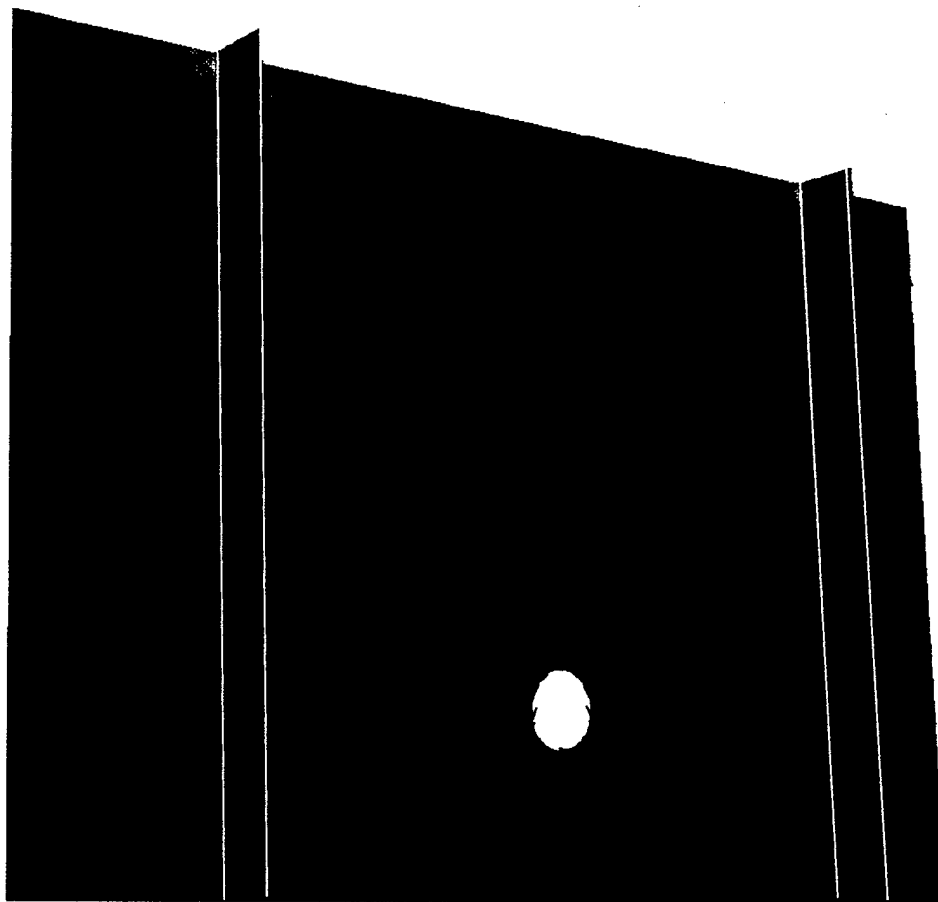


Figure 3.21 Detailed view of the flow from locations A and B into the skin.

Past the hole the flow field again becomes dominantly uni-axial as the disturbance caused by the hole disappears. The flow from the stiffener occurs close to the end of the skin, i.e. at points A and B. Away from this zone, which in Figure 3.20 is approximated by the line L M, the stiffener has little effect on the flow in the panel, which is dominantly axial. Thus, if the crack is contained between the stiffeners and has a reasonable edge distance from the stiffeners, then as a first approximation the stiffeners can be ignored, except for estimating the local bending effects, when estimating the residual strength of repaired rib stiffened panels. Of course if the stiffener was broken one would have to account for the increased stress levels in the panel.

The precise fashion in which the load/energy flows from the stiffeners, at ends I and J, to points C and D can be seen in Figures 3.19, and 3.20. More detailed views of this region are given in Figure 3.22 and 3.23. Indeed, Figure 3.23 clearly highlights the flow in the stiffener, which is dominantly axial until near the ends, i.e. points I and J, where there is a small recirculation zone.

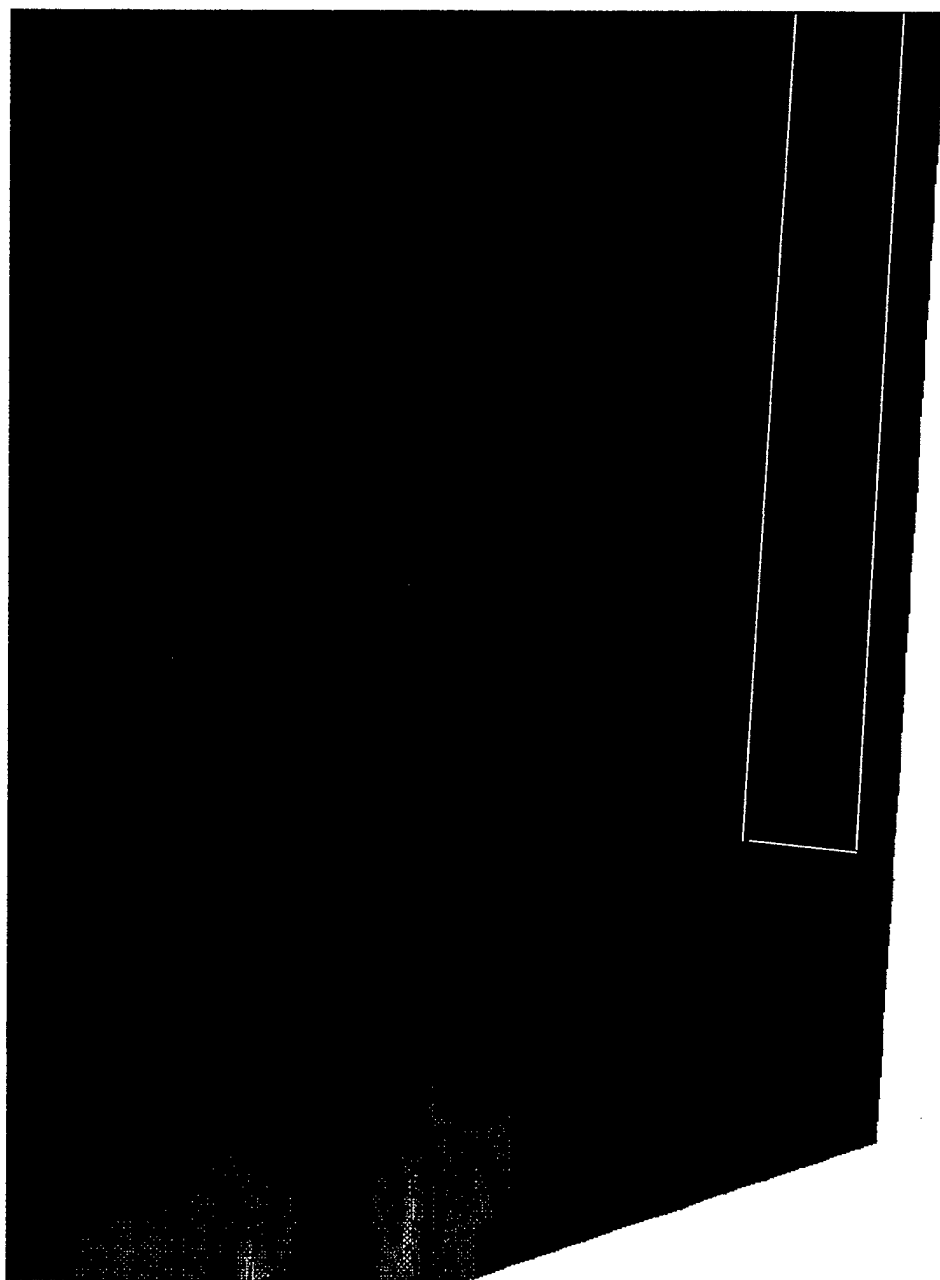


Figure 3.22. The normalised flow field in a rib stiffened panel.

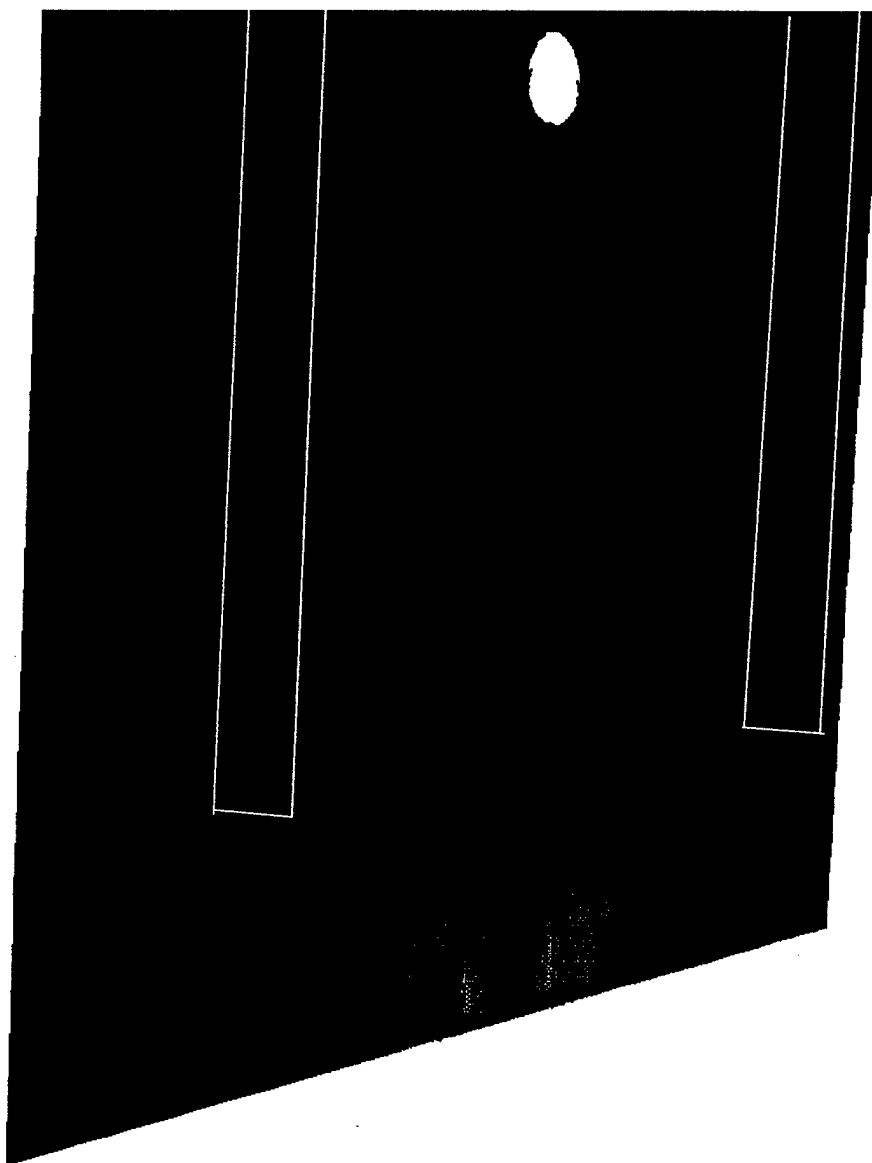


Figure 3.23 The normalised flow field in a rib stiffened panel.

This study has implications for the experimental test program. In this test program it is proposed to load via the skin. We are thus faced with the realisation that, other than bending effects, the stiffener will only marginally effect the load distribution in the skin. Thus the prime role of stiffeners will be to induce bending, due to the shift in the neutral axis.

This study supports/explains the previous numerical findings on the stress intensity factors associated with repaired cracks in rib stiffened (wide) panels where the stiffeners have been found to have little effect.

### 3.6 Simple analytical formulae for predicting the limiting behaviour

The finite element result would indicate that as a first approximation the simple analytical formulae for the case when bending was allowed but the stiffeners were

ignored can be used to obtain a first estimate of the limiting stress intensity factors ( $K_{\infty}$ ) for composite repairs to cracked rib stiffened panels.

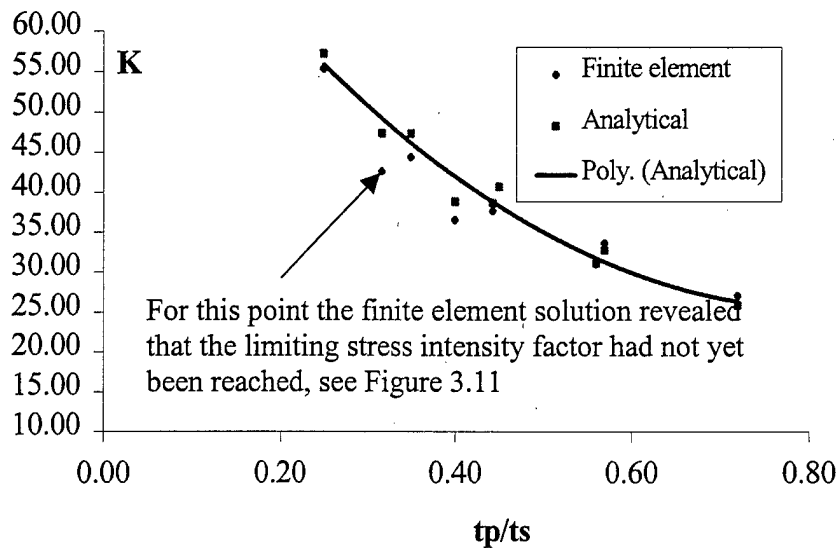


Figure 3.24: Comparison of analytical and finite element values of  $K_{\infty}$ .

Table 3.6: Comparison of prediction for bending problems, Case 3.

$K_{\infty}$ MPa√m	Edge Centre	a mm	$t_p$ mm	$E_p$ MPa	$t_r$ mm	$G_r$ MPa	$t_a$ mm	$G_a$ MPa	$\sigma$ MPa	X mm	B mm
	Centre	80	2.5	71000	1	208000	.25	375	158	200	200
predictd	35.6										
f.e.	c.f. 33.9 for a 50 mm deep stiffener. c.f. 38.3 for a 12 mm deep stiffener.										

Table 3.7: Comparison of prediction for bending problems, Case 3.

$K_{\infty}$ MPa√m	Edge Centre	a mm	$t_p$ mm	$E_p$ MPa	$t_r$ mm	$G_r$ MPa	$t_a$ mm	$G_a$ MPa	$\sigma$ MPa	X mm	B mm
	Centre	40	3.16	71000	1	208000	.25	375	158	200	200
predictd	48.3										
f.e.	c.f. 41.9 for a 50 mm deep stiffener. c.f. 46.2 for a 12 mm deep stiffener. A f.e. analysis found that this value asymptotes to 47.4 as the stiffener depth approached zero.										

The accuracy of this approach can be seen in Figure 3.24 which compares the values of  $K_{\infty}$  with the value predicted using the formulae given in Section 1. This dramatically simplifies the analysis and design methodologies. In this figure the cases presented are as given in Table 3.5. In general the maximum magnitude of the differences between this simple approach and the finite element results was approximately 10%. This can be seen from Tables 3.6 and 3.7.

The accuracy of this fit can be improved by allowing for the effect of the stiffener in equation (8). In this fashion it is proposed to replace equation (8) by the following expression

$$BC = a y_{max} (1 - K_p / K_s) (t_p + t_r) / F \quad (28)$$

Where  $F = F(I, I_s)$  where  $I_s$  is the  $I$  of the stiffener. One simple form under evaluation takes the form

$$F = I + \alpha I_s \quad (29)$$

Where  $\alpha$  is a constant to be determined from the numerical results. This improved formulae will be presented in the next section

### 3.7 Effect of riveted stiffeners

As part of further improvements to the CalcuRep project, the effect of riveted stiffeners on the stress intensity factors for single sided repairs to an aluminium substrate was investigated. The data presented in Section 3 of Chapter 3 was analysed to explain what the addition of the riveted stiffeners had on the limiting stress intensity values of the repaired skin.

For the geometry shown in Figure 3.25, the addition of the riveted stiffeners significantly increases the second moment of area ( $I$ ) of the panel cross section. For the range of geometries used in this study, the increase in  $I$  of the total section of between 80 to 1900 times the skin sections without stiffeners.

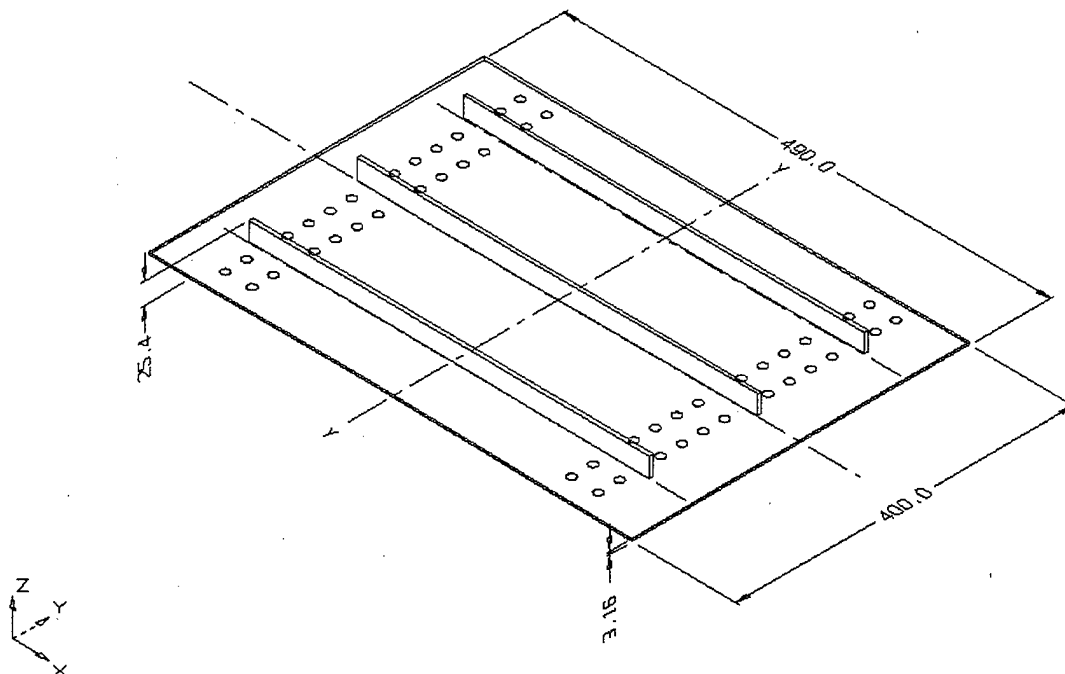


Figure 3.25 Schematic of rib stiffened panel geometry showing how stiffener depth would significantly increase the second moment of area ( $I$ ) of the cross section.

In almost all cases and geometries considered thus far, results of numerical analyses of these panels have shown that stress intensity factor in a repaired skin has almost reached its limiting value for crack length above 40mm in length. Therefore, the stress

intensity values for the various geometries at a crack length of 40mm were used to compare with the estimates obtained using the analytical closed form solution shown in equation (30).

## Results

Figures 3.26 and 3.27 show the relationship that exists between the second moment of area and the percentage change in the stress intensity for the repaired skins. These results clearly show that for a given stiffness ratio (patch to skin), the change in the stress intensity factors with increasing moment of area ( $I$ ) is between 5 and 25%. Stiffness ratios less than 1 are rarely used and can therefore be ignored for the purposes of modelling the behaviour using closed form solutions. If we consider more realistic stiffness ratios of between 1 and 1.2, the limiting analytical solution obtained using  $K^*$  for a repaired plate without a stiffener is approximately 2 to 10% larger than that obtained for a rib stiffened plate. For a particular stiffness ratio, the difference increases with increasing second moment of area although the rate of change of  $K$  with  $I$  is less marked at the higher values (i.e. very deep stiffeners (37.5 and 50mm)).

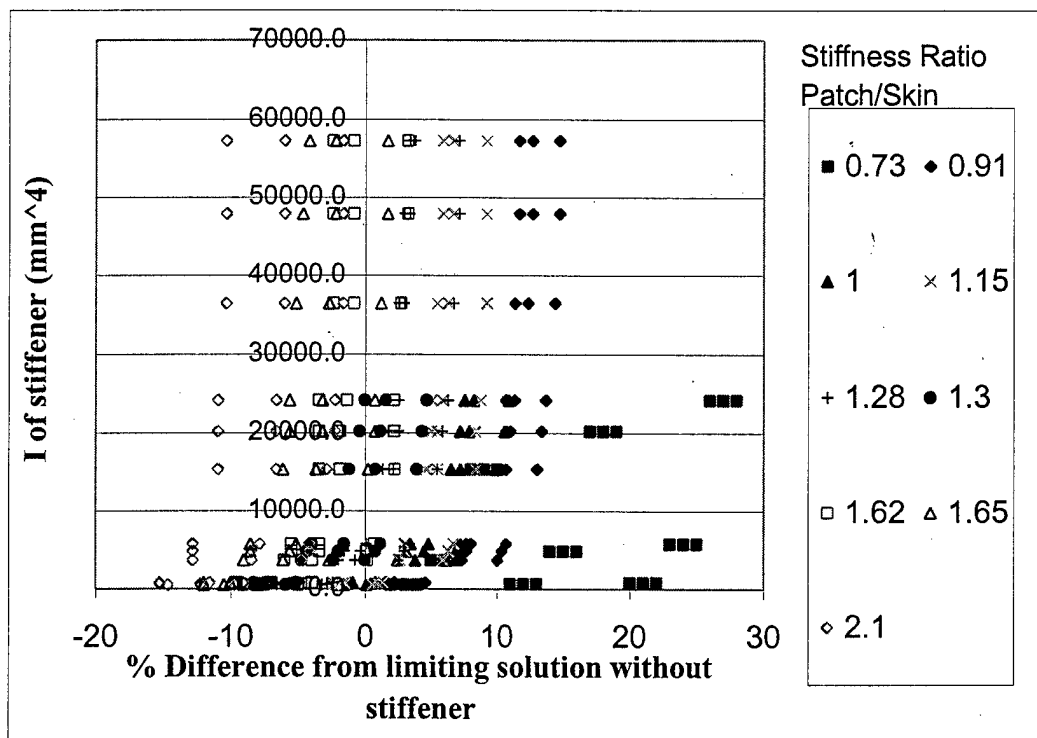


Figure 3.26 Plot showing differences in the value of  $K$  expressed as percentage differences in numerical analysis from closed form solution for a range of stiffness ratios and second moment of areas ( $I$ ).

The relationship between  $I_s$  and difference in  $K$  (which we will call the stiffener correction factor, SCF) for the single sided repairs was derived by fitting logarithmic curves to the data, see Figure 27. From these fits, a table of coefficients was formed, see Table 3.8.



$$SCF = \frac{\left( P \times \ln(10^{12} I_s) - Q \right)}{10^{14}} \quad (31)$$

to determine the size of changes required to the "Bending correction factor" described in equation (31). The new bending correction factor accounts for the contribution of stiffener second moment of area ( $I_s$ ) and enables a more accurate representation of the stress intensity factor for the repaired skin. In this table the data is defined according to the patch to skin stiffness ratio  $E_r t_r / E_p t_p$ .

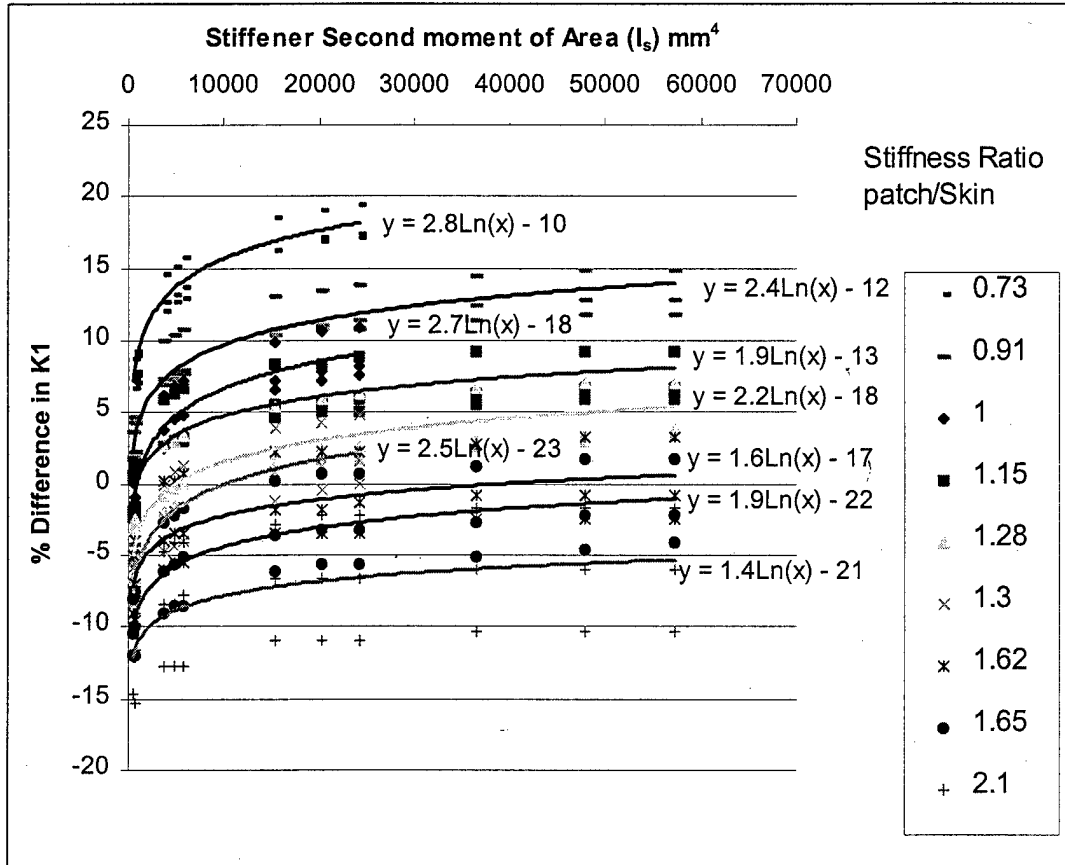


Figure 3.27 Plot of percentage difference in the value of  $K_{IC}$ , defined as  $y$ , of numerical analysis from closed form solution  $v$ 's  $x$ , the second moment of areas ( $I_s$ ) for a range of stiffness ratios.

The new "bending correction factor"  $BC$ , which included stiffener effects, for rib stiffened panels was thus determined to be :

$$BC = \frac{a y_{\max} \left( 1 - \frac{K_p}{K_s} \right) (t_p + t_r)}{I + SCF} \quad (32)$$

where  $I$  is the  $I$  of the unstiffened panel and repair.

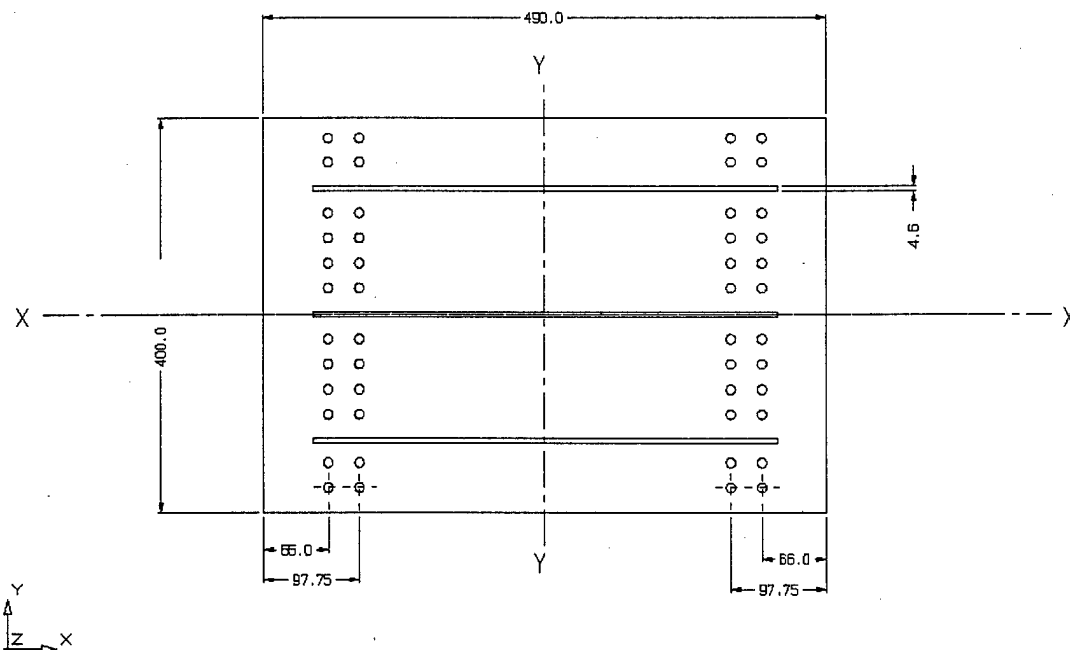
The application of this bending correction factor for the geometries analysed reduces the errors in estimation using the closed form solution (CalcuRep\*) to less than 3%. This fit has been validated by comparison with ~2400 different geometrical cases.

Table 3.8 Table of coefficients "P" and "Q" for given stiffness ratios to calculate stiffener correction factor (SCF) with varying  $I_s$ .

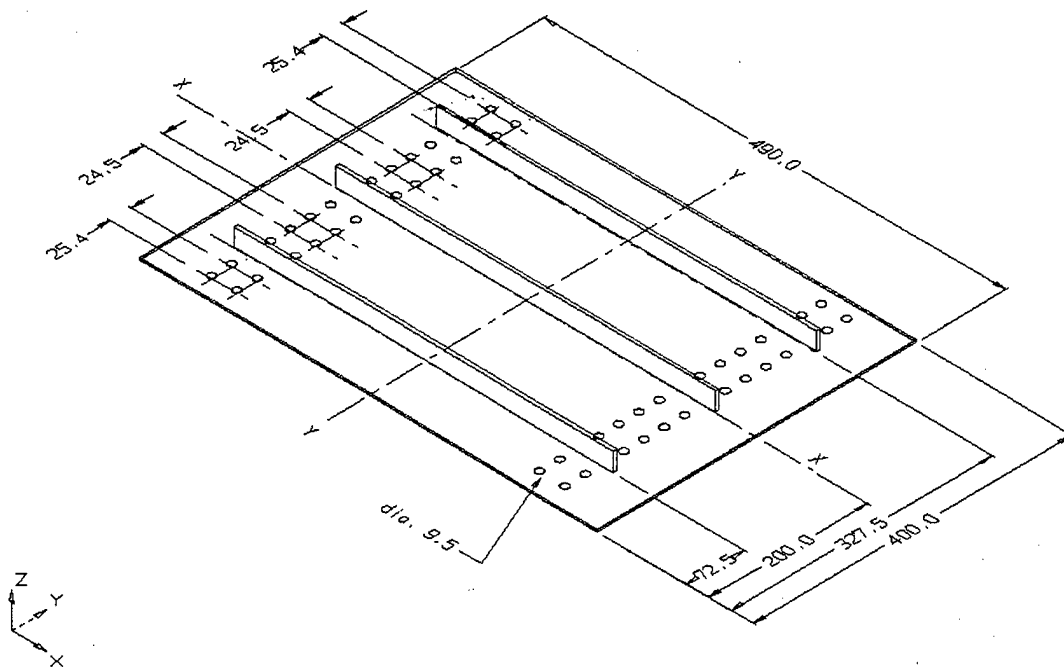
Stiffness ratio $E_{rt}/E_{ptp}$	"P"	"Q"
0.73	2.8	10
0.91	2.4	12
1	2.7	18
1.15	1.9	13
1.28	2.2	18
1.3	2.5	23
1.62	1.6	17
1.65	1.9	22
2.1	1.4	21

#### 4. THE EXPERIMENTAL TEST PROGRAM

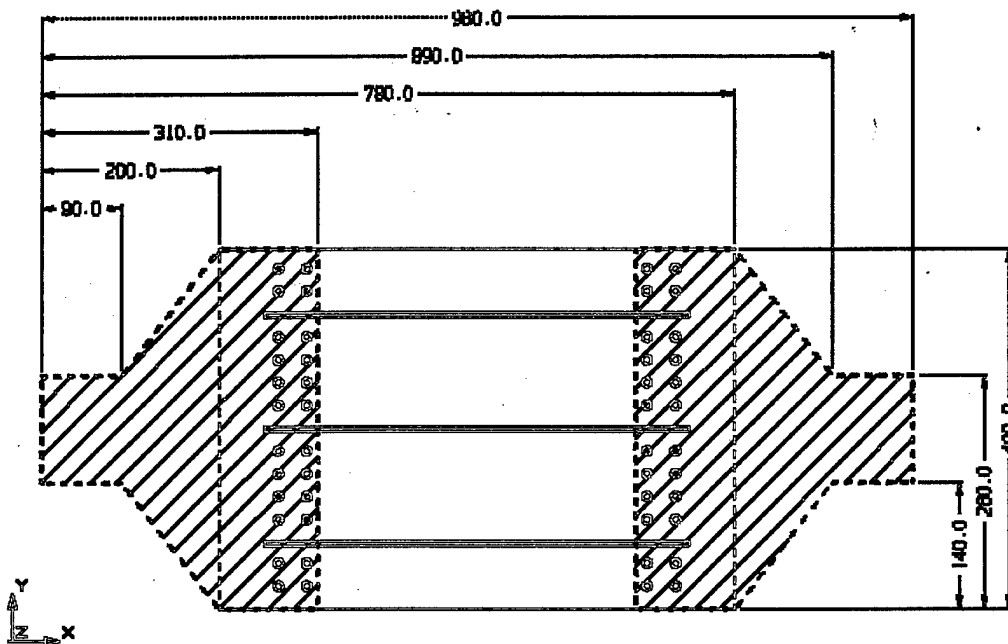
For the experimental program it was initially proposed that we standardised by using essentially the same configuration as used in [19], see Figures 4.1a)-4.1c). However, these test specimens would have riveted stiffeners and not integral stiffeners as in [14]. The cracks were to be cut into the skin of each specimen prior to fabrication. The patch would then be bonded on the external surface of each specimen following fabrication as this will speed up the test program.



(a) Plan view of wide panel test specimen



(b) Dimensions of the wide panel test specimen



(c) View showing end fittings

Figure 4.1 a)-c) Schematic representation of the initial wide panel test geometry

Table 4.1 Specimen Identification

Specimen Number	Skin Thickness (mm)	Initial crack size (mm)	Stiffener broken/unbroken
1	1.25	40.0	unbroken
2	1.25	40.1	unbroken
3	1.25	40.14	broken
4	1.25	40.06	unbroken
5	1.25	40.24	broken
6	1.25	40.15	broken
7	1.25	20.06	unbroken
8	4.15	41.42	broken
9	4.15	40.0	unbroken
10	4.15	19.93	unbroken
11	4.15	40.19	unbroken
12	4.15	40.01	broken
13	4.15	40.03	unbroken
14	4.15	40.06	broken
15	4.15	20.01	unbroken
16	4.15	19.99	unbroken

The thick, 4.15mm, skin panels had 12 ply thick patches, i.e. ~ 1.52mm.

The thin, 1.25mm, skin panels had 4 ply thick patches, i.e. ~0.50 mm.

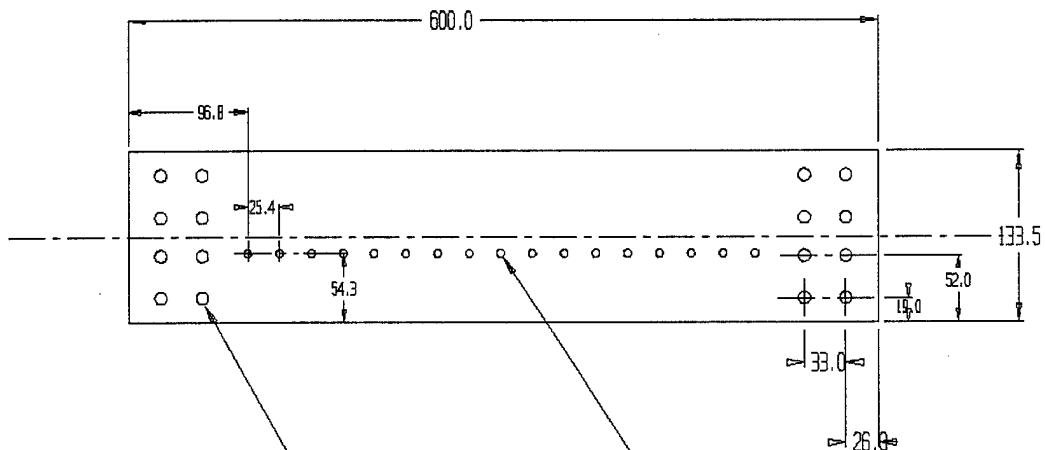
For 40mm cracks the patches were 90mm wide and 280mm long.

For 20mm cracks the patches were 70mm wide and 250mm long.

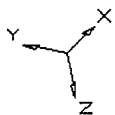
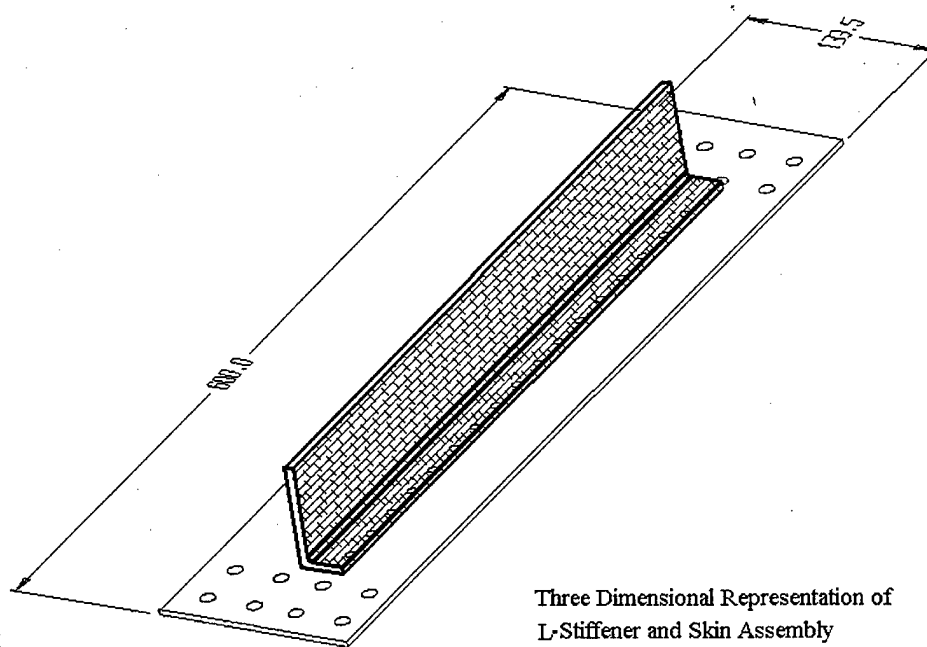
Table 4.2 Specimen Configuration

Skin thickness (mm)	Stiffener dimensions (mm)		
	width	depth	thickness
1.25	23	50	2.2
4.16	25	50	5.

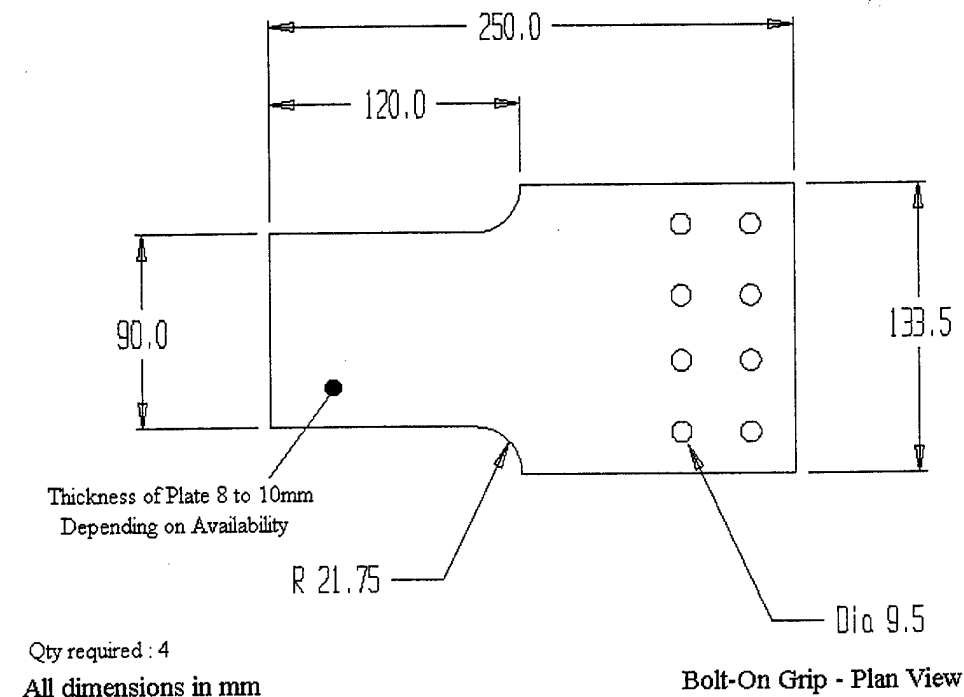
Following the June 99 meeting with the USAF it was decided to adopt a narrower test specimen, see Figure 4.2. These specimens were manufactured in Holland. An outline of the proposed test spectra and the specimen configurations are given in Tables 4.1 and 4.2. In each case the loads applied to the specimens were chosen to give a peak stress in the skin, when the stiffener was intact, of 120 MPa. The specimens were fatigue tested, under constant amplitude loading, in a 500 kN servo-hydraulic MTS fatigue testing machine with a load spectra of  $\sigma_{\max} = 120$  MPa and  $\sigma_{\min} = 6$  MPa, i.e. an R ratio  $R = \sigma_{\min} / \sigma_{\max} = 0.05$ .



All dimensions in mm



a) View of the narrow panel test specimen geometry

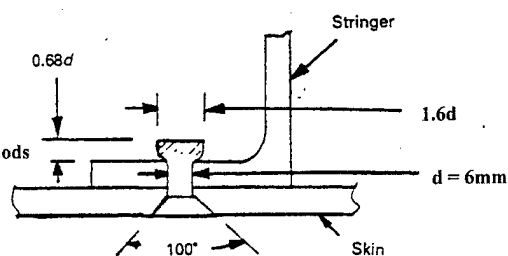


### b) Details of the end fittings

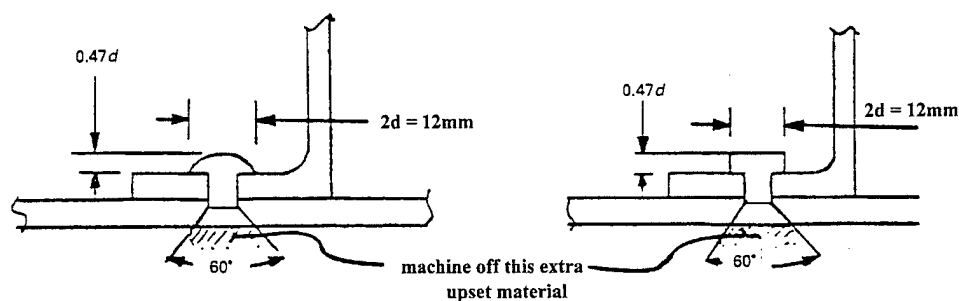
#### Conventional riveting

#### Rivet Detail

First preference is to use the NACA method  
Second option is to use conventional riveting methods



#### NACA riveting



### c) Details of the rivet configuration

Figure 4.2 Schematic representation of the proposed narrow panel test geometry

#### 4.1 Alteration to the narrow panel specimen design

During pre-cracking of the thinner (1.25mm) rib stiffened panels, large cracks were observed to initiate from the rivet holes closest to the end grips, see Figure 4.3. This occurrence arose as a result of localised bending effects induced by the offset of the neutral axis. Remedial measures were taken on the remaining thin and thick specimens. To reduce the stress concentration at this location tapered aluminium doublers were introduced, in the vicinity of the grips, and the ends of the vertical stiffeners were tapered, see Figure 4.4. The aluminium doublers were bonded onto the aluminium skin using a room temperature cure epoxy adhesive. These actions inhibited the development of cracks at the first few rivet holes.

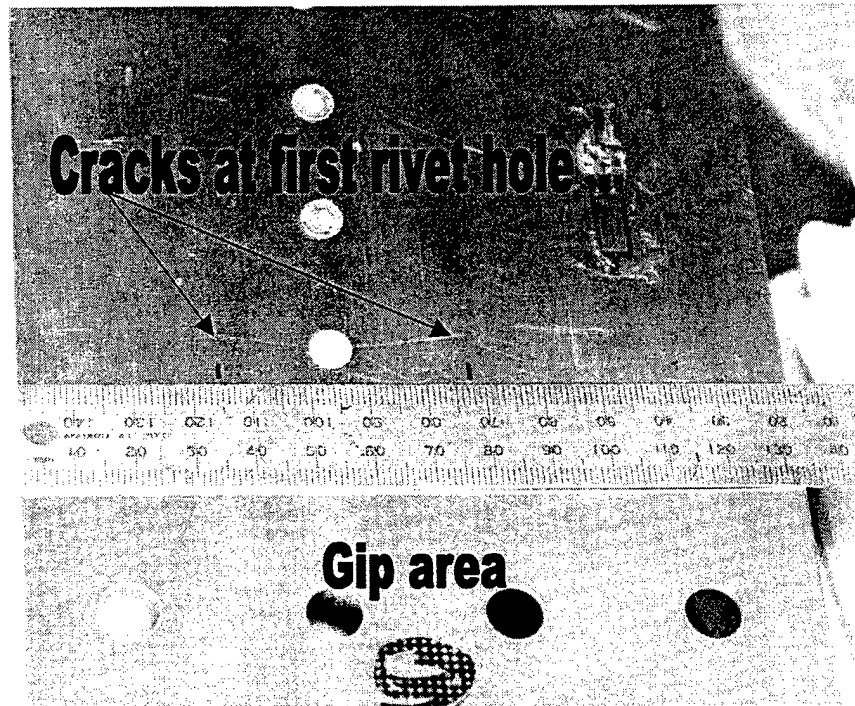


Figure 4.3 Photograph of a 40mm long crack forming from the first rivet hole in a thin skinned specimen with an unbroken stiffener and a 20mm saw cut in the skin

#### 4.2 Summary of Test Program

Two different specimen configurations were tested, see Tables 4.1 and 4.2, viz:

Case 1: The first test case evaluated had a skin thickness of ~1.25 mm and a width of 133mm. The stiffener was 50 mm deep, 2.2mm thick and the upper flange was 23mm wide. The area of the skin  $A_p$  was thus:

$$\begin{aligned} A_p &= [133 \cdot 10^{-3} \text{ m}] \times [1.25 \cdot 10^{-3} \text{ m}] \\ &= 1.665 \cdot 10^{-4} \text{ m}^2 \end{aligned}$$

For this test configuration the cross sectional area of the stiffener  $A_s$  was

$$\begin{aligned} A_s &= [50 \cdot 10^{-3} \text{ m}] \times [2.2 \cdot 10^{-3} \text{ m}] + [23 \cdot 10^{-3} \text{ m}] \times [2.2 \cdot 10^{-3} \text{ m}] \\ &= 1.606 \cdot 10^{-4} \text{ m}^2 \end{aligned}$$

$$\begin{aligned}\text{Total Area } (A_t) &= [1.862 \cdot 10^{-4} \text{ m}^2] + [1.606 \cdot 10^{-4} \text{ m}^2] \\ &= 3.468 \cdot 10^{-4} \text{ m}^2\end{aligned}$$

This gave a total cross sectional Area ( $A_t$ ) of  $3.271 \cdot 10^{-4} \text{ m}^2$ . In this case the maximum  $F_{\max}$  force needed to be applied was

$$F_{\max} = \sigma \times A_t = 39.5 \text{ kN}$$

The fatigue test program was performed with an R ratio of 0.5. Consequently, the loads applied in the fatigue test were  $F_{\min} = 1.96 \text{ kN}$  and  $F_{\max} = 39.5 \text{ kN}$ . The exception to this was the first test specimen where the minimum and maximum loads applied were  $F_{\min} = 2.0803 \text{ kN}$  and  $F_{\max} = 41.6 \text{ kN}$  respectively. In this case the stress amplitude, rather than the maximum stress, was  $\sim 120 \text{ MPa}$ .

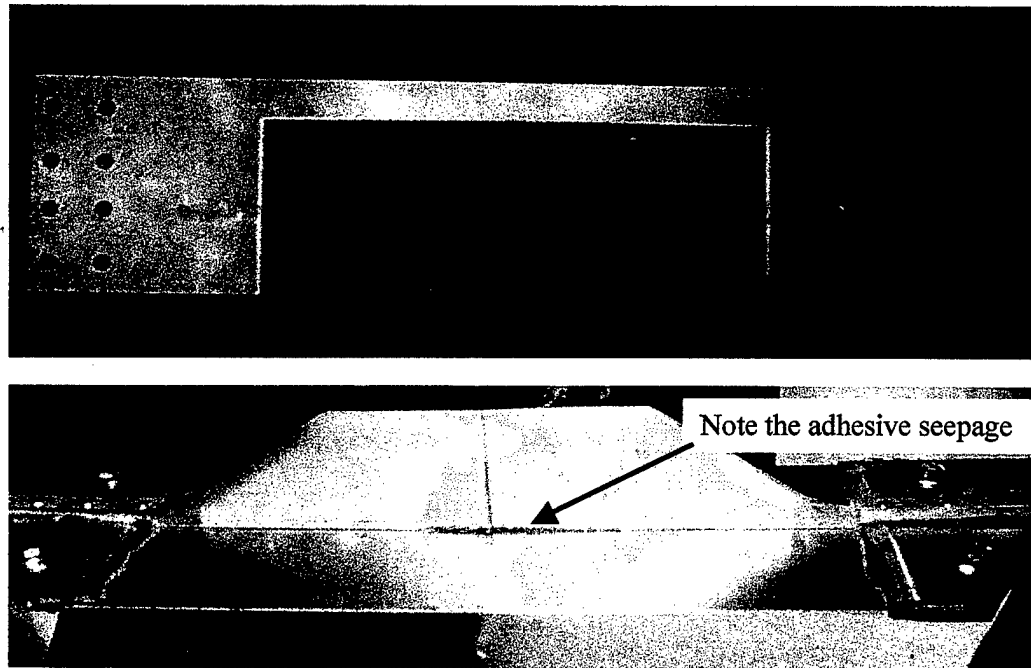


Figure 4.4 View of patched surface and underside of the test configuration with cracked stiffener, note adhesive seepage causing the stiffener to be bonded to the skin.

Case 2: The second test case had a skin thickness of 4.2 mm and a width of 133mm. The stiffener was 50 mm deep, 5mm thick and the upper flange was 25mm wide. The area of the skin  $A_p$  was thus

$$A_p = [133 \cdot 10^{-3} \text{ m}] \times [4.15 \cdot 10^{-3} \text{ m}] = 5.519 \cdot 10^{-4} \text{ m}^2$$

For this test configuration the cross sectional area of the stiffener  $A_s$  was

$$\begin{aligned}A_s &= [50 \cdot 10^{-3} \text{ m}] \times [5 \cdot 10^{-3} \text{ m}] + [25 \cdot 10^{-3} \text{ m}] \times [5 \cdot 10^{-3} \text{ m}] \\ &= 3.75 \cdot 10^{-4} \text{ m}^2\end{aligned}$$

this gave a total cross sectional Area ( $A_t$ ) of  $9.27 \cdot 10^{-4} \text{ m}^2$ . In this case the maximum force  $F_{\max}$  needed to be applied was:



$$F_{\max} = \sigma \times A_t = 111.2 \text{ kN}$$

The fatigue test program was performed with an R ratio of 0.5. Consequently, the loads applied in the fatigue test were  $F_{\min} = 5.56 \text{ kN}$  and  $F_{\max} = 111.2 \text{ kN}$

### 4.3 Test results

Case 1: From the results for specimen number 2, see Figure 4.5, which had an intact stiffener and was tested under a stress amplitude of 120 MPa, we found that the crack growth rate was constant and that

$$da/dN = 5.578 \cdot 10^{-4} \text{ mm/cycle} = 21.96 \cdot 10^{-6} \text{ in/cycle}$$

In this case from the results<sup>2</sup> given in [22], page 8.9-84, for an R ratio of 0.02 and a plate thickness of between 0.02" to 0.2", we found that the experimental crack growth rate corresponds to an (experimental) value of  $\Delta K \sim 11 \text{ MPa } \sqrt{\text{m}}$ . This compares quite favourably with the values of  $\Delta K$  of 12.2 MPa  $\sqrt{\text{m}}$ , obtained using the semi-analytical formulae, and values of 11.4 MPa  $\sqrt{\text{m}}$ , for a 14mm long crack, and 12.6 MPa  $\sqrt{\text{m}}$ , for a 40mm long crack, obtained using 3D finite element analysis.

For the subsequent tests the stress amplitude was  $\sim 114 \text{ MPa}$ . The growth rate again was constant and  $da/dN \sim 3.72 \cdot 10^{-4} \text{ mm/cycle}$ . The experimental crack growth rate corresponded to an (experimental) value of  $\Delta K \sim 10.0 \text{ MPa } \sqrt{\text{m}}$  compared with a predicted value of 11.6 and 10.9 MPa  $\sqrt{\text{m}}$  and 12.04 MPa  $\sqrt{\text{m}}$ , obtained using 3D finite element analysis, for a 14mm long crack and a 40 mm long crack respectively.

When the stiffener was broken the stress in the skin under the stiffener increased from 120 MPa to  $\sim 238 \text{ MPa}$ . In this case we obtained a predicted value of  $\Delta K$  of 23.9 MPa  $\sqrt{\text{m}}$ , obtained using the semi-analytical formulae, and values of 21.9 MPa  $\sqrt{\text{m}}$ , for a 14 mm long crack, and 22.6 MPa  $\sqrt{\text{m}}$ , for a 40 mm long crack, were obtained via a 3D finite element analysis.

The experimental test results were quite repeatable, see the data for specimens 3, 5 and 6 as given in Figure 4.7. For specimens 3 and 6 we again obtained a constant growth rate with a  $da/dN$  of  $\sim 2.4 \cdot 10^{-3} \text{ mm/cycle}$ , whilst for specimen 5 we obtained a growth rate of  $\sim 2.0 \cdot 10^{-3} \text{ mm/cycle}$ . In this case using the results given in [22] this growth rate gave a  $\Delta K$  of  $\sim 22.3 \text{ MPa } \sqrt{\text{m}}$ , for specimens 3 and 6, and  $\sim 20.5 \text{ MPa } \sqrt{\text{m}}$  for specimen 5. These values are in good agreement with the numerical predictions.

During the fatigue tests it was found that failure generally initiated at rivet holes outside of the patched area. The location of the initiation site was essentially random and appeared to associated with the initial fabrication of the specimen. Indeed, specimen 7 failed outside of the test area without any crack growth under the patch and specimen 1 failed outside of the test area with minimal crack growth under the patch, see Figure 4.6. In the latter case the growth rates were distorted by the extensive cracking occurring outside of the patch.

<sup>2</sup> In this case the growth law can be approximated as  $da/dn \cong 1.64 \cdot 10^{-9} (\Delta K)^{2.35}$

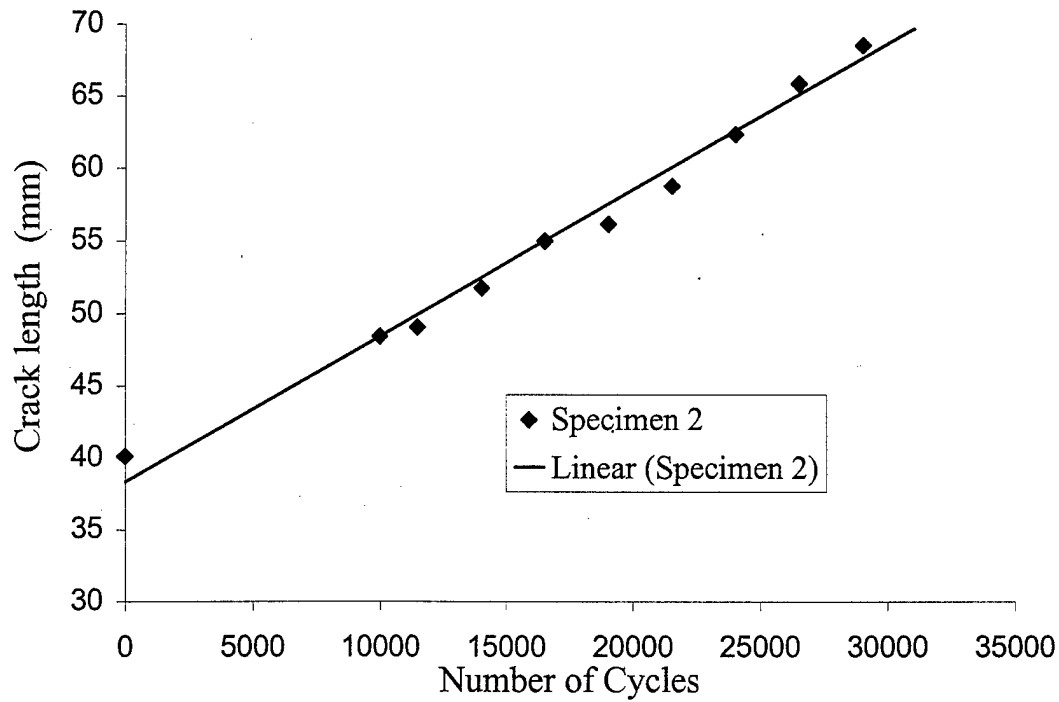


Figure 4.5. Crack growth for a 1.25mm thick skin specimen, number 2, with an intact stiffener, stress amplitude of 120 MPa

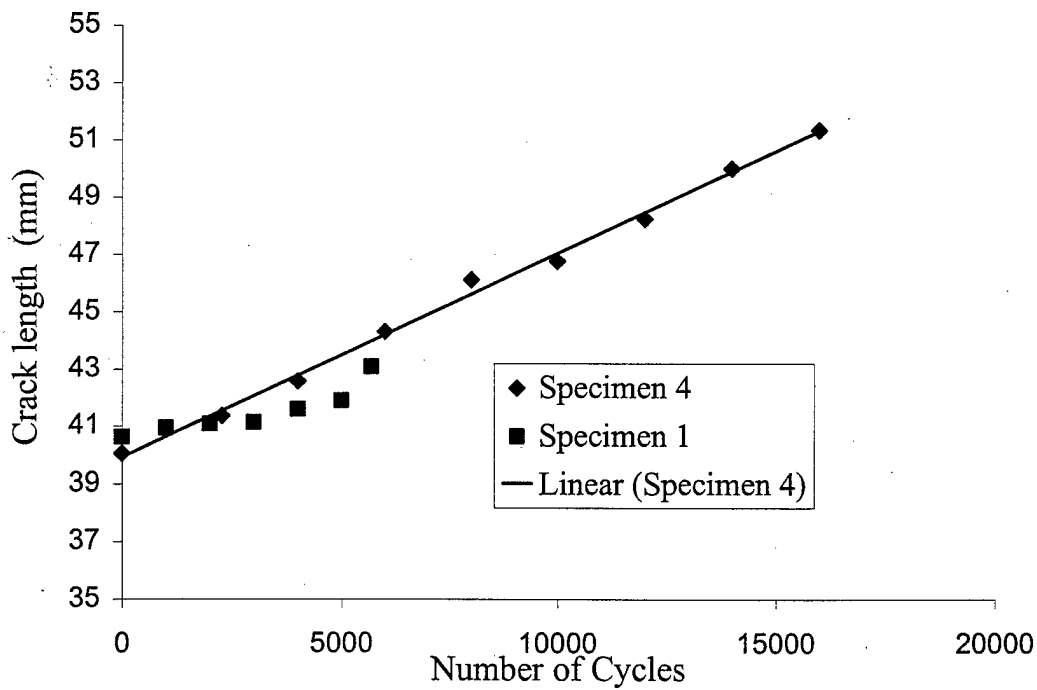


Figure 4.6. Crack growth for specimens 1 and 4, 1.25mm thick skin with an intact stiffener, max stress of 120 MPa

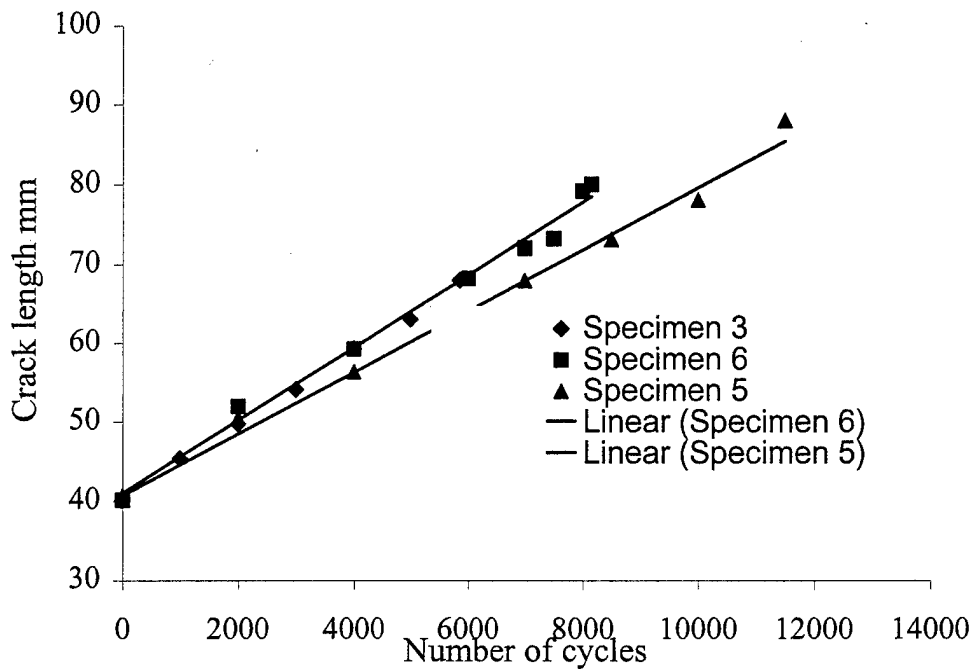


Figure 4.7 Crack growth for a 1.25mm thick skin specimen with a broken stiffener, specimens 3, 5 and 6.

Case 2: For the second test case the test specimens had a skin thickness of  $\sim 4.15\text{mm}$  and a stiffener thickness of  $5\text{mm}$ . Specimens with two initial crack lengths, viz: 20 and 40 mm, were tested. In both cases we (again) saw that when the crack was under the patch the crack growth rate was essentially constant, see the data for specimens 9, 10 and 15 in Figure 4.8. Indeed, as was expected the crack growth rates for both initial crack configurations were (essentially) identical and gave a growth rate of

$$da/dN \sim 8.2 \cdot 10^{-4} \text{ mm/cycle} \sim 32.4 \cdot 10^{-6} \text{ in/cycle}$$

For this plate thickness we obtain from the results given in [22], page 8.9-86, for an R ratio of 0.05 and a plate thickness of  $0.2''$ , i.e.  $\sim 5\text{mm}$ , which is close to the test configuration an experimental crack growth rate of  $\sim 32.4 \cdot 10^{-6} \text{ in/cycle}$  and a corresponding (experimental) value of  $\Delta K \sim 15.95 \text{ MPa } \sqrt{\text{m}}$ .

The present analysis predicts a value of  $\Delta K$  of  $17.1 \text{ MPa } \sqrt{\text{m}}$ , obtained using the semi-analytical formulae. Finite element analysis gave values of  $\sim 12.7 \text{ MPa } \sqrt{\text{m}}$  and  $15.6$  for a 14mm and a 40mm crack respectively. We thus see that the analytical formulae compare quite favourably with the experimental test results.

For specimens 11 and 13 there was extensive seepage of the adhesive through the fasteners with the result that the stiffener became completely bonded to the skin, see Figure 4.10. This meant that the crack growth rates for these specimens were dramatically reduced, see Figure 4.8, and could not be related to the simple formulae as the specimen configuration now differed substantially from the test requirement. However, the crack growth rates for both, modified, specimens were consistent and very similar, see Figure 4.8. The phenomena also occurred in specimens with a cracked stiffener, see Figure 4.4. However, in these cases the stiffener was not bridging the crack and as a result did not transmit load across the crack.

In contrast to the 1.2mm thick specimens the thicker (4.2mm) specimens generally failed due to crack growth under the repair, i.e. inside of the patched area.

When the stiffener was broken the stress in the skin under the stiffener increased from 120 MPa to ~204 MPa. The tests were extremely repeatable, see Figure 4.9, and it was found that crack growth rate was (again) constant with a  $da/dN \sim 4.1 \cdot 10^{-3}$  mm/cycle  $\sim 1.6 \cdot 10^{-4}$  in/cycle, from which we obtain a  $\Delta K$  of  $\sim 26$  MPa  $\sqrt{m}$ . It should be stressed that this value of  $\Delta K$  may have large error bounds since the data for this combination of crack growth rate, plate thickness and test frequency is very scarce. In this case we predicted a value of  $\Delta K$  of  $\sim 28.1$  MPa  $\sqrt{m}$ , obtained using the semi-analytical formulae for a long crack. This compared well with the results of a three dimensional finite element analysis which gave values ranging from 19.9 MPa  $\sqrt{m}$ , for a 14 mm long crack, to 22.4 MPa  $\sqrt{m}$ , for a 40 mm long crack. This configuration had the largest discrepancy between the analytical and the finite element results.

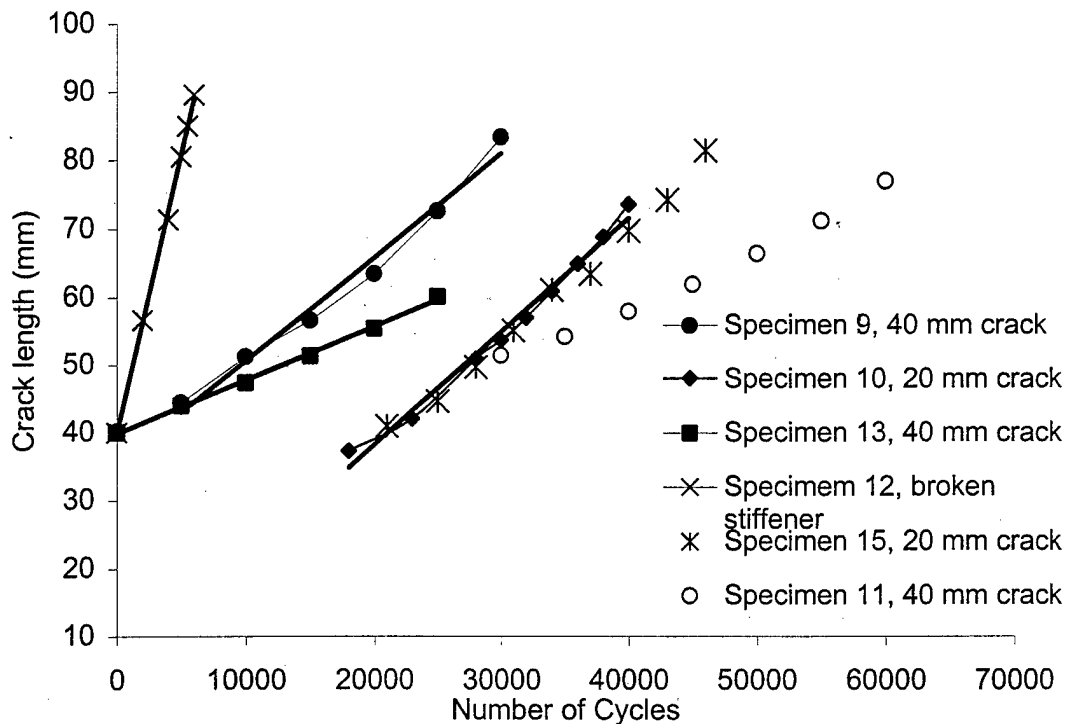


Figure 4.8 Crack growth for 4.2mm thick skin specimens with an intact stiffener

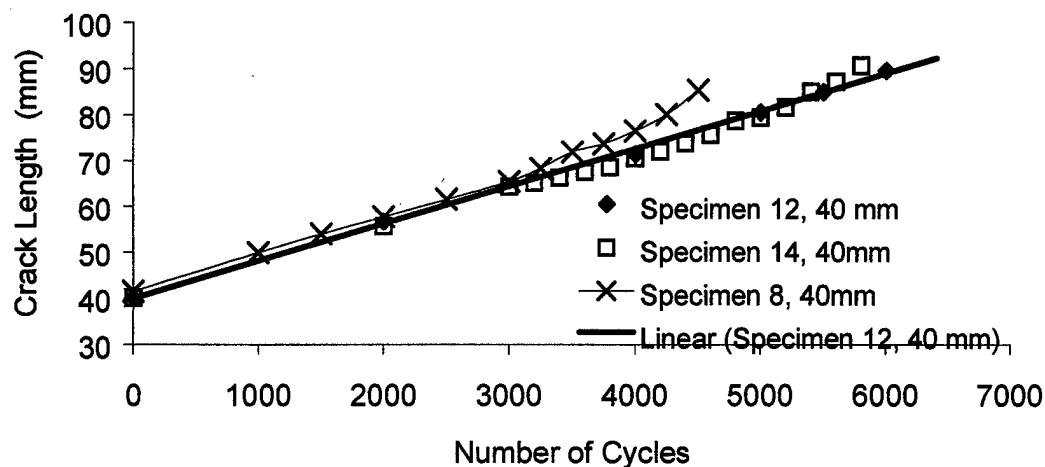


Figure 4.9 Crack growth for 4.2mm thick skin specimens with a broken stiffener

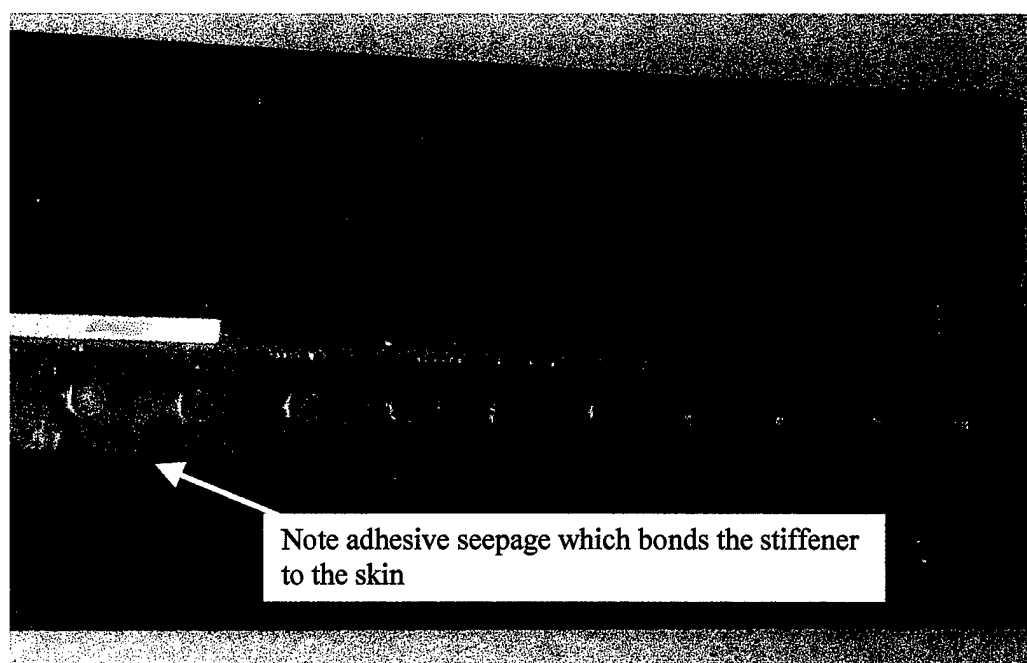


Figure 4.10 Close up of adhesive seepage, showing stiffener bonded to the skin.

#### 4.4 Failure surface

For the thin skinned specimens neither the patch or adhesive failed at any stage during the tests. This was also true for those thicker (4.15 mm) skinned specimens which had an unbroken stiffener, even when the crack grew across the full width of the specimen. For the thicker skinned specimens which had a broken stiffener it was found that when the crack grew across the full width of the specimen the patch system failed in a complex fashion, reminiscent of that described in Section 2.2, in that the first layer of the patch remained attached to the metal indicating that the failure involved interlaminar failure in the composite patch.

This can be seen by looking at the underside of the failed specimen shown in Figure 4.11. The adhesive used to bond the patch to the specimens was green in colour. Yet, as can be seen in Figure 4.11, the first ply of the patch is still largely attached to the skin and there are only small regions of green to be seen on the underside of the specimen. This (again) illustrates the need to consider interlaminar (intra-ply) failure when considering the load bearing capacity of the repair. In this picture the delaminated patch has been placed on the other side of the stiffener so as to show that after (interlaminar) failure the patch was still in one piece.

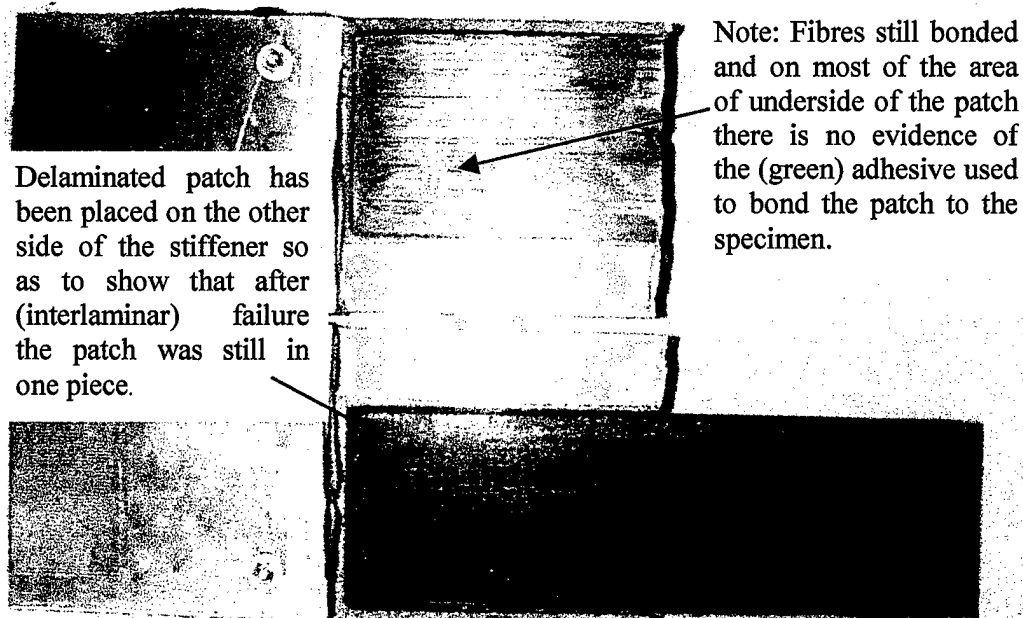


Figure 4.11 Close up of failure surface showing the first ply attached to the skin as well as the doubler being in a single piece after failure.

#### 4.5 Comments

This test program, when taken in conjunction with the results of a three dimensional finite element study of the test configuration(s), has confirmed that the semi-analytical formulae are capable of representing the behaviour of composite repairs to rib stiffened panels.

The test program has also shown that after patching the stress intensity factor rapidly asymptotes to a constant value, which is independent of crack length, so that the crack growth rate becomes constant and is independent of crack length. This phenomena is true regardless of whether the stiffener is broken or not. However, the absolute value of the stress intensity factor, and hence the growth rate, is dependent on the integrity of the stiffener, i.e. whether or not it is broken.

#### 5. EFFECT OF VARIABLE ADHESIVE THICKNESS

Until now we have assumed that the adhesive has a constant thickness. However, for field or depot level repairs the adhesive thickness may vary due to a variety of

application and/or fabrication related problems. The problem of variable adhesive thickness can be associated with:

- i) The inability to maintain an appropriate vacuum/pressure throughout the cure cycle;
- ii) A non-uniform temperature distribution over the region being heated. This can occur due to the presence of spars or ribs which may act as a heat sink.
- iii) Adhesive seepage through the fasteners;
- iv) Geometric discontinuities associated with the structure being repaired. The repair to the F111 wing pivot fitting [16] is a good example of such a problem;
- v) The use of low temperature cure adhesives.

Let us now address the problem of variable adhesive thickness. In this section we will show that the Glinka extension to the Hart Smith design formulae can be used for those cases when the adhesive thickness is not constant.

Before examining the inelastic behaviour of joints with variable adhesive thickness let us first consider the elastic response. Consider the joint as shown in Figure 5.1, the governing equations for this joint are:

$$T_{1,x} = \tau, \quad (33)$$

$$T_{2,x} = -\tau \quad (34)$$

and

$$u_1 - u_2 = t\gamma. \quad (35)$$

From Hooke's law for the adherends we find that:

$$T_1 = E_1 h_1 u_{1,x}, \quad (36)$$

$$T_2 = E_2 h_2 u_{2,x} \quad (37)$$

and for adhesive

$$\tau = G\gamma. \quad (38)$$

where  $E_{1,2}$  and  $h_{1,2}$  are Young's modulus and thicknesses of adherends,  $G$  and  $t$  are the shear modulus and thickness of the adhesive. Other parameters are as shown in Figure 5.1.

Let us consider the case when the adhesive thickness is variable i.e.  $t = t(x)$ . In this case equations (33) to (38) produce the resultant differential equation, viz:

$$(\gamma t)_{,xx} = \beta^2(x) \gamma t \quad (39)$$

$$\text{where } \beta^2(x) = \frac{G}{t(x)} \left( (E_1 h_1)^{-1} + (E_2 h_2)^{-1} \right)$$

In the case of a constant adhesive thickness equation (39) reduces to the well-known equation for the shear stress in adhesive, viz

$$\tau_{,xx} = \beta^2 \tau \quad (40)$$

where  $\beta^2 = \frac{G}{t} \left( (E_1 h_1)^{-1} + (E_2 h_2)^{-1} \right)$ .

For a constant thickness adhesive joint the concept of a characteristic length  $\lambda$  is commonly used. This distance  $\lambda$  is given by the formulae:

$$\lambda = 3/\beta \quad (41)$$

and represents the length of the adhesive playing the major role in the load transfer process transferring the loading.

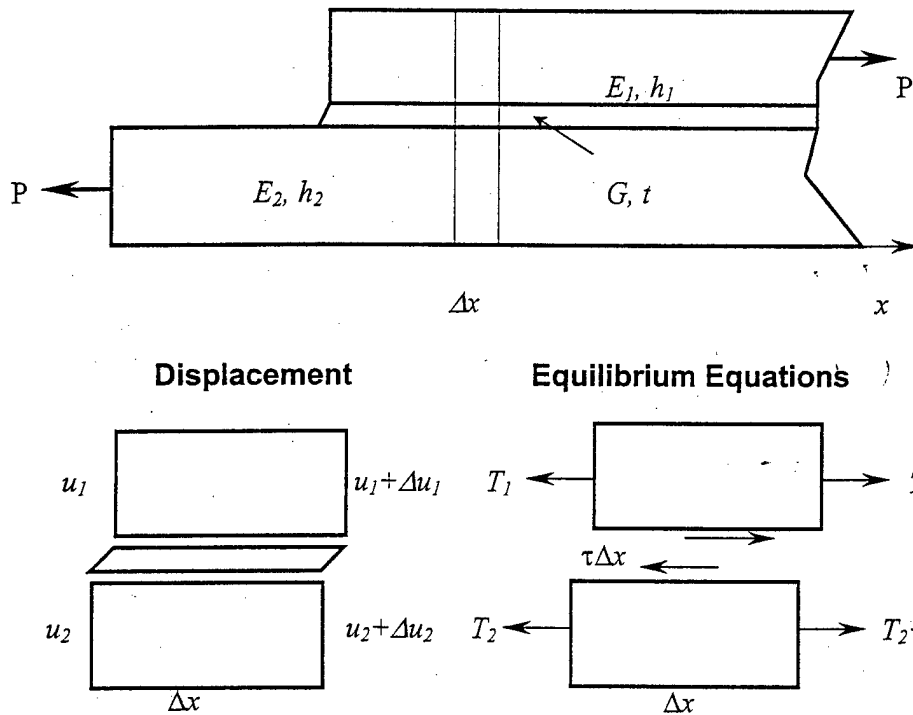


Figure 5.1 Schematic of the adhesive joint

### 5.1. Analytical solutions for variable adhesive thickness

Equation (39) has no a general analytical solution. However by using the transformation  $z = (\gamma t)_{,x} / \gamma t$  it can be reduced to the special Riccati equation [27]:

$$z_{,x} + az^2 = \beta^2(x) \quad (42)$$

with  $a = 1$ . This equation (14) can be solved for a wide class of function  $\beta(x)$ , particularly when this function has the form  $\beta^2(x) = bx^m$ .



Consider the following example. Let the adhesive thickness in the vicinity of the edge is distributed as  $t(x) = t_0 x^4$ . In this case  $\beta^2 = \beta^2(x)$  has the form

$$\beta^2(x) = b^2 x^{-4}, \quad (43)$$

$$\text{where } b^2 = \frac{G}{t_0} \left( (E_1 h_1)^{-1} + (E_2 h_2)^{-1} \right)$$

We thus require a solution to the following equation:

$$(\gamma t)_{,xx} = b x^{-4} \gamma t \quad \text{at} \quad x_0 \leq x \leq \infty \quad (44)$$

The solution of this equation results in the following expression for the adhesive shear stresses

$$\tau(x) = \frac{G}{t_0 x^3} (c \cdot \cosh(b/x) + a \sinh(b/x)) \quad (45)$$

The constants  $a$  and  $c$  in this solution can be found from the boundary conditions, which can be taken in the following form

$$\frac{P E_1 h_1}{E_1 h_1 + E_2 h_2} = \int_{x_0}^{\infty} \tau(x) \cdot dx \quad (46)$$

which represents the balance of forces acting on the adherends and

$$-\frac{P}{E_2 h_2} = (\gamma t)_{,x} \Big|_{x=x_0} \quad (47)$$

From the boundary conditions we find that

$$c = \frac{P E_1 h_1}{E_1 h_1 + E_2 h_2} b^2 \frac{t_0}{G} - \frac{P}{E_2 h_2} \quad (48)$$

and

$$a = \frac{-\frac{P}{E_2 h_2} + \frac{bc}{x_0} \sinh(b/x_0) - c \cdot \cosh(b/x_0)}{\sinh(b/x_0) - b/x_0 \cosh(b/x_0)} \quad (49)$$

In the special case when  $E_1 h_1 = E_2 h_2 = E h$  we have  $c = 0$  and

$$a = -\frac{P}{Eh} (\sinh(b/x_0) - b/x_0 \cosh(b/x_0))^{-1} \quad (50)$$

and the expression for the shear stresses becomes

$$\tau(x) = \frac{P}{Eh} \frac{G}{t_0 x^3} \frac{\sinh(b/x)}{b/x_0 \cosh(b/x_0) - \sinh(b/x_0)} \quad (51)$$

The criterion proposed by Hart-Smith for failure of adhesive joints can be written in the form

$$W_{\max} \leq W_{cr} \quad (52)$$

where  $W_{\max}$  is the maximum value of the strain energy density in the adhesive, and  $W_{cr}$  is the critical value for the energy determined from standard materials tests.

In this problem the maximum strain energy density occurs at the edge of the joint, i.e.  $x = x_0$ , where the shear stress

$$\tau(x_0) = \tau_{\max} = \frac{P}{Eh} \frac{G}{t_0 x^3} \frac{1}{b/x_0 \coth(b/x_0) - 1} \quad (53)$$

where  $\coth(b/x_0)$  is the hyperbolic cotangent.

Consider the case when the value of  $b/x_0 \gg 1$ , this corresponds to small changes of the thickness of the adhesive on the characteristic length of the stress distribution, then

$$\frac{1}{b/x_0 \coth(b/x_0) - 1} \approx \frac{x_0}{b} \quad (54)$$

In this limiting case the solution for  $W_{\max}$  reduces to

$$W_{\max} = \frac{1}{4} \frac{P^2}{Eh t_0 x_0^4} = \frac{1}{4} \frac{P^2}{Eht} \quad (55)$$

This formula, which is independent of the stress strain relationship for the adhesive, coincides with the maximum strain energy density for an adhesive with a constant equal to the thickness at the edge  $x = x_0$ . This means that the present solution asymptotes to the solution for the constant thickness of the adhesive as  $x_0$  reduces to zero.

Let us now we consider the case when the adherends are an equal thickness aluminium alloy with  $h_1 = h_2 = 3\text{mm}$ , and  $E_1 = E_2 = 73\text{ GPa}$ . The thickness of the adhesive is distributed in accordance with a power law in the following form

reveals that, as a first estimate, Glinka's hypothesis is valid, i.e.  $W_{\max} / W_{\max}^e \cong 1$  see Figure 5.3. Consequently, we can use the elastic solution to estimate the strain energy density when the joint experiences significant plasticity. The validity of this approximation for other joint configurations will be investigated in Section 5.2.

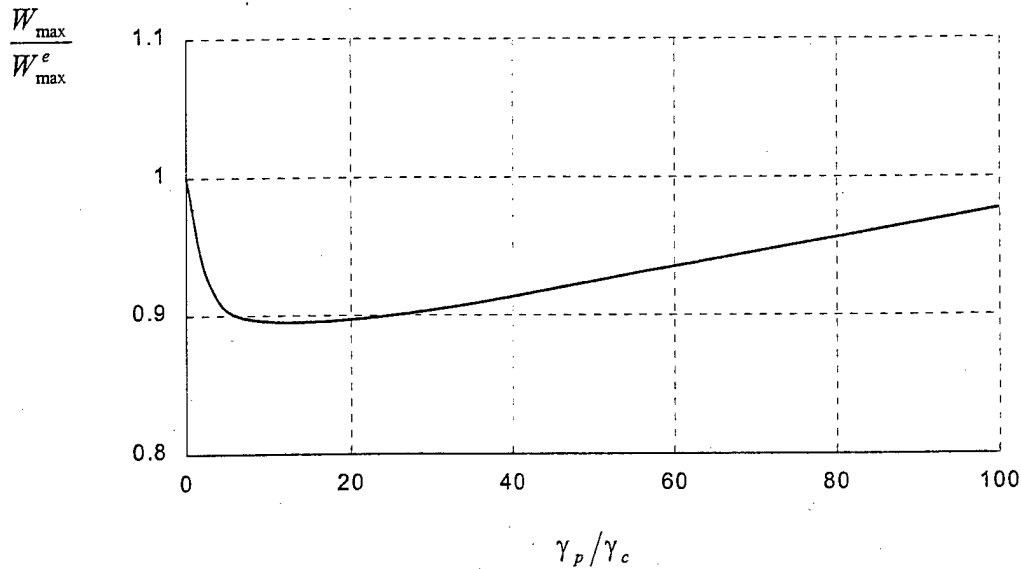


Fig 5.3. Ratio of the maximum strain energy for the elastic-perfectly-plastic solution to value obtained via an elastic analysis for a non-uniform adhesive thickness.

This figure also reveals that the energy density is a function of the local geometry of the joint. As such the Hart-Smith formulation cannot be used to predict the strength of the joint. In this case we must use the Glinka extension to the Hart-Smith formulation.

## 5.2 Effective mechanical properties of micro-inhomogeneous joints

If mechanical geometric characteristics of the adhesive joint vary from point to point and the characteristic scale of these changes is much smaller in comparison with the characteristic length of the joint, then the joint can be considered as micro-inhomogeneous structure (continuum). The problem of averaging of the mechanical properties of micro-inhomogeneous continua has long history. However, its asymptotic nature has only recently been understood and the corresponding mathematical formulation is presented in [20-21].

For the adhesive joint the Lagrangian  $\Lambda$  can be written as

$$2\Lambda = \frac{1}{(E_1 h_1)^{-1} + (E_2 h_2)^{-1}} [(\gamma t)_{,x}]^2 + \frac{G}{h} (\gamma t)^2 \quad (56)$$

This expression represents the sum of the strain energy densities for adherend and adhesive layers. Using Euler's equation it can be shown that this Lagrangian produces the same differential equation for  $\gamma t$ , i.e. equation (39), as presented previously.

The effective, or averaged, mechanical characteristics of a micro-inhomogeneous continuum can be determined by calculating the Legendre transformation,  $\Lambda^*(\gamma t, p)$ , of  $\Lambda$ , with respect to  $(\gamma t)_{,x}$ . In this case we find that

$$2\Lambda^*(\gamma t, p) = \left( (E_1(x)h_1(x))^{-1} + (E_2(x)h_2(x))^{-1} \right) p^2 + \frac{G(x)}{t(x)} (\gamma t)^2 \quad (57)$$

The averaged Lagrangian  $\langle \Lambda^* \rangle$  is then the integral of  $\Lambda^*$ , viz:

$$2\langle \Lambda^* \rangle = \left\langle (E_1 h_1)^{-1} + (E_2 h_2)^{-1} \right\rangle p^2 + \left\langle \frac{G}{t} \right\rangle (\gamma t)^2 \quad (58)$$

Here the expression  $\langle \cdot \rangle$  represents the average value of a function, or material properties, over a representative volume:

$$\langle \cdot \rangle = \frac{1}{V_R} \int_{V_R} (\cdot) dx \quad (59)$$

where  $V_R$  is much bigger than the characteristic scale of changes of the geometry or material properties of the adhesive joint.

Calculating the inverse Legendre transformation we obtain the averaged Lagrangian  $\langle \Lambda \rangle$

$$2\langle \Lambda \rangle = \left\langle (E_1 h_1)^{-1} + (E_2 h_2)^{-1} \right\rangle^{-1} [(\gamma h)_{,x}]^2 + \left\langle \frac{G}{t} \right\rangle (\gamma h)^2 \quad (60)$$

This equation reveals how to calculate effective parameters of the joint. To illustrate this methodology let us consider a simple example. Let the adhesive thickness of the joint has two equal fractions of thicknesses  $t_1$  and  $t_2$  such  $t_1 \ll t_2$ . Then the effective thickness  $\bar{t}$  of the joint is thus

$$\bar{t} = 2(t_1^{-1} + t_2^{-1})^{-1} \approx 2t_1 \quad (61)$$

which reveals that the joint will behave as a joint whose thickness is double the minimum thickness of the adhesive.

Let us now consider when the thickness of the adhesive is randomly distributed in accordance with a uniform probabilistic law between the values  $t_{\min}$  and  $t_{\max}$ . In this case we obtain an effective thickness  $\bar{t}$  where

$$\bar{t} = \frac{t_{\max} - t_{\min}}{\ln(t_{\max}/t_{\min})} \quad (62)$$

The same rule is also applied for the stiffness of the adherends  $Eh$ . However, note that for the shear modulus of the adhesive we have a different law for calculating the effective value. The effective shear modulus of the adhesive can be found as

$$\bar{G} = \langle G \rangle \quad (63)$$

After averaging the mechanical properties and the adherends and adhesive thicknesses we subsequently solve the governing differential equation:

$$(\gamma t)_{,xx} = \bar{\beta}^2 \gamma t \quad (64)$$

where  $\bar{\beta}^2$  is now a constant and represents the effective (or averaged) value for the joint. As a result of this formulation it follows that for joints where the adhesive thickness varies from point to point, and the characteristic scale of these changes is much smaller in comparison with the characteristic length, the value of  $W_{\max}$  is again independent of the shear modulus of the adhesive.

### 5.3 The effect of variable adhesive thickness and material non-linearity

Having established the Glinka hypothesis to be applicable to bonded joints with global bending prohibited let us now numerically consider the effect of both variable adhesive thickness and adhesive plasticity. We have seen that the energy density is a weak function of the adhesive shear modulus. It should thus follow that the hypothesis will also hold if the adhesive thickness is variable.

To further validate this hypothesis let us consider a symmetric double lap joint with a lower adherend (half)thickness  $T_1$  of 3mm, an upper adherend thickness  $T_2$  of 2mm, and  $E_1 = E_2 = 73,000$  MPa. The adhesive, which was assumed to be FM73, was allowed to be either one or two layers thick, i.e. 0.1mm or 0.2 mm thick, and had a Young's modulus of 1890 MPa and a Poisson's ratio of 0.35. Whilst the adhesive was assumed to have a post yield slope  $E'$  of 250 MPa and the yield stress of the adhesive was allowed to vary, see Table 5.1. Furthermore, at the critical end of the joint the thickness  $t_a^1$  was assumed to vary according to the following equation

$$\begin{aligned} t_a^1 &= t_a + A \cos(\pi x/2x_1) & \text{for } 0 < x < x_1 \\ t_a^1 &= t_a & \text{for } x > x_1 \end{aligned} \quad (65)$$

where  $t_a$ ,  $A$ ,  $x$ , and  $x_1$  are the nominal adhesive thickness, the amplitude of the perturbation of the thickness, the distance from the end of the joint and a characteristic length. In this initial study we chose, on the basis of past experience,  $x_1$  to be 3 mm, and varied the values of  $A$ . At this stage only monotonic loading was considered and to increase the amount of yielding the remote stress, in the lower adherend, was taken to be 144 MPa. The results of this analysis are summarised in Table 5.1.

To further illustrate the validity of Glinka's hypothesis for variable adhesive thickness let us consider the case when the adhesive is two layers thick, i.e.  $t_a = 0.2$  mm, and  $A = 0.05$  mm. This corresponds to a perturbation in the adhesive thickness equal to 25% of the base line thickness. In this case the distance over which the perturbation occurred, i.e.  $x_1$ , was varied from 1.5 to 5mm and the results are shown in Table 5.2.

Table 5.1 Percentage difference in  $\sqrt{W}$  and values of  $W$ ,  $\sigma = 360$  MPa

Yield stress and adhesive thickness	A (mm), the local increase in the adhesive thickness.		
	0.025	0.05	0.075
$\sigma_y = 40$ MPa $t_a = 0.2$ mm	18.1 W = 13.27	17.0 W = 11.54	15.5 W = 10.22
$\sigma_y = 68$ MPa $t_a = 0.2$ mm	13.9 W = 14.65	11.5 W = 13.12	9.5 W = 11.78
$\sigma_y = 40$ MPa $t_a = 0.1$ mm	25.0 W = 16.95	22.7 W = 14.80	20.5 W = 12.87
$\sigma_y = 68$ MPa $t_a = 0.1$ mm	21.6 W = 18.76	17.7 W = 16.75	15.33 W = 14.59

From this work we see that, for monotonic loading, although variable adhesive thickness changes the stress and the energy fields Glinka's hypothesis is still valid. This means that, for the present class of problems, even if there is variability in the thickness of the adhesive bond the energy field  $W_{\max}$  can be computed using only the elastic solution of the repair. The strength of the repair, provided failure is due to failure of the adhesive, can be then estimated from a purely linear elastic analysis. This will occur at the load level when  $W_{\max} = W_{\text{crit}}$ . This finding significantly simplifies the design process for repairs with a variable thickness adhesive.

Table 5.2 Percentage difference in  $\sqrt{W}$  and values of  $W$  (MPa),  $A = 0.05$  mm

Yield stress and post yield slope	Remote stress $\sigma$ (MPa)				
	144	200	240	288	360
$\sigma_y = 68$ MPa $t_a = 0.2$ mm, $x_1 = 1.5$ mm	0.0 W = 2.58	0.4 W = 4.90	2.5 W = 6.81	6.0 W = 9.11	11.1 W = 12.7
$\sigma_y = 40$ MPa $t_a = 0.2$ mm, $x_1 = 1.5$ mm	8.7 W = 3.05	5.5 W = 5.49	2.2 W = 6.85	9.0 W = 8.53	16.7 W = 11.1
$\sigma_y = 68$ MPa $t_a = 0.2$ mm, $x_1 = 3$ mm	0.0 W = 2.68	0.5 W = 5.08	2.8 W = 7.03	6.4 W = 9.39	11.5 W = 13.12
$\sigma_y = 40$ MPa $t_a = 0.2$ mm, $x_1 = 3$ mm	7.3 W = 3.09	4.3 W = 5.59	3.5 W = 7.08	9.4 W = 8.80	17.0 W = 11.54
$\sigma_y = 68$ MPa $t_a = 0.2$ mm, $x_1 = 5$ mm	0.0 W = 2.80	0.8 W = 5.28	3.2 W = 7.28	6.9 W = 9.70	12.1 W = 13.53
$\sigma_y = 40$ MPa $t_a = 0.2$ mm, $x_1 = 5$ mm	6.6 W = 3.18	3.7 W = 5.75	3.0 W = 7.32	9.9 W = 9.09	17.5 W = 11.91

## 6. REFERENCES

1. Callinan, R. J. Sanderson, S. Keeley, D. 1997, "Finite Element Analysis of an F-111 Lower Wing Skin Fatigue Crack Repair", DSTO, Melbourne. DSTO-TN-0067.

2. Baker, A.A. Jones, R., "Bonded Repair of Aircraft Structures", Martinus Nijhoff, Dordrecht, 1988.
3. Rose, L. R. F., "An Application of the Inclusion Analogy for Bonded Reinforcements", Int J. Solid Structures Vol 17 pp 827-838, Great Britain, 1981.
4. L. J. Hart-Smith, "Adhesively bonded double lap joints", NASA Langley Research Center Report NASA CR-112235, January 1973.
5. Rose, L. R. F., Minute to WGCdr Eric Wilson regarding corrections to ref [2] and suggestion for the F-111 Boron repair case, 1994.
6. Fredell, R. S., Damage Tolerant Repair Techniques for Pressurized Aircraft Fuselages", Dr. Thesis, Delft University of Technology, June 1994.
7. Baker, A. A. Davis, M. J. Hawkes, G. A., Proceedings on the 10<sup>th</sup> international committee on Aeronautical Fatigue (ICAF) Symposium, paper 4.3, 1979.
8. Wang, C. H. Rose, L. R. F. Callinan, R. Baker, A. A., Thermal Stresses in a plate with a Circular Reinforcement, International Journal of Solid Structures, 1998.
9. Chiu, D. Rees, P. Chalkley and R. Jones, "Designing for damage tolerant repairs", Journal of Composite Structures, 28, 1, 19-38, 1994.
10. D. Roach and P. Walkington, "Full scale structural and NDI validation tests of bonded composite doublers for aircraft applications", Sandia Report, SAND98-1015, February 1999.
11. D. Roach, "Damage tolerance assessment of bonded composite doublers for commercial aircraft applications", Sandia National Laboratories/Department of Energy, Sandia Report, SAND98-1016, August 1998.
12. R. Jones, L. Molent, and S. Pitt, "Australian studies on multi-site damage of fuselage lap joints", Journal of Theoretical and Applied Fracture Mechanics, 32, 18-100, 1999.
13. W.K. Chiu, P.D. Chalkley, R. Jones, Effects of temperature on the stress/strain behaviour of film adhesives FM73, Computers and Structures, pp 1-7, 1994.
14. Glinka G., "Calculation of inelastic notch-tip strain-stress histories under cyclic loading", Engineering Fracture Mechanics, 22, 5, 839-854, 1985.
15. R. Jones, W. K. Chiu and S. Hanna, Potential failure mechanisms of bonded composite repairs for metal and concrete, Theoretical and Applied Fracture Mechanics, 21, 107-119, 1994.

16. L. Molent, R. J. Callinan and R. Jones, Structural aspects of the design of an all boron/epoxy reinforcement for the F-111C wing pivot fitting, *Journal of Composite Structures* 11, 1, 57-83, 1989.
17. R. Jones, W. K. Chiu, and J. P. G. Sawyer, "Composite repairs to cracks in thick metallic components", *Journal of Composite Structures* (in press).
18. P. Chalkley, and A. A. Baker, "Development of a generic repair joint for certification of bonded composite repairs", *Journal of Adhesion and Adhesives*, 19, pp121-137, 1999.
19. J. J. A. Massar, "The fatigue characteristics of repaired and unrepaired C141 panels", Internal Report, HQ USAF Academy/ ADFEM, February 1999.
20. N. Bahvalov, "Averaged characteristics of bodies with periodic structure", Report of the USSR Academy of Sciences, Vol. 218, pp.1046-1048, 1974.
21. V. Zhikov, S. Kozlov, O. Oleinik and H. Ngoan, 1979, "Averaging and G-convergence of differential operators", *Advances of the Mathematical Science*, Vol.34, pp. 65-133, 1979.
22. Damage Tolerance Design Handbook, Volume 4, December 1983.
23. O. C. Zenkiewicz, "The finite element method in engineering science", McGraw-Hill, London, 1971.